Karlsruher Institut für Technologie

IEKP-KA/2015-7

SEARCH FOR HIGGS BOSONS BEYOND THE STANDARD MODEL IN PROTON-PROTON COLLISIONS WITH THE CMS DETECTOR AT THE LHC

ZUR ERLANGUNG DES AKADEMISCHEN GRADES EINES
DOKTORS DER NATURWISSENSCHAFTEN
AN DER FAKULTÄT FÜR PHYSIK
DES KARLSRUHER INSTITUTS FÜR TECHNOLOGIE (KIT)

GENEHMIGTE

DISSERTATION

VON

DIPL.-PHYS. FELIX FRENSCH
AUS BRUCHSAL

Tag der mündlichen Prüfung: 15. Mai 2015

Referent:	Prof. Dr. Wim de Boer
Korreferent:	Prof. Dr. Günter Quast
Betreuer:	Dr. Roger Wolf

Contents

List of Figures

List of Tables

Chapter 1

Introduction

On the fourth July of 2012 a new particle had been discovered [1; 2]. After analysing the full dataset of 2011 and 2012 collected by the ATLAS [3] and CMS [4] detectors the newly found boson is measured to be compatible with the Higgs boson as predicted by the Standard Model (SM) [5–9] within $\mathcal{O}(10\%)$ uncertainty. The SM has been tested in many different experiments and was capable of describing the observation in every single one. However, the SM is known to be insufficient to describe all phenomena observed in nature. Open questions, such as the origin of dark matter [10–12] or the Hierarchy Problem [13], can not be explained in the context of the SM. Theories beyond the SM should describe all observations equally well and in addition should be able to answer these open questions.

In the Higgs boson sector there are in general two different approaches to search for physics beyond the Standard Model (BSM). One possibility is to precisely measure the discovered Higgs boson. Deviations from SM predictions, such as different coupling strengths to fermions and bosons, would be a sign for BSM. Since many BSM theories have an extended Higgs sector the other possibility is to search for additional Higgs bosons. The Minimal Supersymmetric Standard Model (MSSM), a type-2 Two-Higgs-Doublet model, predicts five Higgs bosons: A light scalar, h, a heavy scalar, H, a pseudoscalar, A, and two charged Higgs bosons, $H^{\pm}$. In this thesis the neutral Higgs bosons are jointly denoted by ϕ. The coupling of the Higgs bosons to down-type fermions is usually enhanced over large parameter spaces in the MSSM. Thus, the decay channel to tau leptons, $\phi \to \tau\tau$, is a perfect channel to search for additional neutral Higgs bosons. Object reconstruction methods used in the $\phi \to \tau\tau$ analysis are presented. The backgrounds are suppressed exploiting the missing transverse energy distribution which originates from the neutrinos in the tau lepton decays. Remaining major backgrounds are estimated based on data-driven methods. Smaller backgrounds are estimated relying on Monte Carlo predictions. The results are interpreted in different ways. Since no excess has been found limits on different signal hypothesis are set. As a first approach model dependent upper limits on the considered production processes, gluon-gluon fusion, (ggϕ), and Higgs production in association with b-quarks, (bbϕ), are computed. In addition, model dependent limits are calculated on eight different MSSM benchmark scenarios and a benchmark type-2 Two-Higgs-Doublet model (2HDM). To further enhance the

sensitivity to certain new physic models the $\phi \rightarrow \tau\tau$ analysis is combined with other searches for additional Higgs bosons.
The $\phi \rightarrow \tau\tau$ analysis has been published by the CMS collaboration [14] and is based on the full dataset collected by the CMS detector in the years 2011 and 2012 at a center-of-mass energy of 7 TeV and 8 TeV, respectively. Preliminary results based on a subset of the collected data have been published in [15; 16]. This thesis extends the publication to new interpretations. The analyses used in the combination have been published or are within the process of being published [17; 18].

In chapter 2 a theoretical introduction is given with the focus on the Higgs sector in the SM and in considered new physic models. The CMS detector is briefly described in chapter 3. The $\phi \rightarrow \tau\tau$ analysis strategy is explained in chapter 4. A gist of this thesis is the interpretation of the collected and analysed data. Thus, the statistics chapter 5 is of particular importance for this work. The interpreted results of the $\phi \rightarrow \tau\tau$ analysis are discussed in chapter 6. In chapter 7 a combination of the $\phi \rightarrow \tau\tau$ analysis with other BSM analyses is presented. A summary and outlook is given in chapter 8.

Chapter 2

Theoretical Introduction

This chapter provides a short introduction to the theoretical background of this thesis.

The SM of particle physics [9] is briefly introduced in section 2.1. A special focus is set on the Englert-Brout-Higgs-Guralnik-Hagen-Kibble mechanism. Open questions, which the SM can not explain, are outlined in section 2.1. The minimal supersymmetric extension of the Standard Model (MSSM) is explained in section 2.2. Since the MSSM is a special type of a 2HDM, the general idea of these models is introduced in section 2.3.

A more detailed introduction to the SM can be found in [9]. The theory of Supersymmetry is explained further in [19] and a detailed introduction to 2HDMs is given in [20].

2.1 The Standard Model of Particle Physics

The SM is a gauge theory with the symmetry groups

$$SU(3)_C \otimes SU(2)_{I_3} \otimes U(1)_Y \tag{2.1}$$

with the index C for color charge, I_3 for weak isospin and Y for weak hypercharge. The weak isospin and the weak hypercharge are connected to the charge Q:

$$Q = I_3 + \frac{Y}{2} \tag{2.2}$$

It consists of the elementary particles shown in table 2.1 The possible interactions between the particles are illustrated in figure 2.1. Based on the condition that the action S is extremal $\delta S = 0$, also known as Hamiltons principle, the fundamental motions could be explained by the Lagrange formalism:

$$S = \int L \; dt = \int \mathcal{L}(\phi, \partial\phi) \; d^4x \; , \tag{2.3}$$

where x is the spacetime coordinate and ϕ are fields. The SM Lagrangian $\mathcal{L}_{SM}$ is:

$$\mathcal{L}_{SM} = \mathcal{L}_{\text{ferm}} + \mathcal{L}_{\text{gauge}} + \mathcal{L}_{\text{Higgs}} + \mathcal{L}_{\text{Yukawa}} \; . \tag{2.4}$$

Fermions Spin=1/2							
	1. Gen	2. Gen	3. Gen	SU(3)$_C$	SU(2)$_{I_3}$	Y	Q
Quarks	$\begin{pmatrix}u\\d\end{pmatrix}_L$	$\begin{pmatrix}c\\s\end{pmatrix}_L$	$\begin{pmatrix}t\\b\end{pmatrix}_L$	3	2	1/3	2/3 $-1/3$
	u$_R$	c$_R$	t$_R$	3	1	4/3	2/3
	d$_R$	s$_R$	b$_R$	3	1	-2/3	-1/3
Leptons	$\begin{pmatrix}\nu_e\\e\end{pmatrix}_L$	$\begin{pmatrix}\nu_\mu\\\mu\end{pmatrix}_L$	$\begin{pmatrix}\nu_\tau\\\tau\end{pmatrix}_L$	1	2	-1	0 -1
	e$_R$	μ_R	τ_R	1	1	-2	-1

Gauge bosons Spin=1					
Interaction	Boson	SU(3)$_C$	SU(2)$_{I_3}$	Y	Q
Electromagnetic	γ	1	1	0	0
Weak	Z^0 $W^\pm$	1	3	0	0 ±1
Strong	g$_1$..g$_8$	8	1	0	0

Higgs bosons Spin=0					
Field	Boson	SU(3)$_C$	SU(2)$_{I_3}$	Y	Q
Higgs	h	1	2	1	0

Table 2.1: The particle content of the SM. The matter is built by fermions. The right(left) handed singlets(doublets) are noted by an index R(L). Interactions between the fermions is explained by the gauge bosons. The Higgs boson is needed to explain the masses of the gauge bosons and fermions.

The kinetic fermion part,

$$\begin{aligned}\mathcal{L}_{\text{ferm}} &= i(\overline{\nu}_e, \overline{e})_L \gamma^\mu D_\mu (\nu_e, e)_L + i\overline{e}_R \gamma^\mu D_\mu e_R \\ &+ i(\overline{u}, \overline{d})_L \gamma^\mu D_\mu (u, d)_L + i\overline{u}_R \gamma^\mu D_\mu u_R + i\overline{d}_R \gamma^\mu D_\mu d_R \\ &+ 2.\text{Gen} + 3.\text{Gen} \ ,\end{aligned} \tag{2.5}$$

covers the interaction of fermions through gauge bosons. The covariant derivative, D_μ, includes the gauge boson fields: the photon, Z and W fields, B_μ and W_μ^k, and the gluon fields, G_μ^a. The gauge part of the Lagrangian,

$$\mathcal{L}_{\text{gauge}} = -\frac{1}{4}(B_{\mu\nu}B^{\mu\nu} + W_{\mu\nu}^k W^{\mu\nu,k} + G_{\mu\nu}^a G^{\mu\nu,a}) \ , \tag{2.6}$$

handles the interaction between gauge bosons and the propagation of these. The field strength tensors, $B_{\mu\nu}$, $W_{\mu\nu}$ and $G_{\mu\nu}^a$ include the gauge boson fields.
Initially these two parts fulfil all conditions to describe the elementary particles and the interactions between them. But introducing mass terms to the SM Lagrangian

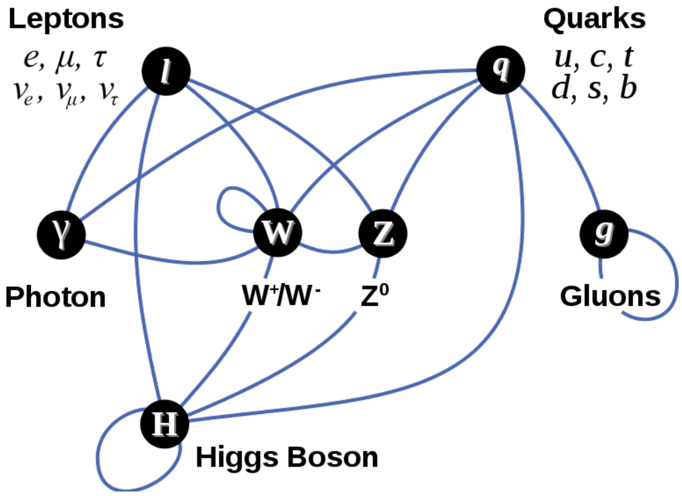

Figure 2.1: This figure shows the possible interactions between different fermions and bosons. The blue lines connecting two different particles or particle groups visualize that these particles can interact with each other. Self-interactions are possible. This picture is taken from [21].

leads to a violation of the gauge symmetry. This problem was solved by the so called Englert-Brout-Higgs-Guralnik-Hagen-Kibble mechanism [5; 7; 8] which describes a spontaneous symmetry breaking [6; 22].
The idea is to introduce a new scalar field doublet, the Higgs field Φ, with the Lagrangian:

$$\mathcal{L}_{\text{Higgs}} = (\tilde{D}^{\mu}\Phi)^{\dagger}(\tilde{D}_{\mu}\Phi) - V(\Phi) \ . \tag{2.7}$$

The covariant derivative $\tilde{D}_{\mu}\Phi$ is introduced to ensure gauge invariance which here does not include the gluon fields, since gluons do not interact with the Higgs field. The Higgs field $\Phi(x)$ is a complex scalar field with four degrees of freedom $\phi_{1-4}(x)$ depending on the spacetime coordinate x. The Higgs field is described as a doublet, carrying hypercharge $Y = 1$ and having a charged, $\phi^{+}(x)$, and a neutral, $\phi^{0}(x)$, component. Thus, the Higgs field Φ could be written as:

$$\Phi(x) = \begin{pmatrix} \phi^{+}(x) \\ \phi^{0}(x) \end{pmatrix} = \frac{1}{\sqrt{2}} \begin{pmatrix} \phi_1(x) + i\phi_2(x) \\ \phi_3(x) + i\phi_4(x) \end{pmatrix} \ . \tag{2.8}$$

To understand the spontaneous symmetry breaking the potential part of the Higgs Lagrangian, equation (2.7),

$$V(\Phi(x)) = \mu^2(\Phi^{\dagger}(x)\Phi(x)) + \lambda(\Phi^{\dagger}(x)\Phi(x))^2 \ . \tag{2.9}$$

has to be studied. The sign of the constant λ has to be positive to ensure a stable energy minimum exists. Depending on the sign of the constant μ^2 the Higgs potential has the shape as shown in figure 2.2. In case of positive values for μ^2 the vacuum expectation value would be zero:

$$|\langle 0|\Phi(x)|0\rangle| = 0 \ . \tag{2.10}$$

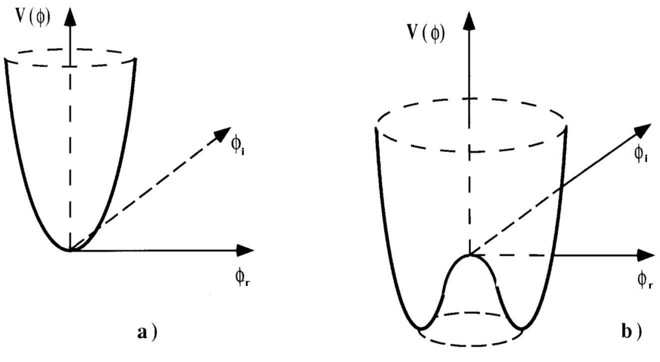

Figure 2.2: This figure shows an two dimensional illustration of the four dimensional Higgs potential $V(\phi(x))$ in the case of $\mu^2 \geq 0$ (left) and $\mu^2 < 0$ (right) is shown. The $\phi_r(x)$ axis represent the real part of the Higgs field $\phi_1(x)$ and $\phi_3(x)$ and analogous the $\phi_i(x)$ axis represent the imaginary part of the Higgs field $\phi_2(x)$ and $\phi_4(x)$. The figure is taken from [23].

In contrast if $\mu^2 < 0$ the energy minimum is not equal to zero. The Higgs potential is minimal at:

$$|\Phi(x)|^2 = \Phi^\dagger(x)\Phi(x) = \frac{1}{2}(\Phi_1(x)^2 + \Phi_2(x)^2 + \Phi_3(x)^2 + \Phi_4(x)^2) = \frac{-\mu^2}{2\lambda} = \frac{v^2}{2}\ . \quad (2.11)$$

In contrast to the $\mu^2 \geq 0$ case the ground state in the case $\mu^2 < 0$ is degenerate. Shown in figure 2.2 by the circle of minima at the right figure in contrast to the single minimum at the point of origin in the left figure. The Higgs potential is symmetric, but not the ground state for the $\mu^2 < 0$ case. This is a spontaneous symmetry breaking [6; 22]. The Goldstone theorem [22; 24] states that every spontaneous broken symmetry leads to a massless Goldstone boson. As shown in the following, this spontaneous symmetry breaking effectively gives the W^-, W^+ and Z boson masses by absorbing Goldstone bosons.
Through a $SU(2)_{I_3}$ transformation a certain ground state can be transformed to another ground state. Since the vacuum should be neutral, a ground state is picked, where the charged part of the Higgs field is set to zero $|\phi^+(x)| = 0$, hence the Higgs field $\Phi(x)$ transforms to:

$$\Phi_0(x) = \begin{pmatrix} 0 \\ v \end{pmatrix}, \text{ with } v = \sqrt{\frac{-\mu^2}{2}}\ . \quad (2.12)$$

Fluctuations around this ground state could be written as:

$$\Phi_0(x) = e^{\epsilon^k(x)\sigma^k} \begin{pmatrix} 0 \\ v + h(x) \end{pmatrix} \quad (2.13)$$

The Pauli matrices are denoted by σ^k. Along the four degrees of freedom there are four fluctuation directions: $\epsilon^k(x)$ and $h(x)$. Three $\epsilon^k(x)$ along the minimum of the potential, meaning along the circle of the right figure 2.2 and one $h(x)$ radial with respect to the circle (note that figure 2.2 is only a two dimensional illustration of the four dimensional Higgs potential). The three tangential fluctuation $\epsilon^k(x)$ do not pass any curvature of the Higgs potential $V(\Phi(x))$, thus they are interpreted as massless Goldstone bosons. Contrary to the tangential fluctuations the single radial fluctuation passes a curvature of $V(\Phi(x))$, leading to the massive Higgs boson, $h(x)$. Since the vacuum expectation value is not equal to zero as seen in equation (2.14), the three Goldstone bosons could be eliminated by a local gauge invariant $SU(2)_{I_3}$ transformation:

$$\Phi(x) \to \Phi'(x) = e^{-\epsilon^k(x)\sigma^k} \begin{pmatrix} 0 \\ v + h(x) \end{pmatrix} \tag{2.14}$$

The three degrees of freedom stay and remain as longitudinal polarizations of the three massive bosons W^-, W^+ and Z, effectively given mass to them.

In a similar way the masses of the fermions are generated in the Yukawa part of the Lagrangian through interactions of the fermions with the Higgs field:

$$\begin{aligned} \mathcal{L}_{\text{Yukawa}} = {} & k_e^{ij}\left[(\overline{\nu}_e, \overline{e})^i_L \Phi e^j_R + \overline{e}^j_R \Phi^\dagger (\nu_e, e)^i_L\right] \\ & + k_u^{ij}\left[(\overline{u}, \overline{d})^i_L \Phi^C u^j_R + \overline{u}^j_R (\Phi^C)^\dagger (u, d)^i_L\right] \\ & + k_d^{ij}\left[(\overline{u}, \overline{d})^i_L \Phi d^j_R + \overline{d}^j_R \Phi^\dagger (u, d)^i_L\right] \ , \end{aligned} \tag{2.15}$$

with an implicit sum over the family indices i and j. The matrices k_e^{ij}, k_u^{ij} and k_d^{ij} define the Yukawa coupling between the Higgs doublet and the charged leptons, up-type and down-type quarks, respectively. The coupling strength of the Higgs field to the corresponding fermion field which is proportional to the mass. A second representation of the Higgs doublet with $Y = -1$ is needed for the coupling to up-type quarks since the mass terms should be hyperchargeless:

$$\Phi^C = -i\sigma^2\Phi^* = \begin{pmatrix} \phi^{0*}(x) \\ -\phi^-(x) \end{pmatrix} . \tag{2.16}$$

Hints for Physics beyond the Standard Model

Although the SM has proven to predict nature in an incredible accuracy, there are some open questions for which the SM does not deliver a satisfactory reply and therefore might give us a hint for BSM physics. Some of them are listed below.

- **Number of free Parameters**:
  The SM includes 18 free parameters[1]. Some BSM theories can reduce the number of free parameters.

- **Fine Tuning**:
  Radiation corrections to the Higgs mass include quadric divergent terms. In the SM at high energies these terms are handled with extreme fine tuning.

---

[1] Neutrino masses and mixing parameters are not counted which originally do not enter the SM

- **Hierarchy Problem**:
  The electroweak energy scale is very small compared to the Grand Unification Theory (GUT) scale, where it is expected that the electroweak and the strong force can be unified. This difference in the energy scale is not explained in the SM [13].

- **Unification of Couplings**:
  The couplings g', g and g_s correspond to the symmetry groups $U(1)_Y$, $SU(2)_{I_3}$ and $SU(3)_C$, respectively. They increase, g', or decrease, g and g_s, with increasing energy. An unification [23; 25] of all three interactions at a certain energy level M_{GUT} would be a manifestation of the unique origin of all three forces, but in the SM this is not possible.

- **Origin of Matter**:
  In the universe obviously the amount of matter dominates anti-matter. The CP violation in the SM can not explain this imbalance.

- **Dark Matter and Dark Energy**:
  Cosmological observation [10–12] have shown that about 25% of mass energy constitutes of so called dark matter in contrast to only about 5% visible matter. The rest is so called dark energy [26]. The SM can neither explain the large amount of dark matter nor the dark energy.

2.2 The Minimal Supersymmetric Standard Model

Supersymmetry as general idea for a BSM theory[2] delivers answers to some of these open questions. It introduces a new symmetry between fermions and bosons. Each fermion gets a bosonic superpartner and vice versa.

$$Q_{\text{SUSY}} \left|\text{fermion}\right\rangle = \left|\text{boson}\right\rangle \quad \text{and} \quad Q_{\text{SUSY}} \left|\text{boson}\right\rangle = \left|\text{fermion}\right\rangle \tag{2.17}$$

Supersymmetric theories can have more than one generator, Q_{SUSY}, but in this thesis only the *minimal* extension of the SM is discussed. The particle content of the MSSM is shown in table 2.2. In contrast to the SM, where only one doublet is needed as shown in equation (2.15), the MSSM needs two Higgs doublets, Φ_u and Φ_d,

$$\begin{aligned} \Phi_u(x) &= \begin{pmatrix} \Phi_u^+(x) \\ \Phi_u^0(x) \end{pmatrix} = \begin{pmatrix} \phi_{u,1}(x) + i\phi_{u,2}(x) \\ \phi_{u,3}(x) + i\phi_{u,4}(x) \end{pmatrix} \\ \Phi_d(x) &= \begin{pmatrix} \Phi_d^0(x) \\ \Phi_d^-(x) \end{pmatrix} = \begin{pmatrix} \phi_{d,1}(x) + i\phi_{d,2}(x) \\ \phi_{d,3}(x) + i\phi_{d,4}(x) \end{pmatrix} \end{aligned} \tag{2.18}$$

to be able to give mass to the up- and down-type fermions. The Higgs doublets have in total eight degrees of freedom, $\phi_{u,1..4}$ and $\phi_{d,1..4}$. The Higgs potential of the

---

[2] Supersymmetry does not name a single well defined theory but more a general idea which has many different realizations.

Superfield	Bosons	Fermions	SU$_C$(3)	SU$_{I_3}$(2)	U$_Y$(1)
Gauge					
G^a	g^a	$\tilde{g}^a$	8	1	0
V^k	W^k (W$^\pm$,Z)	$\tilde{W}^k(\tilde{W}^\pm,\tilde{Z})$	1	3	0
B	B(γ)	$\tilde{B}(\tilde{\gamma})$	1	1	0
Matter					
L$_i$	$\tilde{L}_i = (\tilde{\nu},\tilde{e})_L$	$L_i = (\nu, e)_L$	1	2	-1
E$_i$	$\tilde{E}_i = \tilde{e}_r$	$E_i = e_R$	1	1	-2
Q$_i$	$\tilde{Q}_i = (\tilde{u},\tilde{d})_L$	$Q_i = (u, d)_L$	3	2	1/3
U$_i$	$\tilde{U}_i = \tilde{u}_R$	$U_I = u_R$	3*	1	4/3
D$_i$	$\tilde{D}_i = \tilde{d}_R$	$D_i = d_R$	3*	1	-2/3
Higgs					
Φ_u	Φ_u	$\tilde{\Phi}_u$	1	2	-1
Φ_d	Φ_d	$\tilde{\Phi}_d$	1	2	1

Table 2.2: Shown is the particle content of the MSSM. Each boson gets a fermionic superpartner and vice versa.

MSSM,

$$\begin{aligned} V(\Phi_u,\Phi_d) = (|\mu|^2 + m^2_{\Phi_u})|\Phi^0_u|^2 + (|\mu|^2 + m^2_{\Phi_d})|\Phi^0_d|^2 + (b\Phi^0_u\Phi^0_d + \text{h.c.}) \\ + \frac{1}{8}(g^2 + g'^2)(|\Phi^0_u|^2 - |\Phi^0_d|^2)^2 \ , \end{aligned} \tag{2.19}$$

has to fulfil the conditions

$$\begin{aligned} 2b &< 2|\mu|^2 + m^2_{\Phi_u} + m^2_{\Phi_d} \\ b^2 &> (|\mu|^2 + m^2_{\Phi_u})(|\mu|^2 + m^2_{\Phi_d}) \end{aligned} \tag{2.20}$$

in order to give real and positive solutions.
Equally to the SM case, it is possible to eliminate the charged components of the Higgs doublets using a $SU(2)_{I_3}$ transformation.
From the eight degrees of freedom three are absorbed by the longitudinal modes of the massive Z, and $W^\pm$ gauge bosons. The remaining five manifest in the five Higgs bosons of the MSSM:

- A CP even light neutral scalar boson h
- A CP even heavy neutral scalar boson H
- A CP odd neutral pseudoscalar boson A
- Two charged scalar bosons $H^\pm$

On tree level the Higgs masses can be calculated to:

$$\begin{aligned} m_A^2 &= \frac{2b}{\sin(2\beta)} = 2|\mu|^2 + m_{H_u}^2 + m_{H_d}^2 \ , \\ m_{h,H}^2 &= \frac{1}{2}\left(m_A^2 + m_Z^2 \mp \sqrt{(m_A^2 - m_Z^2)^2 + 4 m_A^2 m_Z^2 \sin^2(2\beta)} \right) \ , \\ m_{H^\pm}^2 &= m_A^2 + m_W^2 \ , \end{aligned} \tag{2.21}$$

with the ratio of the vacuum expectation values of the two doublets:

$$\tan\beta = \frac{\langle \Phi_u \rangle}{\langle \Phi_d \rangle} \ . \tag{2.22}$$

The mixing angle α is defined by:

$$\frac{\sin(2\alpha)}{\sin(2\beta)} = -\left(\frac{m_H^2 + m_h^2}{m_H^2 - m_h^2}\right), \qquad \frac{\tan(2\alpha)}{\tan(2\beta)} = -\left(\frac{m_A^2 + m_Z^2}{m_A^2 - m_Z^2}\right) \tag{2.23}$$

and varies within $-\pi/2 < \alpha < 0$. Therefore, the Higgs sector of the MSSM is fully described by the mass of the pseudoscalar m_A and $\tan\beta$. The mass of the lightest higgs boson h is on tree level bound to:

$$m_h^2 \leq m_Z |\cos(2\beta)| \leq m_Z^2 \ . \tag{2.24}$$

This is already excluded on at least 95% confidence level by collider expiriments [27]. But higher order corrections can significantly shift the mass to higher values. These corrections depend on additional SUSY parameters which will be defined in the following.

2.2.1 MSSM Benchmark Scenarios

In this thesis MSSM benchmark scenarios [28–31] are tested. These scenarios exhibit interesting phenomenology while satisfying the boundaries set by direct searches performed at the Large Electron Positron (LEP) collider, the Tevatron and the LHC. In particular, the scenarios fulfil the mass requirements of the new discovered Higgs boson over large parameter space, hence one of the scalar Higgs bosons has a mass of 125 ± 3 GeV. The mass uncertainty of ± 3 GeV is dominated by theory uncertainties [32].

All scenarios are defined not allowing CP violation. As shown above, the masses of the five Higgs bosons at tree level are defined by the ratio of the vacuum expectation values of the two Higgs doublets, $\tan\beta$, the mass of the pseudoscalar Higgs boson, m_A, the Z boson mass, m_Z, and the W boson mass, m_W. The $t/\tilde{t}$, $b/\tilde{b}$ and $\tau/\tilde{\tau}$ sectors dominate the contributions to the Higgs boson masses coming from radiative corrections. These sectors are described by following parameters, which thus are found to be relevant for defining the MSSM Higgs sector:

- m_t the mass of the top quark,

- m_b the mass of the bottom quark,
- M_{SUSY} the mass of the third generation squarks, namely stops and sbottoms,
- μ the higgsino mass parameter which also influences the mass of the supersymmetric partners of the photon, W and Z boson (charginos and neutralinos),
- $M_{\tilde{l}_3}$ the mass of the third generation sleptons, the staus,
- M_1 the $U(1)_Y$ gaugino mass parameter,
- M_2 the $SU(2)_{I_3}$ gaugino mass parameter,
- A_t, A_b and A_τ the triliniar couplings of the stops, sbottoms of staus and
- X_t, X_b and X_τ the mixing parameter of the stops, sbottoms of staus.

For most scenarios the gaugino mass parameters M_1 and M_2 are assumed to be related at the GUT scale:

$$M_1 = \frac{5}{3}\frac{\sin_{\theta_W}{}^2}{\cos_{\theta_W}{}^2}M_2 \qquad \text{with } \sin_{\theta_W} = \sqrt{1-\cos_{\theta_W}{}^2}\,,\ \cos_{\theta_W} = \frac{m_W}{m_Z}\ . \tag{2.25}$$

The mixing parameters X_i $(i = t, b, \tau)$, the triliniar couplings A_i $(i = t, b, \tau)$ and the higgsino mass parameter μ are related via the off-diagonal elements of the mixing matrices in the sbottom, stop or stau sector:

$$X_t = A_t - \mu\cot\beta\,,\ X_b = A_b - \mu\tan\beta\,,\ X_\tau = A_\tau - \mu\tan\beta\ . \tag{2.26}$$

Following parameters suffice to define the model:

$$m_A, \tan\beta, m_t, m_b, M_{SUSY}, \mu, M_{\tilde{l}_3}, M_2, A_t, A_b, A_\tau, X_t\ . \tag{2.27}$$

The following parameters have only a minor effect on the MSSM Higgs sector and are fixed to the stated values:

- the masses of the first and second generation squarks $M_{\tilde{q}_{1,2}} = 1500\,\text{GeV}$,
- the masses of the first and second generation sleptons $M_{\tilde{l}_{1,2}} = 500\,\text{GeV}$ and
- the triliniar couplings of the first and second generation squarks and sleptons $A_{\tilde{f}_{1,2}} = 0$.

These values are chosen in agreement with current exclusion limits of direct searches. In all scenarios a top mass of 172.5 GeV is used even if it is stated otherwise in the benchmark paper, since the LHC working groups agreed upon the SM parameters defined in [33].

In the following, a brief introduction to each scenario is given. An overview of the different scenarios can be found in table A.1 in appendix A.

$m_h^{\max}$ scenario

This scenario originates from LEP times, meaning it was proposed before the discovery of the Higgs boson at 125 GeV. It yields conservative exclusion limits on $\tan\beta$ in LEP Higgs searches [34]. The ratio of the stop mixing parameter and the masses of the third generation squarks is chosen $|X_t/M_{SUSY}| = 2$. This leads to a maximization of the mass of the lightest scalar h for high m_A and $\tan\beta$. The considered parameter space is spanned by $90\,\text{GeV} \leq m_A \leq 1000\,\text{GeV}$ and $0.5 \leq \tan\beta \leq 60$.
In the light of the discovered Higgs boson at 125 GeV this scenario becomes less relevant, since only a small parameter space agrees with the mass requirement of the new state when taking into account a mass uncertainty of 3 GeV as a combination of experimental and theoretical uncertainties.
An older version of the $m_h^{\max}$ scenario [28] is used in this thesis. In the updated $m_h^{\max}$ scenario the b-quark mass is $m_b = 4.213\,\text{GeV}$. Also the gluino mass is shifted from $m_{\tilde{g}} = 800\,\text{GeV}$ to $m_{\tilde{g}} = 1500\,\text{GeV}$ to address the latest results of direct SUSY searches. However, these changes have only minor effect on the allowed region and on the obtained exclusion limits. To be able to compare the results with past publications, the updated $m_h^{\max}$ scenario is not used.

m_h^{mod} scenario

In the light of the new state at 125 GeV most parts of the $m_h^{\max}$ scenario are already excluded. The m_h^{mod} scenario is obtained by decreasing the ratio of the stop mixing parameter and the masses of the third generation squarks $|X_t/M_{SUSY}|$, hence the mass of the lightest scalar m_h is effectively reduced. Therefore, large parameter spaces again become available. Two versions of the m_h^{mod} scenario have been proposed. In the $m_h^{\text{mod+}}$ scenario, the stop mixing is positive $X_t = 1.5\ M_{SUSY}$, which results in a better agreement with the experimental measurements of $(g-2)_\mu$ [35]. In the $m_h^{\text{mod-}}$ scenario the stop mixing parameter is negative $X_t = -1.9\ M_{SUSY}$. This results in a branching fraction $\mathcal{B}(b \to s\gamma)$ which agrees better with actual measurements [36]. The same m_A and $\tan\beta$ range as in the $m_h^{\max}$ scenario is used.

low-tan β-high scenario

This scenario is in particular interesting for Higgs to Higgs decays. For high values of $\tan\beta$ the decay to down-type quarks are enhanced and therefore the branching fractions $A \to Zh$ and $H \to hh$ are suppressed. Depending on the mass of the supersymmetric partners of the photon, W and Z boson (charginos and neutralinos), decays of the heavy Higgs bosons into these particles are possible. Thus, in this scenario all supersymmetric particles are heavy to suppress such decays. The higgsino mass is set to 1500 GeV which leads to heavy charginos and neutralinos. M_{SUSY} is varied between a few TeV for large values of m_A and/or $\tan\beta$ up to 100 TeV for small m_A and/or $\tan\beta$. X_t is chosen in a way that over large parameter space the mass of the light scalar Higgs is within $125 \pm 3\,\text{GeV}$:

- $\tan\beta \leq 2$: $X_t/M_{SUSY} = 2$,

- $2 < \tan\beta \leq 8.6$: $X_t/M_{SUSY} = 0.0375(\tan\beta)^2 - 0.7\tan\beta + 3.25$,
- $8.6 < \tan\beta$: $X_t/M_{SUSY} = 0$.

The considered parameter space ranges for m_A from 150 to 500 GeV and for $\tan\beta$ from 0.5 to 9.5.

light-stop scenario

The mass of the lightest CP-even scalar depends logarithmically on the stop mass and therefore a value of 125 GeV can still be reached with values of $M_{SUSY} < 1\text{TeV}$, but therefore the mixing in the stop sector has to be large. This necessarily leads to light stops, which could lead to a modification of the gluon-gluon fusion rate. The values of the light-stop scenario are chosen in agreement with current results of direct searches for stops.
The parameters of the light-stop scenario, have slightly changed with respect to the original proposal in [29] to adjust to newest measurements of the direct searches [37–39].
For the cross section calculations $m_H < 2m_{\tilde{t}}$ is assumed. For this scenario the assumption is broken for $m_A \geq 650$ GeV since $m_{\tilde{t}} = 325$ GeV. Therefore, the parameter space is restricted to $90 < m_A \leq 600$ GeV. The ratio of the vacuum expectation values of the two Higgs doublets is scanned from 0.7 to 60.

light-stau scenario

The light-stau scenario addresses the excess of events in the decay channel of the SM Higgs boson decaying into two photons as measured in ATLAS [40], which is above the SM expectation. Light staus lead to a modification of the ratio of the lightest Higgs boson decaying to two photons with respect to the SM expectation.

$$r_{\gamma\gamma} = \frac{\Gamma(h \to \gamma\gamma)_{\text{MSSM}}}{\Gamma(h \to \gamma\gamma)_{\text{SM}}}.$$

For high $\tan\beta$ and high m_A this ratio goes up to values of 1.3. The scenario is constructed for $m_A = 90$ GeV to 1000 GeV and $\tan\beta = 0.5$ to 60.

τ-phobic scenario

The τ-phobic scenario allows for reduced couplings of the lightest scalar Higgs boson to down type fermions. The ratios of the decay rates to tau leptons and b-quarks $r_{\tau\tau}$ and r_{bb}

$$r_{bb} = \frac{\Gamma(h \to bb)_{\text{MSSM}}}{\Gamma(h \to bb)_{\text{SM}}}$$
$$r_{\tau\tau} = \frac{\Gamma(h \to \tau\tau)_{\text{MSSM}}}{\Gamma(h \to \tau\tau)_{\text{SM}}}.$$

is significantly below 1.0 for high $\tan\beta$ and high m_A. The scanned parameter space reaches from $\tan\beta = 1$ to 50. and from $m_A = 90$ GeV to 1000 GeV.

low-m_H scenario

In contrast to all other benchmark scenarios, the low-m_H scenario assumes the heavy CP-even Higgs boson as the SM like Higgs boson. The mass of the pseudoscalar Higgs boson A must be chosen accordingly and in particular not too high. It is fixed to $m_A = 110\,\mathrm{GeV}$. Instead μ is varied from 300 to 3100 GeV. The considered $\tan\beta$ range reaches from 1.5 to 9.5. All other parameters are very similar to the ones in the τ-phobic scenario, see table A.1.
In this scenario the couplings of the lightest Higgs boson h to gauge bosons is significantly reduced by a factor 2-10 with respect to the SM expectations of a Higgs boson with similar mass. This ensures that the lightest Higgs boson h is not already excluded by LEP limits.

2.3 Two-Higgs-Doublet Models

The Higgs sector in the SM consists of only one Higgs doublet. However, besides simplicity there is no physical motivation or explanation why this should be realized in nature. It is possible to add a second Higgs doublet. 2HDMs are discussing these possibilities. With two Higgs doublets the Yukawa part of the Lagrangian, equation (2.15), can be rewritten to:

$$\mathcal{L}_{\text{Yukawa}} = \sum_{n=1,2} \left(k^{ij}_{e,n} (\overline{\nu}_e, \overline{e})^i_L \Phi_n e^j_R + k^{ij}_{u,n} (\overline{u}, \overline{d})^i_L \Phi_n u^j_R + k^{ij}_{d,n} (\overline{u}, \overline{d})^i_L \Phi_n d^j_R + \text{h.c} \right) \ , \tag{2.28}$$

with the implicit sum over the family indices i and j. The index n sums over the two Higgs doublets. The Glashow-Weinberg condition guarantees the absence of flavour changing neutral currents on tree level [41]. All fermions of the same representation are required to have renormalizable Yukawa couplings to a single Higgs doublet. In this case the tree level couplings of neutral Higgs boson are diagonal in the mass eigenbasis. Therefore, the Yukawa part of the Lagrangian, equation (2.28), has to fulfil one of the following conditions:

- **Type-1**:
  All fermions couple to one doublet, $k^{ij}_{u,1} = k^{ij}_{d,1} = k^{ij}_{e,1} = 0$.
- **Type-2**:
  Up-type quarks couple to a different higgs doublets than down type quarks and leptons, $k^{ij}_{u,1} = k^{ij}_{d,2} = k^{ij}_{e,2} = 0$.
- **Type-3**:
  Quarks and leptons couple to a different Higgs doublet, $k^{ij}_{u,1} = k^{ij}_{d,1} = k^{ij}_{e,2} = 0$.
- **Type-4**:
  Up-type quarks and leptons couple to a different higgs doublets than down-type quarks, $k^{ij}_{u,1} = k^{ij}_{d,2} = k^{ij}_{e,1} = 0$.

Following this convention the MSSM is a so called type-2 2HDM.
After having chosen the desired type there are five parameters left for defining a benchmark scenario:

- the mass of the light scalar Higgs boson m_h,
- the mass of the pseudoscalar Higgs boson m_A,
- the mass of the heavy scalar Higgs boson m_H,
- the cosine of the difference of the mixing angle α and arctangent of the ratio of the vacuum expectation values of the two doublets β $\cos(\beta - \alpha)$ and
- the ratio of the vacuum expectation values of the two doublets $\tan\beta$.

In the alignment limit $\cos(\beta - \alpha) = 0$ the little scalar Higgs boson couples like the SM Higgs boson.

Type-2 Two-Higgs-Doublet benchmark scenario

For this thesis a benchmark type-2 2HDM [42] has been tested which does not allow CP violation on tree level. Due to the observation of a Higgs boson at 125 GeV the mass of the light scalar Higgs boson is set to this mass. The masses of the heavy Higgs bosons are set to 300 GeV since the scenario is also used by the analyses which are combined with the $\phi \to \tau\tau$ analysis, see section 7.1, which do only scan the mass range around 300 GeV. The two remaining parameters are scanned within $-1 \leq \cos(\beta - \alpha) \leq 1$ in steps of 0.1 and $1 \leq \tan\beta \leq 10$ in steps of 1.
The LHC cross-section working group currently defines more Two-Higgs-Doublet benchmark scenarios, thus Two-Higgs-Doublet benchmark models will be emphasized in run 2 of the LHC.

Chapter 3

Experimental Setup

This thesis uses the data collected by the the Compact Muon Solenoid (CMS) detector at the Large Hadron Collider (LHC) hosted by *Conseil Européen pour la Recherche Nucléaire* (CERN) in Geneva. In this chapter the experimental setup is described briefly. In section 3.1 the LHC is introduced. The CMS detector is explained in section 3.2. The software tools as used in this thesis are listed in section 3.3. Sources for further details are given in the corresponding sections.

3.1 The Large Hadron Collider

The LHC operates in a tunnel between 50 and 175 meters underground, which was former used by the Large Electron Positron collider (LEP). The LHC operates mainly as a proton-proton collider, but it is also possible to collide lead ions. However, this thesis is based on proton-proton collision data.

The accelerator system of the LHC is shown in figure 3.1. Protons, produced in the source with and voltage of 90 kV, are first accelerated in the Radio Frequency Quadrupole (RFQ) up to an energy of $7.5 \cdot 10^{-4}\,\mathrm{GeV}$. Then they are accelerated in LINAC2 to $5.0 \cdot 10^{-2}\,\mathrm{GeV}$. The accelerator rings Proton Synchrotron Booster (PSB), named as BOOSTER in figure 3.1, Proton Synchrotron (PS) and Super Proton Synchrotron (SPS) accelerate the protons furthermore to 1.4, 26 and 450 GeV, respectively. Finally, in the LHC the protons can reach an energy to 7000 GeV, meaning they can collide with a center-of-mass energy of $\sqrt{s} = 14\,\mathrm{TeV}$. Nevertheless, it was planned to operate the LHC in the first run period with a center-of-mass energy of 7 TeV (8 TeV) in 2011 (2012). Mid of 2015 the planned upgrade of the LHC will be finished and the center-of-mass energy will be increased to 13 TeV which as mentioned is still not the maximal center-of-mass energy.

The LHC can be separated into eight regions as illustrated in figure 3.1. The proton beam of the LHC reaches unprecedented intensities. As a consequence, even tiny fractions of the transverse energy (10^{-6}) are suffice to quench a super-conducting LHC magnet, which means the temperature increases above the critical temperature so that the electric resistance abruptly jumps and therefore the temperature increases further leading to high temperatures damaging the electric system of the magnet. Moreover, even parts of the accelerators could be destroyed. In order to

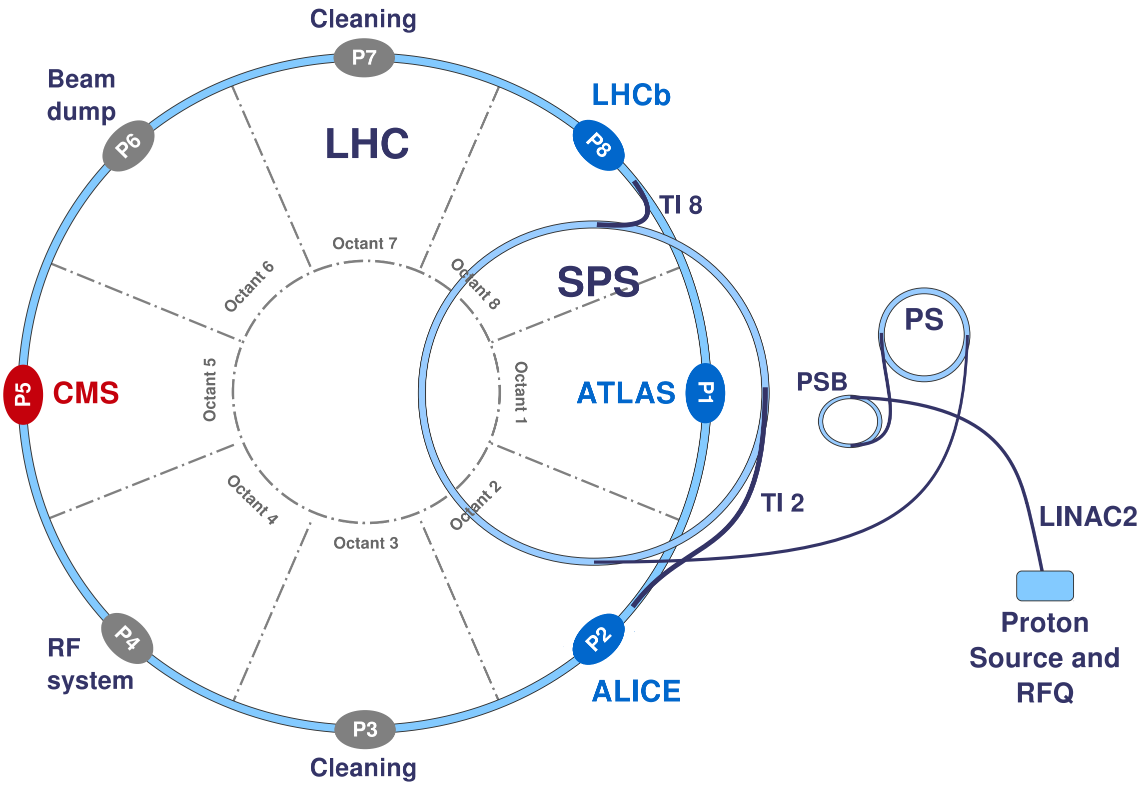

Figure 3.1: Schematic overview of the different parts within the accelerator chain at CERN (not to scale). The protons produced in the proton source are preaccelerated within the RFQ, LINAC2, the PSB and the SPS. Thereafter the yielding proton bunches are injected into the LHC main ring via transfer lines TI 2 and TI 8, leading to two counter-rotating beams. The LHC main ring provides eight possible collision points, Point 1 ($P1$) to Point 8 ($P8$) with particle detectors at four of them. This figure is taken from [43].

avoid damage to the LHC the proton beams are collimated at the two cleaning points $P3$ and $P7$. The point $P6$ is the dumping point. With a system of kicker magnets it is possible to get rid of the proton beams by directing them into so called dump blocks, which are capable of handling the enormous energy stored in the beams. The radio frequency (RF) cavities are responsible to bunch the maximal 2808 bunches within a proton beam as tightly as possible. These cavities are located at $P4$.

The four main experiments are located at $P1$, $P2$, $P5$ and $P8$. The *A Large Ion Collider Experiment* (ALICE) detector [44] at $P2$ is constructed to study the heavy ion collisions. The *Large Hadron Collider beauty* (LHCb) detector [45] at $P8$ is optimized to detect rare decays of hadrons, which contain bottom quarks. The *Compact Muon Solenoid* (CMS) detector [46] at $P5$ and the *A Toroidal LHC Apparatus* (ATLAS) detector [47] at $P1$ are testing SM parameters, searching for the Higgs boson and for BSM physics. At these four points $P1$, $P2$, $P5$ and $P8$, the proton beams can collide. The rate,

$$\dot{N}_p = \sigma_p \cdot \mathcal{L} \ , \tag{3.1}$$

of a process p depends on the total inelastic cross section for this process, σ_p, and the luminosity, $\mathcal{L}$. It depends on the number of protons, N_a and N_b, in the corresponding bunches, a and b, the revolution frequency, f, and the gaussian transverse profiles of the two proton beams, σ_x and σ_y:

$$\mathcal{L} = f \cdot \frac{N_a N_b}{4\pi\sigma_x\sigma_y} \ . \tag{3.2}$$

There are maximal 2808 bunches per proton beam in the LHC. Each bunch is filled with about $1.15 \cdot 10^{11}$ protons. The time spacing between bunches can reach a minimum of 25 ns. However, in the data taking in 2011 and 2012 the bunch crossing was 50 ns. Protons in the LHC have a revolution frequency of 40 MHz.
The integrated luminosity, L_{int}, is the luminosity integrated over time. The total number of events, N, of a process p is calculated to:

$$N_p = \int \dot{N}_p \; dt = \int \sigma_p \cdot \mathcal{L} \; dt = \sigma_p \int \mathcal{L} \; dt = \sigma_p \cdot L_{int} \ . \tag{3.3}$$

Figure 3.2 shows the daily peak (top) and integrated (bottom) luminosity recorded in run 1 by the CMS experiment. In this thesis $L_{int} = 4.9\,\text{fb}^{-1}$ at a center-of-mass energy of 7 TeV in the year 2011 and $L_{int} = 19.7\,\text{fb}^{-1}$ at a center-of-mass energy of 8 TeV in the year 2012 have been used.

3.2 The Compact Muon Solenoid Detector

The Compact Muon Solenoid detector (CMS) is one of the four detectors at the LHC. It is located at $P5$ as seen in figure 3.1. Besides testing the SM and measuring its parameters, the CMS detector is build to search for BSM physics. Although with a diameter of 14.6 m, a length of 21.6 m and a weight of about 12500 t, naming this monstrosity *compact* seems ironic. The reason is that the tracker and the calorimeter system is completely embedded in the magnetic field. Still, CMS is smaller but heavier than the other multi-propose detector, ATLAS (45 m length, 22 m diameter and weighting about 7000 t). The term *Muon* is used due to the ability to detect and reconstruct muons outstandingly good. *Solenoid* refers to the form of the magnet used in the detector which results in an enormous magnet field of 3.8 T. A three dimensional pattern of the CMS detector and its subdetectors is show in figure 3.3.

3.2.1 Coordinate System

Following coordinate system is introduced to describe collisions unambiguously.

- The origin is in the middle of the detector. The z-axis is along the beam line, the x axis is horizontal and the y axis vertical. All are orthogonal to each other, forming a right-handed coordinate system.
- The azimuth angle ϕ is measured anti-clockwise starting from the positive x-axis.

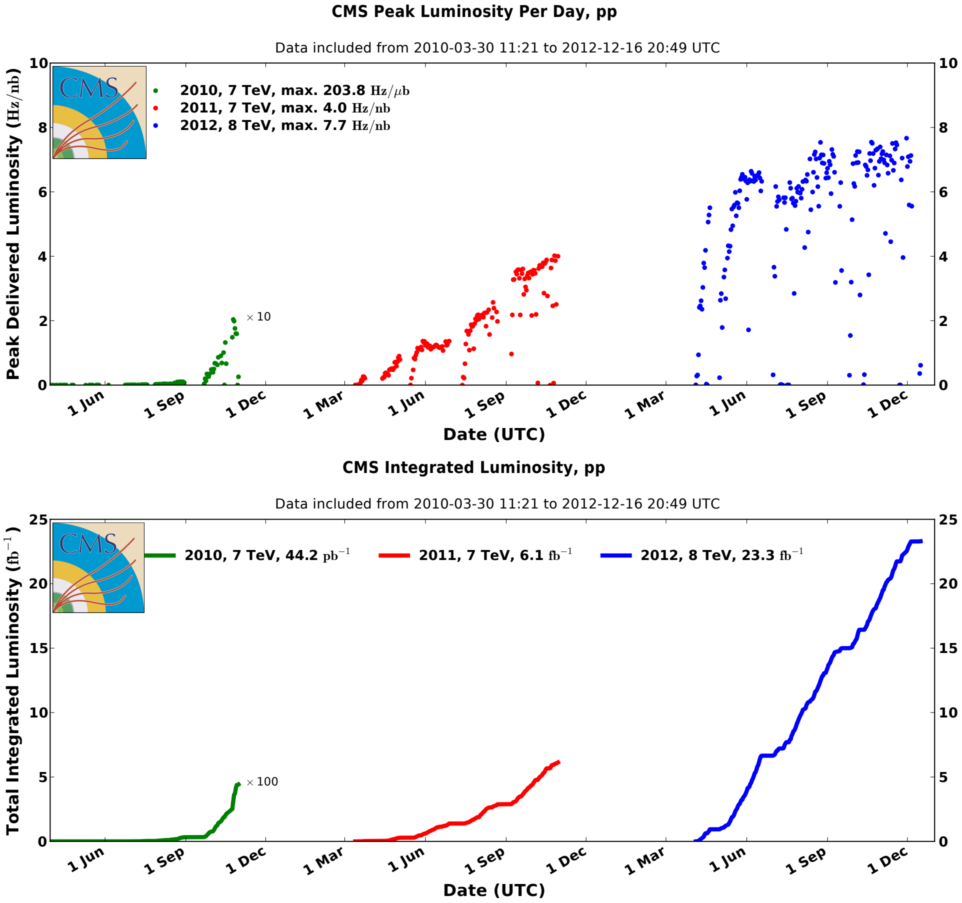

Figure 3.2: The daily peak instantaneous (top) and integrated (bottom) luminosity delivered by the LHC throughout the proton-proton run periods in run 1 of the LHC. The picture is taken from [48].

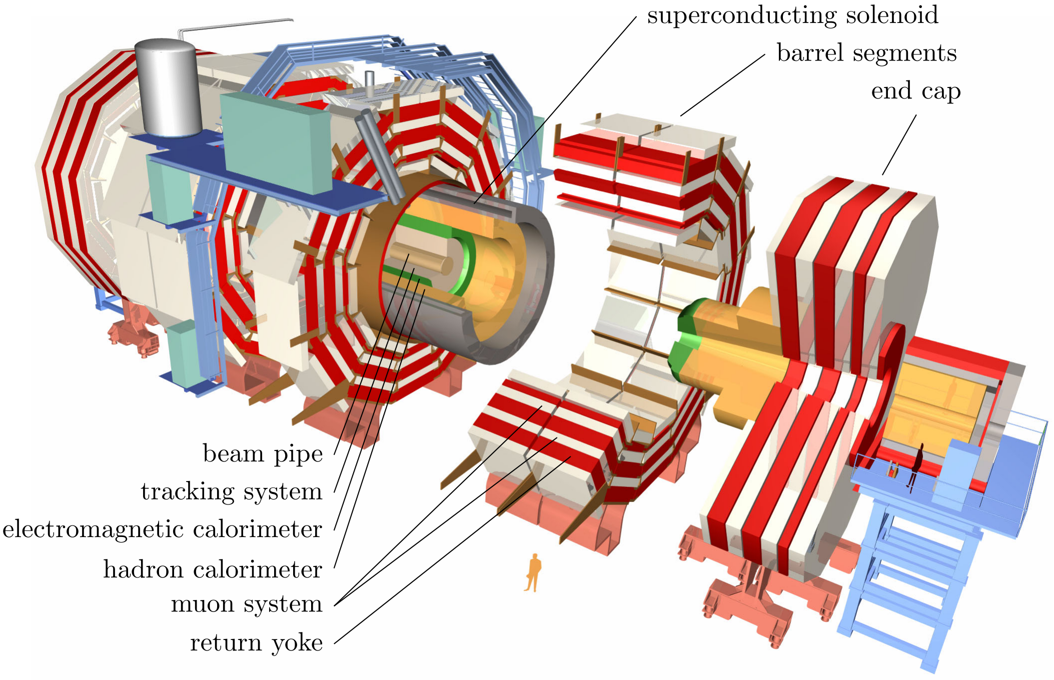

Figure 3.3: Schematic overview of the CMS apparatus and its sub-detectors adapted from [43; 49]. The typical onion-shaped structure of the detector around the beam pipe which is located in the center is shown. The beam pipe is environed by the tracking system, the electromagnetic and hadron calorimeters, the superconducting solenoid and the muon system, which is embedded in the iron return yoke. It is nearly hermetic.

- The polar angle θ is measured anti-clockwise from the z-axis. But instead of using the polar angle θ, the pseudorapidity η is introduced (3.4), since differences are invariant under a boost along the z-axis. In hadron collisions the particle production is nearly constant as a function of η. The pseudorapidity η is defined as:

$$\eta = -\ln\left[\tan\left(\frac{\theta}{2}\right)\right] \tag{3.4}$$

In figure 3.4, the ways through the subdetectors of different types of detectable particles are shown. A charged particle with electric charge q and velocity $\vec{v}$ perceives the Lorentz force

$$\vec{F}_L = q(\vec{E} + \vec{v} \times \vec{B}) \tag{3.5}$$

due to the perpendicular magnetic field $\vec{B}$. There are no electric fields, $\vec{E}$, strong enough to influence the charged particles. Therefore charged particles take a curved way through the CMS detector. In the following, the subdetectors of the CMS detector are introduced starting from the inner most.

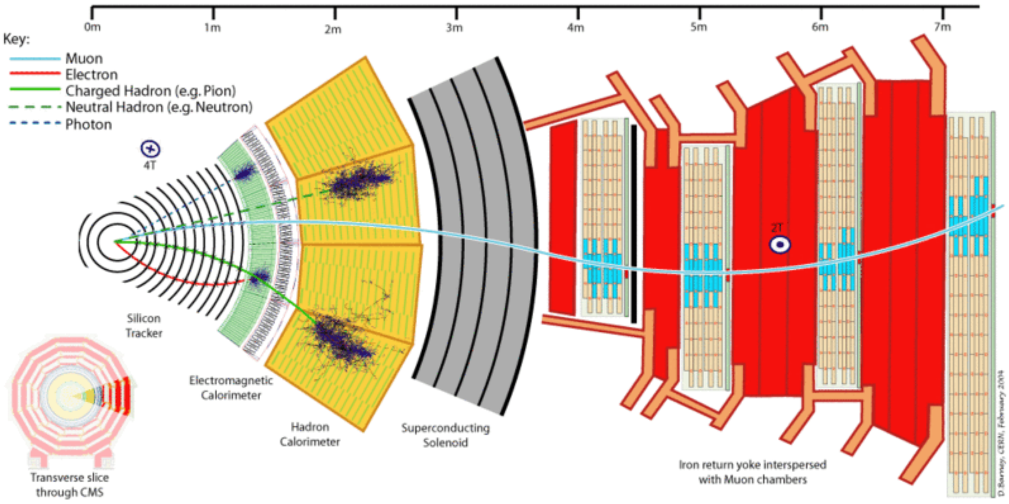

Figure 3.4: The way of detectable particles originating from the beam spot through the CMS detector is shown. The Silicon Tracker detects the curved tracks of all charged particles. The Electromagnetic Calorimeter (ECAL) absorbs photons and electrons and measures their energies. The Hadron Calorimeter (HCAL) measures the energy of all hadrons. The remaining particles are muons which passes the superconducting solenoid and are detected in the muon chambers. The muon chambers are interspersed in the iron return yoke. The picture is taken from [50; 51].

3.2.2 Tracker System

The tracker system [52–55] is centered cylindrical around the beam pipe in the middle of the CMS detector with a diameter of 2.5 m and a length of 5.8 m. The tracker system is built to measure the trajectories of charged particles with a high precision and efficiency and to reconstruct primary and secondary vertices. Assuming the designed luminosity of $\mathcal{L} = 1034\ \mathrm{cm}^{-2}\mathrm{s}^{-1}$ it has to handle an average of 1000 charged particles per bunch crossing, meaning every 50 (2011 and 2012) or 25 ns (2015 onwards). The tracker system is designed to cope with these demands as a combination of silicon pixel, at low radii and silicon strip detectors at higher radii. In total 1440 pixel detectors and 15158 strip detectors cover a range of up to $\eta < 2.5$ with an active material of nearly 200 m^2. The tracker system and its substructure is illustrated in figure 3.5.

Silicon Pixel Detectors

The silicon pixel detectors are the inner most detectors. Three cylindrical layers at radii of 4.4 cm, 7.3 cm and 10.2 cm are arranged in the barrel region and two layers at $z = \pm 34.5$ cm and $z = \pm 46.5$ cm in the endcap region. In total 66 million pixels with the size of a single cell of $100 \times 150\ \mu\mathrm{m}^2$ forming an active material of 1 m^2. Thus, a position resolution of 10 μm in the x-y-plane and 20 μm in the z-direction is achieved.

A charged particle passing such a cell induces an electron-hole pair. This small

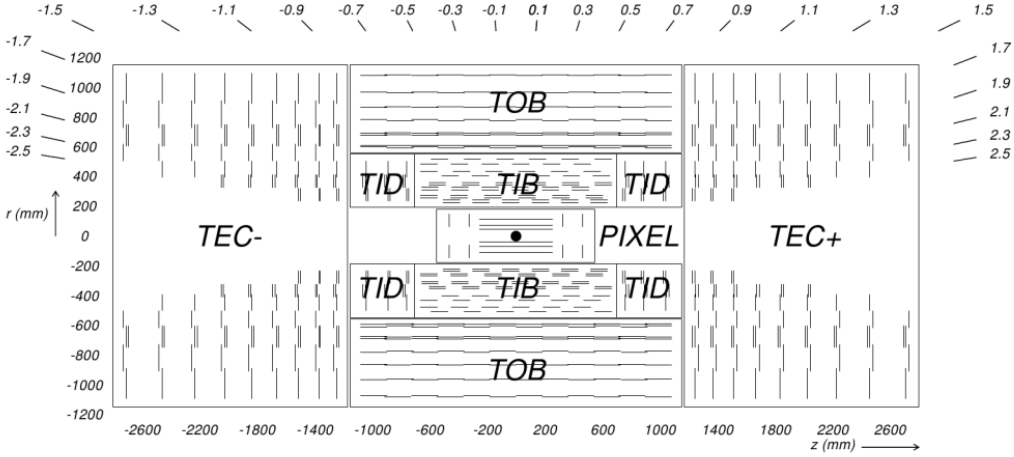

Figure 3.5: A schematic overview of the CMS inner tracking system. The substructure of the tracker is shown: the Pixel detectors (PIXEL), the inner barrel (TIB), the outer barrel (TOB), the inner disks (TID) and the endcaps (TEC). The picture is taken from [52].

potential change is read out. Due to the Lorentz force, equation 3.5, the charge particles are passing several cells in one layer, thus the resolution is better than the size of the pixel cell.

Silicon Strip Detectors

Further away from the beam pipe and the collision point the occupancy due to particle flux is decreasing with increasing radii, hence larger surfaces could be used (thickness of strips is around 320-500 μm). The tracker inner barrel (TIB) and the outer barrel (TOB) consist of four layers and six layers, respectively. If all these strips are parallel to the z-axis, this coordinate could not be measured. Therefore, the first two layers are so called stereo layers, which means that they are installed back to back with an angle of 0.1 rad to each other. This enables a z-measurement with a resolution 230 μm. The resolution in the x-y-plane varies from 23 to 34 μm. The tracker inner discs (TID) have three layers and the endcaps (TEC) have nine layers on both sides. Again the first two layers and for the TEC also the fifth layer are stereo layers. The resolution is between 35 to 52 μm in the x-y-plane and 530 μm in the z-direction.

3.2.3 Calorimeter System

The calorimeter system of the CMS detector is parted in the electromagnetic calorimeter (ECAL) and the hadron calorimeter (HCAL). The ECAL measures the energies of photons, electrons, positrons and the electromagnetic constitutes of jets, whereas the HCAL measures the hadron constitutes of jets. A jet is a narrow cone of nearby hadrons. A jet originates from hadronization of gluons or quarks. Beside of muons, which are measured in the muon chambers and in the tracking system,

all visible particle energies are measured in the calorimeter system. Following the law of energy conservation, the vectorial sum of the energy of all measured particles should be zero in the x-y plane. Invisible particles, such as neutrinos, or mismeasurements lead to missing transverse energy, $\vec{\not{E}}_{\mathrm{T}}$.
The calorimeters consists of material which absorbs the particles energy. The more distance a particle travels in such a material the more energy is absorbed by interacting with the material. The energy of the decay products in the material and of the initial particles are able to be measured if they are below a certain energy threshold, hence the initial energy of the particle is effectively measured. How far a particle travels before getting completely absorbed relies on the so called radiation length X_0 and in the case of a hadronic particle on the hadronic interaction length λ_I. Both are material constants.
The calorimeter system is shown together with the muon system in figure 3.7.

Electromagnetic Calorimeter

The ECAL encloses the tracker system hermetically. It is shown in figure 3.6. A total of 75848 lead tungstate (PbWO4) crystals are used. In the barrel are 61200 crystals with a front face cross section of 22×22 mm^2 and a rear face of 26×26 mm^2. The length of 230 mm corresponds to a radiation length of $25.8 X_0$. Each crystal covers $\Delta\eta \times \Delta\phi = 0.00174 \times 0.00174$. The electromagnetic barrel calorimeter (EB) covers $|\eta| < 1.479$.
In the electromagnetic endcap calorimeter (EE) the crystals, on both sides 7324, have a front face cross section of 28.62×28.62 mm^2, a rear face of 30×30 mm^2 and a length of 220 mm corresponding to a radiation length of $24.7 X_0$. It covers $1.479 < |\eta| < 3.0$.
The electromagnetic preshower system (ES) covers a range of $1.653 < |\eta| < 2.6$. It is installed to additionally further improve the detection of neutral pions and the position resolution of photons and electrons in the endcap. It is a two layer sampling calorimeter, the first layer is composed of lead radiators and the second layer is build of silicon strip sensors. The energy resolution of the ECAL,

$$\begin{aligned}\left(\frac{\sigma_{ECAL}}{E}\right)^2 &= \left(\frac{S}{\sqrt{E}}\right)^2 + \left(\frac{N}{E}\right)^2 + C^2 \\ &= \left(\frac{2.8\%}{\sqrt{E}}\right)^2 + \left(\frac{0.12}{E}\right)^2 + (0.30\%)^2 ,\end{aligned} \tag{3.6}$$

was measured in 2004 with electron beams having momenta between 20 and 250 GeV [46]. The stochastic term, S, which is proportional to $\sqrt{E}$, includes the effects from the fluctuations in the photon statistic and the shower containment. The noise term, N, is proportional to E and considers the uncertainties of the electronic and of pile-up (more than one proton-proton collision in one bunch crossing). The constant, C, handles calibration uncertainties and other systematic uncertainties.

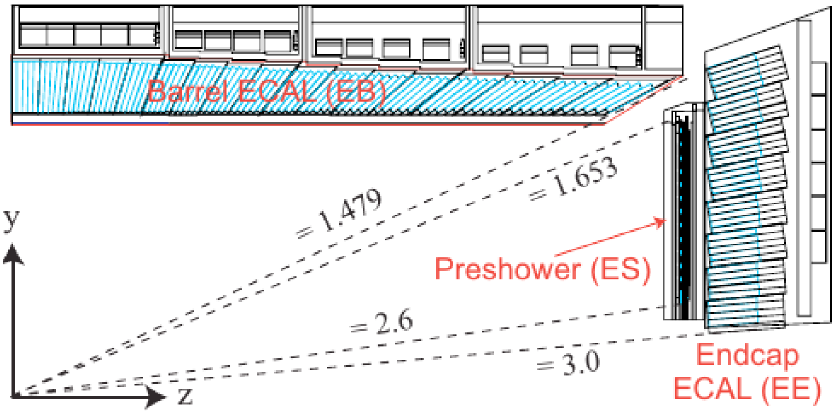

Figure 3.6: A slice through the CMS detector showing a schematic overview of the ECAL configuration. It consists of three subsystems: the ECAL barrel (EB), the endcap (EE) and a electromagnetic preshower system (ES). The picture is taken from [46].

Hadron Calorimeter

Just as the ECAL surrounds the tracker system the hadron calorimeter (HCAL), shown in figure 3.7, encloses the ECAL. It is made of four parts. A pseudorapidity of $|\eta| < 1.3$ is covered by the hadron barrel (HB). The absorber material is based on steel and brass. Scintillators tiles are used as active material. The hadron endcap (HE) enlarges the pseudorapidity up to $|\eta| < 3.0$. Each segment of the HB and HE covers $\Delta\eta \times \Delta\phi = 0.087 \times 0.087$. Due to the limited size and therefore limit absorber material of the HB and HE, a hadron outer calorimeter (HO), the so called tail catcher, is installed outside of the superconducting solenoid. The hadron forward calorimeter (HF) covers the pseudorapidity range of $3.0 < |\eta| < 5.0$. The energy resolution in the endcap and barrel region (HB, HE and HO) is [56]:

$$\begin{aligned} \left(\frac{\sigma_{HCAL}}{E}\right)^2 &= \left(\frac{S}{\sqrt{E}}\right)^2 + C^2 \\ &= \left(\frac{84.7\%}{\sqrt{E}}\right)^2 + (7.4\%)^2 \; . \end{aligned} \tag{3.7}$$

In the forward region the energy resolution is worse [57]:

$$\begin{aligned} \left(\frac{\sigma_{HCAL}}{E}\right)^2 &= \left(\frac{S}{\sqrt{E}}\right)^2 + C^2 \\ &= \left(\frac{198\%}{\sqrt{E}}\right)^2 + (9\%)^2 \; . \end{aligned} \tag{3.8}$$

In contrast to the ECAL, the HCAL has a worse energy resolution since the brass and steel is not scintillation active material.

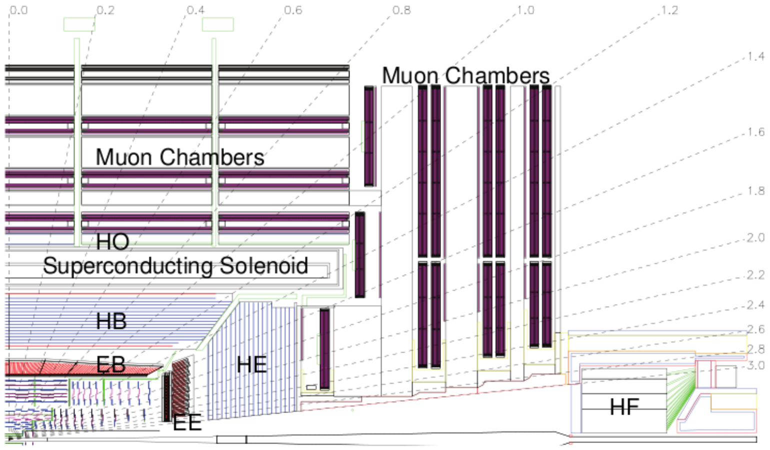

Figure 3.7: Longitudinal view of the calorimeters and the muon system in one quarter of the CMS detector. The tracker system shown in figure 3.5 is surrounded by the electromagnetic barrel (EB) and the hadron barrel (HB). The electromagnetic (EE) and the hadron endcaps (HE) enclose it on each side. The superconducting solenoid, the hadron outer calorimeter (HO) and the muon system, which is embedded in the iron return yoke, complete the onion-shaped structure. Close to the beam pipe the hadron forward calorimeter (HF) is located. The fine dashed lines show the values of the pseudorapidity. The picture is taken from [46].

3.2.4 Muon System

In figure 3.8 the muon system is shown with more details than in figure 3.7. The muon system consists of gaseous detectors to identify and measure the momentum of muons. If a muon passes such a chamber it knocks electrons off the atoms of the gas. These follow the electric field ending up at the positively-charged wire. This can be read out as a signal. In a pseudorapidity range of $|\eta| < 1.2$ drift tube chambers (DT) are installed. These chambers are filled with gas (Ar and CO_2). The range of $0.9 < |\eta| < 2.4$ is covered by cathode strip chambers (CSC). Both have a good position resolution but the dead times are long. Therefore, both systems are supported by restive plate chambers (RPC), which have a worse position resolution than DTs and CSCs, but a better time resolution. In total 250 DTs and 468 CSCs are installed in the muon system.

3.2.5 Trigger and Data Handling

After a collision, the CMS detector has to handle enormous amounts of data. For example, assuming a 50 ns bunch spacing (=20 MHz event rate) and an average event size of 1.5 MB would lead to 30 TB per second - far too much to be able to store every event, thus triggers are required. The trigger system has the task to select interesting, well reconstructible events, depending on the wanted process, and skip others. The so called Level 1 (L1) trigger [59] is a hardware trigger which uses information from the muon and calorimeter systems as illustrated in figure 3.9. It reduces the event rate to 750 kHz. After an event is selected by the L1 trigger

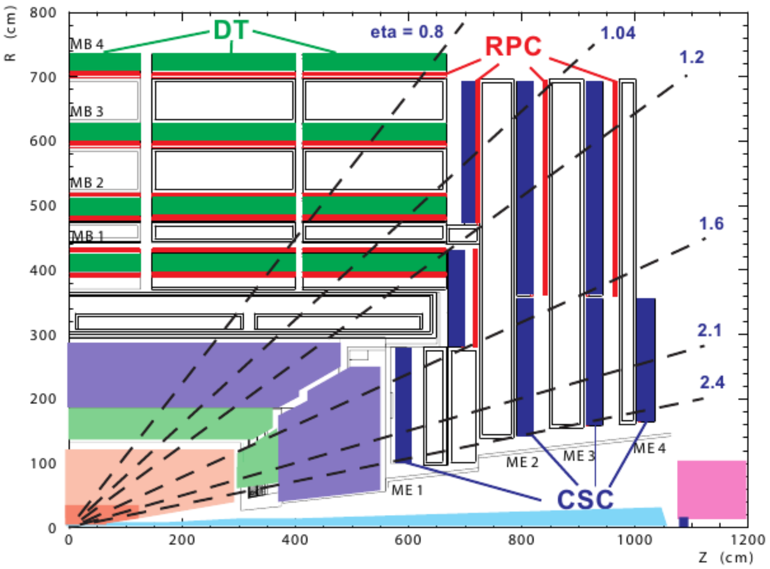

Figure 3.8: The muon system is the largest part of the CMS detector embedded in the iron return yoke of the solenoid. In the barrel region four stations including several layers of DTs and RPCs are installed, whereas in the endcap region four disks mounted with CSCs and RPCs are in usage. The picture is taken from [58].

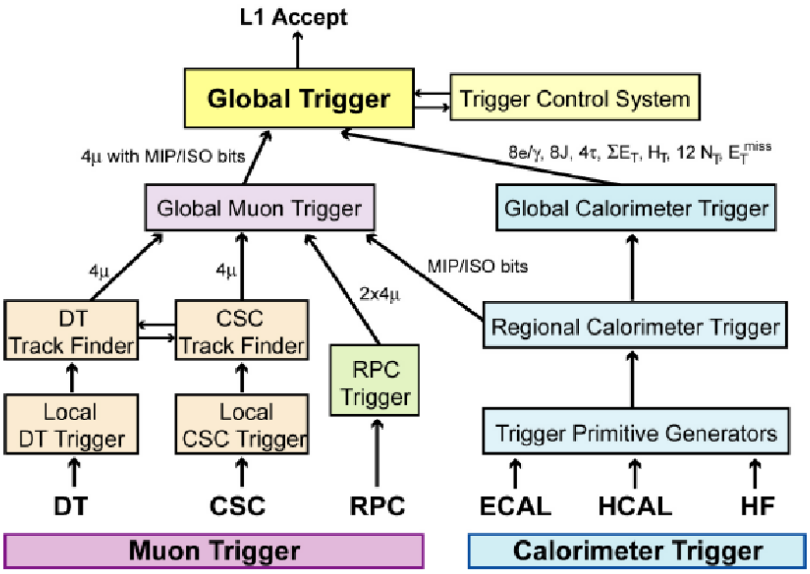

Figure 3.9: The L1 trigger system uses information from the muon system and from the calorimeter system to catch interesting events. This figure is taken from [60].

the High Level Trigger (HLT) [61] reduces the rate of data to 150 Hz (225 MB/s), making it possible to store the events at the computing center at CERN. The HLT is a software based computing system and therefore flexible and adaptable [46; 59; 61]. Afterwards, a first complete event reconstruction on the raw dataset is performed. The new reconstructed dataset is stored together at national computer facilities, such as the GridKa at the Karlsruhe Institute of Technology in Germany. At these centers simulated datasets, Monte Carlo datasets, are also stored.

3.3 Software

In order to handle the huge amount of data and properly treat it, powerful software tools are required. The following tools which are used in this analysis are briefly described and references to more detailed documentations are given. Private codes are written in C++ [62] and Python [63]. All software tools used by people working at the CMS or with data from the CMS detector are open source software.

ROOT

The object-orientated analyse kit ROOT [64], which was developed at CERN, simplifies handling the huge amount of data. It is written in C++ and provides many classes allowing it to rapidly coding tools needed for analysis. Based on the ROOT framework, the two extra packages ROOTFIT [65] and ROOTSTATS [66] provide standardized fitting methods and statistical analyse tools.
ROOT is a constantly improving software and steadily provides new packages and solutions for arising problems.

CMSSW

The CMSSW (CMS Software) framework [58] is especially developed to analyse data from the CMS detector. It is coded in Python and C++ and uses the ROOT software package. The framework is modular. Other software tools can be integrated which are needed by the simulation, calibration and alignment, and reconstruction modules that process real data or Monte Carlo simulations so that physicists can perform analysis.

Combined Limit

The *Combined Limit* tool [4; 67; 68] is build as a CMSSW module which offers excess to ROOTSTATS. As an input a standardized text file, called datacard, is used. A datacard summarizes the information of an analysis needed for the statistic interpretation. Input parameters for each datacard are uncertainties, their values and assumed distributions (see section 5), background and signal predictions and the actual observation.

Tools to calculate Higgs Properties

For the calculation of the cross-sections and branching fractions for the BSM benchmark scenarios, as described in section 2 and 6, various software tools have been used:

- Supersymmetric Higgs: Cross-section calculation for the gluon-gluon fusion and Higgs production associated with b-quarks in the five flavour scheme in the MSSM and 2HDM benchmark scenarios [69–78].
- bbH NLO (4FS): Cross-section calculation in the associated Higgs production with b-quarks in the four flavor scheme [79; 80]
- FeynHiggs: Calculation of branching fractions and masses for the MSSM benchmark scenarios [32; 81–84].
- Two-Higgs-Doublet Model Calculator: Calculation of branching fractions and masses for the 2HDM benchmark scenario [85].

Chapter 4

The Search for Neutral Higgs Bosons decaying to Tau Leptons in the Context of the MSSM

In this chapter the $\phi \rightarrow \tau\tau$ analysis will be explained as published by the CMS collaboration [14]. The analysis is based on the full dataset collected by the CMS detector in 2011 and 2012 which corresponds to an integrated luminosity of $4.9 fb^{-1}$ at a center-of-mass energy of 7 TeV and $19.7 fb^{-1}$ at 8 TeV, respectively. The analysis is split into five different channels based on the decay of the tau leptons: $\phi \rightarrow \tau\tau \rightarrow (e\mu, e\tau_{\text{had}}, \mu\mu, \mu\tau_{\text{had}}, \tau_{\text{had}}\tau_{\text{had}})$ where a hadronically decaying tau lepton is denoted τ_{had}.

The $\phi \rightarrow \tau\tau$ analysis is a search for BSM physics. In particular the MSSM is examined. Therefore, two signal productions mechanism are considered: gluon-gluon fusion (ggϕ) and associated production with b-quarks (bbϕ) as the coupling to down-type quarks increases with $\tan\beta$. In figure 4.1 the Feynman diagrams of these processes are shown.

In section 4.1 the objects and variables used in this thesis are presented. The event selection and categorization are explained in section 4.2 and 4.3, respectively. The background estimation is described in section 4.4. At the end of this chapter, the systematic and statistical uncertainties are discussed in section 4.5.

4.1 Object Selection and Reconstruction

Physics objects have to be identified in order to be able to match the event to a certain physics process. Each object has a special signature, which distinguish it from other objects. The information which is obtained from the CMS detector consists of energy deposits in the calorimeter systems and of signals in the active material of the inner tracking or/and muon system. To reconstruct muons, electrons, photons, charged and neutral hadrons of a dedicated proton-proton collision event the particle flow (PF) algorithm [86] is used. The approach combines the information gathered in all CMS subdetectors stored per event. Higher level objects like hadronically decaying tau leptons, jets and the missing transverse energy are constructed using

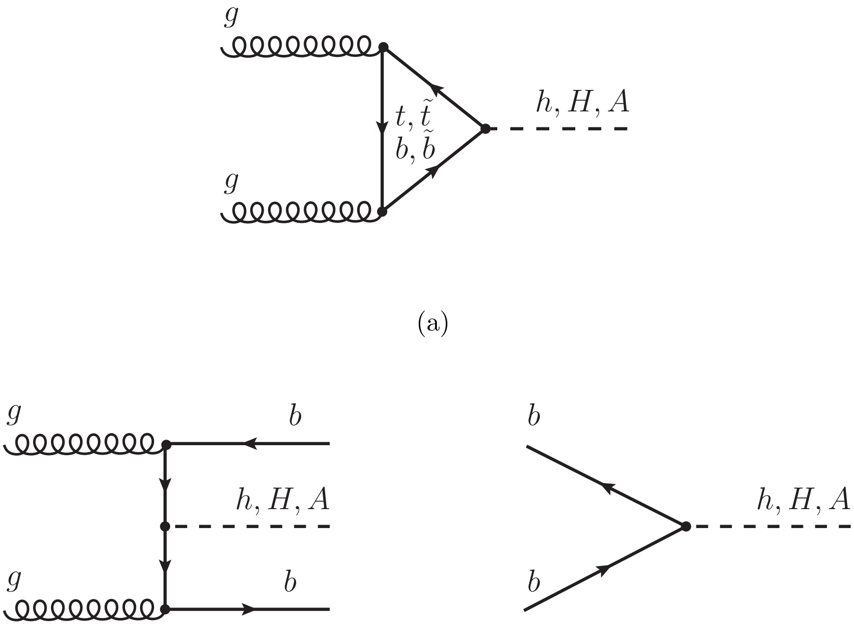

(a)

(b)

Figure 4.1: Shown are the purpose production processes in the search for neutral Higgs bosons decaying to tau leptons. In figure 4.1(a) the gluon gluon process is shown. Supersymmetric particles included in the MSSM are considered in the loop and in the final states. Figure 4.1(b) shows the Feynman diagrams for the associated production with b-quarks. On the left plot the gluon splitting into b-quarks process is shown. On the right the merging of two sea b-quarks is shown. The contribution to the total cross-section of the associated production with b-quarks is highly dominated by the gluon splitting process.

the identified particles.
For the $\phi \rightarrow \tau\tau$ analysis the objects of interest are the collision vertices, electrons, muons, tau leptons, jets and missing transverse energy. This section will introduce the dedicated selections to identify these objects (4.1.1 - 4.1.6). In this analysis some variables are constructed using the selected objects of an event. The missing transverse mass m_T (subsection 4.1.6) and the P_ζ variable (subsection 4.1.8) are used to suppress backgrounds. The invariant di-τ mass, $m_{\tau\tau}$, subsection 4.1.9, is the final discriminator between background and signal distributions.

4.1.1 Vertex Reconstruction

The event vertices in CMS are reconstructed using the *Deterministic Annealing* clustering algorithm [87]. For the selected event vertices the distance of a vertex candidate from the nominal interaction point is required to be within 24 cm along the z-axis and 2 cm along the transverse plane. Each vertex fit must have more than 4 degrees of freedom. The vertex which has the highest squared transverse momentum p_T^2 of all tracks associated to it is chosen to be the collision vertex. All other vertices are by construction defined as low scattering vertices (pile-up). Typically, analyses are only interested in the collision vertex while pile-up aggravates the reconstruction of particles, but is a natural side effect of increasing number of protons per bunch, more focused beams and less time between collisions. In 2011 (2012) 9 (21) proton-proton collisions have been reconstructed per LHC bunch crossing.

4.1.2 Electrons

The reconstruction of an electrons track is based on the *Gaussian-sum filter* [88]. The bremsstrahlung energy loss distribution of electrons propagating in matter is non-gaussian. The GSF takes that into account by modelling the bremsstrahlung energy loss distribution by a mixture of gaussians rather than by a single gaussian. An electron candidate is reconstructed by a GSF track and a deposit in the ECAL. To further separate electrons from jets misidentified as electrons a multivariate approach (MVA) [89] is used. The training is performed in two p_T and three η bins and in total 19 different variables based on track quality, cluster shape and kinematic quantities are used to separate electrons from misidentified jets. A $Z \rightarrow ee$ data sample is used for the training. The opposite sign electron pair is selected. If more electrons are selected in an event than those two they are likely to result from misidentified jets. In addition to the MVA identification, electron candidates coming from photon conversions are rejected by requiring a hit in each pixel layer that the track is crossing. For the same reason electron candidates are rejected which can be paired with an opposite sign track that can be matched to the same secondary vertex.

4.1.3 Muons

In the CMS detector, apart from muons, all other particles are usually stopped either in the electromagnetic or hadronic calorimeter, except for neutrinos, which are not detected at all. On the other hand muons leave a track in the pixel detector as well as in the muon chambers. Still, they may escape the detector due to their long lifetime and weak interaction with matter. The tight muon identification [90] is used to select muons: candidates are required to have a minimum number of hits in the muon chambers as well as in the pixel detector to guarantee a good track measurement and therefore allow for a good p_T measurement. Furthermore, the muon track has to originate from the a reconstructed vertex within some minimal distance in transverse and longitudinal direction to suppress muons from cosmic rays.

Electron and Muon Isolation

In order to suppress multi-jet backgrounds electrons and muons are required to be isolated from other particles. Therefore, a cone around the candidate is constructed with $\Delta R = 0.4$ where ΔR is constructed using the azimuth angle ϕ and the pseudorapidity η:

$$\Delta R = \sqrt{(\Delta\phi)^2 + (\Delta\eta)^2}\ . \tag{4.1}$$

The transverse momentum of all charged and neutral particles is summed within this cone, excluding particles originating from the candidate itself, for example due to Bremsstrahlung processes. Therefore, inner cones are built around the electron or muon candidate. In table 4.1 the size of the veto cone depending on the type of the particle is shown for electron and muon candidates.

In case of the muon candidates a further p_T threshold of 0.5 GeV is introduced for photons and neutral hadrons to reduce pile-up effects. Furthermore, all charged particles associated to pile-up vertices are excluded from the calculation of the isolation sum, $I_{e/\mu}$. Neutral particles are not detected in the pixel detector therefore leaving no tracks. Thus, they can not be associated to a reconstructed vertex. A correction factor for neutral pile-up components, $\Delta\beta_{e,\mu}$, is calculated by using an estimated ratio of neutral to charged energy of 0.5 in equation (4.2) [91]. The transverse momentum of all charged particles which originate more than 2 mm away from

Candidate	Particle type	ΔR	p_T
Electron	Charged particles	0.01 (EB) / 0.001 (EE)	–
	Photons	0.08	–
	Neutral hadrons	–	–
	$\Delta\beta$	–	–
Muon	Charged particles	0.0001	–
	Photons	0.01	> 0.5 GeV
	Neutral hadrons	0.01	> 0.5 GeV
	$\Delta\beta$	0.01	> 0.5 GeV

Table 4.1: Definition of the inner cone for the isolation calculation of muon and electron candidates. The barrel and endcap regions in the ECAL are abbreviated EB and EE, respectively.

the collision vertex and therefore can be associated with pile-up is added up using the empirical factor.

$$\Delta\beta_{e,\mu} = 0.5 \cdot \sum p_T^{charged}(\Delta z > 2 \text{ mm}) \tag{4.2}$$

The isolation sum $I_{e/\mu}$ is then built by summing the transverse momentum of all charged particles $p_T^{charged}$, neutral hadrons p_T^{h0}, photons p_T^{γ} between the inner and the outer cone and correcting for pile-up effects $\Delta\beta_{e,\mu}$.

$$I_{e/\mu} = \sum \left(p_T^{charged}(\Delta z < 2 \text{ mm})\right) + \max\left(\sum(p_T^{h0} + p_T^{\gamma}) - \Delta\beta_{e,\mu}, 0\right) \tag{4.3}$$

4.1.4 Jets

All particles reconstructed by the particle flow approach are clustered using the anti-k$_T$ algorithm [92] with a distance parameter of $R = 0.5$ to construct jets. A jet is a narrow cone of hadrons produced by the hadronization of gluons or quarks. In this thesis only jets with $|\eta| < 4.7$ are considered. A BDT is trained to distinguish between jets from pile-up interactions and from jets coming from the collision vertex. It takes the compatibility of the contained tracks with the selected vertex, different jet shape variables, and the multiplicity of both neutral and charged components within the jet into account. In this thesis the loose working point of the *MVA full jet id* is used [93]. Other sources of misidentification, mainly calorimeter noise, are reduced by requiring additional jet identification criteria [94] which are based on moderate cuts on p_T and $|\eta|$ and ensures that the jet composites of neutral and charged particles.

The energy of the jets is corrected for the absolute energy scale in bins of p_T and η. Further pile-up effects are corrected for by subtracting the median transverse momentum density of pile-up, $median(\rho)$, times the jet area A[1] from the p_T of the reconstructed jet. More details can be found in [95; 96]. The total correction depends on p_T and η and sums up to 20% for particle flow jets.

The combined secondary vertex (CSV) algorithm [97] is used to mark jets with calibrated $p_T > 20$ GeV as b-tagged. A B-meson has an enhanced lifetime compared to mesons not originating from a b-quark. Therefore, a secondary vertex where the B-meson hadronizes can be found which separates b-jets from jets originating from lighter quarks and gluons. Also the b-quark mass leads to a broader jet cone compared to jet cones originating from lighter quarks and gluons. The CSV algorithm utilizes these informations. The medium working point of the CSV discriminator $d > 0.679$ is used in this analysis which corresponds to a miss-tag rate of 1-2% for light flavoured jets, 15-20% for c-quarks at an efficiency of 60-70% depending on η and p_T [97; 98].

---

[1] The jet area is constructed by adding infinitely soft four-momentum vectors to the event randomly distributed in the ϕ-η plane. The vectors are clustered by the jet algorithm together with the true jet components and define an area in ϕ-η space.

4.1.5 Tau Leptons

A tau lepton decays either leptonically or hadronically. In table 4.2 the branching fractions of the most important decays are summarized [27]: There are more exotic decays but they have a tiny branching fraction and can not be identified with the CMS detector. Leptonically decaying tau leptons are identified as electrons and muons in the CMS detector.

tau lepton decay channel	$\mathcal{B}$
$\tau^{\mp} \to e + \overline{\nu}_e(\nu_e) + \nu_\tau(\overline{\nu}_\tau)$	$\sim 17\%$
$\tau^{\mp} \to \mu + \overline{\nu}_\mu(\nu_\mu) + \nu_\tau(\overline{\nu}_\tau)$	$\sim 18\%$
$\tau^{\mp} \to \pi^{\mp} + \nu_\tau(\overline{\nu}_\tau)$	$\sim 11\%$
$\tau^{\mp} \to \rho^{\mp} + \nu_\tau(\overline{\nu}_\tau) \to \pi^{\mp} + \pi^0 + \nu_\tau(\overline{\nu}_\tau)$	$\sim 25\%$
$\tau^{\mp} \to a_1^{\mp} + \nu_\tau(\overline{\nu}_\tau) \to \pi^{\mp} + \pi^0\pi^0 + \nu_\tau(\overline{\nu}_\tau)$	$\sim 9\%$
$\tau^{\mp} \to a_1^{\mp} + \nu_\tau(\overline{\nu}_\tau) \to \pi^{\mp}\pi^{\pm}\pi^{\mp} + \nu_\tau(\overline{\nu}_\tau)$	$\sim 10\%$

Table 4.2: The branching fractions of the most important tau lepton decays are shown.

Hadronically decaying Tau Leptons

Following the definition of a jet as explained in section 4.1.4 a hadronically decaying tau lepton is a jet, as the last four decay modes listed in table 4.2 include hadrons. For the $\phi \to \tau\tau$ analysis it is necessary to distinguish a reconstructed non-τ_{had} jet from the hardonically decaying tau lepton. Charged and neutral pions are matched to the hardonic decays mentioned in table 4.2. The presence of extra particles which can not be brought in accordance with a decay mode of the tau lepton are used to discriminate hadronic tau decays from non-τ_{had} jets.

Hardonically decaying tau leptons (τ_{had}) are reconstructed using the *Hadron plus Strips* (HPS) algorithm [99; 100]. The algorithm uses the particles reconstructed by the PF algorithm as input. The HPS algorithm is a multi-step approach. First π^0 candidates are built. Photons coming from a decaying π^0 are searched by building 0.20×0.05 large η-ϕ "strips". A π^0 candidate is defined as a strip which contains at least one photon with a sum of transverse momentum larger than 2.5 GeV.

In the following, π^0 candidates together with charged pions reconstructed by the PF algorithm are matched to a hadronic tau decay as mentioned in table 4.2. The resulting τ_{had} candidates are ordered by the matched decay.

- **$\tau^{\mp} \to \pi^{\mp} + \nu_\tau(\overline{\nu}_\tau)$:**
  No π^0 candidate has been found. Only one charged hadron is reconstructed by the PF algorithm within the jet cone.

- **$\tau^{\mp} \to \rho^{\mp} + \nu_\tau(\overline{\nu}_\tau) \to \pi^{\mp} + \pi^0 + \nu_\tau(\overline{\nu}_\tau)$:**
  One π^0 candidate and one charged hadron are reconstructed. Depending on the transverse momentum of the τ_{had} candidate the candidate is required to be within a certain mass window:

$$\begin{aligned} p_T(\tau_{\text{had}}) < 200 \text{ GeV}: &\quad 0.4 < M < 1.3 GeV \\ 200 \text{ GeV} < p_T(\tau_{\text{had}}) < 800 \text{ GeV}: &\quad 0.4 < M < \sqrt{p_T(\tau_{\text{had}})[\text{GeV}]/200} \text{ GeV} \\ p_T(\tau_{\text{had}}) > 800 \text{ GeV}: &\quad 0.4 < M < 2.1 GeV \end{aligned}$$

- $\boldsymbol{\tau^{\mp} \to a_1^{\mp} + \nu_\tau(\overline{\nu}_\tau) \to \pi^{\mp} + \pi^0\pi^0 + \nu_\tau(\overline{\nu}_\tau)}$ **:**
  Two π^0 candidates and one charged hadron are reconstructed. Again the τ_{had} candidate is required to be within a mass window depending on its transverse momentum:

$$\begin{aligned} p_T(\tau_{\text{had}}) < 200 \text{ GeV}: &\quad 0.4 < M < 1.2 GeV \\ 200 \text{ GeV} < p_T(\tau_{\text{had}}) < 800 \text{ GeV}: &\quad 0.4 < M < \sqrt{p_T(\tau_{\text{had}})[\text{GeV}]/200} \text{ GeV} \\ p_T(\tau_{\text{had}}) > 800 \text{ GeV}: &\quad 0.4 < M < 2.0 GeV \end{aligned}$$

- $\boldsymbol{\tau^{\mp} \to a_1^{\mp} + \nu_\tau(\overline{\nu}_\tau) \to \pi^{\mp}\pi^{\pm}\pi^{\mp} + \nu_\tau(\overline{\nu}_\tau)}$ **:**
  Three charged hadrons have been reconstructed by the PF algorithm with $p_T > 0.5$ GeV. The summed charge of the three hadrons has to be ±1. The combined mass has to be within a mass window of $0.8 < M < 1.5$ GeV. All three charged hadrons are required to originate from the same event vertex within $\Delta z < 2$ mm.

The charged hadrons used for the τ_{had} candidate construction have to be within a cone of size

$$\Delta R = \begin{cases} 0.05 & \text{if } P_T > 56 \text{ GeV} \\ 2.8/P_T[GeV] & \text{if } 28 < P_T < 56 \text{ GeV} \\ 0.10 & \text{if } P_T < 28 \text{ GeV} \end{cases}$$

along the jet-axis to exclude other sources of charged hadrons like pile-up. If there are different decay mode possibilities to construct a τ_{had} candidate the decay mode is taken for which the energy of its constituents is closest to the summed energy of the constitutes in the jet cone.

In the last step, the isolation of the τ_{had} candidate is computed. Analogous to the electron and muon isolation, equation 4.1.3, the transverse momentum of charged particles with $p_T > 0.5$ GeV and photons with $E_T > 0.5$ GeV is summed in a cone with $\Delta R < 0.5$ around the τ_{had} candidate direction. Photons and charged hadrons which have been used to construct the τ_{had} candidate are not considered in this sum. Furthermore, the charged hadrons used in the isolation sum have to originate from the same vertex as the charged hadron with the highest transverse momentum of the τ_{had} candidate. Pile-up effects are corrected for via $\Delta\beta_\tau$ corrections.

$$I_\tau = \sum \left(p_T^{charged}(\Delta z < 2 \text{ mm}) \right) + \max \left(\sum (p_T^{\gamma}) - \Delta\beta_\tau, 0 \right) \tag{4.4}$$

The pile-up corrections $\Delta\beta_\tau$ include all charged particles within a cone of $\Delta R < 0.8$ around the τ_{had} direction and with a longitudinal impact parameter $\Delta z > 2$ mm with respect to the τ production vertex. Neutral components of pile-up is accounted for by the factor of 0.4576 obtained empirical to obtain a constant tau lepton identification efficiency independent from the number of pile-up vertices.

$$\Delta\beta_\tau = 0.4576 \cdot \sum p_T^{charged}(\Delta z > 2 \text{ mm}) \tag{4.5}$$

In this thesis the actually used threshold of I_τ for which a τ_{had} candidate is considered isolated depends on the channel.

Anti-μ Discriminator

Misidentified muons might mimic a τ_{had}. The anti-μ discriminator is based on information of muons nearby the τ candidate. Three working points are defined corresponding to different hadronic tau lepton efficiencies and misidentification rates.

- **Loose working point:**
  A τ_{had} candidate is vetoed if a track segment is found in the muon system within $\Delta R < 0.5$ to the candidate.
- **Medium working point:**
  A τ_{had} candidate is vetoed if the loose working point requirements are not met or if there are hits in the two outermost muons stations located within $\Delta R < 0.5$ to the candidate.
- **Tight working point:**
  A candidate is vetoed if the medium working point requirements are not met or if the energy in the electromagnetic and hadron calorimeter associated with the highest transverse momentum track of the τ_{had} candidate falls short of 20% times the track momentum.

Efficiencies are p_T and η dependent and reach for loose working point to tight working point from 95% to 99% at a misidentification rate of 1% to 0.01%, respectively, measured in Z$\to$ $\tau\tau$ and $Z \to \mu\mu$ events [101]. Depending on the decay channel of the di-τ system different working points are chosen.

Anti-e Discriminator

This discriminator is built to remove electrons which have been wrongly identified as τ_{had}. In a multivariate approach 16 BDTs are trained depending on the decay mode of the τ_{had} candidate, the pseudorapidity η and whether the candidate is matched to an electron reconstructed using the Gaussian-sum filter algorithm, see above or [88]. Making use of the output of the BDTs loose, medium, tight and very tight working points are defined depending on $e \to \tau_{\text{had}}$ misidentification rate for a fixed τ_{had} identification efficiency. Further information can be found in [101]. An identification efficiency of 95.0%, 91.2%, 85.2% and 80.8% at a misidentification rate of 16.7%, 7.1%, 3.4% and 2.2% is measured for the loose, medium, tight and very tight working point, respectively, using Z$\to$ $\tau\tau$ and Z$\to$ ee events [101]. Different working points are chosen for different analysis channels.
Next to this MVA based discriminator, also a cut based anti-e discriminator, described in [102], is used. The loose working point of this discriminator is used in the $\mu\tau_{\text{had}}$ decay channel to distinguish electrons from hadronically decaying tau leptons. In this context, it also separates between the $e\mu$ and $\mu\tau_{\text{had}}$ final state. The number of selected events is rather low in the $\mu\tau_{\text{had}}$ channel and the above mentioned MVA based discriminator would reduce the number too much.

4.1.6 Missing transverse Energy

In the CMS detector protons are colliding along the z-axis. The transverse energy deposits in the detector of all resulting particles should be zero. In the SM the only particle which would lead to an imbalance of this sum is the neutrino since it is not detected and therefore its energy is not measured. For the $\phi \rightarrow \tau\tau$ analysis it is crucial to understand the missing transverse energy $\not\!\!E_{\mathrm{T}}$ variable, since in each signal event there are at least two neutrinos present, as shown in the branching fractions given in table 4.2. Other sources of $\not\!\!E_{\mathrm{T}}$ are calorimeter noise or detectable particles which escape the detector, for example along the z-axis where no detector is present or because of failing/dead detector parts. Furthermore, the more pile-up vertices are present the harder it gets to reconstruct the $\not\!\!E_{\mathrm{T}}$. This analysis models the $\not\!\!E_{\mathrm{T}}$ using a multivariate algorithm [103; 104], MVA $\not\!\!E_{\mathrm{T}}$, which is in particular reduces pile-up dependency of the $\not\!\!E_{\mathrm{T}}$. A BDT is trained using all particle-flow reconstructed objects, jets as described in section 4.1.4 and the number of reconstructed vertices as defined in section 4.1.1 as input.

The MVA $\not\!\!E_{\mathrm{T}}$ improves the resolution by 40% compared to more the particle-flow reconstructed $\not\!\!E_{\mathrm{T}}$ [103].

4.1.7 Transverse Mass

The transverse mass, m_T, is a variable which original was used in the discovery of the W boson [105]. The m_T is calculated in events with $\not\!\!E_{\mathrm{T}}$ and an additional object[2]:

$$m_T = \sqrt{2 p_T \not\!\!E_{\mathrm{T}} (1 - \cos \Delta\phi)}\ . \tag{4.6}$$

In this analysis m_T is used in the $e\tau_{\mathrm{had}}$ and $\mu\tau_{\mathrm{had}}$ channel to suppress the W+jets background.

4.1.8 The P_ζ variables

The P_ζ variable utilizes the observation that in $\phi \rightarrow \tau\tau$ events the angle between the missing transverse energy and the visible tau lepton products is typically small as in contrast to W+jets, QCD or $\mathrm{t\bar{t}}$ events. An axis $\vec{\zeta}$ is constructed bisecting the directions $\vec{p}_T^{\,vis_1}$ and $\vec{p}_T^{\,vis_2}$ of the visible tau lepton decay products. The quantities P_ζ and P_ζ^{vis} are then defined as:

$$P_\zeta = \left(\vec{p}_T^{\,vis_1} + \vec{p}_T^{\,vis_1} + \vec{\not\!\!E}_{\mathrm{T}}\right) \cdot \frac{\vec{\zeta}}{|\vec{\zeta}|} \quad \text{and} \quad P_\zeta^{vis} = \left(\vec{p}_T^{\,vis_1} + \vec{p}_T^{\,vis_1}\right) \cdot \frac{\vec{\zeta}}{|\vec{\zeta}|}\quad . \tag{4.7}$$

In figure 4.2 the construction of the P_ζ and P_ζ^{vis} variables is illustrated on figure 4.2(a) a $\phi \rightarrow \tau\tau$ event and on figure 4.2(b) for a W+jets or $\mathrm{t\bar{t}}$ event.

---

[2] here its either an electron or a muon

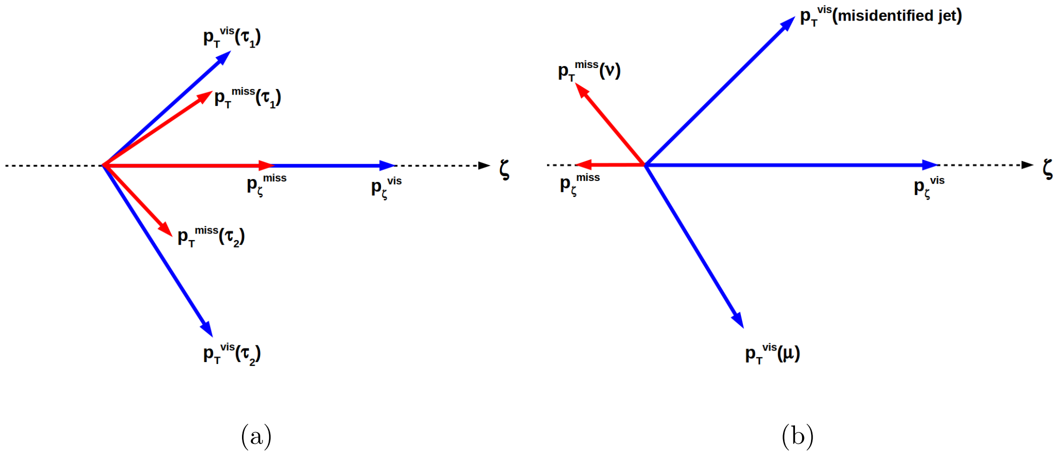

Figure 4.2: Illustration of the construction idea of the P_ζ variable: On the left figure 4.2(a) for a genuine $\phi \to \tau\tau$ event and on the right figure 4.2(b) for a W+jets or $t\bar{t}$ event.

4.1.9 Invariant di-τ Mass

The fully reconstructed invariant di-τ mass, $m_{\tau\tau}$, is used as the final discriminator to separate background and signal distributions. The di-τ system is underconstrained because of the neutrinos present in the event. It is also possible to separate background and signal distribution only based on the invariant di-τ mass of the visible particles, m_{vis}. However, the resolution using $m_{\tau\tau}$ is $10 - 20\%$ better compared to m_{vis} as shown in figure 4.1.9.

CMS has developed a maximum likelihood (see section 5.1.3) based method to estimate the fully reconstructed mass of the di-τ system. For each of the two tau leptons in the di-τ event there are three parameters known from the measurement: The absolute value of the momentum of the visible tau lepton decay product, p_{vis}, the pseudorapidity of the visible tau lepton decay product, η_{vis} and the azimuthal angle of the visible tau lepton decay product ϕ_{vis}. In case of multiple tau decay products, they are a treated as a single four-vector. These three variables can be combined to the vector of the momenta of the visible tau product $\vec{p}_{vis}$. Depending on the tau lepton decay mode, leptonically or hadronically, there are two or three unconstrained parameters which can be chosen as:

- The fraction of the tau lepton energy which is carried by the visible decay products, x.
- The azimuthal angle of the tau lepton, ϕ. Note that this is in general not the same angle as ϕ_{vis}, since ϕ is the azimuthal angle of the fully reconstructed tau lepton including neutrinos.
- The mass of the neutrino system, $m_{\nu\nu}$. For a hadronically decaying tau the

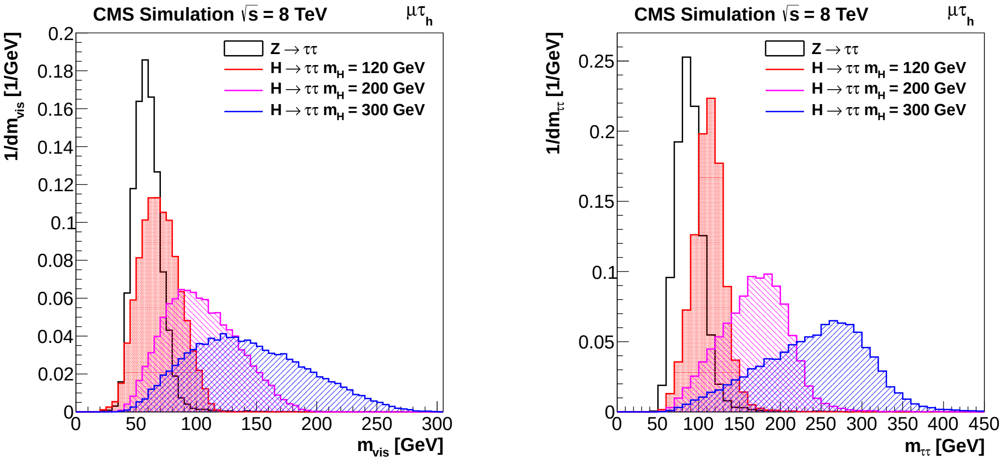

(a) (b)

Figure 4.3: The visible m_{vis} 4.3(a) and $m_{\tau\tau}$ 4.3(b) distributions are shown for different masses of a potential MSSM Higgs boson signal $H \rightarrow \tau\tau \rightarrow \mu\tau_{\mathrm{had}}$ of $m_H = 120$, 200 and 300 GeV as well as for the $Z \rightarrow \tau\tau \rightarrow \mu\tau_{\mathrm{had}}$ decay. This figure is taken from [14].

mass is zero since there is only one neutrino.

For notation reasons these parameters are summarized by $\vec{a} = (x, \phi, m_{\nu\nu})$. Additionally, each event is further constrained by the measured missing transverse energy $\vec{\not{E}}_{\mathrm{T}} = (\vec{\not{E}}_{\mathrm{T}}^{\,x}, \vec{\not{E}}_{\mathrm{T}}^{\,y})$.

A likelihood is built which describes the probability to measure $\vec{\not{E}}_{\mathrm{T}}$ if the constrained and unconstrained parameters take certain values.

$$L = L(\vec{\not{E}}_{\mathrm{T}} | \vec{p}^{\,1}_{vis}, \vec{p}^{\,2}_{vis}, \vec{a}^{\,1}, \vec{a}^{\,2}) \tag{4.8}$$

The indices 1 and 2 mark the two involved tau leptons. This likelihood is than used to compute the probability:

$$\begin{aligned} P(M^i_{\tau\tau}) = \int \delta\left(M^i_{\tau\tau} - M_{\tau\tau}(\vec{p}^{\,1}_{vis}, \vec{p}^{\,2}_{vis}, \vec{a}^{\,1}, \vec{a}^{\,2})\right) \\ \cdot L(\vec{\not{E}}_{\mathrm{T}} | \vec{p}^{\,1}_{vis}, \vec{p}^{\,2}_{vis}, \vec{a}^{\,1}, \vec{a}^{\,2}) \cdot d\vec{a}^{\,1} d\vec{a}^{\,2} \quad . \end{aligned} \tag{4.9}$$

The probability $P(M^i_{\tau\tau})$ is computed for different hypotheses i from $m_\tau < M^i_{\tau\tau} < 2$ TeV. The value which maximizes the probability, $\hat{M}^i_{\tau\tau}$, is taken as best estimate $m_{\tau\tau} = \hat{M}^i_{\tau\tau}$. Further details can be found in [106].

4.2 Event Selection

At least one successful reconstructed vertex as described in section 4.1.1 is required to be present in each event.

For the $e\mu$, $e\tau_{\text{had}}$ and $\mu\tau_{\text{had}}$ decay channels cross-triggers are used to select potential interesting events. For the $\mu\mu$ ($\tau_{\text{had}}\tau_{\text{had}}$) decay channels di-$\mu$ (di-τ_{had}) triggers are used, respectively. In the $\mu\mu$ channel additionally single muon triggers are used to further enhance the efficiency to trigger an interesting event. These triggers select events with certain p_T, η and isolation requirements. The actual thresholds depend on the data-taking period as the LHC instantaneous luminosity increased. As an example, in figure 4.2 the turn-on curves for the $e\tau_{\text{had}}$ trigger as used in 8 TeV data-taking period is shown.

In the offline selection kinematic cuts on the leptons are chosen in order to guarantee a high and stable trigger efficiency. An opposite sign lepton pair has to be present in each event. Additionally, each channel defines additional cuts to suppress specific backgrounds. In the following chapters 4.2.1, 4.2.2, 4.2.3, 4.2.4 and 4.2.5 a detailed event selection for each channel is given.

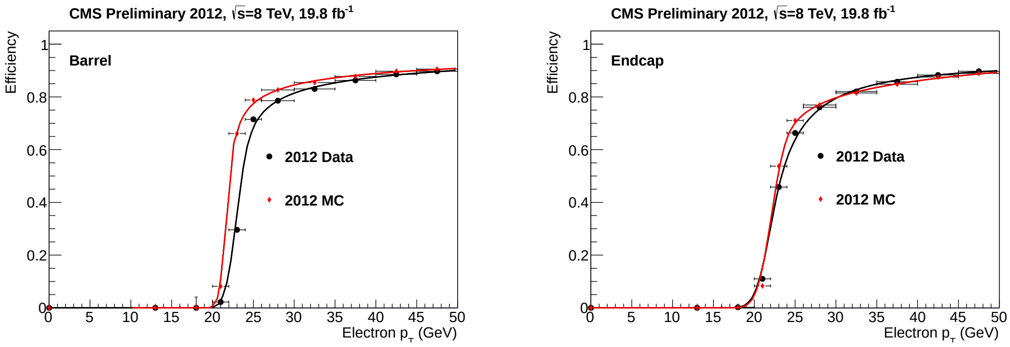

(a) (b)

Figure 4.4: Trigger turn-on curves for the electron leg of the $e\tau_h$ trigger for 2012 data and simulation. On the left side 4.4(a) the barrel region ($|\eta| < 1.479$) and on the right side 4.4(b) the endcap region ($|\eta| \geq 1.479$) of the ECAL is shown. The plots are taken from [107].

4.2.1 The $e\mu$ Channel

An event passes the selection in the $e\mu$ channel if the following requirements are matched:

- An $e\mu$ trigger has to be passed.
- A high level trigger (HLT) electron object should be matched within $\Delta R < 0.5$ with an offline reconstructed electron with the following criteria:
  - transverse momentum of $p_T^e > 10$ GeV
  - pseudorapidity of $|\eta^e| > 2.3$

  - loose MVA based electron identification (section 4.1.2)
  - isolation of $I_e < 0.15(0.1) \cdot p_T^e$ (section 4.1.3) for electrons in the barrel $|\eta^e| < 1.479$ (endcap $|\eta^e| \geq 1.479$) region

- A HLT electron object should be matched within $\Delta R < 0.5$ with an offline reconstructed muon with following criteria:
  - transverse momentum of $p_T^\mu > 10$ GeV
  - pseudorapidity of $|\eta^\mu| > 2.1$
  - tight PF muon identification (section 4.1.3)
  - isolation of $I_e < 0.15(0.1) \cdot p_T^\mu$ (section 4.1.3) for muons in the barrel $|\eta^e| < 1.479$ (endcap $|\eta^e| \geq 1.479$) region
- Due to the trigger threshold either the muon or the electron is required to have a transverse momentum of $p_T > 20$ GeV to ensure high and stable trigger efficiency.
- The electron and muon are required to be of opposite charge.
- In case of more than one candidate the one with the highest $p_T^e + p_T^\mu$ is chosen.
- The quantity $P_\zeta - 1.85 P_\zeta^{vis}$, see section 4.1.8, is required to be greater than -20 GeV. The factor 1.85 was derived maximizing the sensitivity of the analysis[3]. The cut reduces in particular the W+jets background.

4.2.2 The $e\tau_{\text{had}}$ Channel

The requirements for the $e\tau_{\text{had}}$ channel are listed in the following:

- An $e\tau_{\text{had}}$ trigger has to be passed.
- A HLT electron object should be matched within $\Delta R < 0.5$ with an offline reconstructed electron with following criteria:
  - transverse momentum of $p_T^e > 24$ GeV
  - pseudorapidity of $|\eta^e| > 2.1$
  - tight MVA based electron identification (section 4.1.2)
  - isolation of $I_e < 0.1 \cdot p_T^e$ (section 4.1.3)
- A HLT tau object should be matched within $\Delta R < 0.5$ with an offline reconstructed hadronic tau lepton with following criteria:
  - transverse momentum of $p_T^{\tau_{\text{had}}} > 20$ GeV

---

[3] In contrast to the $e\tau_{\text{had}}$ and $\mu\tau_{\text{had}}$ channel in the $e\mu$ channel a cut on $P_\zeta - 1.85 P_\zeta^{vis}$ instead on m_T is used since having an electron and a muon in the channel makes it ambiguous to construct the transverse mass with either electron or muon and $\not{E}_{\text{T}}$. Cutting on both combinations would reduce the signal efficiency too much.

  - pseudorapidity of $|\eta^{\tau_{\mathrm{had}}}| > 2.3$
  - isolation of $I_\tau < 1.5$ GeV (section 4.1.5)
  - medium WP of the MVA based anti-e discriminator (section 4.1.5)
  - loose WP of the anti-μ discriminator (section 4.1.5)

- The electron and the hadronic tau lepton are required to be of opposite sign.
- If there are more than one pair of opposite sign electron and hadronic tau lepton the one with the highest $p_T^e + p_T^{\tau_{\mathrm{had}}}$ is chosen.
- An event with one or more additional electrons with $p_T > 10$ GeV, $|\eta| < 2.5$, $d_z < 0.2$ cm, $d_0 < 0.045$ cm, $I_e < 0.3 \cdot p_T^e$, which pass the loose MVA based identification, as described in section 4.1.2 is vetoed.
- Events with a muon with $p_T > 10$ GeV, $|\eta| < 2.4$, $d_z < 0.2$ cm, $d_0 < 0.045$ cm, $I_\mu < 0.3 \cdot p_T^\mu$ which passes the tight identification criteria, as described in section 4.1.3 are vetoed.
- No opposite sign electron pair should be present in which both electrons fulfil the veto cut-based criteria defined by the EGamma particle object group [108]. Both electrons should have $p_T > 15$ GeV, $|\eta| < 2.5$, $d_z < 0.2$ cm, $d_0 < 0.045$ cm, $I_e < 0.3 \cdot p_T^e$ and have a minimum separation from each other of $\Delta R > 0.15$. This veto cut is used to reject $Z/\gamma^* \rightarrow ee$ events.
- The transverse mass, see section 4.1.7, is required to be $m_T < 30$ GeV to reject W+jets background.

4.2.3 The $\mu\mu$ Channel

Below the event selection for the $\mu\mu$ channel is described:

- A $\mu\mu$ trigger has to be passed.
- Two HLT muon objects should be matched within $\Delta R < 0.5$ with two offline reconstructed muons with following criteria:
  - transverse momentum for both $p_T^\mu > 10$ GeV and one with $p_T^\mu > 20$ GeV
  - pseudorapidity of $|\eta^\mu| > 2.1$ ($|\eta^\mu| > 2.3$ if the single muon trigger has been passed)
  - tight PF muon identification (section 4.1.3)
  - isolation of $I_\mu < 0.15(0.1) \cdot p_T^\mu$ (section 4.1.3) for muons wit $p_T < 20$ GeV (> 20 GeV) 4.1.5)
- The muons are required to be of opposite charge.
- Due to the overwhelmingly large background from Z$\rightarrow$ $\mu\mu$ a boosted decision tree is trained to suppress these events. A detailed description is given in [109; 110].

4.2.4 The $\mu\tau_{\text{had}}$ Channel

An event passes the selection in the $\mu\tau_{\text{had}}$ channel if the following requirements are matched:

- A $\mu\tau_{\text{had}}$ trigger has to be passed.

- A HLT muon object should be matched within $\Delta R < 0.5$ with an offline reconstructed muon with following criteria:
  - transverse momentum of $p_T^\mu > 20$ GeV
  - pseudorapidity of $|\eta^\mu| > 2.1$
  - tight PF muon identification (section 4.1.3)
  - isolation of $I_\mu < 0.1 \cdot p_T^\mu$ (section 4.1.3)

- A HLT tau object should be matched within $\Delta R < 0.5$ with an offline reconstructed hadronic tau lepton with following criteria:
  - transverse momentum of $p_T^{\tau_{\text{had}}} > 20$ GeV
  - pseudorapidity of $|\eta^{\tau_{\text{had}}}| > 2.3$
  - isolation of $I_\tau < 1.5$ GeV (section 4.1.5)
  - loose WP of the cut based anti-e discriminator (section 4.1.5)
  - tight WP of the anti-μ discriminator (section 4.1.5)

- The muon and the hadronic tau lepton are required to be of opposite sign.

- If there are more than one candidate for an opposite sign pair of a hadronic tau lepton and a muon the pair with the highest $p_T^\mu + p_T^{\tau_{\text{had}}}$ is chosen.

- Events with one or more electrons with $p_T > 10$ GeV, $|\eta| < 2.5$, $d_z < 0.2$ cm, $d_0 < 0.045$ cm, $I_e < 0.3 \cdot p_T^e$, which passes the loose MVA based identification, as described in section 4.1.2 are vetoed.

- Events with an additional muon with $p_T > 10$ GeV, $|\eta| < 2.4$, $d_z < 0.2$ cm, $d_0 < 0.045$ cm, $I_\mu < 0.3 \cdot p_T^\mu$, which passes the tight identification, as described in section 4.1.3 are vetoed.

- No opposite sign muon pair is present in the event in which each muon has $p_T > 15$ GeV, $|\eta| < 2.4$, $d_z < 0.2$ cm, $d_0 < 0.045$ cm, $I_\mu < 0.3 \cdot p_T^\mu$ and is reconstructed by the tracker and global algorithms. The muons must also have a minimum separation of $\Delta R > 0.15$. This veto is optimised to reject the background of $Z/\gamma^* \to \mu\mu$ events.

- The transverse mass, see section 4.1.7, is required to be below 30 GeV to reject W+jets background.

4.2.5 The $\tau_{\text{had}}\tau_{\text{had}}$ Channel

In the $\tau_{\text{had}}\tau_{\text{had}}$ channel the following requirements have to be fulfilled:

- A di-τ trigger has to be passed.
- Two HLT tau objects should be matched within $\Delta R < 0.5$ with two offline reconstructed hadronic tau leptons with following criteria:
  - transverse momentum of $p_T^{\tau_{\text{had}}} > 45$ GeV
  - pseudorapidity of $|\eta^{\tau_{\text{had}}}| > 2.1$
  - isolation of $I_\tau < 1.0$ GeV (section 4.1.5)
  - the tau lepton with the lower p_T has to pass the loose WP of the MVA based anti-e discriminator (section 4.1.5)
- The two hadronic tau leptons are required to be of opposite sign.
- If there are more than one opposite sign hadronic tau lepton pair the one with the lowest $I_\tau^{(1)} + I_\tau^{(2)}$ is chosen.
- Events with one or more electrons with $p_T > 10$ GeV, $|\eta| < 2.5$, $d_z < 0.2$ cm, $d_0 < 0.045$ cm, $I_e < 0.3 \cdot p_T^e$, which pass the loose MVA based identification, as described in section 4.1.2 are vetoed.
- Events with a muon with $p_T > 10$ GeV, $|\eta| < 2.4$, $d_z < 0.2$ cm, $d_0 < 0.045$ cm, $I_\mu < 0.3 \cdot p_T^\mu$, which passes the tight identification, as described in section 4.1.3 are vetoed.

4.3 Event Categorization

Events which pass the event selection as described in section 4.2 are further categorized into a b-tag and no-b-tag event category with the aim to exploit the considered signal production mechanisms, Higgs production in association with b-quarks (bbϕ) and gluon-gluon fusion (ggϕ), respectively:

- **b-tag**:
  A least one b-tagged jet as defined in section 4.1.4 is present in the event, but not more than one jet with $p_T > 30$ GeV is allowed. The latter requirement reduces $\mathrm{t\bar{t}}$ background.
- **no-b-tag**:
  All events are picked up which contain no b-tagged jet with $p_T > 20$ GeV.

A further categorization, like in the SM analysis [106], is not performed to reduce possible model dependencies, which can occur since for example the transverse momentum of the Higgs boson and therefore of its decay products in the gluon-gluon fusion process depends on the particles in the fermion loop. A further categorization by requiring high p_T leptons could thus lead to an increasing sensitivity to particular models while at the same time reducing the sensitivity to others. It should be noted that the separation of the categories is nit perfect in respect to the signal production processes. Especially the b-tag category also contains ggϕ signal events due to misidentified jets, final or initial state radiation.

4.4 Background Estimation

After applying the event selection and categorization as described in 4.2 and 4.3 non negligible background contributions remain. These irreducible fractions need to be estimated as precisely as possible in order to be able to separate the contribution from background in the observation from a potential signal. Data-driven methods are used for the main backgrounds to reduce systematic uncertainties and dependencies from Monte Carlo simulations like the modelling of the underlying event. Different backgrounds are estimated using different approaches.

4.4.1 $Z/\gamma^* \to \tau\tau$

To model this background the embedding technique is used. The main idea is to select $Z/\gamma^* \to \mu\mu$ events in data and to replace the muons with simulated tau lepton decays. The sample is normalized to the yield measured in a control region of $Z/\gamma^* \to \mu\mu$ events. In order to obtain the number of $Z/\gamma^* \to \tau\tau$ events after the event selection a scale factor is applied to the embedded sample. The factor is computed as the ratio of the Monte Carlo simulated $Z/\gamma^* \to \mu\mu$ yield measured in the control region to the simulated $Z/\gamma^* \to \tau\tau$ yield measured in the signal region. Further details can be found in [110].

In contrast to Monte Carlo based methods, the embedding technique has the advantage that it describes the underlying event, $\not{E}_\mathrm{T}$ or number of jets, perfectly as it is taken from data.

4.4.2 QCD

eμ

The fake-rate method [111] is used to determinate the normalization of this background. In a QCD event there are no non isolated electrons or muons. Thus, a reconstructed electron must be due to a jet which is misidentified as an electron. The idea of the fake-rate method is to measure this fake-rate in a QCD enriched region by selecting events with loosened isolation and identification criteria. The fake-rate is than the ratio of the number of events which also pass the electron event selection criteria as defined in section 4.2.1 to the number of events which pass the loosened requirements. This factor is applied to the number of events obtained in each category after applying all cuts except for electron identification and isolation cuts which are kept loose as used for the determination of the ratio. Contaminations from other background sources are subtracted based on Monte Carlo simulation.

The shape of the kinematic distributions is taken from a selection before the P_ζ and the categorization cuts have been applied in a sample where the muon and the electron have the same sign.
The fake-rate for jets → μ was found to be negligible.

$e\tau_{\text{had}}$, $\mu\mu$ and $\mu\tau_{\text{had}}$

The main sources of the QCD background in this channel are misidentified jets which either mimic a muon or more often a hadronically decaying tau lepton. The QCD background is obtained by the ABCD method. Four regions are defined based on whether the leptons have the same or opposite sign and the whether the electron/muon is isolated or not[4]. In the anti-isolated region the ratio of opposite-sign to same-sign events is measured. Other backgrounds are subtracted based on Monte Carlo simulation. The factor is than applied to the same-sign isolated region to obtained the opposite-sign isolated region, which is the signal region.

$\tau_{\text{had}}\tau_{\text{had}}$

In the $\tau_{\text{had}}\tau_{\text{had}}$ channel the QCD background is estimated similarly as in the $e\tau_{\text{had}}$, $\mu\mu$ and $\mu\tau_{\text{had}}$ channels with the ABCD method. Three control regions are defined: same-sign isolated, same-sign anti-isolated and opposite-sign anti-isolated. Other background sources are subtracted in each of the three regions taken from Monte Carlo simulations. In contrast to the $e\tau_{\text{had}}$, $\mu\mu$ and $\mu\tau_{\text{had}}$ decay channels, the normalization is obtained by multiplying the opposite-sign anti-isolated region by the ratio of the same-sign isolated to the same-sign anti-isolated region. The shape is taken from the opposite-sign anti-isolated region.

4.4.3 W+jets

$e\mu$

The fake-rate method is applied, see 4.4.2, to estimate the W+jets background in the $e\mu$ channel.

$e\tau_{\text{had}}$, $\mu\tau_{\text{had}}$ and $\tau_{\text{had}}\tau_{\text{had}}$

A W+jets enriched control region with $m_T > 70$ GeV is constructed. Other contributions in this background are subtracted based on Monte Carlo predictions. The yield in the control region is extrapolated into the signal region using an extrapolation factor computed from simulation. The shape is taken from Monte Carlo simulation. To enhance the number of events the shape in the b-tag category is obtained by relaxing the b-tag requirement to $d > 0.244$ which corresponds to a miss-tag rate of 10% instead of $d > 0.679$. The relaxation has been checked not to distort the shape.
In the $\tau_{\text{had}}\tau_{\text{had}}$ channel the correction factor of the $\mu\tau_{\text{had}}$ channel is applied assuming

---

[4] A relaxed isolation is defined.

that the misidentification rate of jet → τ_{had} is independent from the lepton coming from the W decay, either muon or hadronically decaying tau lepton.

$\mu\mu$

The W+jets background in the $\mu\mu$ channel is estimated from Monte Carlo simulation.

4.4.4 $Z/\gamma^* \to ee$ and $Z/\gamma^* \to \mu\mu$

$e\tau_{\text{had}}$, $\mu\tau_{\text{had}}$ and $\tau_{\text{had}}\tau_{\text{had}}$

In these channels the background is estimated by relying on Monte Carlo simulation. In the $e\tau_{\text{had}}$ channel the yield is corrected for the differences in Monte Carlo simulations compared to data with respect to the $e \to \tau_{\text{had}}$ misidentification probability. The $\mu \to \tau_{\text{had}}$ misidentification probability has been found negligible. Further details can be found in [14].

$\mu\mu$

The $Z/\gamma^* \to \mu\mu$ background is by far the most dominant background in the $\mu\mu$ channel. A boosted decision tree is trained to separate $Z/\gamma^* \to \mu\mu$ from $Z/\gamma^* \to \tau\tau \to \mu\mu$ and $\phi \to \tau\tau \to \mu\mu$ events. The boosted decision tree is similar to the one mentioned in section 4.2.3, but the distance of closest approach significance variable is not used to train the tree. This variable quantifies the distance of the vertices of two muons. The closer they are the less likely they are coming from tau lepton decays. Monte Carlo templates for the distance of closest approach significance of the two muons of $\phi/Z/\gamma^* \to \tau\tau \to \mu\mu$ and $Z/\gamma^* \to \mu\mu$ events are then fitted to the data in bins of the boosted decision tree discriminator and the di-muon mass. Other background sources are subtracted from data using Monte Carlo simulations before performing the fit. The derived scale factors are applied to the $Z/\gamma^* \to \mu\mu$ Monte Carlo samples. Further details can be found in [109].

4.4.5 $\mathrm{t\bar{t}}$

In both event categories the shape of the $\mathrm{t\bar{t}}$ background is modelled by Monte Carlo simulation. The background is normalized to the measured cross-section by the CMS collaboration [112] in the 7 TeV analysis and to the NNLO cross-section [113] in the 8 TeV analysis. In an $e\mu$ $\mathrm{t\bar{t}}$ control region, defined by two b-tagged jets, the Monte Carlo simulation is checked and correction factors are obtained which are applied to the $\mathrm{t\bar{t}}$ background.

4.4.6 Single Top and Di-boson

The background contribution coming from di-boson production or from single tops is found to be small[5]. Monte Carlo simulation is used to model these backgrounds.

4.5 Uncertainties

Several uncertainties effect the background or signal expectations in the $\phi \to \tau\tau$ analysis. The uncertainties are distinguished in:

- **Systematic Uncertainties:**
  These uncertainties arise due to imperfections in the reconstruction of objects, event selection or background estimation. The used uncertainties are given in section 4.5.1. A further separation between uncertainties which effect the total normalization and uncertainties which effect the shape of a background or signal distribution is done.

- **Statistical Uncertainties:**
  These uncertainties arise from a limited number of simulated events in certain bins of the $m_{\tau\tau}$ distribution. The treatment of these uncertainties is described in section 4.5.2.

The technical description of the incorporation of all uncertainties in the statistical model is given in chapter 5.

4.5.1 Systematic Uncertainties

In table 4.3 the uncertainties on the backgrounds are listed, respectively. The effect of the uncertainties for both considered event categories is given. Also the correlations of the uncertainties are given. An uncertainty is treated either fully correlated or not correlated. Depending on the correlation they enter the statistical model as explained in chapter 5.

Note that not all uncertainties effect each category in each channel, e.g. the electron identification and trigger efficiencies do obviously not effect the $\mu\tau_{\text{had}}$ or $\mu\mu$ channel. Further details about the uncertainties can be found in [14; 110].

The theory uncertainties on the MSSM signal cross-section depends on the considered scenario, the chosen point in the two dimensional model space, the center-of-mass energy and the type of the Higgs boson (h, A or H). It can account up to 25%. The *MSTW 2008* parton density function is used in the cross-section calculation and the uncertainties are calculated as described in [114; 115]. The combined parton density function and α_s uncertainty, just depends on the type and the mass of the Higgs boson an reaches from about 2% at 90 GeV to 13% at 1000 GeV. There

---

[5] The maximum contribution of about 3% of the total background is found in the $\mu\tau_{\text{had}}$ channel in the b-tag category in the 8 TeV dataset.

Experimental Uncertainties		Event category			
	Uncertainty	no-b-tag	b-tag	Typ	Correlation
Integrated luminosity 7(8) TeV	2.2% (2.6%)	2.2% (2.6%)	2.2% (2.6%)	N	[1]
Electron identification and trigger	2%	2%	2%	N	[2]
Muon identification and trigger	2%	2%	2%	N	[2]
Tau lepton identification and trigger	8%	8%	8%	N	[3]
Tau lepton identification at high p_T	$0-20\%$	$0-20\%$	$0-20\%$	S	[3]
Jet energy scale	$1-10\%$	$1-5\%$	$1-8\%$	N	[1]
Missing transverse energy	$1-5\%$	$1-2\%$	$1-2\%$	N	[1]
b-tagging efficiency	$2-7\%$	$2-4\%$	$2-9\%$	N	[1]
b-mistag rate	$10-20\%$	2%	$2-5\%$	N	[1]
Electron energy scale	1%	1%	1%	S	[1]
Tau lepton energy scale	3%	3%	3%	S	[3]
Normalization, Z production	$2-3.3\%$	$2-3.3\%$	$2-3.3\%$	N	[1]
$Z \to \tau\tau$ category selection	3%	3%	$1-3\%$	N	[4]
$\mathrm{t\bar{t}}$	10%	10%	$10-17\%$	N	[1]
Di-boson	$15-30\%$	$15-30\%$	$15-30\%$	N	[1]
QCD	$10-35\%$	$10-35\%$	$20-35\%$	N	[4]
W+jets	$10-30\%$	$10-30\%$	30%	N	[4]
Z: $e \to \tau_{\mathrm{had}}$ fake	20%	20%	20%	N	[3]
Z: $\mu \to \tau_{\mathrm{had}}$ fake	30%	30%	30%	N	[3]
Z: jet$\to \tau_{\mathrm{had}}$ fake	20%	20%	20%	N	[3]

[1] treated correlated between channels and categories with the same center-of-mass collision energy

[2] treated correlated across channels, categories and center-of-mass collision energy

[3] treated correlated between categories of the same channel and same center-of-mass collision energy

[4] treated uncorrelated

Table 4.3: Listed are the systematic uncertainties on the various backgrounds. Some uncertainties depend on p_T and η. The type of the uncertainty, either normalization (N) or shape (S), is given in the second column from the right. Whether channels are correlated across categories, channels and center-of-mass energy of proton-proton collisions is given in the last column.

are no theoretical uncertainties available for the 2HDM. The SM uncertainties for all processes relying on the quark density function is $4-5\%$, while the uncertainties for the processes relying on the gluon density function is 10%. The SM Higgs boson (125 GeV) scale variation uncertainties depend on the event category and are computed to 10%, $1-4\%$ and 4% for the gluon-gluon fusion, vector boson fusion or Higgsstrahlung process, respectively. The uncertainty on the underlying event and parton shower for SM Higgs boson production is $2-10\%$ depending on the production process and the event category. The uncertainties on the SM Higgs boson are needed in the cases where the SM Higgs boson hypothesis is tested against a BSM Higgs boson hypothesis. All theory uncertainties on the signal processes are treated correlated between channels, categories and data-taking periods.

4.5.2 Statistical Uncertainties

In the $\phi \to \tau\tau$ analysis the $m_{\tau\tau}$ distribution between 0 and 1500 GeV is used for the limit calculation. Limitations in the number of events in the high mass tails for several Monte Carlo samples can lead to fluctuating bin contents in the shapes for the high mass tail and therefore lead to fluctuations in the limit calculation. Since the respective backgrounds show an exponential decay for $m_{\tau\tau} >$ 120-300 GeV a one dimensional analytical fit with two free and real parameters c_0 and c_1 of the form

$$f(m_{\tau\tau}) = \exp\left(-\frac{m_{\tau\tau}}{c_0 + c_1 \cdot m_{\tau\tau}}\right) , \tag{4.10}$$

can be used to overcome the shortage of Monte Carlo statistics. Therefore, function (4.10) is fitted to the original Monte Carlo templates in the $e\mu$, $e\tau_\mathrm{h}$, $\mu\tau_\mathrm{h}$ and $\tau_\mathrm{h}\tau_\mathrm{h}$ channel. In the $\mu\mu$ channel two dimensional histograms $m_{\tau\tau}$ over $m_{\mu\mu}$ are used as final discriminators between background and signal distributions. Thus, no analytical fit has been performed in this channel. The exact range of the fit depends on the stability of the fit and has been determined by getting the best χ^2 testing the compatible of the analytical fit and the original Monte Carlo shape. In table 4.4 the backgrounds are listed for which an analytical fit has been performed.

The analytical fit returns the normalized Eigenvectors v_i and the Eigenvalues λ_i of the covariance matrix $cov(c_0, c_1)$ as well as the best fit values for the fitted parameters c_0 and c_1. With these parameter two shape uncertainties $(i = 0, 1)$ are built by varying the most probable values of c_0 and c_1 up and down:

Channel	Period	no-b-tag	b-tag
$e\mu$	7 TeV	EWK	EWK
	8 TeV	EWK	EWK
$e\tau_\mathrm{had}$	7 TeV	QCD, W+jets	-
	8 TeV	QCD, $\mathrm{t\bar{t}}$, W+jets	QCD, $\mathrm{t\bar{t}}$, W+jets
$\mu\tau_\mathrm{had}$	7 TeV	W+jets	-
	8 TeV	$\mathrm{t\bar{t}}$, W+jets	$\mathrm{t\bar{t}}$, W+jets
$\tau_\mathrm{had}\tau_\mathrm{had}$	8 TeV	QCD	QCD

Table 4.4: List of backgrounds per channel for which an analytical fit has been performed.

$$c_j \to c_j \pm \sqrt{\lambda_i} \cdot v_{ji} , \tag{4.11}$$

where v_{ji} is the j-th element of the Eigenvector v_i. In case of a diagonal covariance matrix, the eigenvalues would just correspond to the variance. Thus, the square root is equal to the standard deviation. The first Eigenvector points in the direction where the data varies the most. The following Eigenvector is orthogonal to the first. For the case of a diagonal covariance matrix the first (second) shape uncertainty therefore would just vary the most probable value of c_0 (c_1) up by $\pm 1\sigma$. The shape uncertainties are then treated in the likelihood as described in chapter 5.1.2.

In figure 4.5 the analytical fit to the QCD template in the $e\tau_\mathrm{had}$ channel in the b-tag and no-b-tag category is shown together with the up and down shape variations corresponding to the parameters c_0 and c_1. Since the χ^2 probability is close to one a good performance of the analytical fit can be concluded. The Kolmogorov–Smirnov (KS) test is another test to check the performance of the fit. Since the p-value of this test, $P(KS)$, is also close to one a very good performance is seen.

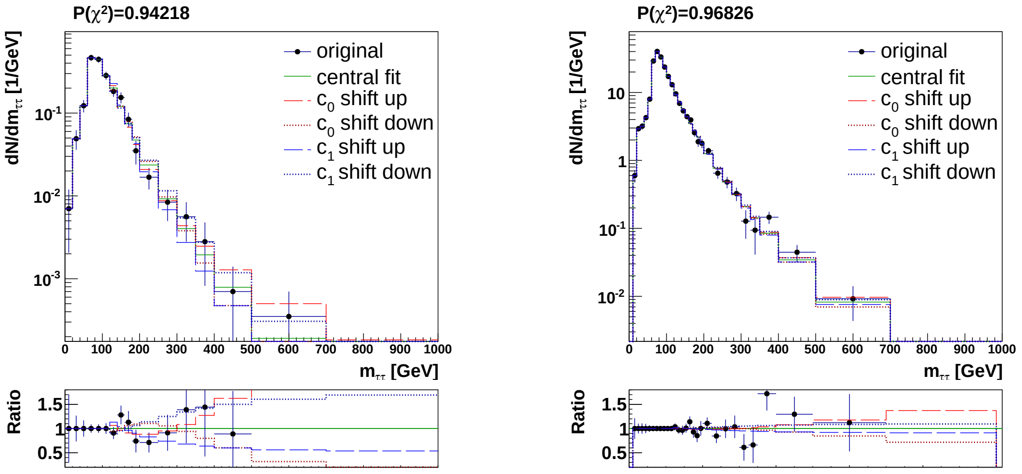

(a) (b)

Figure 4.5: Shown are the distributions of the analytical fit to the original QCD background template in the $e\tau_{\text{had}}$ channel in the b-tag (4.5(a)) and no-b-tag category (4.5(b)). A good performance is seen, indicated by a χ^2 probability close to one. The up and down shape variation of the parameters c_0 and c_1 are also shown.

Next to the analytical fit, the Barlow-Beeston method [116; 117] is used to take limited Monte Carlo statistics into account. If a considered bin is not within the range of the analytical fit described above and if the ratio of the statical uncertainty in one bin for a certain background to the total number of events in this bin is above 5% a shape uncertainty is added by varying the considered bin in the nominal shape by $\pm 1\sigma$ of its statistical uncertainty. Running the limit calculation with so many uncertainties will lead to stability issues in the minimization procedure as well as increasing the computing time. Therefore, an uncertainty is dropped if the shift on its best estimate times the size of the original uncertainty is below a certain fraction of the original bin content. This relative shift is calculated by performing in each channel a maximum likelihood fit, as described in section 5.1.3, with the full list of added statistical uncertainties. It is not possible to run the maximum likelihood fit on the combination of all channels due to the mentioned stability issues for the large number of uncertainties. In figure 4.6(a) the relative fraction of discarded uncertainties is shown depending on this relative shift. In the analysis a cut on the relative shift of 10% is chosen. The pruning of uncertainties is checked to have no significant impact on the expected and observed limit relative to the case where no uncertainties are pruned, as seen in figure 4.6(b). The $\sigma \cdot \mathcal{B}$ limit has been calculated on the gg$\phi \to \tau\tau$ process for a single resonance at $m_\phi = 500\,\text{GeV}$ testing the H_b against $H_{\phi+b}$ hypothesis. Choosing a cut value of 10% on the relative shift does discard 85% of the all uncertainties. Non Barlow-Beeston uncertainties are protected from being dropped. A more aggressive pruning does only slightly enhance the fraction of discarded uncertainties while on the other hand increase the effect on the observed and expected limit. More masses have been checked leading to an equally satisfying result. Also the effect on the $\sigma \cdot \mathcal{B}$ limit for the bb$\phi \to \tau\tau$ process has been controlled. More details on the $\sigma \cdot \mathcal{B}$ limit calculation can be found in chapter 5 and in section 6.3.2.

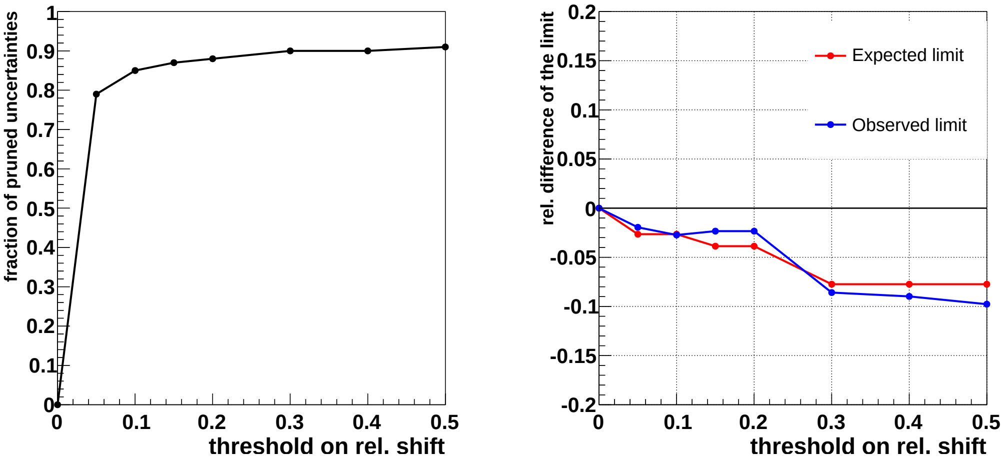

(a) (b)

Figure 4.6: In figure 4.6(a) the relative fraction of discarded uncertainties is shown depending on the cut value on the relative shift of the uncertainties. The effect on the observed and expected limit depending on the relative shift cut is shown in figure 4.6(b). The $\sigma \cdot \mathcal{B}$ limit has been calculated on the gg$\phi \to \tau\tau$ process for a single resonance at $m_\phi = 500\,\text{GeV}$ testing the H_b against $H_{\phi+b}$ hypothesis.

There are 171 uncertainties without counting Barlow-Beeston uncertainties or the uncertainties related to the analytical fit. Adding Barlow-Beeston uncertainties enlarges this number to 2198. By introducing the analytical fit in the backgrounds listed in table 4.4, the number is reduced to 2065. Dropping the uncertainties with the chosen cut value of 0.1 on the relative shift reduces the uncertainties to the final number of 316 uncertainties.

Chapter 5

Statistics

The purpose of this chapter is to give a general overview without being to case-dependent. More analysis-specific details will be given in chapter 6. In high energy physics hypotheses tests are performed. A hypothesis usually corresponds to a physics model. In this thesis for example the SM is tested against a certain extension of the SM. Since no significant excess or deviation from the SM prediction has been found the chapter will focus on limit setting approaches.
In section 5.1 the definition of a likelihood model is explained. First, the likelihood function, section 5.1.1, is introduced and the incorporation of uncertainties will be described. After building the model the Maximum Likelihood method and the Goodness-of-Fit test, as introduced in section 5.1.3, can be used for validating. Thereafter, the $\mathrm{CL_s}$ (section 5.2.1) and the Feldman-Cousins method (section 5.2.2) are explained as examples of setting an upper limit for the cross-section of a given process. The treatment of the uncertainties is discussed in the context of these methods.

5.1 Building Likelihood Models

When searching for a signal on top of a background-only hypothesis the experimental inputs are: the background expectation b, the signal expectation s and the actual number of observed events n. In a simple counting experiment these parameters are single numbers. In this thesis a shape analysis has been performed, where the signal and background expectation and the observation are provided in form of binned distributions (histograms), s_i, b_i and n_i respectively, which can be viewed as a set of potentially correlated counting experiments. In addition, systematic and statistic uncertainties θ are assigned to the signal and background expectations.

5.1.1 The Likelihood Function

Statistic provides the tools to quantify the agreement between the observation n and different hypothesis. In particle physics usually a *background hypothesis*, H_b, and a *signal+background hypothesis*, H_{s+b}, are defined. The likelihood function, L, quantifies the agreement between the observation and the considered hypotheses.

In a shape analysis each bin i is treated independently as a counting experiment. Therefore, the full likelihood is a product of the likelihood values for each bin:

$$L(n|r \cdot s + b) = \prod_i \text{Poisson}(n_i|r \cdot s_i + b_i) = \prod_i \frac{(r \cdot s_i + b_i)^{n_i}}{n_i!} \cdot e^{-(r \cdot s_i + b_i)} \ . \tag{5.1}$$

The likelihood function depends on the observation n, the background expectation b and the signal expectation s, where n, b and s are the vector of the individual bins n_i, b_i and s_i respectively. It follows a Possion distribution, which is discrete and describes the probability of a given number of events. The events have to be independent and the average has to be known. Furthermore, the *signal strength modifier* r is introduced. As shown later, limits will be expressed in terms of r.
In cases with multiple backgrounds, enumerated by j, the background expectation in bin i will be expressed by $b_i = \sum_j b_{ij}$. Analogous for multiple signal contributions, numbered by k, the signal expectation in bin i will be exp $s_i = \sum_k s_{ik}$.

5.1.2 Incorporating Uncertainties

Background and signal expectations are always measured within uncertainties. A single systematic or statistic uncertainty is denoted by θ_l while θ is used to refer to all uncertainties of a given background or signal contribution. The uncertainties θ are given in absolute values, e.g. if the expectation of a certain background is 50 events and the uncertainty amounts to 5 events the uncertainty is given as $\theta_l = 5$. In this thesis and other analyses using the *combined limit* tool (see section 3.3) uncertainties are treated as being either fully correlated or uncorrelated. Uncertainties can either change the normalization of a certain histogram as a whole, change the shape of a histogram or change only single bins.
Including these changes the likelihood function (5.1) to:

$$L(n|r \cdot s(\theta) + b(\theta)) = \prod_i Poisson(n_i|r \cdot s_i(\theta) + b_i(\theta)) \cdot \prod_l p(\tilde{\theta}_l|\theta_l) \ , \tag{5.2}$$

where the index l is running over the total amount of uncertainties. Both the signal and background expectations can depend on uncertainties, but in general they will neither depend on them in the same way nor on the exact same set of θ. The quantity $\tilde{\theta}_l$ denotes the *a priori* known best estimate of the nuisance parameter θ_l, before any kind of additional knowledge is obtained about the uncertainty model by performing a fit to the observation. In contrast to this a priori knowledge, the term *a posteriori* refers to quantities such as uncertainties which have been constrained by a fit to the observation.

Uncertainties which effect the total normalization of a background or signal yield follow a probability density function $p(\tilde{\theta}_l|\theta_l)$. Ideally, the probability density functions are measured, but for uncertainties which change the total normalization this is often not the case. Only the variation of the uncertainty and the best fit value are known. Historically, there are three analytical expressions which could be chosen [118]: Lognormal (Log-$\mathcal{N}$), Gamma or Gaussian distributions. Using Gaussians could lead to numerical and conceptual issues as shown in [119]. Gamma distributions are used for uncertainties on backgrounds which have been measured in control regions, thus often used for statistical uncertainties. Lognormal distributions are recommended for multiplicative corrections such as efficiencies and cross-sections. In this thesis Lognormal distributions are used:

$$\text{Log-}\mathcal{N}(\theta_l;\tilde{\theta}_l,\kappa_l) = \frac{1}{\theta_l \cdot \kappa_l \cdot \sqrt{2\pi}} \cdot \exp - \left(\frac{(ln(\theta_l/\tilde{\theta}_l))^2}{2\kappa_l^2}\right) , \tag{5.3}$$

where κ_l is the scale parameter, the standard deviation of the natural logarithm of the variable.

Uncertainties which change the shape are treated by *vertical template morphing.* For each uncertainty which changes a certain background or signal shape h^0 two extra shapes, $h_x^{(-1\sigma)}$ and $h_x^{(+1\sigma)}$, are created by varying the quantity x on which h^0 depends by $\pm 1\sigma$. Typically, x is a physical observable such as the jet energy scale. Multiple shape uncertainties are treated such that they add up to the final shape. For each shape uncertainty a nuisance parameter λ_x is added which has to guarantee a smooth interpolation between the varied and the nominal shape. The final shape then depends on these nuisance parameters:

$$h(\lambda) = h^0 + \sum_x \left(a(\lambda_x) \cdot h_x^{(+1\sigma)} + b(\lambda_x) \cdot h^0 + c(\lambda_x) \cdot h_x^{(-1\sigma)}\right) , \tag{5.4}$$

with

$$a = \begin{cases} \lambda_x \cdot (\lambda_x + 1)/2, & |\lambda_x| \leq 1 \\ 0, & \lambda_x < -1 \\ \lambda_x, & \lambda_x > +1 \end{cases} ,$$
$$b = \begin{cases} -\lambda_x^2, & |\lambda_x| \leq 1 \\ -(|\lambda_x| - 1), & |\lambda_x| > 1 \end{cases} ,$$
$$c = \begin{cases} \lambda_x \cdot (\lambda_x - 1)/2, & |\lambda_x| \leq 1 \\ 0, & \lambda_x > +1 \\ |\lambda_x|, & \lambda_x < -1 \end{cases} .$$

The shape is minimized within the likelihood function (5.2). Since each shape is a combination of all bins

$$h^0 = \begin{cases} b_1 \\ b_2 \\ \vdots \end{cases} \tag{5.5}$$

the shape uncertainty effects each bin and therefore each bin is transformed with λ_x:

$$h^0 \rightarrow h(\lambda_x) = \begin{cases} b_1 + \sum_x \left(a(\lambda_x) \cdot b_{1x}^{(+1\sigma)} + b(\lambda_x) \cdot b_1 + c(\lambda_x) \cdot b_{1x}^{(-1\sigma)}\right) \\ b_2 + \sum_x \left(a(\lambda_x) \cdot b_{2x}^{(+1\sigma)} + b(\lambda_x) \cdot b_2 + c(\lambda_x) \cdot b_{2x}^{(-1\sigma)}\right) \\ \vdots \end{cases} . \tag{5.6}$$

Note that λ_x takes a fixed value across all bins for each shape uncertainty, meaning λ_x is correlated across all bins.

5.1.3 Validation Methods for Likelihood Models

The validation of the likelihood model for the H_b and H_{s+b} hypothesis is in particular important since a wrong likelihood model can lead to wrong interpretations of the observation. It has been agreed within the CMS collaboration to follow a well defined approach of judging the likelihood model. The idea is to not look at data before not being sure that the used model is able to describe possible expected outcomes, such as an observation of a signal. This approach is known as *blinding*. The analysis strategy as well as the likelihood model should be fixed before looking at data to neglect any kind of bias. Therefore, this section describes how the capability of the model to describe possible observations, like a signal excess or background only observation, can be tested. In this thesis the maximum likelihood method and a Goodness-of-Fit test using a saturated model, were chosen. Both methods have been frequently used at the LHC to review the likelihood model, defined by the likelihood function (5.2).

The Maximum Likelihood Fit

The maximum likelihood fit is used to find the parameters $\hat{\theta}$ and $\hat{r}$ which maximize the likelihood function (5.2)

$$\hat{L}(n|r \cdot s(\theta) + b(\theta)) = \max\left[L(n|r \cdot s(\theta) + b(\theta))\right] = L(n|\hat{r} \cdot s(\hat{\theta}) + b(\hat{\theta}) \ , \qquad (5.7)$$

in a certain range $r_{min} < r < r_{max}$. The fit returns the parameters $\hat{\theta}$ with the information how they are shifted and constrained under the H_b and H_{s+b} hypothesis. The returned values dependent on the observation, background and signal expectation and on the a posteriori signal strength modifier $\hat{r}$. Normally, the a posteriori value for an uncertainty, $\hat{\theta}_l$, is expected to agree with the a priori estimate $\tilde{\theta}_l$ within the expected uncertainty. Also the a priori chosen constraint is usually expected not to change when performing the maximum likelihood fit. However, in some analysis the fit is used to constrain the a priori uncertainties. Therefore, signal free control regions are used to fit the background expectation to the observation constraining the uncertainties in the signal region. If this is not the case a strong constraint or a large shift of the uncertainty helps to identify weaknesses in the definition of the likelihood model. A strong constraint can indicate an uncertainty which is estimated too large. In cases where the uncertainty is constrained very strongly the uncertainty might even be dropped. This can happen if there are uncertainties in the likelihood model which have the same purpose, such as two nuisance for the luminosity uncertainty. A large pull can indicate problems in the background and/or signal estimation.

It is also possible to run toy studies by replacing the observation n by some pseudo dataset which might be the sum of all backgrounds and some (realistic) signal contribution to test the behaviour of the statistical method to different kind of possible

observations.
Multiplying the most probable value of the signal strength parameter $\hat{r}$ with the signal expectation s gives the yield of the signal for which the H_{s+b} hypothesis agrees best with the observation n. The most probable value $\hat{r}$ is not checked before the validation of the likelihood model has been finished successfully in order to prevent any bias.

The Goodness-of-Fit Test

Goodness-of-Fit tests are widely used to describe how well a likelihood model fits the observation. There are many different choices or approaches, such as the Kolmogorov–Smirnov test [120; 121] or the χ^2-test [122].
It this thesis a Goodness-of-Fit test based on a saturated model is used. The method is similar to a χ^2-test with the addition that it can be used for an arbitrary number of binned channels with different constraints. In a saturated model the prediction, either background only or signal+background has so many degrees of freedom for the fit that it can agree perfectly with data. Therefore, the expectation $r \cdot s + b$ in equation (5.2) can be replaced by the observation n:

$$L_{\text{sat}}(n|n) = \prod_i \text{Poisson}(n_i|n_i) \cdot \prod_l p(\tilde{\theta}_l|\theta_l) \ . \tag{5.8}$$

The next step is to build a likelihood ratio

$$\begin{aligned} \lambda &= \frac{L(n|r \cdot s(\theta) + b(\theta))}{L_{\text{sat}}(n|n)} \\ &= \prod_i \left(\frac{r \cdot s_i(\theta) + b_i(\theta)}{n_i} \right)^{n_i} \cdot \exp\left(-(r \cdot s_i(\theta) + b_i(\theta)) + n_i\right) \end{aligned} \tag{5.9}$$

which can be simplified to:

$$\begin{aligned} q_{\text{GoF}} &= -2\ln(\lambda) \\ &= 2\sum_i \left((r \cdot s_i(\theta) + b_i(\theta)) - n_i + n_i \ln \frac{n_i}{r \cdot s_i(\theta) + b_i(\theta)} \right) \ . \end{aligned} \tag{5.10}$$

In cases where data follows a Gaussian distribution instead of a Poisson distribution the simplified likelihood ratio follows a χ^2 distribution: $q_{\text{GoF}}^{\text{Gauss}} = \chi^2$.
The Goodness-of-Fit likelihood ratio q_{GoF} is calculated for the observation n by minimizing q_{GoF} which is equal to maximizing λ. The minimization can either be done by fixing the signal strength modifier r or letting it float freely in the fit to be independent of the presence or absence of a signal. If it is left floating, it is technically treated just as an uncertainty and will take the value which minimizes q_{GoF} without looking at the value $\hat{r}$. A perfect agreement between the observation and the expected signal and/or background expectation would result in $q_{\text{GoF}} = 0$.
It is not possible to judge the likelihood model only by the observed q_{GoF} without a reference. Thus, the next step is to create a large set of Monte Carlo pseudo datasets (toys) n_{MC} according to the probability given in the likelihood function

(5.2). For each generated toy the q_{GoF} distribution is minimized and a probability density function $f(q_{\text{GoF}})$ is obtained. The probability density function is normalized to unity. The p-value, defined as,

$$p_{\text{GoF}} = \int_{q_{\text{GoF}}^{\text{obs}}}^{\infty} f(q_{\text{GoF}})\, dq_{\text{GoF}} \ , \tag{5.11}$$

is used to quantify the agreement between the observation and expectation of the generated pseudo datasets. Since the probability density function $f(q_{\text{GoF}})$ is normalized to unity the p-value takes values between zero and one. The p-value can be interpreted as the probability of finding an equally or less likely result as the observed, when the tested hypothesis is actually true. Thus, a small p-value describes a worse agreement between observation and expectation than a large p-value.
In figure 5.1 an example of a Goodness-of-Fit using a saturated model is given for the combination of all channels[1] in the $\phi \to \tau\tau$ analysis. More complete results are presented in chapter 6.

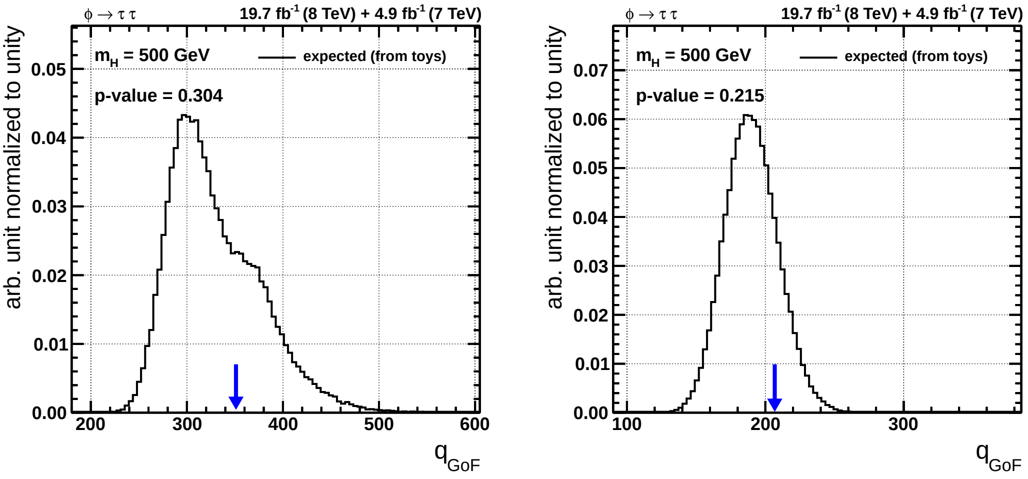

(a) (b)

Figure 5.1: Goodness-of-Fit tests for the all channels considered in the $\phi \to \tau\tau$ analysis in the no-b-tag (a) and the b-tag (b) category. The blue arrow indicates the position of the one observed value q_{GoF}. For the no-b-tag category the p-value is 0.304 and for the b-tag category 0.215.

5.1.4 Quantifying the Agreement between Observation and different Hypothesis

In this thesis and other analyses performed at the LHC frequentist approaches are chosen to quantify the agreement between the observation and the H_0 or H_{s+b} hypothesis. In frequentist approaches probabilities are only associated with data. That

---

[1] $e\mu$+$e\tau_{had}$+$\mu\mu$+$\mu\tau_{had}$+$\tau_{had}\tau_{had}$

means the probability to find a certain number of events n under a certain hypothesis X could be found to be $P(n|X)$, but not, like in the Bayesian approach, the probability that a certain hypothesis is true if that number of events have been observed $P(X|n)$. For more detailed explanations and comparisons between frequentist and Baysesian philosophies can be found in [123–125].

Using a frequentist based approach to quantify the agreement between observation and the H_0 or H_{s+b} hypothesis requires the choice of a test statistic, which is a one dimensional random variable which distinguishes between two different hypotheses. Historically, three different types of test statistics have been used [67] named by the experiment where they were used first. Note that for this thesis only the **TEV** and **LHC** test statistic are used, but for completeness the **LEP** test statistic is also briefly described here.

LEP Test Statistic

The LEP test statistic is a likelihood ratio of the H_b and the H_{s+b} hypothesis. Uncertainties are treated in an hybrid way [126] which means while the likelihood function (5.13) follows a frequentist paradigm, the incorporation of the uncertainties is done in a Bayesian way by modifying the $\prod_l p(\tilde{\theta}_l|\theta_l)$ term in the likelihood of equation (5.2) to become

$$\prod_l p(\theta_l|\tilde{\theta}_l) = \prod_l \frac{p(\tilde{\theta}_l|\theta_l) \cdot \delta(\theta_l)}{\int_\theta p(\tilde{\theta}_l|\theta_l) \cdot \delta(\theta_l) d\theta} \,. \tag{5.12}$$

Obtained is a Bayesian statement about the probability to find θ_l if $\tilde{\theta}_l$ is given, in contrast to the frequentist probability to find $\tilde{\theta}_l$ if θ_l is given. In this Bayesian way a hypothesis can be connected to a probability, while in frequentist philosophy a hypothesis is either true or false.

In most cases, the Bayesian prior $\delta(\theta_j)$ is chosen flat, but in principle it can carry any prior knowledge about θ_l. Using this the likelihood function, as given in equation (5.2), leads to:

$$L(n|r \cdot s(\theta) + b(\theta)) = \prod_i Poisson(n_i|r \cdot s_i(\theta) + b_i(\theta)) \cdot \prod_l p(\theta_j|\tilde{\theta}_j) \,. \tag{5.13}$$

The uncertainties now get eliminated by a numerical integration

$$L(n|r \cdot s + b) = \frac{\int_\theta L(n|r \cdot s(\theta) + b(\theta)) d\theta}{\int_\theta d\theta} \tag{5.14}$$

which is usually referred to as marginalization. Finally, the test statistic can be built:

$$q_r = -2\ln(\lambda) = -2\ln\left(\frac{L(n|r \cdot s + b)}{L(n|b)}\right) \,, \quad \text{with } \; 0 \leq r \,. \tag{5.15}$$

The constraint $0 \leq r$ ensures that the signal rate is positive and therefore physically meaningful. Since no uncertainties enter the likelihood function the uncertainties do not change if a fit of the likelihood function (5.14) to the observation is performed. That also means that the uncertainties are not constrained or shifted by the fit.

TEV Test Statistic

In the TEV approach the likelihood function of equation (5.2) is modified just as in the LEP case, as shown in equation (5.13), but in contrast the nuisance parameters are not marginalized:

$$q_r = -2\ln(\lambda) = -2\ln\left(\frac{L(n|r\cdot s(\hat{\theta}_r) + b(\hat{\theta}_r))}{L(n|b(\hat{\theta}_0))}\right) , \quad \text{with } \ 0 \leq r \ . \tag{5.16}$$

The numerator is maximized for a specific signal strength modifier r by finding the uncertainties for a given value of r, $\hat{\theta}_r$, whereas the denominator is maximized for $r = 0$ by finding the corresponding uncertainties $\hat{\theta}_0$. This effective elimination of the uncertainties by maximization is called profiling. Like in the LEP test statistic the constraint $0 \leq r$ guarantees a positive signal rate and therefore a valid physical interpretation.

LHC Test Statistic

The LHC test statistic differs from the LEP and TEV test statistics in two ways. First, the likelihood function, as given in equation (5.2), is not modified using a Bayesian way. Secondly, instead of a likelihood ratio the so called profile likelihood is used as a test statistic:

$$q_r = -2\ln(\lambda) = -2\ln\left(\frac{L(n|r\cdot s(\hat{\theta}_r) + b(\hat{\theta}_r))}{L(n|\hat{r}\cdot s(\hat{\theta}) + b(\hat{\theta}))}\right) , \quad \text{with } \ 0 \leq \hat{r} \leq r \ . \tag{5.17}$$

In contrast to the TEV test statistic the denominator is maximized for all possible values of r by finding the most probable value $\hat{r}$. In other words, the denominator takes its global maximum. The numerator is maximized for a specific signal strength modifier r, which suffice the constraint $\hat{r} \leq r$. Additional to the constraint $0 \leq r$, the constraint $\hat{r} \leq r$ can be introduced to obtain one sided confidence intervals, in other words only upper limits are considered.

Comparing the different test statistics the first difference appears between the LEP test statistic and the TEV or LHC test statistic. The latter ones have the advantage of profiling. This means the uncertainties θ and the signal strength modifier r are effectively constrained by the measurement. In other words, the a priori signal strength modifier r and the uncertainties θ are fitted to describe the data in the best possible way. The fit will chose the values for the parameters which will lead to the best agreement of the tested hypothesis in the denominator or numerator of equation (5.16) or (5.17) with the observation. The a posteriori values are used to quantify the agreement between the observation and the H_b and H_{s+b} hypothesis. In the LEP approach a priori uncertainties are used to compute this agreement. For uncertainties which supposed to make only sense after fitting/profiling, e.g. normalization uncertainties of a certain background, the LEP statistic leads can lead to wrong results. The profiling is a complex computation step and therefore the LEP test statistic is less computing intensive than the other two.

The agreement can be quantified using p-values. First, the observed value of the chosen test statistic, q_r^{obs}, for the r under test is evaluated. Next, large number of Monte Carlo measurements n_0^{MC} (n_r^{MC}) are simulated by using the likelihood function (5.2) and fixing the uncertainties to $\hat{\theta}_0^{\mathrm{obs}}$ ($\hat{\theta}_r^{\mathrm{obs}}$)[2]. For each pseudo dataset the chosen test statistic is evaluated. The probability density function for the H_{s+b} hypothesis, $f(q_r|r)$, and for the background hypothesis H_b, $f(q_0|0)$, are constructed. The p-values for the hypothesis can now be computed:

$$\begin{aligned} p_b &= P(q_0 \geq q_r^{\mathrm{obs}}|b) = \int_{-\infty}^{q_r^{\mathrm{obs}}} f(q_0|0)\ dq \\ p_r &= P(q_r \geq q_r^{\mathrm{obs}}|s+b) = \int_{-\infty}^{q_r^{\mathrm{obs}}} f(q_r|r)\ dq\ . \end{aligned} \tag{5.18}$$

A large p-values indicates a good agreement with the tested hypothesis. A large p_r for a considered r with a simultaneous low p_b can be interpreted as an excess.

5.2 Limit Setting in the Absence of a Signal

In analyses where no excess is observed, upper limits can be set on the signal strength modifier r to exclude different signal models. There are different approaches of setting limits such as the CL_{s+b} [67; 127], the Power Constrained Limits [128] or purely Baysian methods [67; 129].
The CMS and ATLAS collaborations have agreed upon using the $\mathrm{CL_s}$ method [67; 127; 130; 131] for setting limits. The method is a derivative of the $\mathrm{CL_{s+b}}$ method. In cases where less events are observed than expected from the background hypothesis the $\mathrm{CL_{s+b}}$ method could lead to a overoptimistic hardly interpretable exclusion limit. In extreme examples where the background prediction is far larger than the observation this can even lead to exclusion of negative signal predictions. Although, such extreme cases should only rarely appear if the background has been predicted correctly, still it should not be allowed to exclude all kinds of signal models, even those for which no sensitivity is given. The $\mathrm{CL_s}$ method prevents such cases in setting conservative limits which by definition are greater than zero.
In the following, the steps towards an upper limit are presented. In section 5.2.1 the CL_s technique is explained and differences to the $\mathrm{CL_{s+b}}$ method are pointed out. The Feldman-Cousins method is briefly explained in section 5.2.2.

5.2.1 The $\mathrm{CL_s}$ Method

After having made the choice of a certain test statistic the exclusion limit using the $\mathrm{CL_s}$ method can be computed. Observed and expected limit calculation will be explained in the following. A technical description is given in appendix B.

---

[2] In case the LEP test statistic has been chosen the a priori uncertainties are chosen

Calculation of the Observed and Expected Limit

The observed test statistic q_r^{obs} for a certain r and the probability density functions for the H_b and the H_{s+b} hypothesis with a certain r are computed as described in 5.1.4. A negative value for the test statistic indicates a more H_b hypothesis like observation whereas a positive value favours the H_{s+b} hypothesis. As shown in figure 5.2(a) the observed value alone is not sufficient to exclude one hypothesis. In the $\text{CL}_{\text{s+b}}$ approach the H_{s+b} hypothesis is excluded if

$$p_r = P(q_r \geq q_r^{\text{obs}} | s+b) = \int_{-\infty}^{q_r^{\text{obs}}} f(q_r|r)\ dq < 0.05\ . \tag{5.19}$$

The upper limit on r is found for the signal strength modifier r which suffices:

$$\text{CL}_{\text{s+b}}(r_{\text{UL}}) = p_r = 0.05\ . \tag{5.20}$$

This is illustrated in figure 5.2(b). Note that the H_{s+b} hypothesis in this picture is the MSSM τ-phobic scenario at $m_A = 130\,\text{GeV}$ and $\tan\beta = 6$ and is denoted by $H_{h+A+H+b}$. In contrast to the $\text{CL}_{\text{s+b}}$ approach the CL_{s} takes the sensitivity to the H_b hypothesis into account:

$$\text{CL}_{\text{s}}(r) = \frac{p_r}{p_b}\ . \tag{5.21}$$

This is illustrated in figure 5.2(c). The upper limits on r is found for:

$$\text{CL}_{\text{s}}(r_{\text{UL}}) = \frac{p_r}{p_b} = 0.05\ . \tag{5.22}$$

Comparing the $\text{CL}_{\text{s+b}}$ and the CL_{s} method it is obviously that the CL_{s} method is more conservative. In cases where the observation is below the background expectation and thus p_b is small, the $\text{CL}_{\text{s+b}}$ method will give overoptimistic results, which often are hard to interpret in a physical sense.

The expected median limit in the CL_{s} method as well as the $\pm\sigma$ error bands are calculated by finding:

$$\text{CL}_{\text{s}}(r_{\text{UL}}^X) = \frac{p_r}{p_b} = \frac{\int_{-\infty}^{q_r(p_b=X)} f(q_r|r)\ dq}{X} = 0.05\ . \tag{5.23}$$

where X is either 0.025, 0.16, 0.5, 0.84 or 0.975 for the -2σ, -1σ, median, $+1\sigma$ or 2σ upper limit, respectively.

Asymptotic Formula

The LHC test statistic has an additional advantage over the others. For the calculation of the CL_{s} method large number of Monte Carlo generations are needed. In the presence of many uncertainties, channels and categories the computing of these limits gets extremely CPU intensive. The profile likelihood, equation (5.17), has the advantage that an asymptotic approximation following Wilks theorem [132]

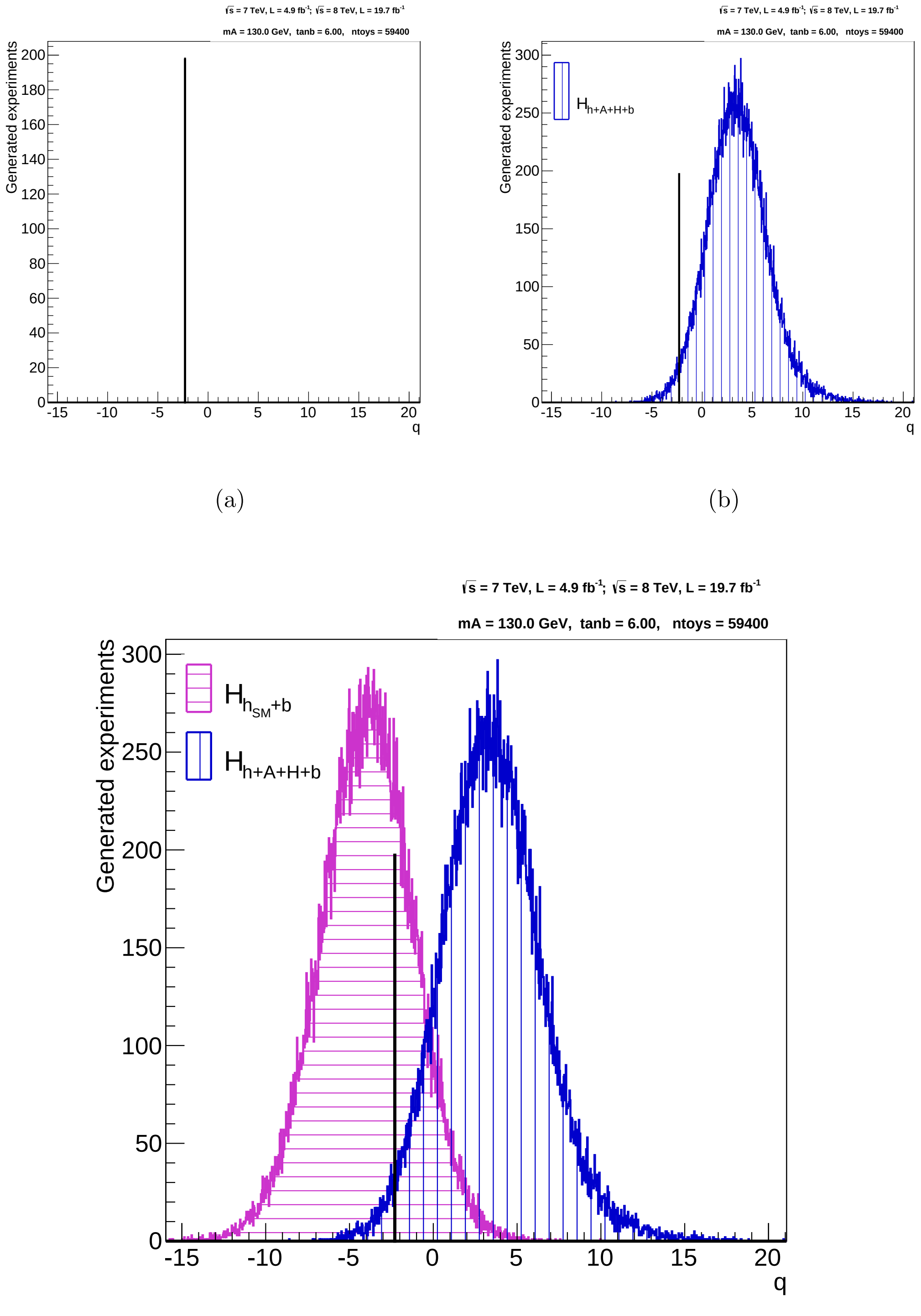

(a)

(b)

(c)

Figure 5.2: Exclusion limit construction using the CL$_s$ method testing a SM hypothesis, $H_{h_{\text{SM}}+b}$, against the MSSM τ-phobic at $m_A = 130\,\text{GeV}$ and $\tan\beta = 6$ hypothesis, $H_{h+A+H+b}$ in the search for additional Higgs boson decaying to tau leptons. Nearly 60000 toys have been generated to construct the background probability density function $f(q_0|0)$ and the signal+background probability density function $f(q_r|r)$. The observed value is shown by the black vertical line. By eye it agrees better with $H_{\text{SM}+b}$ hypothesis (including the SM Higgs boson at 125 GeV) than with the $H_{h+A+H+b}$ hypothesis. Nevertheless, the signal hypothesis is not separated enough to be excluded based on the CL$_s$ criterion.

can be used and so an analytic expression can be found. Hence, Monte Carlo toy production is not needed and therefore much faster computing is possible. Wilks theorem states that in cases with large number of expected and observed events the test statistic q_r is distributed like half a χ^2 for one degree of freedom if the constraint $0 < \hat{r}$ is ignored. Allowing the constraint does not lead to a χ^2 distribution but still gives an analytical expression

$$f(q_r|r) = \frac{1}{2}\delta(q_r) + \begin{cases} \frac{1}{2\sqrt{2\pi \cdot q_r}} \exp(-\frac{q_r}{2}), & 0 < q_r \leq r^2/\sigma^2 \\ \frac{1}{\sqrt{2\pi} \cdot \frac{2r}{\sigma}} \exp(-\frac{1}{2}\frac{(q_r + r^2/\sigma^2)^2}{2r/\sigma}), & q_r > r^2/\sigma^2 \end{cases} \tag{5.24}$$

with $\sigma^2 = r^2/q_{r,A}$, where $q_{r,A}$ is the test statistic evaluated for a pseudo dataset by replacing the observation with the background expectation b and using a priori uncertainties. Equation (5.24) is used to calculate the observed limit. An analytical expression for the background probability density function $f(q_0|0)$ can be found in [133]. The observed upper limit is than derived by:

$$\mathrm{CL_s} = 0.05 = \frac{1 - \Phi(\sqrt{q_r})}{\Phi(\sqrt{q_{r,A}} - \sqrt{q_r})} \ , \tag{5.25}$$

where Φ is the cumulative distribution of the standard Gaussian. The median expected limits r_{exp} as well as the one ($N = \pm 1$) and two ($N = \pm 2$) sigma bands are found by:

$$r_{\mathrm{exp}+N} = \sigma \cdot (\Phi^{-1}(1 - 0.05 \cdot \Phi(N)) + N) \ . \tag{5.26}$$

The approximation is formally only allowed for large number of events so the use of the method for smaller event numbers is not validated and can lead to overoptimistic results.

5.2.2 The Feldman-Cousins Method

The Feldman-Cousins method [134] approach guarantees correct coverage of the 95% Confidence Interval by allowing lower and upper limits to exist. It uses the LHC test statistic but without the $\hat{r} \leq r$ constraint. The idea is to calculate the test statistic for different values of the observation n_i. The observations n_i are than ordered by their corresponding value of the test statistic. The 95% confidence interval includes the values of n_i for which

$$\mathrm{CL}_{95\%} \leq \sum_i L(n_i|r \cdot s + b) \tag{5.27}$$

with $q_r(n_1) < q_r(n_2) < ..$. Note that the uncertainties have been profiled in the test statistic for each value n_i and therefore do not enter in equation (5.27). This step is iterated for different values of r. A typical result for a Poisson distributed likelihood function is illustrated in figure 5.3. The upper and lower limit are found by looking at a fixed n_i and searching for the corresponding values of r.

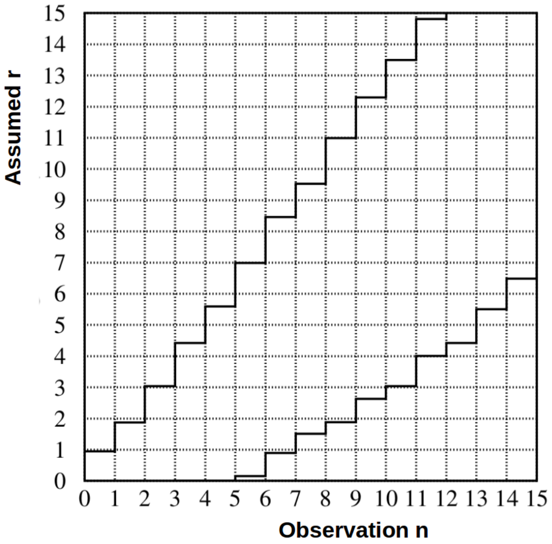

Figure 5.3: Feldman-Cousins confidence bell for a Poisson distributed likelihood function. Shown is the exclusion interval for a given observation n. No uncertainties are assumed.

Chapter 6

Results

The results of the $\phi \to \tau\tau$ analysis are presented in this chapter. Scrutiny tests, as discussed in section 6.1, have been performed in order to check the likelihood model as described in chapter 5. In section 6.2 the event yields and the distributions of the invariant di-τ mass, which are the input of the statistical inference, are shown after the maximum likelihood fit that has been applied prior to the limit calculation.
Since no significant excess is found exclusion limits are set. As a model independent approach, $\sigma \cdot \mathcal{B}$ limits assuming a single narrow resonance ϕ are set (section 6.3.2). Also the ggϕ-bbϕ plane (section 6.3.1) has been scanned as a function of the mass of the assumed resonance m_ϕ. Furthermore, the limits are interpreted in different extensions of the SM (section 6.4).
The calculated limits are based on hypothesis test. Different hypothesis have been tested. In the model independent limits the BSM signal hypothesis assuming a single narrow resonance, $H_{\phi+b}$, is either tested against the background only hypothesis, H_b, or against a SM signal hypothesis $H_{h_{\mathrm{SM}}+b}$. In the model dependent limits the neutral MSSM hypothesis $H_{h+A+H+b}$ is tested again either against the background only hypothesis, H_b, or against a SM signal hypothesis $H_{h_{\mathrm{SM}}+b}$.

6.1 Test on the Statistical Model

In order to test whether the likelihood model is capable of explaining any expected observation which may includes a potential signal, different scrutinies are performed. In the $\phi \to \tau\tau$ analysis this is done by checking the shifts and constraints of the uncertainties after a maximum likelihood fit and by performing a goodness-of-fit test as described in section 6.1.1 and section 6.1.2, respectively. For technical details about these tests see section 5.1.3.

6.1.1 Maximum Likelihood Fit

In figure 6.2 the uncertainties after the maximum likelihood fit are shown for the $\mu\tau_{had}$ channel, excluding Barlow-Beeston uncertainties (see section 4.5.2). On the y-axis the used uncertainty names are listed which follow the CMS conventions. For example, the last considered uncertainty, *CMS_htt_zttNorm_8TeV*, corresponds to the normalization uncertainty on the Z→ $\tau\tau$ yield in the 8 TeV data-taking period. It is correlated among all channels. On the x-axis the pull is given in units of the one σ uncertainty on the a priori estimate of the uncertainty. In the figure, the black dots give the a posteriori estimate. The error bars show the a posteriori constraints. In total 67 uncertainties are shown. Figure 6.2 shows the pulls and constraints

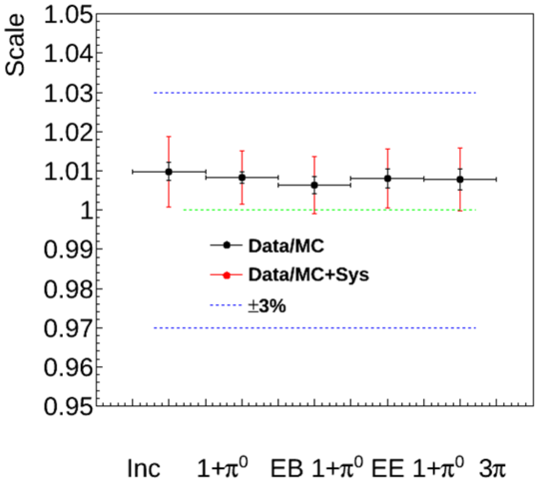

Figure 6.1: Results of the energy scale fit for the different hadronic tau lepton decay modes as measured in [135]. The inclusive result is denoted *Inc*. The hadronic tau lepton decay channel into one charged pion, named $1+\pi^0$ has been separately measured in the electromagnetic calorimeter endcap, *EE*, and the barrel region, *EB*. The decay moded into three charged pions is named 3π.

on the $H_{\phi+b}$ hypothesis assuming a mass of 160 GeV. Differences when testing a different mass or the H_b hypothesis are small. In principle, all masses and the H_b hypothesis can be tested, but a signal for a certain mass when testing a different mass would lead to significant shifts on different uncertainties since the observed excess can not be explained by the assumed signal in the fit. The uncertainties have been measured in dedicated control regions. Thus, the a posteriori pulls and constraints on the estimated are not expected to change significantly in respected to the a priori constraints and estimates. In total 67 uncertainties are shown. Only two uncertainties have a posteriori estimates which have changed by more than one sigma with respect to the a priori estimate. Assuming a normal distribution about eleven uncertainties are expected to shift by more than one sigma. From the 67 uncertainties only six are constrained by more than 50%. If the maxim likelihood fit is done using a pseudo dataset obtained by replacing the observation by the sum of all backgrounds and the SM Higgs boson expectation, five uncertainties show a constraint of more than 50%. These comparisons prove an overall good understanding of the uncertainties.

The systematic uncertainties on the tau energy scale (*CMS_scale_t_mutau_7TeV* and *CMS_scale_t_mutau_8TeV*) are strongly constrained. The uncertainty is set to 3% before the fit. This number is motivated by measurements from 2010 [99]. The

uncertainty was measured to about 1% as shown in figure 6.1, but these results are not published. As a second reason, the sheer number of observed events in the Z→ $\tau\tau$ peak in the di-τ invariant mass spectrum provides a strong constraint. Due to a lack of official numbers and with the knowledge that the fit will constrain the uncertainty the conservative uncertainty of 3% is taken.
The shift of the QCD shape uncertainty in the no-b-tag category for 8 TeV (*CMS_htt_QCDShape_mutau_nobtag_8TeV*) is due to the lack of knowledge of the QCD shape for invariant di-τ masses below 70 GeV. In this region the shape extrapolation from the same sign to opposite sign region (see section 4.4.2) is not validated. Therefore, it should be noted that this particular region is not considered in the limit calculation, but only the region $m_{\tau\tau} \geq 90\,\mathrm{GeV}$.
In other channels the maximum likelihood fit is equally satisfying as shown in appendix C.

6.1.2 Goodness-of-Fit Test

In figure 6.3 the results of the goodness-of-fit test, as described in section 5.1.3, are shown for all individual channels of the $\phi \to \tau\tau$ analysis at a chosen signal mass of $m_\phi = 500\,\mathrm{GeV}$ with arbitrary signal strength, therefore also covering the H_b hypothesis. A signal at some other mass is not checked by this single mass. Thus, the test should be done for each considered signal mass. However, a signal excess at a certain mass would lead to a bad result when testing other signal masses since the assumed likelihood model would not be able to explain the signal excess. The signal is assumed to behave as a narrow resonance, therefore expected to be MSSM like. Thus, an extremely broad resonance can lead to a failing goodness-of-fit test since the likelihood model, in particular the expected signal component, is not able to describe the broad resonance well.
On the x-axis the computed value of the test-statistic, q_{GoF}, is plotted which is related to the number of degrees of freedom in the fit. The $\tau_{had}\tau_{had}$ for example shows the smallest values for q_{GoF}, whereas the combination shows the biggest. Summing up the median q_{GoF} for all channels results in the median q_{GoF} of the combination. Also the shape of the combination can be explained by looking at the individual channels. The slightly longer tail on the right than on the left side is also seen in the other channels in particular in the $\tau_{had}\tau_{had}$ channel. The non gaussian shape of the probability density functions can be explained by the non gaussian shape of the likelihood function (5.2). The $e\mu$ and $e\tau_{had}$ channels show an p-value of about 2% which can be explained by fluctuations in the data. The observed q_{GoF} in the $\mu\mu$ is better than the median expected that means that the observation agrees better with the expectation than expected from generated pseudo-datasets. Overall, in the combination and in the individual channels a satisfying agreement is observed.

In summary: the decision if a likelihood model is accepted to be sufficient to describe the observations is done by taking the goodness-of-fit test and the shifts and constraints obtained by the maximum likelihood fit into account. Large constraints and shifts as well as low p-values in the goodness-of-fit test need to be understood.

6.2 Event Yields and invariant di-τ Mass

After having checked that the likelihood model is able to describe the observations the a posteriori invariant di-τ mass plots and event yields have been produced. The tables and plots show the yields after the maximum likelihood fit has been performed as described in section 5.1.3. The yields and plots for the $e\mu$ channel are shown in table 6.2 and figure 6.4, for the $e\tau_{had}$ channel in table 6.3 and figure 6.5, for the $\mu\mu$ channel in table 6.4 and figure 6.6, for the $\mu\tau_{had}$ channel in table 6.5 and figure 6.7 and for the $\tau_{had}\tau_{had}$ channel in table 6.6 and figure 6.8. The observed distribution is plotted by the black dots. The backgrounds and the SM Higgs boson are stacked. The Z-peak is nice to see in all invariant mass plots except for the $\tau_{had}\tau_{had}$ one where the Z-peak is suppressed by the $p_T > 45\,\text{GeV}$ requirement on the hadronically decaying tau leptons. At the Z-peak the dominant background in the $e\mu$, $e\tau_{had}$ and $\mu\tau_{had}$ channel is Z$\rightarrow \tau\tau$. In the $\mu\mu$ channel the Z$\rightarrow \mu\mu$ background highly dominates. For the high mass tail the $\mathrm{t\bar{t}}$, QCD and Electroweak (W+Jets and Dibosons) backgrounds are important. The combined statistical and systematic uncertainties on the backgrounds and on the SM Higgs boson are shown by the dashed grey band. As a signal example, the expected yield for the MSSM $m_h^{\text{mod+}}$ scenario at $m_A = 500\,\text{GeV}$ and $\tan\beta = 30$ is shown. It is not stacked with the backgrounds. It is clear to see that the MSSM signal expectation is a combination of the three neutral MSSM Higgs bosons. The signal shows two peaks: the light scalar Higgs bosons shows the same shape as the SM Higgs boson. The second peak comes from the heavy scalar and pseudoscalar Higgs bosons. In table 6.1 the properties of the Higgs bosons in the chosen MSSM model and the SM Higgs bosons are shown. The table shows that the light scalar Higgs boson has the properties as the SM Higgs boson which explains why their shapes are similar in the invariant mass plots. Since the invariant mass plots are shown in log-scale the ratio plots between the observation and the background including the SM Higgs boson expectation is also shown. Also an excess would be hardly visible in the log-scale plot. In the ratio plot it would show up as an peak of the dots above the background uncertainty for several bins. No significant excess is seen in any distribution.

Higgs typ	mass [GeV]	$\sigma(gg\phi)$ [pb]	$\sigma(bb\phi)$ [pb]	$\mathcal{B}(\phi \rightarrow \tau\tau)$
$\mathrm{h_{SM}}$	125.00	19.27	$2.04 \cdot 10^{-1}$	$6.63 \cdot 10^{-2}$
h	126.00	17.54	$2.46 \cdot 10^{-1}$	$6.65 \cdot 10^{-2}$
A	500.00	$4.06 \cdot 10^{-2}$	$4.43 \cdot 10^{-1}$	$1.00 \cdot 10^{-1}$
H	499.72	$3.34 \cdot 10^{-2}$	$4.45 \cdot 10^{-1}$	$9.81 \cdot 10^{-2}$

Table 6.1: Properties of the Higgs bosons for the model point $m_A = 500\,\text{GeV}$ and $\tan\beta = 30$ in the MSSM $m_h^{\text{mod+}}$ scenario and the SM Higgs boson at a center-of-mass energy of 8 TeV.

The χ^2 value, defined as

$$\chi^2 = \sum_i \frac{(n_i - b_i)}{\sigma^2_{b_i}} \, , \tag{6.1}$$

is given as a measure for the agreement between the data and the sum of all backgrounds including the SM Higgs boson. The χ^2 test assumes that the number of events in each bin i behave independent to each other and are standard normal distributed. Since uncertainties are not gaussian distributed, but log-normal and shape uncertainties do also contribute the results of the χ^2 test are understand with caution. The ratio of χ^2 over number of degrees of freedom (ndf), here number of bins, in the maximum likelihood fit should be at one. The likelihood to obtain such a χ^2 or worse is given by $P(\chi^2)$, which is a p-value. Overall, a satisfying agreement is observed. The no-b-tag category of the $\mu\mu$ channel shows a very unlikely $P(\chi^2)$-value. Different reasons are responsible for this disagreement. The effect is emphasized by the combination of the 7 TeV and 8 TeV datasets since the separated center-of-mass energies show an agreement of $P(\chi^2) = 0.009$ and $P(\chi^2) = 0.017$, respectively. Also, the $\mu\mu$ channel does not use the invariant di-τ mass to separate the background and signal, but a two dimensional distribution of the invariant visible mass of the tau lepton decay products, the muons, over the invariant di-τ mass. Thus, the observation and the expectations can show discrepancies in this one dimensional representation of the used two dimensional distribution. Furthermore, the uncertainties are not treated proper in this one dimensional representation. In contrast, the goodness-of-fit test, which has not the pitfalls of the χ^2 test and uses the two dimensional distribution as input, results in a p-value of 0.753. In conclusion, the χ^2 seems to fail for the $\mu\mu$ channel[1].

In the $e\mu$ channel the binning is unfavourable, especially in the b-tag category. This can be explained by fluctuations in nearby bins in the data. A more adjusted binning would increase the $P(\chi^2)$ value, but to prevent any bias the binning has to be chosen before the data is analysed.

The $m_{\tau\tau}$ distribution is used as the final discriminator between background and observation in all channels but the $\mu\mu$ channel. As described above, in the $\mu\mu$ channel the invariant visible mass of the tau lepton decay products, the muons, over the invariant di-τ mass is used to obtain a better separation between signal events and Z→ $\tau\tau$ events. The distributions for the observation, background and signal expectations are the input for the limit inference.

---

[1] The p-value of the b-tag category in the $\mu\mu$ channel for the goodness-of-fit test is 0.935.

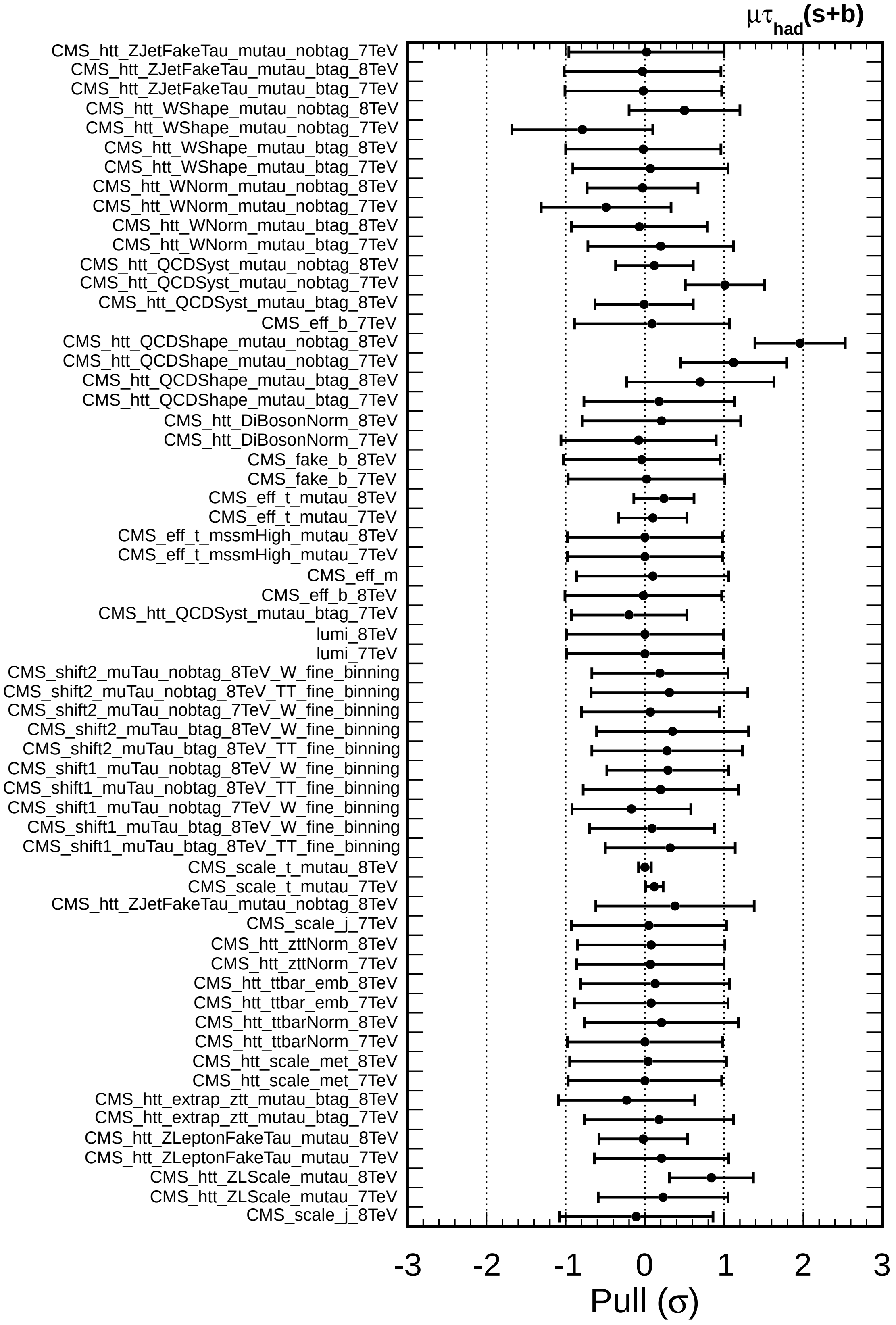

Figure 6.2: Constraints and shifts of the uncertainties in the $\mu\tau_{had}$ channel after having performed the maximum likelihood fit for the $H_{\phi+b}$ hypothesis. The signal expectation used here is a single narrow resonance at a mass of 160 GeV. The naming follows official CMS collaboration naming scheme.

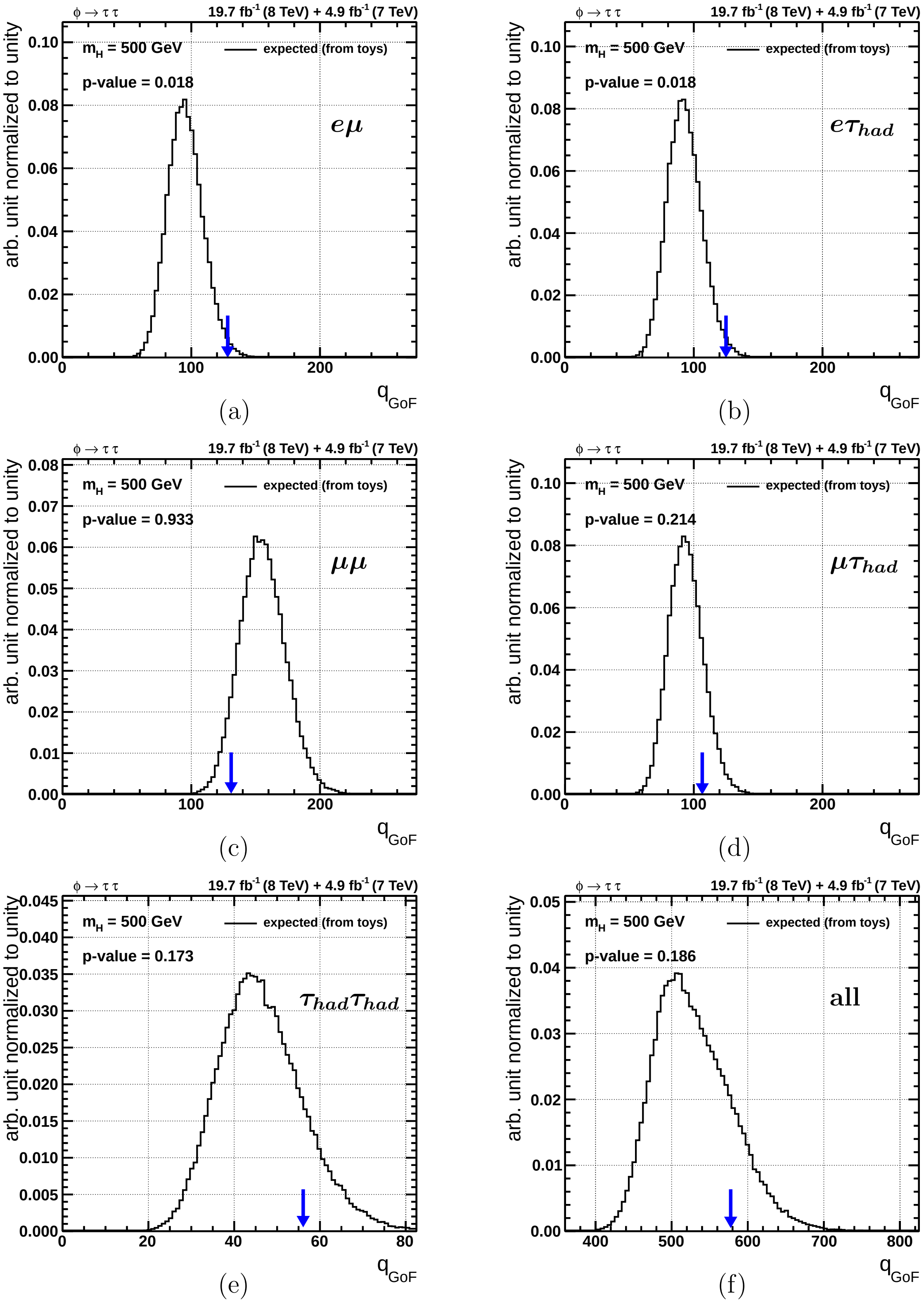

(a) (b) (c) (d) (e) (f)

Figure 6.3: Goodness-of-Fit test for the all channels considered in the $\phi \to \tau\tau$ analysis combining the no-b-tag and the b-tag categories. The $e\mu$ channel is shown in (a), $e\tau_{had}$ in figure (b), $\mu\mu$ in figure (c), $\mu\tau_{had}$ in figure (d), $\tau_{had}\tau_{had}$ in figure (e). The combination of all channels is shown in the last figure (f). The blue arrow indicates the position of the observation.

Table 6.2: Number of events observed and expected in the $e\mu$ channel for both categories in both center-of-mass periods. The signal yield is given for the $m_A = 500\,\text{GeV}$ and $\tan\beta = 30$ in the MSSM $m_h^{\text{mod+}}$ scenario. The a posteriori uncertainties are given on yields. Correlations are taken into account.

$e\mu$ channel				
	$\sqrt{s} = 7\,\text{TeV}$		$\sqrt{s} = 8\,\text{TeV}$	
Process	no b-tag	b-tag	no b-tag	b-tag
Z→ $\tau\tau$	13762 ± 137	165 ± 6	48140 ± 294	678 ± 8
QCD	799 ± 113	14 ± 3	4284 ± 340	147 ± 17
$\mathrm{t\bar{t}}$	468 ± 30	310 ± 18	2219 ± 148	1187 ± 47
Di-bosons + single top	502 ± 58	63 ± 8	2371 ± 260	308 ± 40
SM Higgs (125 GeV)	44 ± 5	1 ± 0.1	159 ± 19	3 ± 0.4
Total Background	15574 ± 121	553 ± 20	57173 ± 249	2324 ± 40
gg(A+H+h) → $\tau\tau$	38 ± 1	0 ± 0.0	147 ± 4	2 ± 0.1
bb(A+H+h) → $\tau\tau$	6 ± 0.2	1 ± 0.1	32 ± 0.8	7 ± 0.2
Data	15436	558	57285	2353

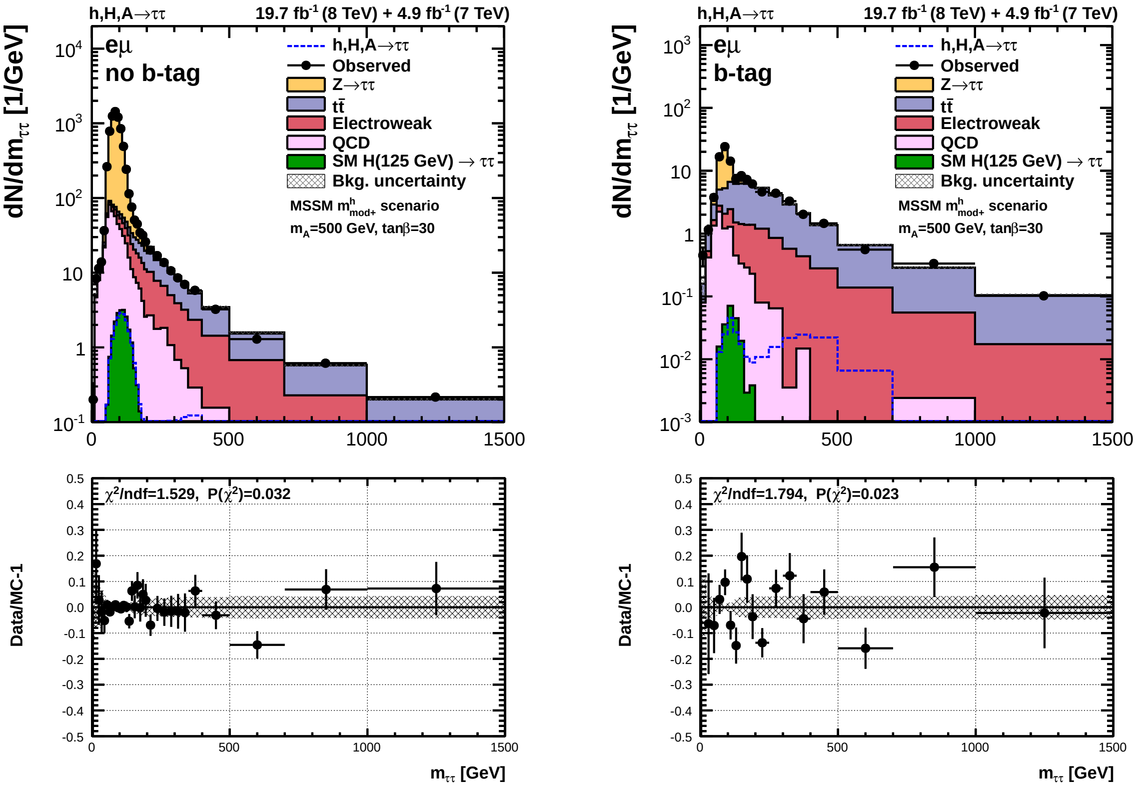

Figure 6.4: Invariant $m_{\tau\tau}$ distribution observed in the $\sqrt{s} = 7\,\text{TeV}$ and $\sqrt{s} = 8\,\text{TeV}$ data for the no-b-tag (left) and b-tag (right) category of the $e\mu$ channel compared to background expectations. Expected background contributions are shown for the values of the uncertainties as obtained by fitting the expectation to the observation.

Table 6.3: Number of events observed and expected in the $e\tau_{had}$ channel for both categories in both center-of-mass periods. The signal yield is given for the m_A = 500 GeV and $\tan\beta = 30$ in the MSSM $m_h^{\mathrm{mod}+}$ scenario. The a posteriori uncertainties are given on yields. Correlations are taken into account.

	$e\tau_{had}$ channel			
	$\sqrt{s}$ = 7 TeV		$\sqrt{s}$ = 8 TeV	
Process	no b-tag	b-Tag	no b-tag	b-tag
Z→ $\tau\tau$	11795 ± 205	135 ± 5	30127 ± 340	452 ± 13
QCD	4162 ± 210	78 ± 11	11895 ± 597	195 ± 28
W+jets	1350 ± 113	29 ± 8	5686 ± 401	114 ± 24
Z+jets (l/jet faking τ)	1323 ± 146	9 ± 1	6156 ± 364	83 ± 6
$t\bar{t}$	43 ± 3	20 ± 3	290 ± 22	103 ± 11
Di-bosons + single top	47 ± 5	7 ± 0.8	224 ± 23	30 ± 4
SM Higgs (125 GeV)	50 ± 6	1 ± 0.1	159 ± 18	3 ± 0.4
Total Background	18769 ± 138	279 ± 12	54537 ± 260	980 ± 26
gg(A+H+h) → $\tau\tau$	39 ± 1	0 ± 0.0	146 ± 3	2 ± 0.1
bb(A+H+h) → $\tau\tau$	7 ± 0.3	1 ± 0.1	34 ± 0.9	7 ± 0.2
Data	18785	274	54547	975

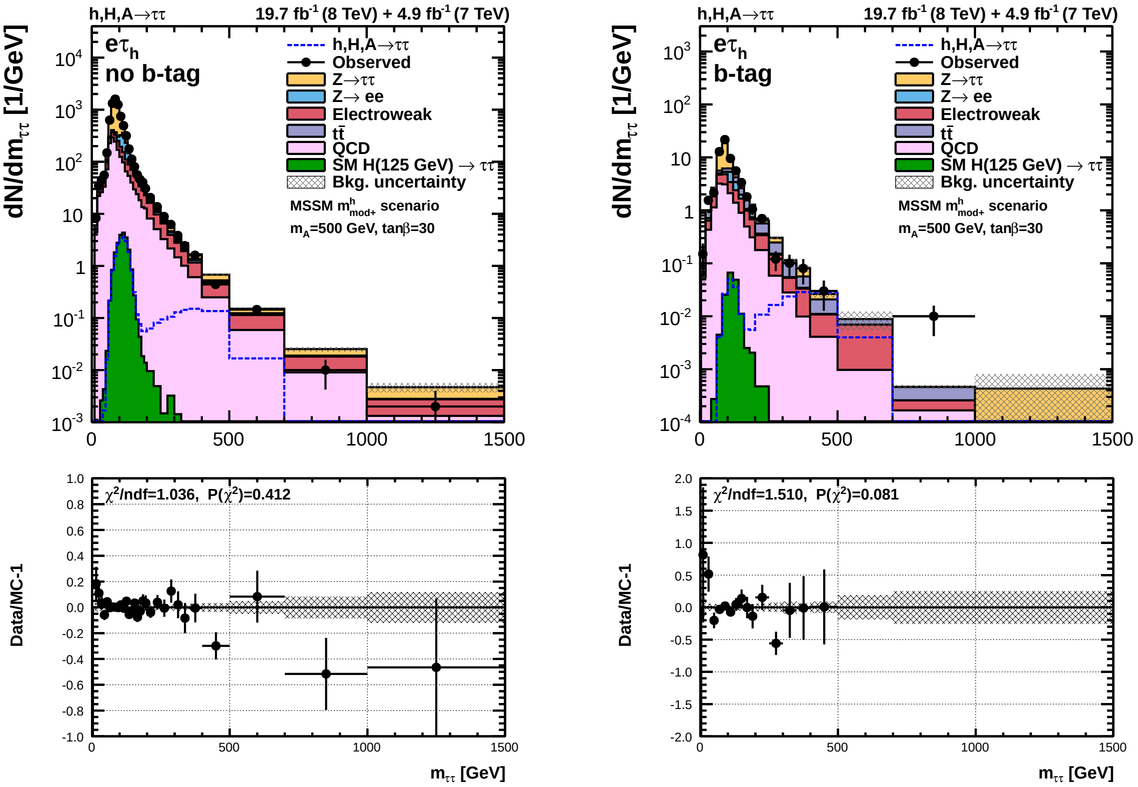

Figure 6.5: Invariant $m_{\tau\tau}$ distribution observed in the $\sqrt{s}$ = 7 TeV and $\sqrt{s}$ = 8 TeV data for the no-b-tag (left) and b-tag (right) category of the $e\tau_{had}$ channel compared to background expectations. Expected background contributions are shown for the values of uncertainties as obtained by fitting expectation to the observation.

Table 6.4: Number of events observed and expected in the $\mu\mu$ channel for both categories in both center-of-mass periods. The signal yield is given for the $m_A =$ 500 GeV and $\tan\beta = 30$ in the MSSM $m_h^{\text{mod}+}$ scenario. The a posteriori uncertainties are given on yields. Correlations are taken into account.

$\mu\mu$ channel				
	$\sqrt{s} = 7\,\text{TeV}$		$\sqrt{s} = 8\,\text{TeV}$	
Process	No B-Tag	B-Tag	No B-Tag	B-Tag
Z→ $\tau\tau$	6825 ± 117	34 ± 1	20878 ± 363	101 ± 5
Z→ $\mu\mu$	562016 ± 736	1436 ± 33	1894537 ± 1622	5126 ± 73
QCD	380 ± 55	4 ± 2	1131 ± 111	31 ± 7
$\mathrm{t\bar{t}}$	184 ± 16	83 ± 7	810 ± 64	325 ± 16
Di-bosons + single top	1112 ± 200	10 ± 2	5528 ± 685	48 ± 7
SM Higgs (125 GeV)	21 ± 3	0 ± 0.0	71 ± 10	1 ± 0.1
Total Background	570538 ± 700	1566 ± 36	1922956 ± 1444	5631 ± 73
gg(A+H+h) → $\tau\tau$	17 ± 0.5	0 ± 0.0	57 ± 2	0 ± 0.0
bb(A+H+h) → $\tau\tau$	3 ± 0.1	0 ± 0.0	16 ± 0.5	3 ± 0.1
Data	570616	1559	1922924	5608

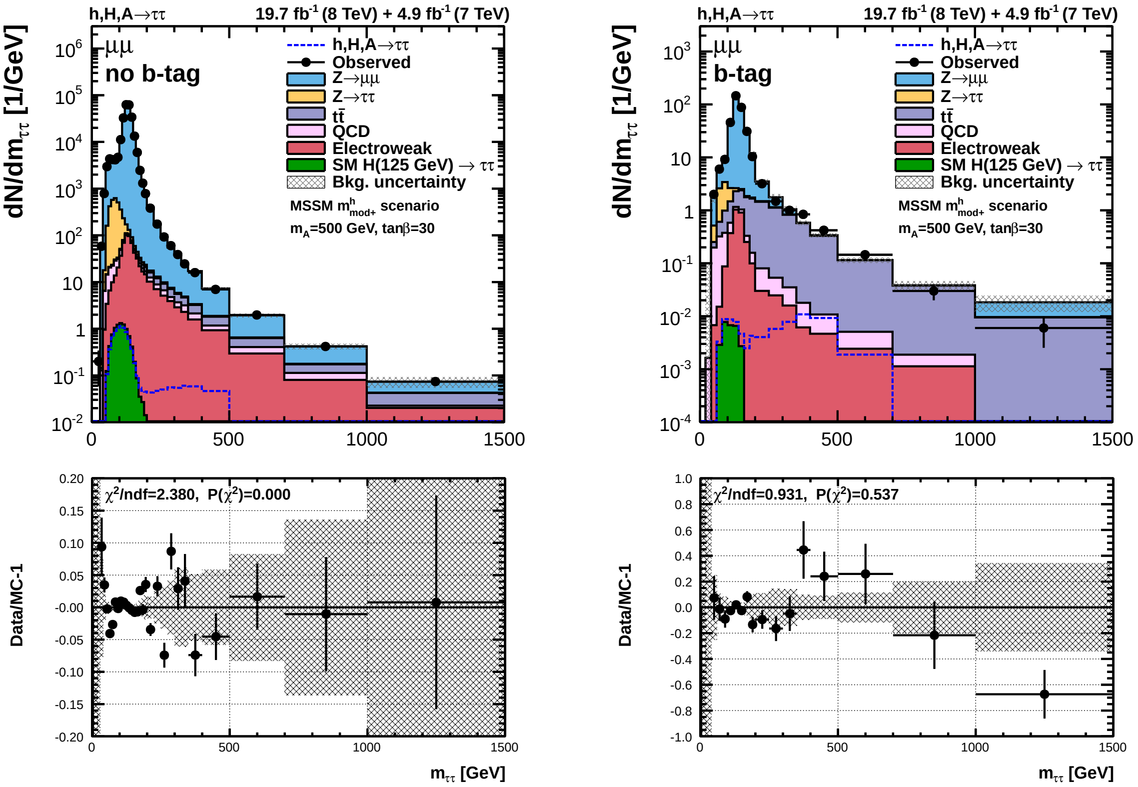

Figure 6.6: Invariant $m_{\tau\tau}$ distribution observed in the $\sqrt{s} = 7\,\text{TeV}$ and $\sqrt{s} = 8\,\text{TeV}$ data for the no-b-tag (left) and b-tag (right) category of the $\mu\mu$ channel compared to background expectations. Expected background contributions are shown for the values of uncertainties as obtained by fitting the expectation to the observation.

Table 6.5: Number of events observed and expected in the $\mu\mu$ channel for both categories in both center-of-mass periods. The signal yield is given for the $m_A = 500\,\text{GeV}$ and $\tan\beta = 30$ in the MSSM $m_h^{\text{mod+}}$ scenario. The a posteriori uncertainties are given on yields. Correlations are taken into account.

$\mu\tau_{had}$ channel				
	$\sqrt{s} = 7\,\text{TeV}$		$\sqrt{s} = 8\,\text{TeV}$	
Process	No B-Tag	B-Tag	No B-Tag	B-Tag
Z→ $\tau\tau$	26803 ± 237	283 ± 8	87258 ± 502	1115 ± 29
QCD	5488 ± 256	132 ± 17	18051 ± 888	553 ± 62
W+jets	2781 ± 211	56 ± 14	12874 ± 806	241 ± 58
Z+jets (l/jet faking τ)	703 ± 111	11 ± 2	3618 ± 430	53 ± 9
$\text{t}\bar{\text{t}}$	82 ± 6	37 ± 5	566 ± 43	196 ± 21
Di-bosons + single top	95 ± 10	13 ± 1	507 ± 50	60 ± 8
SM Higgs (125 GeV)	89 ± 11	1 ± 0.1	341 ± 39	5 ± 0.7
Total Background	36040 ± 202	533 ± 18	123215 ± 362	2224 ± 45
gg(A+H+h) → $\tau\tau$	72 ± 2	1 ± 0.0	303 ± 6	3 ± 0.1
bb(A+H+h) → $\tau\tau$	9 ± 0.4	2 ± 0.1	49 ± 1	9 ± 0.3
Data	36055	542	123239	2219

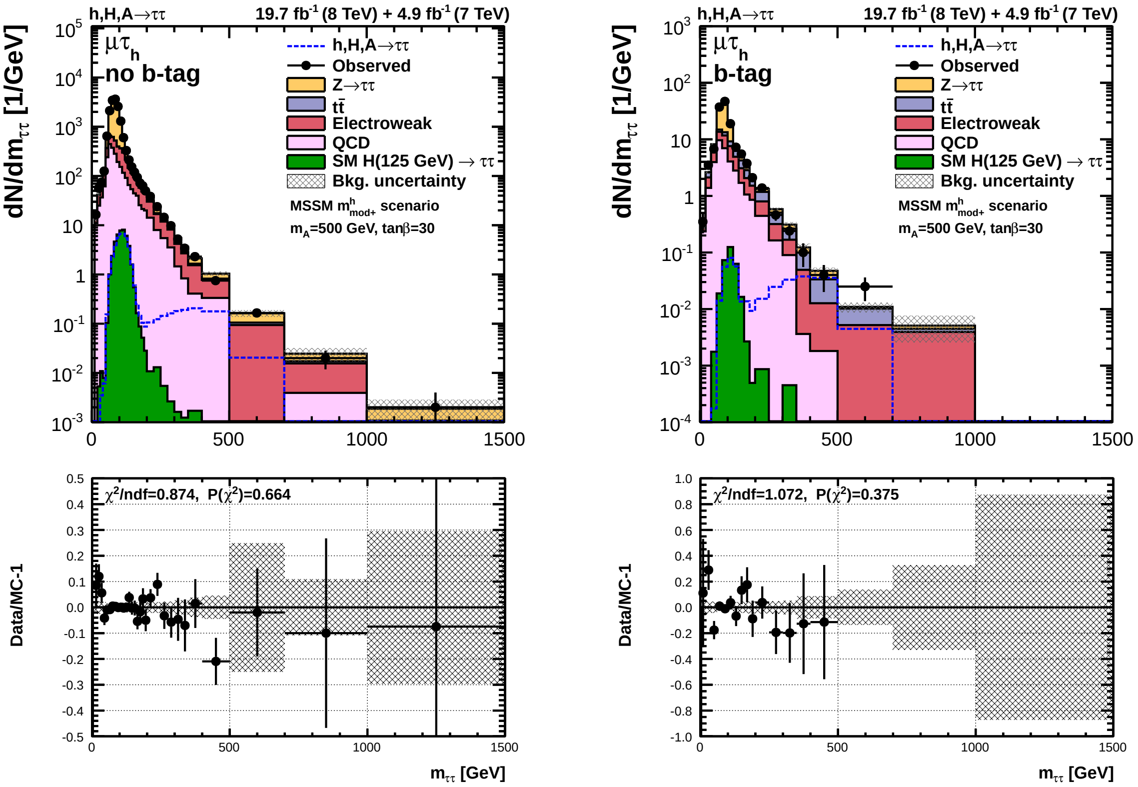

Figure 6.7: Invariant $m_{\tau\tau}$ distribution observed in the $\sqrt{s} = 7\,\text{TeV}$ and $\sqrt{s} = 8\,\text{TeV}$ data for the no-b-tag (left) and b-tag (right) category of the $\mu\tau_{had}$ channel compared to background expectations. Expected background contributions are shown for the values of uncertainties as obtained by expectation to the observation.

Table 6.6: Number of events observed and expected in the $\tau_{had}\tau_{had}$ channel for both categories in both center-of-mass periods. The signal yield is given for the $m_A = 500\,\text{GeV}$ and $\tan\beta = 30$ in the MSSM $m_h^{\text{mod+}}$ scenario. The a posteriori uncertainties are given on yields. Correlations are taken into account.

$\tau_{had}\tau_{had}$ channel		
	$\sqrt{s} = 8\,\text{TeV}$	
Process	No B-Tag	B-Tag
Z→ $\tau\tau$	2492 ± 93	60 ± 3
QCD	20190 ± 230	277 ± 19
W+jets	632 ± 158	17 ± 5
Z+jets (l/jet faking τ)	115 ± 20	2 ± 0.4
$t\bar{t}$	38 ± 4	16 ± 2
Di-bosons + single top	63 ± 12	5 ± 1
SM Higgs (125 GeV)	69 ± 13	1 ± 0.2
Total Background	23599 ± 165	379 ± 18
gg(A+H+h) → $\tau\tau$	62 ± 3	1 ± 0.1
bb(A+H+h) → $\tau\tau$	61 ± 4	13 ± 1
Data	23606	381

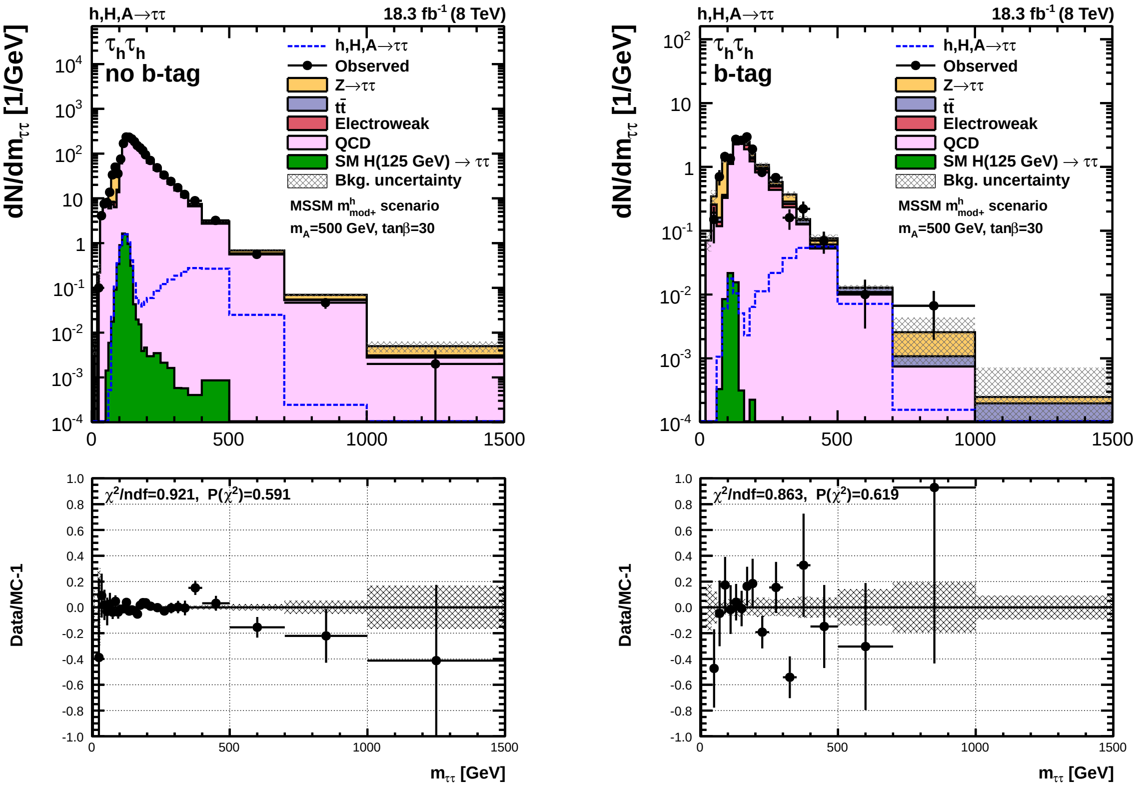

Figure 6.8: Invariant $m_{\tau\tau}$ distribution observed in the $\sqrt{s} = 8\,\text{TeV}$ data for the no-b-tag (left) and b-tag (right) category of the $\tau_{had}\tau_{had}$ channel compared to background expectations. Expected background contributions are shown for the values of uncertainties as as obtained by fitting the expectation to the observation.

6.3 Model independent Limits

The input distribution have been used to obtain model independent interpretations, which aim to be sensitive to a large amount of possible scenarios by giving limits on $\sigma \cdot \mathcal{B}$ with respect to the considered signal process which in case of the $\phi \rightarrow \tau\tau$ analysis is either gluon-gluon fusion (ggϕ) or production in association with b-quarks (bbϕ).

In order to be model independent, no information depending on the signal model enters the likelihood function (5.2). Usually, the signal as well as the background prediction is given in the dimension of a number of expected events

$$\begin{aligned} b &= L_{int} \cdot A \cdot \sigma(b) \cdot \mathcal{B}(b) \\ s &= L_{int} \cdot A \cdot \sigma(s) \cdot \mathcal{B}(s) \ . \end{aligned} \tag{6.2}$$

L_{int} is the used integrated luminosity in the analysis. The acceptance A is the number of selected events over the number of generated events for the considered process, $A = N_{sel}/N_{gen}$, and $\sigma \cdot \mathcal{B}$ is the product of the cross-section times the branching fraction of the considered signal or background process, for example gg$\rightarrow \phi \rightarrow \tau\tau$. However, since no model information shall enter the likelihood the signal is scaled to 1pb^{-1} which means that the quantity s is calculated by only considering A and L_{int} in units of pb^{-1}:

$$s = L_{int} \cdot A \ . \tag{6.3}$$

Using this definition s depends on the probed mass since the acceptance and shape changes with the mass hypothesis. In the statistical methods described in section 5 the quantity r will then take the dimension of a cross-section and will yield an upper limit on $\sigma \cdot \mathcal{B}$. The upper limit on an expected number of a certain signal can be obtained by calculating $r_{\mathrm{UL}} \cdot s$.

6.3.1 2D Likelihood Scan of the ggϕ-bbϕ Plane

In a first representation of the model independent limits, a two dimensional likelihood scan has been done in the quadrant spanned by the two considered signal processes, on the x-axis ggϕ and on the y-axis bbϕ. Both axis are given in units of $\sigma \cdot \mathcal{B}$. The lower edge of the axis is zero while the upper edge depends on the probed signal mass since for higher masses the sensitivity increases due to less background expectations and therefore the limits on $\sigma \cdot \mathcal{B}$ are smaller. In this likelihood scan at each probed mass 40000 equally distributed points in the constructed ggϕ-bbϕ quadrant are evaluated. The quantity $r \cdot s$ is split into the considered signal processes:

$$r \cdot s = r_{\mathrm{gg}\phi} \cdot s_{\mathrm{gg}\phi} + r_{\mathrm{bb}\phi} \cdot s_{\mathrm{bb}\phi} \ . \tag{6.4}$$

Therefore, the likelihood function (5.2) changes to:

$$L(n|r \cdot s(\theta) + b(\theta)) \rightarrow L(n|r_{\mathrm{gg}\phi} \cdot s_{\mathrm{gg}\phi}(\theta) + r_{\mathrm{bb}\phi} \cdot s_{\mathrm{bb}\phi}(\theta) + b(\theta)) \ . \tag{6.5}$$

The signal expectations $s(\mathrm{gg}\phi)$ and $s(\mathrm{bb}\phi)$ are scaled as in equation (6.3). No model information is used. In contrast, the values for the signal strength modifiers $r_{\mathrm{gg}\phi}$

and $r_{\mathrm{bb}\phi}$ are given by the position of the point in the quadrant. Thus, $r_{\mathrm{gg}\phi}$ and $r_{\mathrm{bb}\phi}$ are fixed in the likelihood scan, meaning that the scan effectively test the agreement between the observation and the H_{s+b} hypothesis for fixed signal expectations for given scanned point in the quadrant. At each mass hypothesis, the negative log-likelihood, $NLL = -2 \ln L$, of the likelihood function (6.5) is evaluated for all 40000 points. The transformation of the likelihood to the negative log-likelihood is done to obtain smaller numbers. The minimum NLL value of the scan is marked. The one and two sigma contours are found by searching for the points x for which

$$\begin{aligned} \Delta(NLL)_{1\sigma} &= NLL_{\mathrm{min}} - NLL(x) = 0.5 \\ \Delta(NLL)_{2\sigma} &= NLL_{\mathrm{min}} - NLL(x) = 1.92 \end{aligned} \tag{6.6}$$

is obtained. Where x is the point in the ggϕ-bbϕ quadrant.

It is not possible to combine the 7 TeV and 8 TeV datasets since the limit is set on the cross-section times branching fraction which depends on the center-of-mass energy. Therefore, the 2012 dataset corresponding to a center-of-mass energy of 8 TeV is used. In figure 6.9 the results are shown for masses between 90 and 600 GeV. 68% (1σ) and 95% (2σ) confidence intervals are plotted together with the point of the minimum of the scan, x_{min}, at each mass. The yellow diamonds refer to what would have been expected if a SM Higgs boson would be present in data. The position of the yellow diamonds are obtained by replacing the observation n in the likelihood function (6.5) with a pseudo dataset including all backgrounds and all production processes of the SM Higgs boson at 125 GeV. Using the pseudo dataset the two dimensional likelihood scan is computed and x_{min} are found. At $m_\phi = 125\,\mathrm{GeV}$ x_{min} is found at:

- $\sigma(\mathrm{gg}\phi) \cdot \mathcal{B}(\phi \to \tau\tau) = 1.325^{+2.181}_{-1.324}\,\mathrm{pb}$ and
- $\sigma(\mathrm{bb}\phi) \cdot \mathcal{B}(\phi \to \tau\tau) = 0.057^{+1.415}_{-0.057}\,\mathrm{pb}$,

which is in perfect agreement with the theory predictions of $\sigma(\mathrm{gg}h_{\mathrm{SM}}) \cdot \mathcal{B}(h_{\mathrm{SM}} \to \tau\tau) = 1.218\,\mathrm{pb}$ and $\sigma(\mathrm{bb}h_{\mathrm{SM}}) \cdot \mathcal{B}(h_{\mathrm{SM}} \to \tau\tau) = 0.013\,\mathrm{pb}$ within the quoted uncertainties. This also validates the two dimensional likelihood scan. The position of the minimum of NLL corresponds to the injected pseudo dataset. Comparing the pseudo dataset to the actual observation an agreement within 1σ is seen for the minima. The data shows a slightly more pronounced "excess" than what would have been expected from the SM Higgs boson. The highest deviation of about 1.3σ between the SM Higgs boson expectation and the observation is seen at $m_\phi = 90\,\mathrm{GeV}$, where the SM Higgs boson expectation would be at zero. The observation is compatible with the background only expectation ($\sigma(\mathrm{gg}\phi) \cdot \mathcal{B}(\phi \to \tau\tau) = 0\,\mathrm{pb}$ and $\sigma(\mathrm{bb}\phi) \cdot \mathcal{B}(\phi \to \tau\tau) = 0\,\mathrm{pb}$) for all probed masses. The highest deviations is also seen at $m_\phi = 90\,\mathrm{GeV}$. To demonstrate the usefulness of these plots, in figure 6.9 the signal point with $m_A = 500\,\mathrm{GeV}$ and $\tan\beta = 30$ in the MSSM $m_h^{\mathrm{mod+}}$ scenario has been added and displayed by a red diamond. Similar to the yellow diamond a pseudo dataset summing up all backgrounds and the signal expectation for the MSSM $m_h^{\mathrm{mod+}}$ scenario with $m_A = 500\,\mathrm{GeV}$ and $\tan\beta = 30$ is constructed and

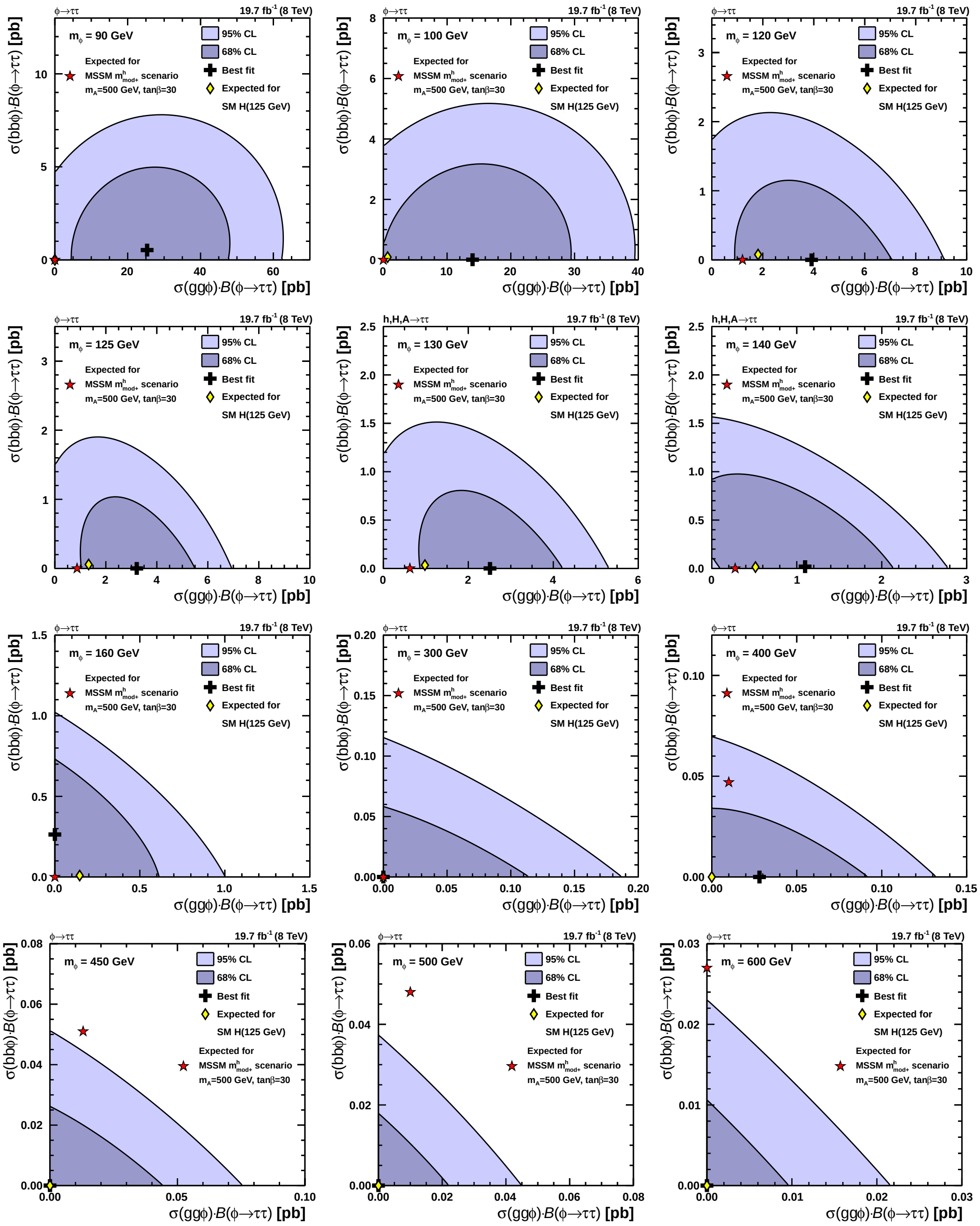

Figure 6.9: Likelihood scan of $\sigma \cdot \mathcal{B}(\mathrm{gg}\phi)$ and $\sigma \cdot \mathcal{B}(\mathrm{bb}\phi)$ at 8 TeV center-of-mass energy for different Higgs boson masses. The best fit point of the SM 125 GeV Higgs boson is plotted as a yellow diamond. The red diamond shows the best fit point for a signal in the MSSM $m_h^{\mathrm{mod}+}$ scenario with $m_A = 500\,\mathrm{GeV}$ and $\tan\beta = 30$.

the likelihood scan is performed testing the pseudo dataset against the background expectation. The chosen MSSM model is the same as used in the invariant $m_{\tau\tau}$ plots in section 6.2. The properties of the Higgs bosons for this model are given in table 6.1. The multiple peak structure of the MSSM signal is reproduced by

the two dimensional fit. The contribution of the light scalar Higgs to the MSSM signal expectation is seen for the masses $90-160$ GeV and behaves similar to the expectation from the SM Higgs boson. For masses between 300 and 600 GeV the peak of the heavy Higgs bosons, A and H, is seen. At $\phi = 450$ GeV, 500 GeV and 600 GeV the expectation is outside of the 95% area. Therefore this signal model is not compatible with the observation within 2σ.
More masses have been checked. Those can be found in appendix E.
In a strict statistical interpretation, the likelihood scan is not an (upper) exclusion approach but tests the compatibility of the data with a given hypothesis. If $NLL_{\text{min}} = 0$ the likelihood scan can be directly compared to the $\text{CL}_{\text{s+b}}$ method as described in section 5.2.1. Comparisons with Feldman-Cousin limits as described in section 5.2.2, shown in figure 6.10, show good agreement. Thus model predictions outside of the 95% confidence level of the likelihood scan can effectively be interpreted as excluded. Slight deviations are seen due to a coarse binning in the the Feldman-Cousins method: 121 equally distributed points in the quadrant for Feldman-Cousins compared to 40000 for the likelihood scan. The coarse binning is done because the Feldman-Cousins method is extremely computing intensive and therefore has not been used for practical reasons. In the shown comparison, 1000 Monte Carlo pseudo datasets have been generated at each point.

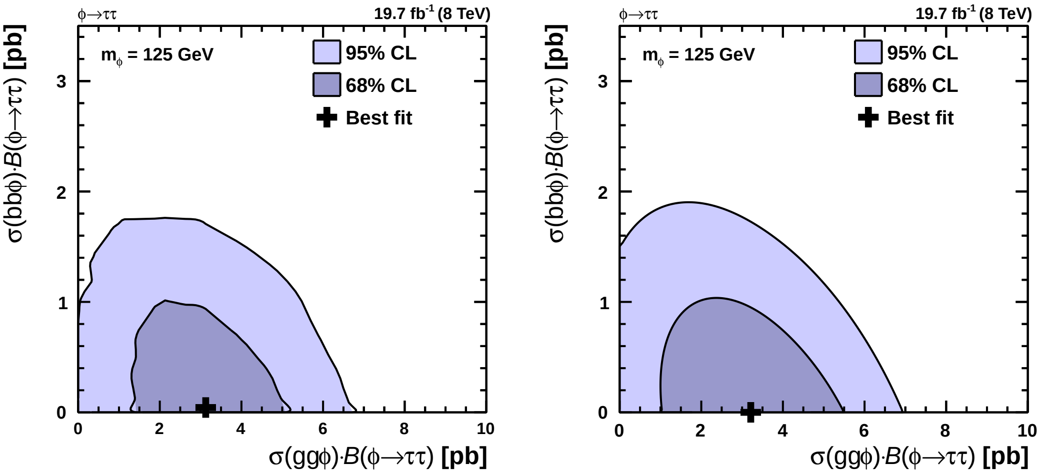

(a) (b)

Figure 6.10: On the left figure 6.10(a) the confidence intervals as computed with the Feldman-Cousins method are shown for a mass of 125 GeV. On figure 6.10(b) the same mass is probed with the likelihood scan described above. A good agreement between both methods is observed. Due to extremely computing intensive calculation the quadrant is only split into 121 grid points with 1000 generated Monte Carlo pseudo datasets at each point.

6.3.2 1D $\sigma \cdot \mathcal{B}$ Limits

Compared to the two dimensional likelihood scan, a more sophisticated way of setting exclusion limits is used in the one dimensional $\sigma \cdot \mathcal{B}$ limit calculation. Upper limits are set separately on the gg→ $\phi \to \tau\tau$ and bb→ $\phi \to \tau\tau$ process using the asymptotic $\mathrm{CL_s}$, hence a profile likelihood, equation (5.17). Again the likelihood, as shown in equation (5.2), is changed into the likelihood function (6.5). Upper limits are set on $r_{\mathrm{gg}\phi}$ ($r_{\mathrm{bb}\phi}$) while the other signal strength modifier $r_{\mathrm{bb}\phi}$ ($r_{\mathrm{gg}\phi}$) is treated as an uncertainty in the fit which means it is left floating freely and effectively will get profiled taking a value which maximizes the likelihood function.

In figure 6.11 the upper limits for the mass range between 90 and 1000 GeV on the considered processes gg$\phi \to \tau\tau$ (left side) and bb→ $\phi \to \tau\tau$ (right side) are shown. The expected median limit is shown as a black dashed line. The ±1 and $\pm 2\sigma$ expected error bands are shown as coloured bands. The observation is shown by a solid black line. Probed mass points are indicated by black dots. The probed masses are connected by straight lines. The plots demonstrate the possibilities how a the SM Higgs boson at 125 GeV can be treated. The $\phi \to \tau\tau$ analysis is not sensitive to the SM Higgs boson since the analysis strategy does not aim not to discover the SM Higgs boson, but stays model independent to cover a broad range of possible models as described in 4.3. Thus all plots look similar.

On the top a single narrow resonance signal hypothesis is tested against a background hypothesis which does not included the SM Higgs boson. This hypothesis test is used to search for any signal above the background only expectation. In figure 6.11 upper limits are set on gg→ $\phi \to \tau\tau$. The observation and the expectation agree within 2σ. An upward fluctuation of the data can be seen for low masses. This is also seen in the two dimensional likelihood scans, see figure 6.9. The downward fluctuation of the data in the high mass tail can also be seen in the invariant mass plots especially in the $e\tau_{had}$, $\mu\tau_{had}$ and $\tau_{had}\tau_{had}$ channel which are the dominant ones in the high mass region. In the middle, figures 6.11 (c) and (d), the SM Higgs boson at 125 GeV is added to the nominal background. These plots are used to search for additional Higgs bosons on top of the discovered one. Since no sensitivity to the discovered Higgs boson is reached the plots do not visibly differ from the top row.

Figures 6.11 (e) and (f) test the observation against what would have been expected for a SM Higgs boson at 125 GeV in data. Therefore, next to the nominal calculation of the observed the expected is calculated by replacing the observation n in the likelihood function (6.5) by a pseudo dataset including all backgrounds and the SM Higgs boson. This is done multiple times to obtain the expected 1 and 2 σ bands by varying the pseudo dataset within its statistical[2] uncertainties. Numerical results for the shown figures are available in appendix D.

In figure 6.12 the expected limits of the channels of the $\phi \to \tau\tau$ analysis are shown. On the left figure the limits on the gg→ $\phi \to \tau\tau$ and on the right side on the bb→ $\phi \to \tau\tau$ process are compared. The $e\tau_{had}$, $\mu\tau_{had}$ and $\tau_{had}\tau_{had}$ channels have the highest sensitivity. The $\mu\mu$ channels suffers from the extremely large Z→ $\mu\mu$ background. The $e\mu$ channel can compete with the leading channels in the low mass

---

[2] The number of events follows a Poisson distribution.

region, but due to a large $t\bar{b}$ background it is not comparable in the high mass region.

6.3.3 Projection to 13 TeV and 300 fb^{-1}

The LHC is expected to collect about 300 fb^{-1} with a center-of-mass energy of 13 TeV in the coming years. In figure 6.13 the expected sensitivity is shown. Therefore, all background expectation have been scaled by the expected cross section at 13 TeV [136]. The uncertainties were kept as described in chapter 4. The projection is compared to the 8 TeV result as shown in figure 6.11 (a) and (b). To be able to compare the projection to the 8 TeV result the 8 TeV result is scaled by the expected parton luminosity [137] when going from 8 TeV to 13 TeV center-of-mass energy. The SM 125 GeV Higgs boson theory expectation indicated by a blue cross. It is clearly visible that in the gluon fusion process the $\phi \to \tau\tau$ analysis as described in chapter 4 will get sensitive to the SM Higgs boson even with a very inclusive analysis (see section 4.3). In contrast, the inclusive analysis will not get sensitive to the production of the SM Higgs boson in association with b-quarks. In the appendix D numerical results for the projections are given.

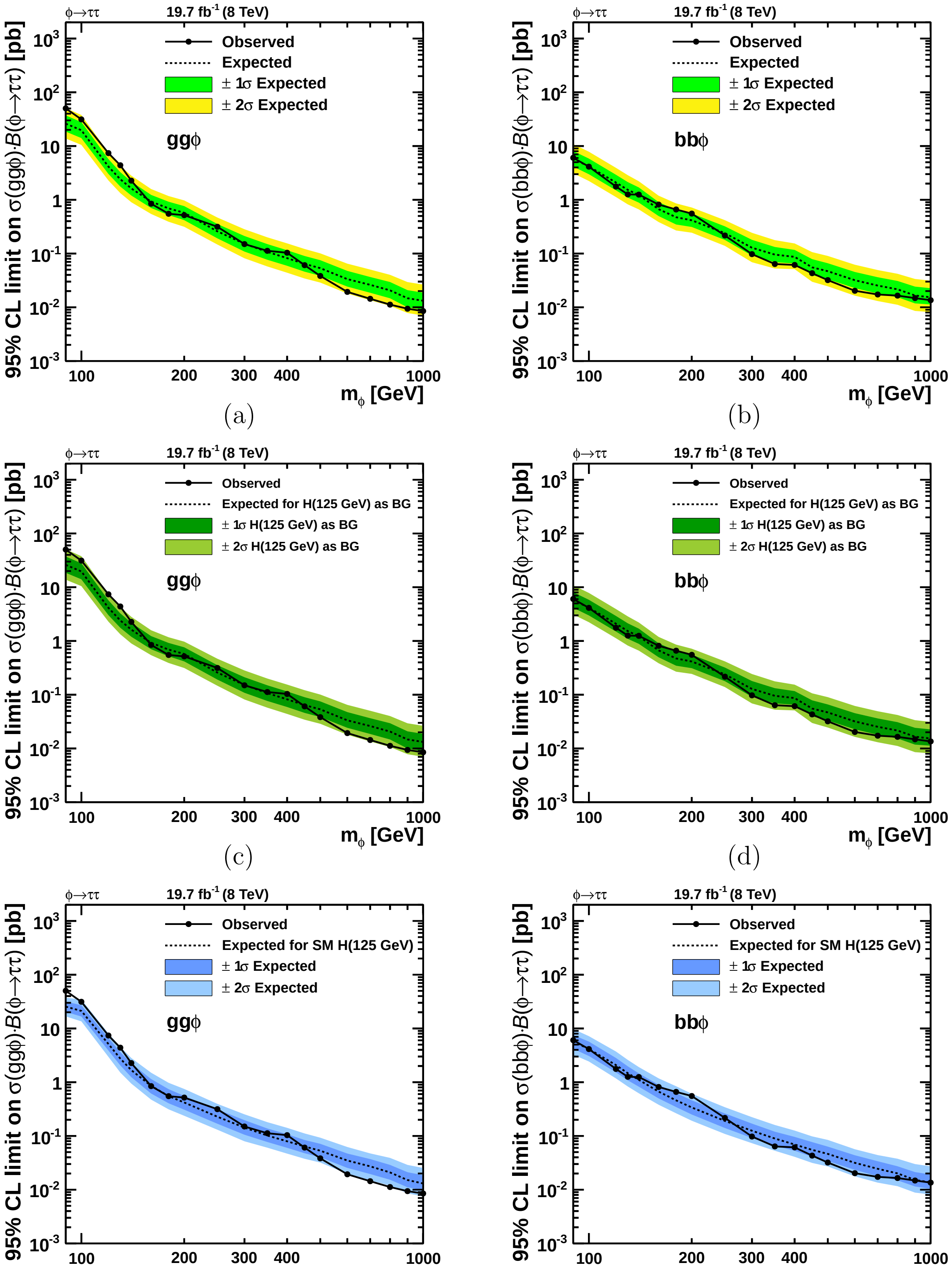

(a) (b)

(c) (d)

(e) (f)

Figure 6.11: Limits on $\sigma \cdot \mathcal{B}$ for both considered signal processes. On the left side the limits on gg→ $\phi \to \tau\tau$ and on the right side the bb→ $\phi \to \tau\tau$ limits are shown. In the top row the $H_{\phi+b}$ hypothesis is tested against the H_b hypothesis. In the middle the $H_{\phi+b}$ hypothesis is tested against the $H_{h_{\mathrm{SM}}+b}$ hypothesis and on the bottom the agreement of the observation is tested against the expectation of a SM Higgs boson at 125 GeV in data.

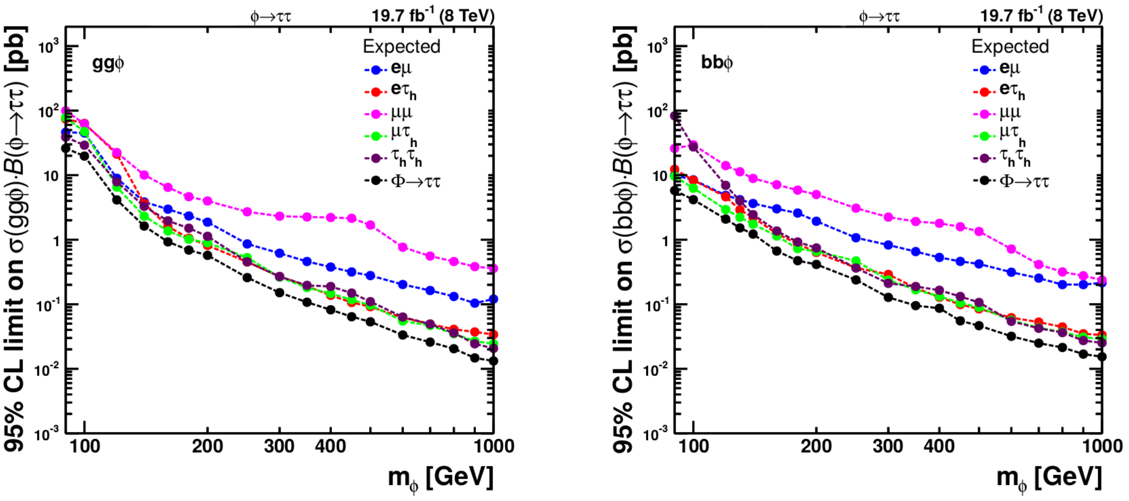

Figure 6.12: Shown are the expected limits of the channels in the $\phi \to \tau\tau$ analysis. On the left on the gg→ $\phi \to \tau\tau$ process and on the right side on the bb→ $\phi \to \tau\tau$ process. The channels with the highest sensitivity are the $e\tau_{had}$, $\mu\tau_{had}$ and $\tau_{had}\tau_{had}$ channels. The $\mu\mu$ channels suffers from the extremely large Z→ $\mu\mu$ background. The $e\mu$ channel can compete with the leading channels in the low mass region, but due to a large t$\bar{\text{b}}$ background it is not comparable in the high mass region.

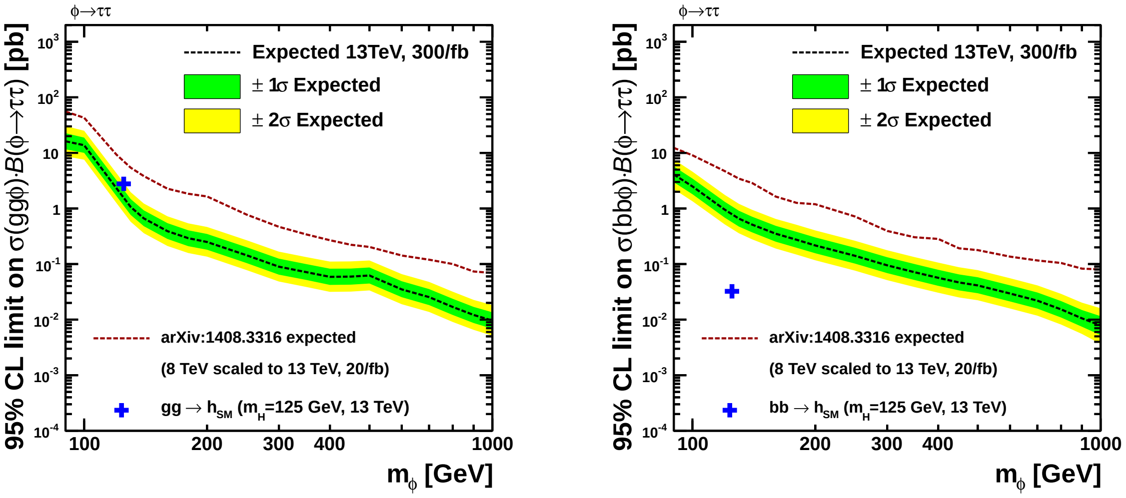

Figure 6.13: Projections of the one dimensional, model independent limits on the cross-section times branching fraction for the production of a single narrow resonance in the di-τ final state (left) via gluon fusion and (right) in association with b-quarks, for an analysis similar to the one described in chapter 4, for 300 fb^{-1} at a center-of-mass energy of 13 TeV. The red dashed line indicates the expected limits as shown in figure 6.11 (a) and (b) scaled by a factor taking the change in parton luminosity into account when going from 8 TeV to 13 TeV center-of-mass energy. The blue cross-indicates the cross section times branching fraction as expected for the SM Higgs boson, via gluon fusion and in association with b-quarks, respectively. For these limit projections all acceptances and efficiencies and any effects of event pileup have been left as found for the 8 TeV case.

6.4 Model dependent Limits

In addition to model independent limits, the results are also interpreted in different new physics models. Eight different MSSM benchmark scenarios, see [29–31; 138], and a benchmark 2HDM of type-2 [42] have been tested. These scenarios exhibit interesting phenomenology while satisfying the boundaries set by direct searches performed at the Large Electron Positron (LEP) collider, the Tevatron and the LHC. In particular, the scenarios fulfil the mass requirements of the new discovered Higgs boson over large parameter space, such that one of the scalar Higgs bosons has a mass of $125 \pm 3\,\mathrm{GeV}$, where the mass uncertainty of $\pm 3\,\mathrm{GeV}$ is dominated by theory uncertainties [32]. Exact parameters of the MSSM benchmark scenarios can be found in table A.1. A brief introduction of each benchmark scenario has been given in chapter 2.

In each of these defined BSM scenario the signal prediction in form of the expected invariant di-τ mass shape consists of three neutral Higgs bosons. The shape at a certain point in the parameter space of a considered model is obtained in the following way: At each parameter point of a considered 2HDM or MSSM model the signal consists of a linear combination of the three neutral Higgs bosons h, A and H. The masses of these Higgs bosons are defined by the considered point in the parameter space of the model. The $m_{\tau\tau}$ shape of each Higgs boson signal is defined by the mass, while the normalization is defined by the cross-section and branching fraction. The shapes can than be obtained using the generated Monte Carlo signal samples for the corresponding Higgs mass. The signal samples are scaled to $1\mathrm{pb}^{-1}$ as described in section Model independent Limits and equation 6.3. Higgs boson signal shapes with masses in between two available Monte Carlo signal samples are obtained using the *horizontal template morphing* technique [139]. Each obtained shape is scaled by the corresponding cross-section and branching fraction defined by the considered point in the parameter space of the model. The numbers are provided by the LHC cross-section working group for the MSSM benchmark scenarios [138; 140] and for the 2HDMs [42]. All three shapes added together form the final signal $m_{\tau\tau}$ template. The invariant di-τ mass distributions of the multiple peak structure for the signal point of $m_A = 500\,\mathrm{GeV}$ and different values of $\tan\beta$ in the MSSM $m_h^{\mathrm{mod}+}$ scenario are shown in figure 6.14. The number of events divided by the bin width is plotted on the y-axis. The first peak shows the little Higgs boson h, while the broader second peak shows the combination of both heavy Higgs bosons A and H. In the bbϕ production processes the $A + H$ peak is more pronounced while in the ggϕ production process the h peak is dominant. The total number of events is higher for the no-b-tag categories. Due to the logarithmic scale on the y-axis it is hard to see, but the number of events in the light Higgs peak is nearly independent from $\tan\beta$ in the parameter space where the mass of h is $125 \pm 3\,\mathrm{GeV}$. As shown in table 6.1, the light Higgs boson has SM like properties. In the limit calculation the likelihood function (5.2) is used. A common signal strength modifier r is used since contributions of the Higgs bosons or production mechanisms are fixed relative to each other. The ratios are defined by the considered point in the parameter space

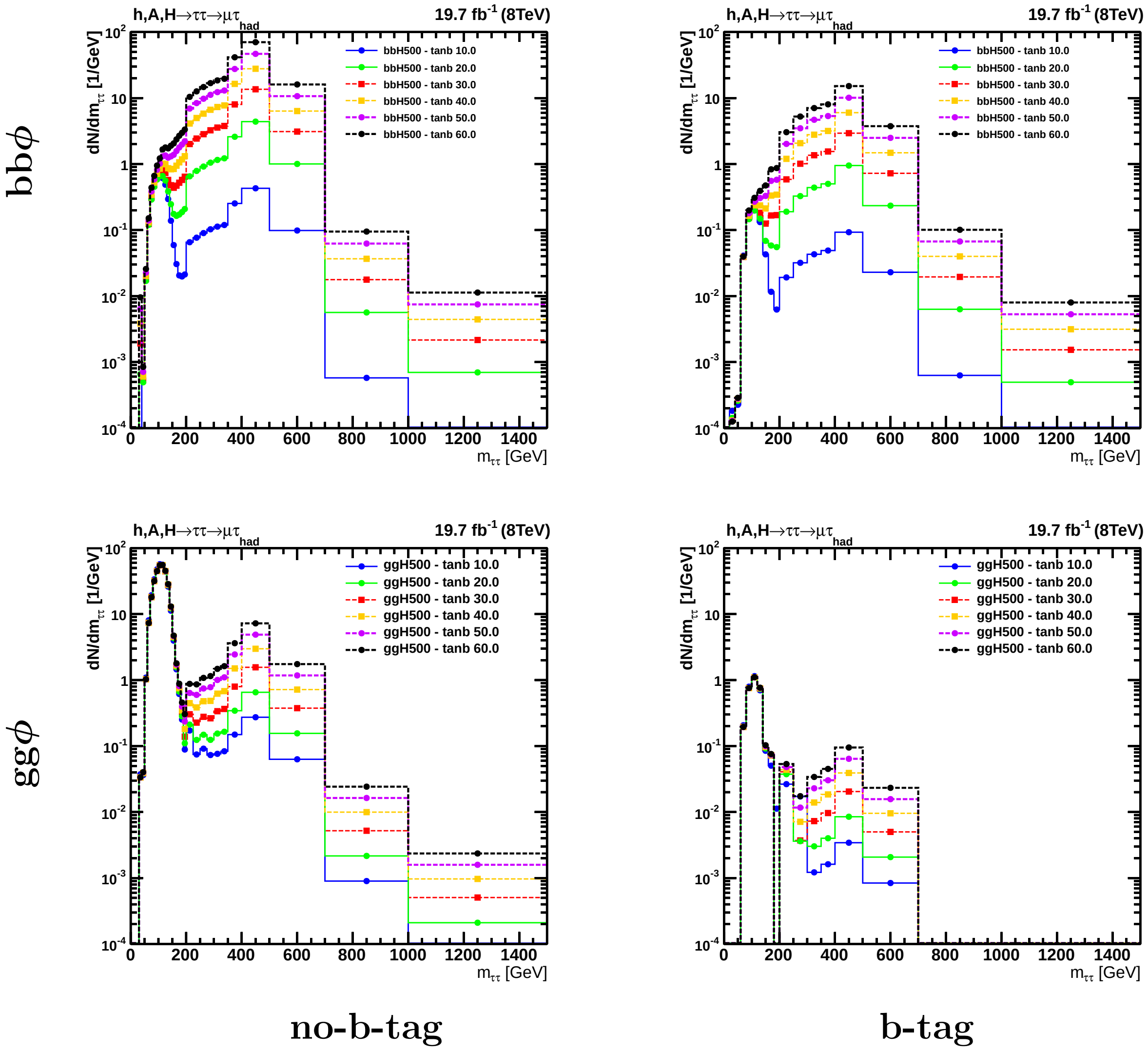

Figure 6.14: Multiple peak structure of the MSSM $m_h^{\text{mod}+}$ scenario at $m_A = 500\,\text{GeV}$ and for different $\tan\beta$ values. All plots show the expected signal in the $\mu\tau_{had}$ channel scaled by cross-sections corresponding to a center-of-mass energy of 8 TeV and branching fractions. The number of events divided by the bin width is plotted on the y-axis. The top row shows the invariant di-τ mass distribution in the bbϕ production process while the bottom row shows the expected distribution for the ggϕ production process. The left column shows the no-b-tag category. The right shows the b-tag category.

of the model.

To obtain the exclusion curve of 95% confidence level a scan is performed in the two dimensional parameter plane. At each x-axis point, in most models the m_A-axis, the $\tan\beta$ points are scanned from top to bottom. The CL_s value is calculated at every model point. A point is then marked as excluded if $\text{CL}_\text{s} < 0.05$ or not excluded if $\text{CL}_\text{s} > 0.05$, see equation (B.2). The crosspoint $\text{CL}_\text{s} = 0.05$ is obtained by linear interpolation between nearby excluded ($\mathrm{CL}_s < 0.05$) to not excluded ($\mathrm{CL}_s > 0.05$) points. A typical scan is seen in figure 6.15 for $m_A = 130$ in the MSSM τ-phobic scenario. Here the $H_{h_{\mathrm{SM}}+b}$ hypothesis is tested against the $H_{h+A+H+b}$ hypothesis. The minimal exclusion power is seen at $\tan\beta = 2$ due to destructive interference of stops and tops in the loop of the gluon-gluon fusion and therefore decreased cross-section. For lower $\tan\beta$ the separation power between the hypothesis increases again. All MSSM benchmark scenarios show this behaviour expect for the low-m_H scenario where the heavy Higgs boson is assumed to have SM like properties.

6.4.1 Background against BSM Signal Model

In a first representation of model dependent limits the H_b hypothesis is tested against the $H_{h+A+H+b}$ hypothesis. This test was also used in past publications [15; 16]. Exclusion limits are set within a two dimensional plane, usually defined by m_A and $\tan\beta$. The limits are set using the asymptotic $\mathrm{CL_s}$ method.
The observed and expected exclusion limits in the $m_h^{\mathrm{mod}+}$ scenario are shown in figure 6.16 (a). The parameter space is spanned by m_A and $\tan\beta$. The black dashed area marks the region which is excluded at 95% confidence level by the observation. The red dashed area shows the parameter space where $m_h \neq 125 \pm 3\,\mathrm{GeV}$. The black dashed line shows the median expected limit while the green and yellow bands show the ± 1 and $\pm 2\sigma$ expected exclusion limit. The blue solid line shows the expected exclusion limit if a SM Higgs boson at 125 GeV would be present in data. The limit is obtained by replacing the data in the likelihood function (5.2) by a pseudo dataset summing up all backgrounds and adding the expected shapes of all production mechanisms of the SM Higgs boson. The exclusion limit basically follows the product of the sensitivity times the cross-section times the branching fraction. While the sensitive increases the cross sections decreases rapidly for increasing m_A, especially for the heavy Higgs bosons. For high m_A the cross-section and branching fraction of the light Higgs is constant. The maximal exclusion power is found at $m_A = 140\,\mathrm{GeV}$. Due to destructive interferences of SUSY (stops and sbottoms) and SM particles (top and bottom quarks) in the ggϕ loop and thus lower cross-section the minimal exclusion power for a fixed m_A is found around $\tan\beta = 1-4$. For lower $\tan\beta$ the exclusion power increases again. This can be seen at $m_A = 140\,\mathrm{GeV}$ where also the low $\tan\beta$ region is excluded. The upward fluctuation in data as discussed and seen in the model independent limits (section 6.3.2 and 6.3.1) for low masses also shows up here. The SM Higgs boson alone can not be responsible for the slight excess as seen when comparing the observed and the expected limit of the SM Higgs boson. For higher m_A a good agreement between observation and expectation is found. The downward fluctuation as seen in the one dimensional limits (section 6.3.2) is not seen because the exclusion limit for high masses does also dependent on the light Higgs and not only on the heavy Higgs bosons. Therefore, the downward fluctuation at low masses and the upward fluctuation at high masses cancel each other. In the MSSM $m_h^{\mathrm{mod}+}$ scenario as well as in other MSSM scenarios a good agreement between the observation and the expectation of the H_b hypothesis is observed. All other considered scenarios as well as numerical results can be found

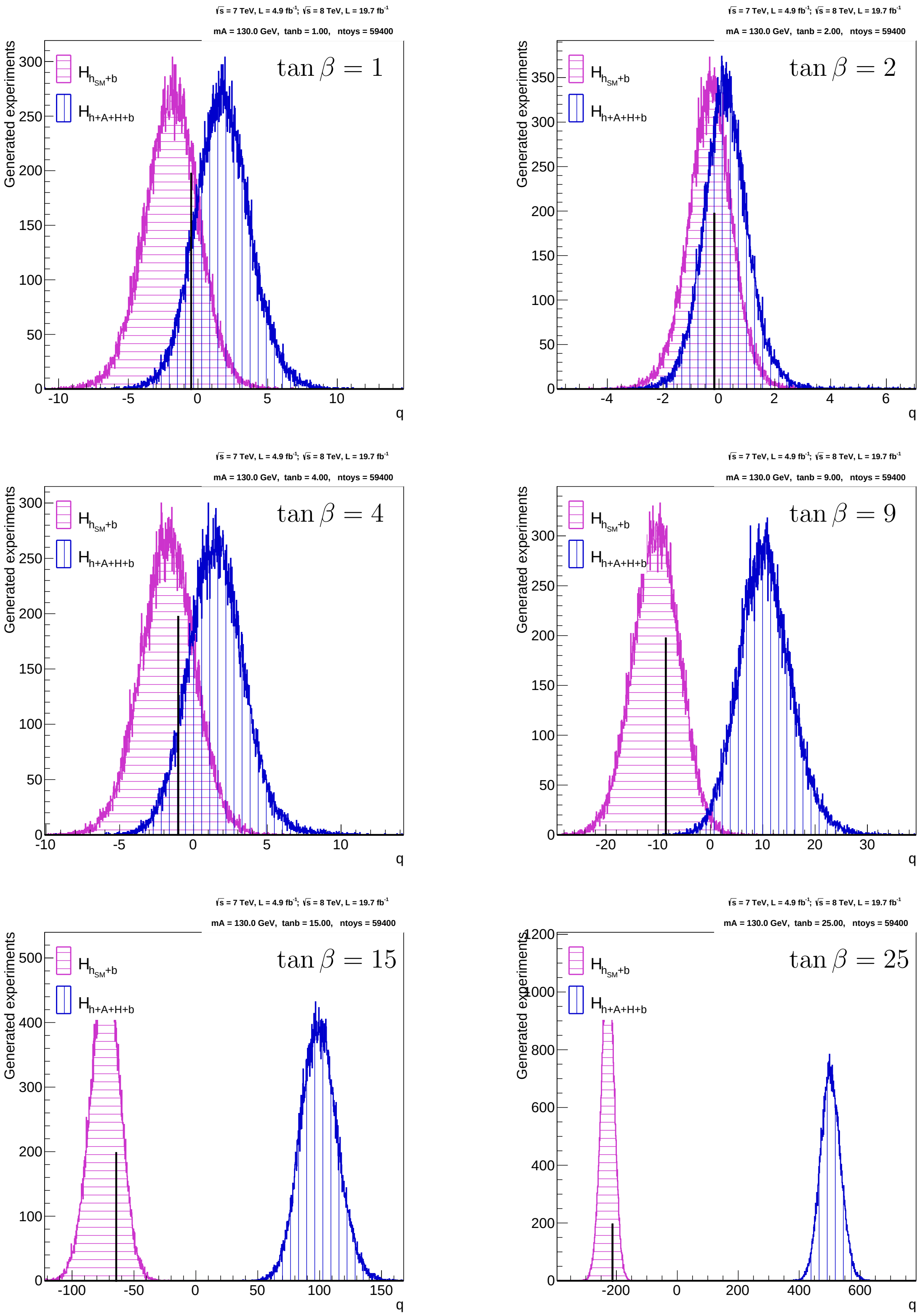

Figure 6.15: Distributions of the particle density functions for the $H_{h+A+H+b}$ hypothesis (blue) and the $H_{h_{\mathrm{SM}}+b}$ hypothesis (violet) in the MSSM τ-phobic scenario at $m_A = 130\,\mathrm{GeV}$ and $\tan\beta = 1$ to $\tan\beta = 25$. Each distributions consists of 59400 Monte Carlo evaluations of the test statistic. The separation exclusion power is seen at $\tan\beta = 2$ due to destructive interference of stops and tops in the loop of the gluon-gluon fusion and therefore decreased cross-section. The separation power increases for lower and higher $\tan\beta$ values.

in the appendix F.
There is little sensitivity to the SM Higgs boson since the expected limit and the expected limit of the SM Higgs boson are close. Nevertheless, for higher m_A there is a overall discrepancy of 0.5σ between the SM expectation and the observation. This is a indication for the limited use of testing the H_b hypothesis against the $H_{h+A+H+b}$ hypothesis, since with increasing data the limits will further drift apart from each other and therefore the presence of the SM Higgs boson will fake an excess. For high m_A and medium to low $\tan\beta$ the sensitivity is driven by the light Higgs boson since the cross-sections of H and A are small. Thus this whole $\tan\beta$ range can be excluded based on the H_b hypothesis if a SM Higgs boson is seen in data. This means that the upward fluctuation in data as seen in section 6.3.2 and 6.3.1 has significant impact on the high mass exclusion. This progress is already seen by the broadened -1 and -2σ bands which reach into this low-to-medium $\tan\beta$ region. In figure 6.16 (c) the $\phi \to \tau\tau$ analysis has been scaled to a luminosity of 500 fb^{-1} at a center-of-mass energy of 8 TeV. Due to a lack of theory cross-section predictions for 13 TeV it was not possible to perform a projection to 300 fb^{-1} at 13 TeV. The observation is replaced by a pseudo dataset summing up all backgrounds and adding the SM Higgs boson. The presence of a SM Higgs boson yields an excess over the whole mass range which will be difficult to interpret. The light Higgs boson h has SM properties nearly everywhere in the parameter plane which explains the broadness of the excess. Therefore, the presence of the SM Higgs boson in data will look like a signal even thought the signal furthermore includes the heavy Higgs bosons H and A.

6.4.2 Background including SM Higgs Boson against BSM Signal Model

In the light of the Higgs boson discovery a hypothesis test of the H_b against the $H_{h+A+H+b}$ hypothesis as described in section 6.4.1 no longer reflects the current knowledge of physics. Instead, a statement is needed if an appearing signal is more SM-like or favours a 2HDM or MSSM signal model. Thus the $H_{h_{\text{SM}}+b}$ hypothesis is tested against the $H_{h+A+H+b}$ hypothesis.
The signal expectation in the likelihood function (5.2) is split into a SM Higgs boson signal expectation including gluon-gluon fusion, vector boson production and Higgs Strahlung and the 2HDM or MSSM signal expectation

$$L(n|r \cdot s(\theta) + b(\theta)) \to L(n|M(r = 0, 1/\theta)) \tag{6.7}$$

with

$$M(r = 0, 1/\theta) = r \cdot s_{\text{BSM}}(\theta) + (1 - r) \cdot s_{\text{SM}}(\theta) + b(\theta) \ .$$

The BSM signal expectation s_{BSM} is obtained following the steps described in section 6.4.1. The BSM and the SM signal expectations, s_{SM} and s_{BSM}, are scaled to the expected yield, see equation (6.2). The signal strength modifier connects both expectations. The $H_{h_{\text{SM}}+b}$ hypothesis is considered for $r = 0$, the $H_{h+A+H+b}$ hypothesis $r = 1$.

After having build the likelihood function, the $\mathrm{CL_s}$ method is used to find the exclusion limit. For this purpose, the TEV test statistic, equation 5.16, has to be used because it tests a priori known value $r = 0$ in the denominator against a certain value for r in the numerator. It is not possible to use the LHC test statistic, equation (5.17), for this purpose, since in the denominator the signal strength modifier takes $r = \hat{r}$, which is the value of the signal strength modifier for which the denominator in equation (5.17) takes its global maximum for all possible values of r. But for the model defined in equation (6.7) r must either be 0 or 1 to have physical meaning and also known a priori. The value $\hat{r}$ is due to the constraint $0 \leq \hat{r} \leq r$ is not a priori known and in general it will not be 0. Since two well defined theories, the MSSM (or 2HDM) and the SM, are tested against each other fixed values for r are tested. In the numerator of the test statistic, equation (5.16), r is set to 1, in addition to $r = 0$ which is used in the denominator. Using the likelihood of equation (6.7) the test statistic

$$q_{\mathrm{BSMvsSM}} = -2\ln(\lambda) = -2\ln\left(\frac{L(n|M(1/\hat{\theta}_1))}{L(n|M(0/\hat{\theta}_0))}\right) \tag{6.8}$$

separates the $H_{h_{\mathrm{SM}}+b}$ from the $H_{h+A+H+b}$ hypothesis.

The LEP test statistic, equation (5.15) could in principle be used but does not include profiling of the uncertainties and therefore has the disadvantages described in section 5.1.4. There is no asymptotic formula known for the TEV test statistic, so the full $\mathrm{CL_s}$ method has to be used which is computing intensive due to the involved Monte Carlo pseudo dataset generation.

In conclusion, using the TEV test statistic with the designed likelihood function, equation (6.7), suffices the requirements to perform the hypothesis test. Probability density function for the $H_{h_{\mathrm{SM}}+b}$ hypothesis and the $H_{h+A+H+b}$ hypothesis are obtained by generating large number of Monte Carlo pseudo datasets, $O(50000)$, for each distribution. In figure 6.15 the distributions are shown for the MSSM τ-phobic scenario at $m_A = 130$ GeV and $\tan\beta = 1$ to $\tan\beta = 25$. The expected and observed $\mathrm{CL_s}$ values are than calculated as described in section 5.2.1.

In figure 6.16 the results testing the H_b or the $H_{h_{\mathrm{SM}}+b}$ hypothesis against the $H_{h+A+H+b}$ hypothesis are shown. Figure 6.16 (b) and (d) shows the result for the testing the $H_{h_{\mathrm{SM}}+b}$ hypothesis against the $H_{h+A+H+b}$ hypothesis for the available dataset and for a projection to 500 fb^{-1}. The results of testing the H_b hypothesis against the $H_{h+A+H+b}$ hypothesis for the available dataset and for a projection to 500 fb^{-1} are shown in figure 6.16 (a) and (c), as explained in section 6.4.1. The median expected of the $H_{h_{\mathrm{SM}}+b}$ versus $H_{h+A+H+b}$ hypotheses test, figure 6.16 (b), agrees with the expectation from the SM Higgs boson shown as a blue curve in figure 6.16 (a). Also the -1 and -2σ bands are not broadened since the $H_{h_{\mathrm{SM}}+b}$ includes the SM higgs boson. Figure 6.16 (d) shows that the SM Higgs boson will not yield an excess when testing the $H_{h_{\mathrm{SM}}+b}$ hypothesis against the $H_{h+A+H+b}$ hypothesis as it is the case in figure 6.16 (c) for the same dataset but testing H_b against $H_{h+A+H+b}$. The little circle at $m_A \approx 125\,\mathrm{GeV}$ and $\tan\beta \approx 3$ in figure 6.16 (d) shows that at this point the SM Higgs boson looks like the combination of the three Higgs bosons. In conclusion: Testing the H_b against the $H_{h+A+H+b}$ hypothesis will in future lead to results which are hard to interpret, since an excess disfavours the H_b hypothesis but not necessary origins from one (or more) unknown particle since it could well be the SM Higgs boson yielding the excess. This development is already seen in current results. In contrast, the $H_{h_{\mathrm{SM}}+b}$ versus $H_{h+A+H+b}$ results behave as wanted. An excess will disfavour the $H_{h_{\mathrm{SM}}+b}$ hypothesis and origin from one (or more) unknown particle.

In figure 6.17 the results for the MSSM m_h^{max} (a), $m_h^{\mathrm{mod\text{-}}}$ (b), low-tan β-high (c) and low-m_H (d) scenario are shown. In the m_h^{max} scenario the allowed parameter space defined by the mass constraint $m_h = 125 \pm 3\,\mathrm{GeV}$ is very small, which shrinks the interesting parameter space. Thus, this model is no longer used as reference. Nevertheless, exclusion limits are set to be able to compare with older results. The exclusion curves of the MSSM m_h^{max}, $m_h^{\mathrm{mod+}}$ (figure 6.16 (b)) and $m_h^{\mathrm{mod\text{-}}}$ scenario are very similar since the only difference, besides the b-quark mass and the gluino mass, which has only minor influence on the cross-sections and branching fractions, is the value of the stop-mixing parameter X_t: 2000 GeV in the m_h^{max} scenario, 1500 GeV in the $m_h^{\mathrm{mod+}}$ scenario and −1900 GeV in the $m_h^{\mathrm{mod+}}$ scenario. All other SUSY parameters are equal.

In contrast to all other MSSM scenarios, in the low-m_H scenario the heavy scalar Higgs boson H sits at 125 GeV and has the properties of the SM like Higgs boson. Thus, there is no low $\tan\beta$ excluded region like in all other MSSM benchmark scenarios. This scenario is in particular interesting for the light ($m_{H^+} < m_t - m_b$) charged Higgs boson searches which in fact excluded it [17].

The exclusion curves for the MSSM light-stau (a), light-stop (b), τ-phobic (c) scenarios and the 2HDM of type-2 (d) are shown in figure 6.18. The light-stau, light-stop and τ-phobic scenarios shows a bigger low $\tan\beta$ exclusion region than the m_h^{max}, $m_h^{\mathrm{mod+}}$ and $m_h^{\mathrm{mod\text{-}}}$ scenarios due to a higher Higgsino mass. Thus the branching fraction of the pseudoscalar and the heavy scalar Higgs boson decaying to the supersymmetric partners of the gauge bosons, charginos and neutralinos, is reduced, leading to an enhanced branching fraction to tau leptons. The light-stop scenario is only scanned up to $m_A = 600\,\mathrm{GeV}$ due to the assumption $m_H < 2 \cdot m_{\tilde{t}}$ in the cross-section calculations. The τ-phobic shows weaker exclusion power in the high m_A region since there the branching fraction of the light Higgs boson decaying to tau leptons is reduced.

In the benchmark 2HDM of type-2 the mass of little Higgs boson is by definition 125 GeV. The alignment limit $\cos(\beta - \alpha) = 0$, where the light Higgs boson has SM couplings, is excluded at expected -2σ level.

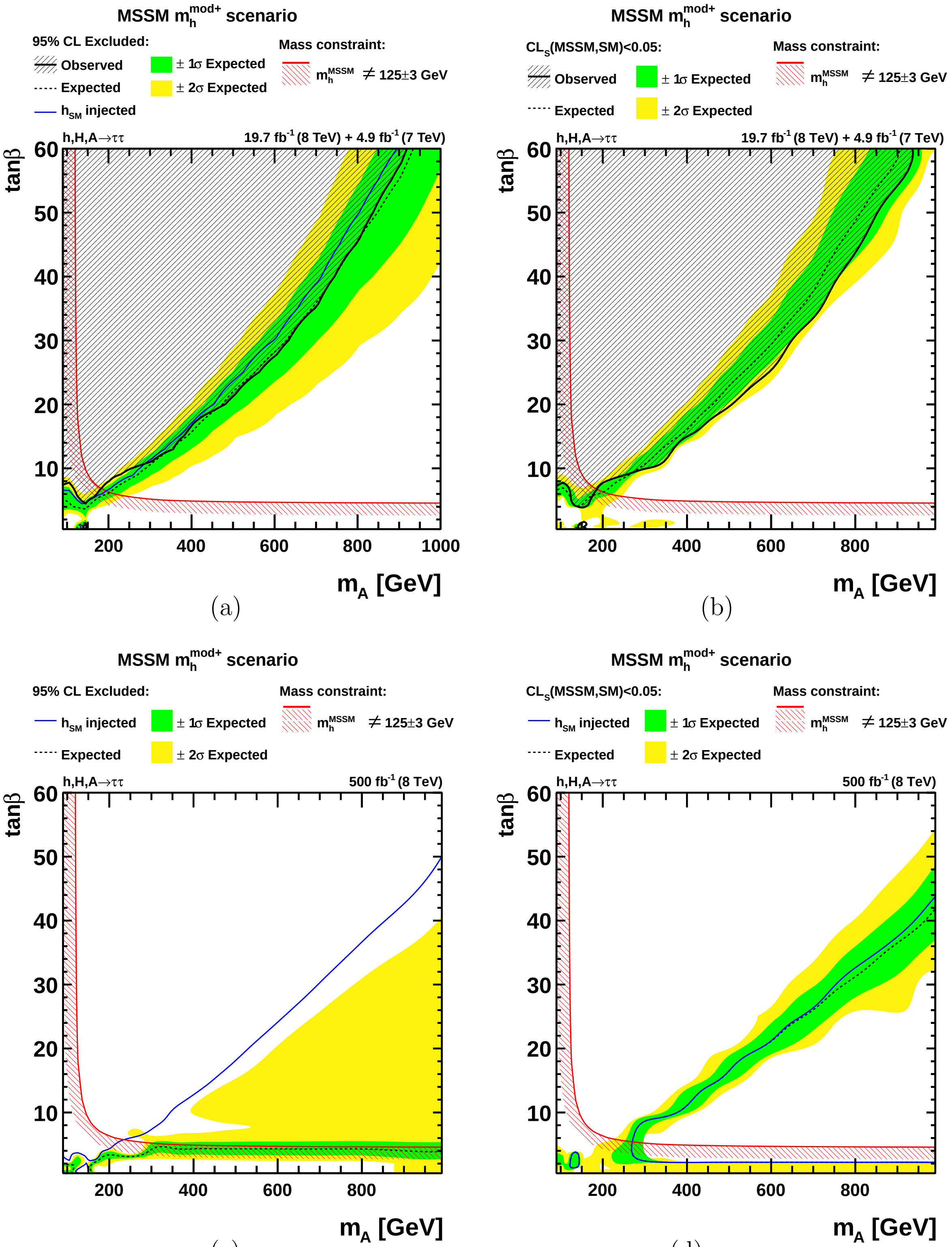

(a) (b) (c) (d)

Figure 6.16: The figures show the 95% Confidence Level exclusion limit on the MSSM $m_h^{\text{mod+}}$ scenario. In figure (a) the H_b hypothesis is tested against the $H_{h+A+H+b}$ hypothesis. Figure (c) shows the same test without the observed limit for a integrated luminosity of 500 fb^{-1}. The test of the $H_{h_{\text{SM}}+b}$ hypothesis against the $H_{h+A+H+b}$ hypothesis is shown in figure (b) and scaled in figure (d). A more detailed explanation is given in the text.

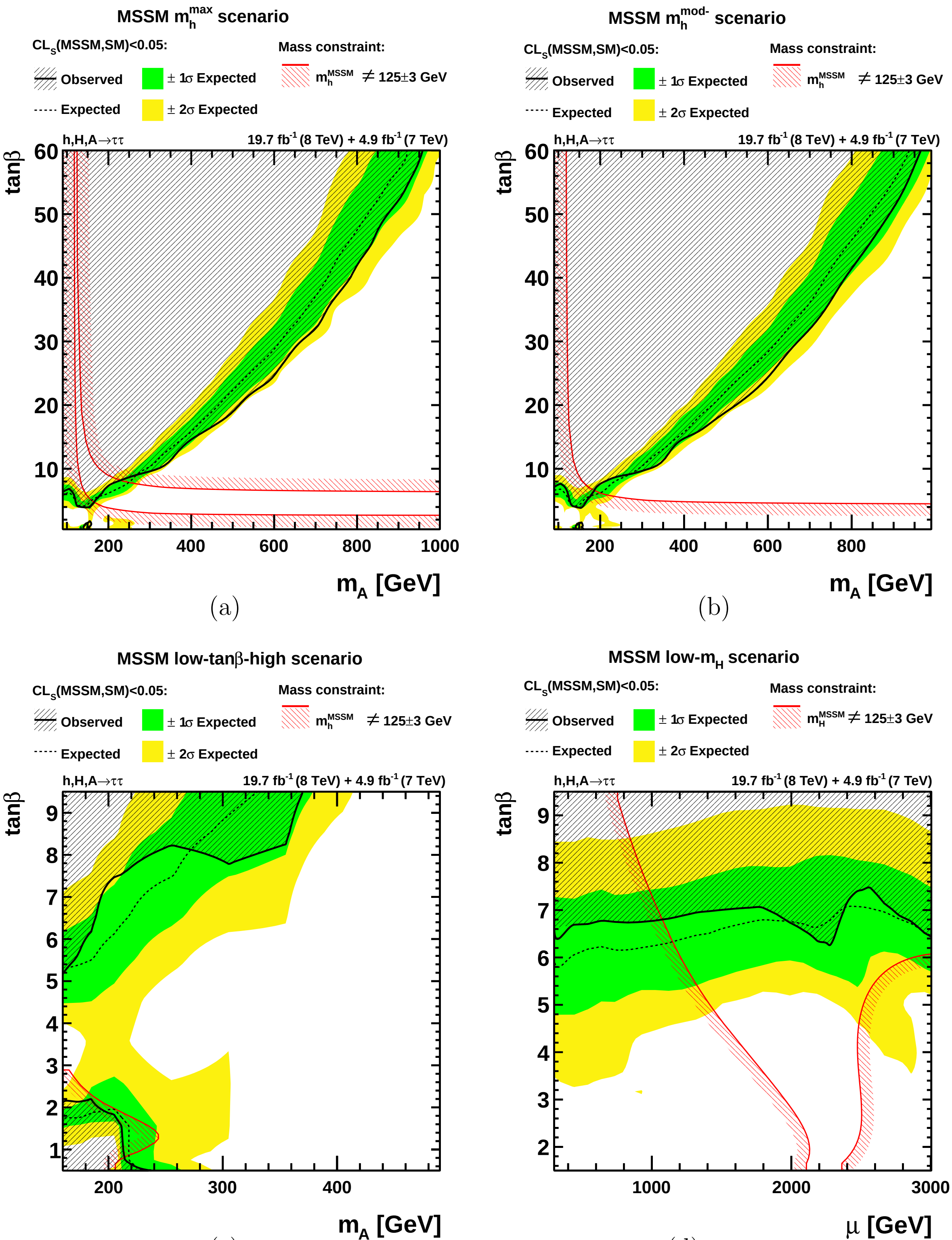

(a) (b)

(c) (d)

Figure 6.17: The figures show the 95% Confidence Level exclusion limit on the MSSM m_h^{max} (a), $m_h^{\text{mod-}}$ (b), low-$\tan\beta$-high (c) and low-m_H (d) scenarios. The region where the SM like Higgs boson is not within $125 \pm 3\,\text{GeV}$ is indicated by the red area. The observed excluded area is shaded with black lines. The median expected limit is plotted as a dashed black line. The expected ±1 and $\pm 2\sigma$ bands are shown as green and yellow bands, respectively. No deviations from the background expectation including the SM Higgs boson is seen.

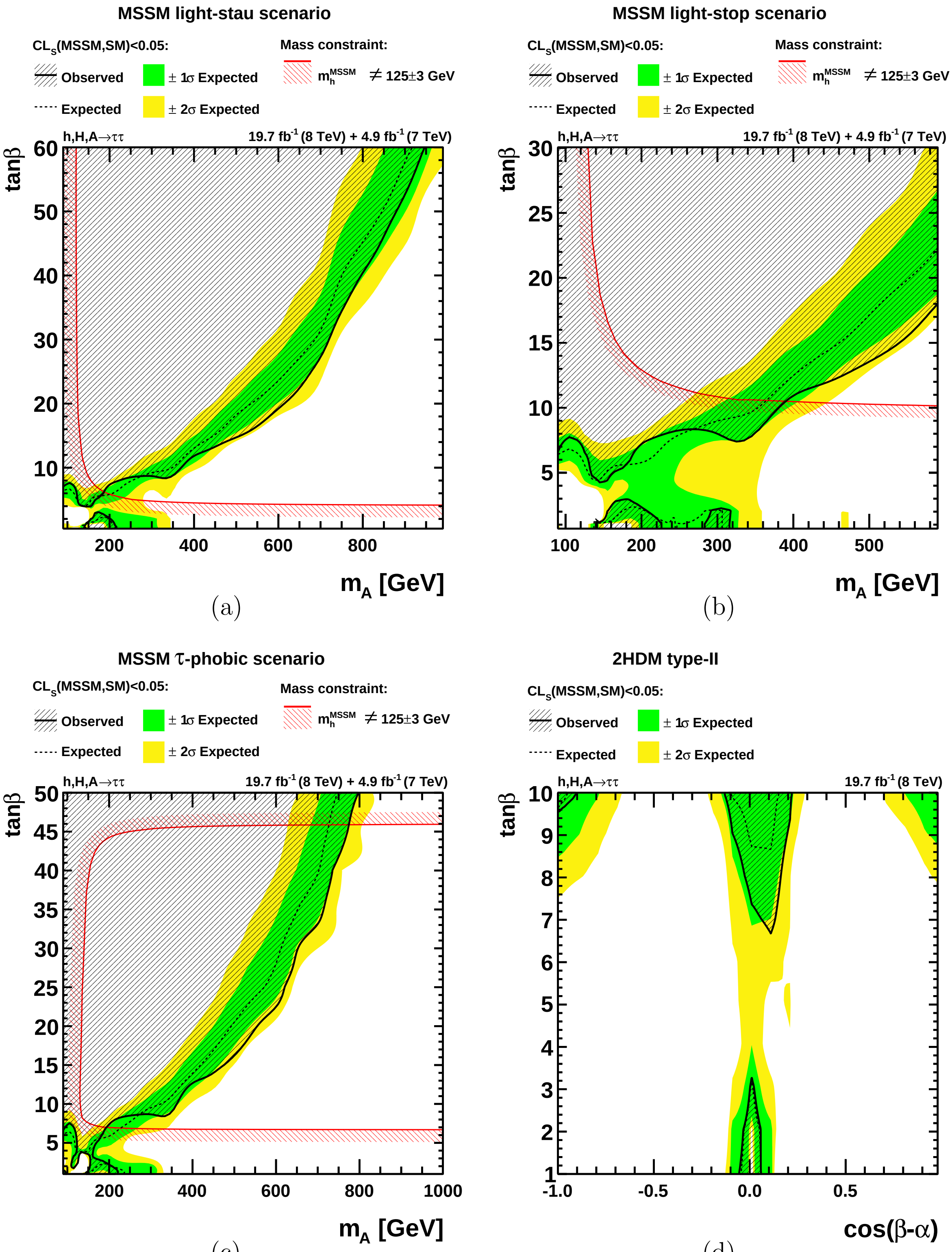

(a) (b) (c) (d)

Figure 6.18: The figures show the 95% Confidence Level exclusion limit on the MSSM light-stop (a), light-stau (b), τ-phobic (c) scenarios and the 2HDM of type-2 (d). The region where the SM like Higgs boson is not within 125 ± 3 GeV is indicated by the red area. The observed excluded area is shaded with black lines. The median expected limit is plotted as a dashed black line. The expected ±1 and ±2σ bands are shown as green and yellow bands, respectively. No deviations from the background expectation including the SM Higgs boson is seen.

Chapter 7

BSM Combination

In this chapter the combination of the $\phi \to \tau\tau$ analysis with other analyses in selected BSM benchmark scenarios will be presented. The considered analyses besides the $\phi \to \tau\tau$ analysis are introduced in section 7.1. The technical approach of the combination is discussed in section 7.2. The results are presented in section 7.3.
It should be stressed that this combination is not only done in order to push the limits further but to explore the frontier of technical and statistical possibilities in order to set the scope for the run 2 data-taking period of the LHC. A combination based on the likelihood model takes all correlations across uncertainties properly into account.

7.1 Other Analyses used in the Combination

For the combination with the $\phi \to \tau\tau$ analysis different analyses are considered. The analyses have to be exclusive, thus without any overlap in the selected events. In addition, the analyses should significantly contribute to the exclusion limit in the combination. The considered analysis besides the $\phi \to \tau\tau$ analysis are introduced in the following. The analysis strategies are summarized. More detailed descriptions can be found here:

- $H^{\pm} \to \tau\nu$: [17]
- $H \to hh \to \tau\tau b\bar{b}$: [18]
- $A \to Zh \to ll\tau\tau$: [18]

This list of analyses could well be extended in future studies.

7.1.1 The Search for charged Higgs Bosons in the $H^{\pm} \to \tau\nu$ Decay Channel in the fully hadronic Final State

The $H^{\pm} \to \tau\nu$ analysis is based on the 2012 dataset which corresponds to 19.7 fb^{-1} of integrated luminosity recorded by the CMS detector. The search for charged Higgs bosons is performed in two different mass regions separated by the mass difference of the top and bottom quark, $m_t - m_b$. Depending whether the mass of the charged Higgs boson is below or above $m_t - m_b$, the charged Higgs boson can be produced in SM $\mathrm{t\bar{b}}$ production where the top decays into a charged Higgs boson and a bottom quark or in top-bottom fusion. In figure 7.1.1 the Feynman diagrams of typical production processes are shown for both signal regions. The analysis is restricted to the decay into a hadronically decaying tau lepton and a tau-neutrino. The hadronically decaying tau lepton and missing transverse energy are used for the online recording of the event.

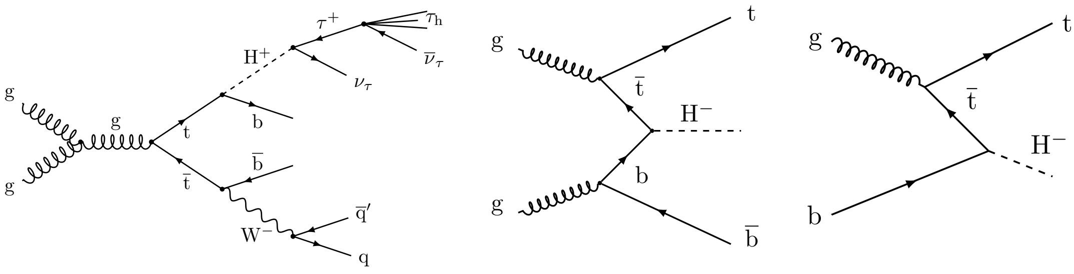

(a) (b) (c)

Figure 7.1: These figures show the production processes which are considered in the $H^\pm \to \tau\nu$ analysis. On figure 7.1(a) the signal process for the $m_{H^\pm} < m_t - m_b$ region is shown. The process is similar to SM $\mathrm{t\bar{t}}$ production with the extension that the top quarks can decay into a charged Higgs bosons in addition to the decay channel into W bosons. In the analysis the process where one top quark decays into a charged Higgs boson and the case where both produced top quarks decay into charged Higgs bosons is considered. In figure 7.1(b) and figure 7.1(c) the signal processes for the high mass regions are shown.

Since the heavy charged Higgs boson exclusion limit shows much weaker exclusion limits as the $\phi \to \tau\tau$ analysis in all considered BSM scenarios, only the light mass regions will be used in the combination. In figure 7.1.1 a comparison between the exclusion limit in the MSSM $m_h^{\mathrm{mod}+}$ scenario of the $\phi \to \tau\tau$ analysis and the heavy charged Higgs boson analysis is shown. Since the efficiency to select SM Higgs bosons using the event selection strategy of the charged Higgs boson analysis, the H_b hypothesis is equivalent to the $H_{h_{\mathrm{SM}}+b}$ hypothesis which includes a SM Higgs boson.

Event selection

The event selection strategy aims to select events as presented in figure 7.1(a).

- One hadronically decaying tau lepton with $p_T > 41\,\mathrm{GeV}$ and $|\eta| < 2.1$. Only the decay channels with one charged hadron are considered (see table 4.2).
- Missing transverse energy $\not{E}_\mathrm{T} > 60\,\mathrm{GeV}$.

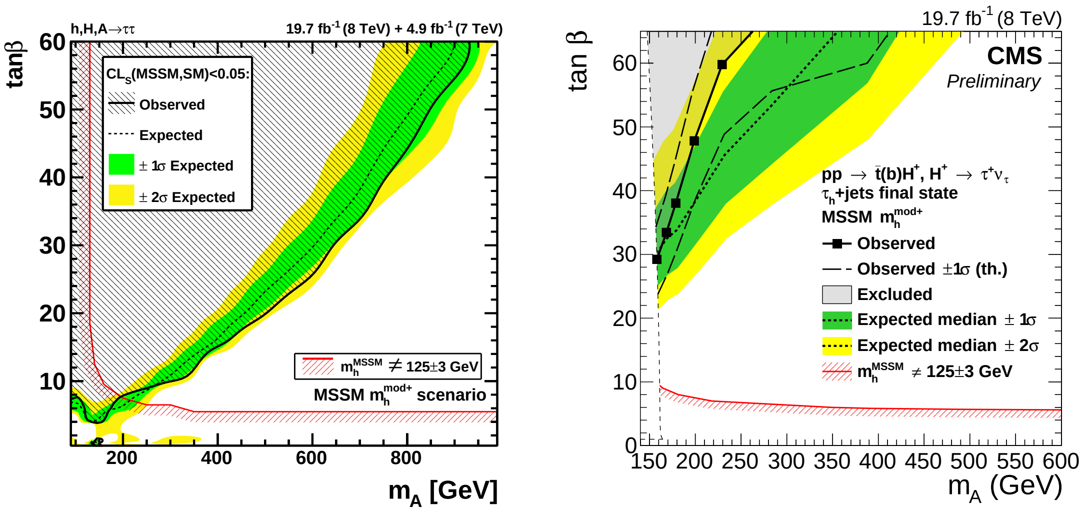

(a) (b)

Figure 7.2: Comparison of the exclusion limit in the MSSM $m_h^{\text{mod}+}$ scenario of the $\phi \to \tau\tau$ analysis on figure 7.2(a) to the heavy charged Higgs boson search on figure 7.2(b). The heavy charged Higgs boson result is taken from [17].

- At least three jets with $p_T > 30\,\text{GeV}$ and $|\eta| < 2.4$.
- At least one of the selected jets has to be identified as a b-jet.
- Events with further leptons that pass lose identification criteria are vetoed.
- Tau leptons coming from W bosons are opposite polarized compared to the ones coming from charged Higgs boson decays. A helicity base variable to suppress $W \to \tau\nu$ events is introduced: $R_\tau = p^{\text{charged hadron}}/p^{\tau_{had}} > 0.7$.
- Variables to suppress the multijet background $R_{\text{bb}}^{\text{min}} > 40°$ and $R_{\text{coll}}^{\text{min}} > 40°$ which protect against mismeasurements of the missing transverse energy in which case the $\vec{\not{E}}_{\text{T}}$ is often aligned with one of the jets or the tau lepton:

$$\begin{aligned} R_{\text{bb}}^{\text{min}} &= \min\left\{\sqrt{\left(\pi - \Delta\phi(\tau_{had}, \vec{\not{E}}_{\text{T}})\right)^2 + \left(\Delta\phi(\text{jet}_n, \vec{\not{E}}_{\text{T}})\right)^2}\right\} \\ R_{\text{coll}}^{\text{min}} &= \min\left\{\sqrt{\left(\Delta\phi(\tau_{had}, \vec{\not{E}}_{\text{T}})\right)^2 + \left(\pi - \Delta\phi(\text{jet}_n, \vec{\not{E}}_{\text{T}})\right)^2}\right\} \end{aligned} \tag{7.1}$$

Background estimation

The $H^\pm \to \tau\nu$ analysis suffers from three different kinds of backgrounds which are handled in different ways.

- **Multijet events**:
  Background from multijet events with high missing transverse energy and jets that have been misidentified as hadronically decaing tau leptons. It is suppressed using the variables $R_{\mathrm{bb}}^{\mathrm{min}}$ and $R_{\mathrm{coll}}^{\mathrm{min}}$ described above. The fake-rate technique as used in the $e\mu$ channel described in section 4.4.2 is used to estimate the background yield and shape.

- **Electroweak processes and $\mathrm{t\bar{t}}$ production with τ_{had}**:
  This background is measured using the embedding technique. In a control data sample μ+jets events are selected. The muons are replaced by simulated hadronically decaying tau leptons.

- **Electroweak processes and $\mathrm{t\bar{t}}$ production without τ_{had}**:
  This background arises from events with jets which have been misidentified as hadronic decaying tau leptons. Monte Carlo predictions have been used to estimate this background.

Results

The transverse mass, m_T, is used as the final discriminator between signal and background distributions. In the low mass region the signal samples are scaled to the $\mathrm{t\bar{t}}$ SM production cross-section. A model independent limit is calculated on the signal strength modifier $r = \mathcal{B}(t \to H^{\pm}b) \cdot \mathcal{B}(H^{\pm} \to \tau^{\pm}\nu)$. Depending on the tested value of r the simulated $\mathrm{t\bar{t}}$ background process, the single charged Higgs boson production and the double charged Higgs boson production have to be rescaled differently. Therefore, the $r \cdot s + b$ term in the likelihood function (5.2) is replaced by

$$r^2 \cdot s(H^{\pm}H^{\mp}) + 2r(1-r) \cdot s(H^{\pm}W^{\mp}) + (1-r)^2 \cdot s(W^{\pm}W^{\mp}) + b \ , \tag{7.2}$$

where b corresponds to all background expectations except for the simulated $\mathrm{t\bar{t}}$ process. Note that the embedded $\mathrm{t\bar{t}}$ background is data driven and therefore does not need to be rescaled. The obtained limit on $\mathcal{B}(t \to H^{\pm} + b) \cdot \mathcal{B}(H^{\pm} \to \tau^{\pm}\nu)$ is presented in figure 7.3(a).

In order to obtain limits in different benchmark scenarios, the model dependent limits are translated into the considered parameter space. Therefore, the model independent limits are recalculated adding a theory uncertainty of 21%, which accounts for missing higher order corrections in the theory cross-section calculations and pdf uncertainties. Afterwards, the branching fractions in the considered BSM parameter space are scanned and compared to the branching fraction exclusion limit as obtained in the model independent procedure. If the calculated branching fraction is above the exclusion limit the considered point in the model parameter space is excluded. Note that this approach of obtaining model dependent limits significantly differs from the one used in the $\phi \to \tau\tau$ analysis as described in section 6.4. It only works since only one Higgs boson is searched for. Compared to the $\phi \to \tau\tau$ analysis the expected signal yields in the model dependent search does not consist of different Higgs bosons but only one and therefore can be compared to the one from the model independent single narrow resonance search. The results for the low mass analysis are shown in figure 7.3(b). The white space on the right side of the dashed line has been excluded from limit calculation since the charged Higgs mass is not well below $m_t - m_b$ and for higher charged Higgs boson masses heavy and light charged Higgs boson production processes, see figure 7.1.1, interfere and theoretical cross-sections and branching fractions are become unstable. The minimum exclusion power is obtained for $\tan\beta \approx 7.8$, since the coupling of the top quark to the bottom quark and charged Higgs boson is proportional to $\cot\beta + \tan\beta \cdot \mathcal{B}(t \to H^{\pm} + b)$.

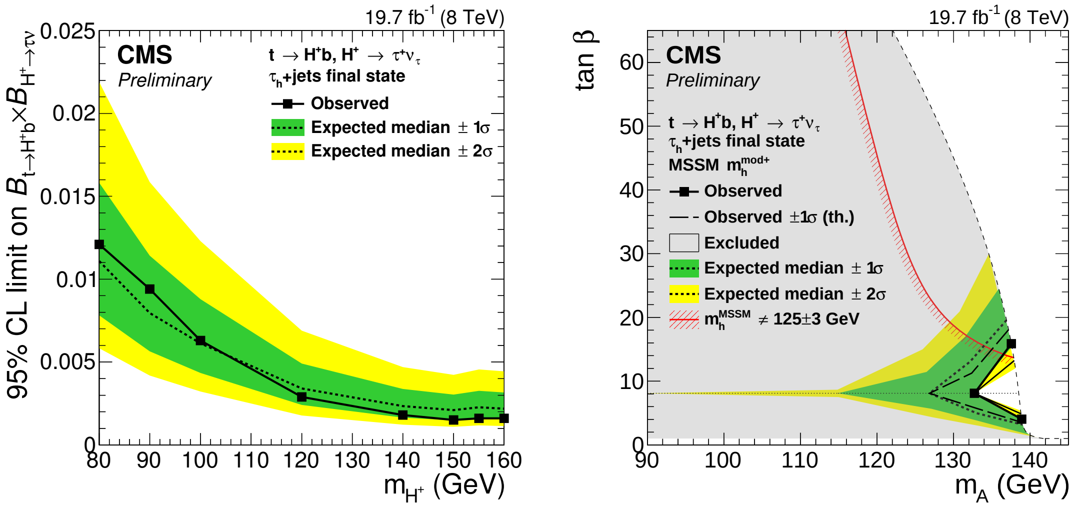

(a) (b)

Figure 7.3: Expected range and observed 95% confidence level upper limits on $\mathcal{B}(t \to H^{\pm}b) \cdot \mathcal{B}(H^{\pm} \to \tau^{\pm}\nu)$ obtained by the low mass $H^{\pm} \to \tau\nu$ analysis are shown in figure 7.3(a). The interpretation of the limits in the MSSM $m_h^{\mathrm{mod}+}$ scenario is shown in figure 7.3(b). Note that in figure 7.3(a) the limit is set on the mass of the charged Higgs boson while in figure 7.3(b) the limit is translated into m_A dependent limits. The figures are taken from [17].

7.1.2 The Search for a Higgs Boson decaying to a pair of 125 GeV Higgs bosons with Tau Leptons in the Final State

The $H \to hh \to b\bar{b}\tau\tau$ analysis is aimed for heavy Higgs bosons which decay into SM like Higgs bosons (at 125 GeV) which decay further to a pair of bottom quarks and a pair of tau leptons. Since the coupling to down-type fermions increase with $\tan\beta$ and therefore the branching fraction to bosons or up-type fermions is reduced the low-$\tan\beta$ region is interesting for this analysis. The low-$\tan\beta$-high scenario is in particular designed for this search by tuning the Higgsino mass parameter in order to increase the masses of the superpartners of the gauge bosons that decays of the heavy scalar Higgs boson to these particles are not allowed leading to higher branching fractions of the decay into light Higgs bosons. In the following, the analysis strategy, which is similar to the $\phi \to \tau\tau$ one, will be explained briefly. The search is based on the full dataset of 2012 recorded by the CMS detector which corresponds to 19.7 fb^{-1} of integrated luminosity at a center-of-mass energy of 8 TeV.

Event selection

Three different channels, $e\tau_{had}$, $\mu\tau_{had}$ and $\tau_{had}\tau_{had}$, are considered. The event selection for these channels are the same as for the $\phi \to \tau\tau$ analysis described in section 4.2. The only addition is that at least two jets with $p_T > 20GeV$ in $|\eta| < 2.4$ are required per event. Furthermore, each channel is separated into three categories:

- **2jet-0tag**:
  This category does not contain any b-tagged jet as defined by the medium working point of the Combined Secondary Vertex b-tagging algorithm. It is the least sensitive category.
- **2jet-1tag**:
  One of the selected jets passes the medium working point.
- **2jet-2tag**:
  Two jets pass the medium working point.

Background estimation

Since this analysis is very similar to the $\phi \to \tau\tau$ analysis the same backgrounds occur and similar background estimation techniques are used.

- **t$\bar{\text{t}}$**:
  The dominant background in this analysis is t$\bar{\text{t}}$ production. It is estimated from Monte Carlo predictions and cross checked in t$\bar{\text{t}}$ enhanced control regions.
- **QCD**:
  The QCD background is estimated in the same way as described in section 4.4.2. Note that the estimation in the $e\tau_{had}$ and $\mu\tau_{had}$ channels differs from the one used in the fully hadronic $\tau_{had}\tau_{had}$ channel.

- **Z→ $\tau\tau$**:
  Even thought the requirement of at least two jets reduces the background significantly it remains still important. The data-driven embedding technique is used, see section 4.4.1.

- **W+jets**:
  In the $e\tau_{had}$ and $\mu\tau_{had}$ channel this background is important due to the non negligible jet→ τ_{had} misidentification rate. The shape is estimated from Monte Carlo simulations. The rate is obtained in a W+jets control region. In the $\tau_{had}\tau_{had}$ channel the background is smaller and thus fully estimated by Monte Carlo simulation.

- **Dibosons and single-top**:
  These backgrounds are small. Monte Carlo simulations are used to estimate these backgrounds.

Results

In the $H \to hh \to \tau\tau b\bar{b}$ analysis the four body mass, $m_{b\bar{b}\tau\tau}$, is reconstructed by a kinematic fit. It is used as the final discriminator between background and signal distributions. To further enhance the sensitivity mass cuts of $70 < m_{b\bar{b}} < 150\,\text{GeV}$ and $90 < m_{b\bar{b}} < 150\,\text{GeV}$ are used, where the invariant di-τ mass has been reconstructed using the SVFit algorithm as described in section 4.1.9.
Since no significant deviation between the background expectation and the observation have been found upper limits have been set. In figure 7.4(a) the model independent limits on $\sigma(\text{ggH})\cdot\mathcal{B}(\to\text{hh})\cdot\mathcal{B}(\to b\bar{b}\tau\tau)$ are presented. The results are interpreted in the MSSM low-tan β-high scenario, figure 7.4(b), and the benchmark type-2 2HDM, figure 7.4(c). There are no simulated mass samples available for $m_H < 260\,\text{GeV}$ and $m_H > 350\,\text{GeV}$. In the MSSM low-tan β-high scenario this region is indicated by the gray dashed lines. Outside of these lines no limit has been calculated. The sudden drop of the exclusion limit for low $\tan\beta$ is due to a sudden drop in the branching fraction of the $h \to \tau\tau$ and $h \to b\bar{b}$ decays. Elsewhere, the expected exclusion limit follows the gg$H$ cross-section and branching fraction of the heavy scalar Higgs boson decaying to a pair of light scalar Higgs boson. The cross-section decreases with increasing m_A and increasing $\tan\beta$. In contrast, the branching fraction has its maximum around $m_A = 320\,\text{GeV}$ and $\tan\beta = 1.3$ leading to the shape of the expected exclusion limit. In the benchmark type-2 2HDM the exclusion limit follows the branching fractions and the gg$H$ cross-section. The sharp edges, for example at the left side of the top left, are caused due sudden drops of either $\mathcal{B}(h \to \tau\tau)$ or $\mathcal{B}(H \to hh)$.
The analysis tests the H_b hypothesis against a BSM signal hypothesis, H_{H+b}. The SM Higgs boson at 125 GeV is not considered in the background hypothesis, since there is negligible small sensitivity to the SM Higgs boson.

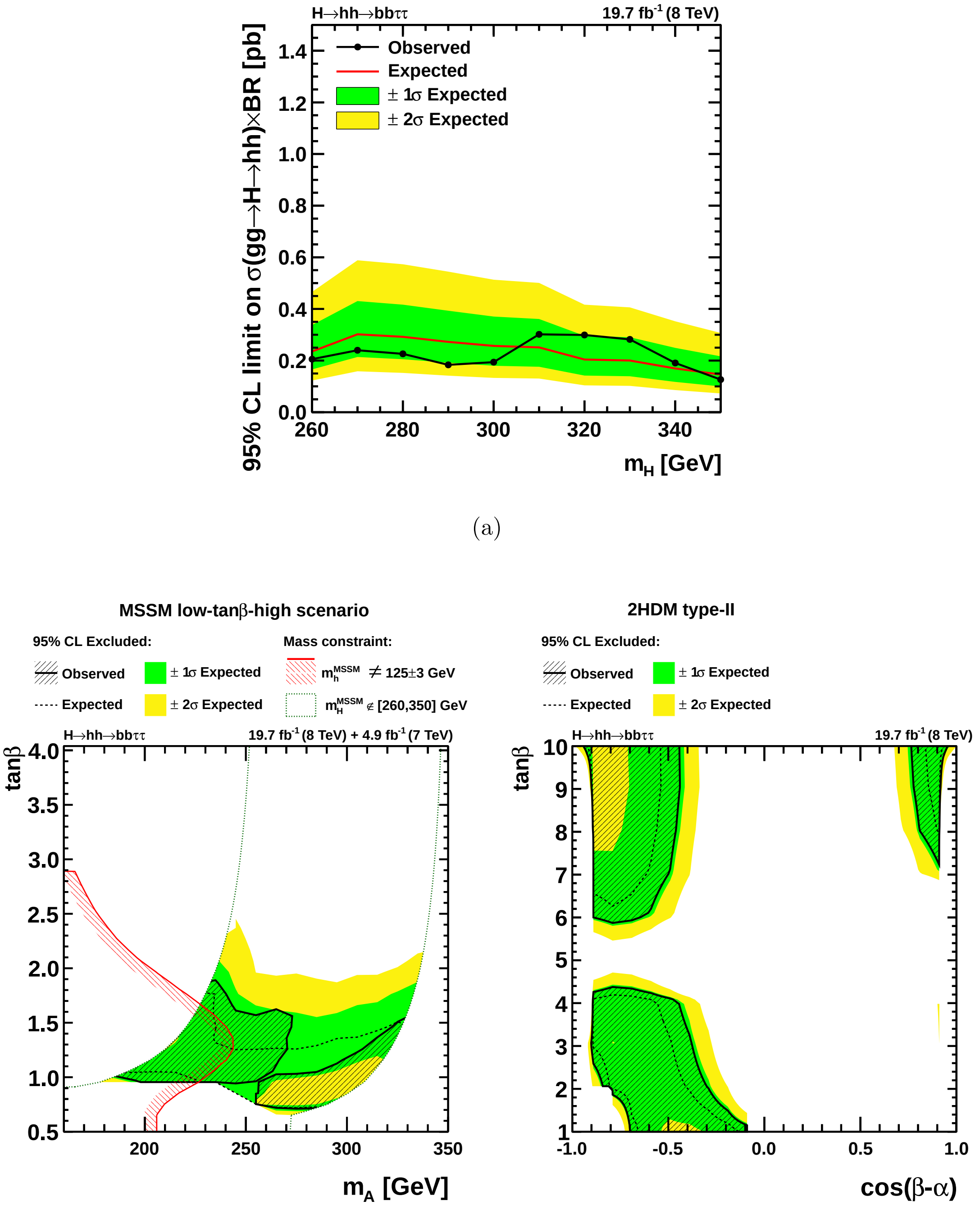

(a)

(b)

(c)

Figure 7.4: Expected and observed 95% confidence level upper limits on σ(ggH)$\cdot\mathcal{B}$(→hh)$\cdot\mathcal{B}$(→ $b\bar{b}\tau\tau$) obtained by the $H \rightarrow hh \rightarrow b\bar{b}\tau\tau$ analysis are given in figure 7.4(a). The interpretation in the MSSM low-tan β-high scenario is presented in figure 7.4(b). Between the grey dashed lines the mass of the heavy scalar Higgs boson is between 260 and 350 GeV which corresponds to the available simulated mass samples. Outside these lines no limits have been set. In figure 7.4(c) the interpretation in the 2HDM of type-2 is shown.

7.1.3 The Search for a Higgs Boson decaying to Zh with Tau Leptons in the Final State

The $A \to Zh \to ll\tau\tau$ analysis is based on the 8 TeV dataset of 19.7 fb^{-1} of integrated luminosity recorded by the CMS detector in the year 2012. In BSM scenarios the decay of a pseudoscalar Higgs boson to a Z boson and a SM like Higgs boson at 125 GeV is possible.

Event Selection

The analysis is restricted to the final state where the Z boson decays to either electrons or muons and where the SM like Higgs boson decays into tau leptons. Depending on the decay of the Z boson and the decay of the tau lepton different channels are constructed: $ee + e\mu$, $\mu\mu + e\mu$, $ee + e\tau_{had}$, $\mu\mu + e\tau_{had}$, $ee + \mu\tau_{had}$, $\mu\mu + \mu\tau_{had}$, $ee + \tau_{had}\tau_{had}$ and $\mu\mu + \tau_{had}\tau_{had}$.

- The Z boson is reconstructed by two well defined and isolated opposite sign leptons, either electrons in $|\eta| < 2.5$ or muons in $|\eta| < 2.4$ with $p_T > 20$ GeV and $p_T > 10$ GeV respectively for the leading and subleading lepton. The invariant mass of the same flavour and opposite sign lepton pair should be around the Z boson mass, $60 < m_{ll} < 120$ GeV.

- The electrons, muons or hardonically decaying tau leptons coming from the $h \to \tau\tau$ decay are required to have $p_T > 10$ GeV in $|\eta| < 2.5$, $p_T > 10$ GeV in $|\eta| < 2.4$ or $p_T > 21$ GeV in $|\eta| < 2.3$, respectively.

- A cut on the scalar sum of the transverse momentum of the legs of the $h \to \tau\tau$ decay is applied. It is tuned to maximize the sensitivity of the analysis in the considered mass range between 220 GeV and 350 GeV and depends on the channel.

- To reduce $\mathrm{t\bar{t}}$ background a b-jet veto is applied.

- The four final state objects have to be separated by $\Delta R > 0.5$ from each other.

Background Estimation

The backgrounds in the $A \to Zh \to ll\tau\tau$ analysis are separated into irreducible backgrounds which yield the same final state as the signal and reducible backgrounds which arise from processes with misidentified objects.

- **Irreducible backgrounds**:
  This background component consists mainly of rare processes like triboson events, ZZ, $\mathrm{t\bar{t}Z}$ and SM Higgs boson producton in association with a Z boson. All irreducible backgrounds are estimated fully relying on Monte Carlo simulations and checked in control regions.

- **Reducible backgrounds**:
  The main backgrounds of this component are Z+jets and WZ+jets events. They are estimated by measuring the probability that a jet is misidentified as a lepton in a signal free region and applying the misidentification rate to control regions where the backgrounds are enriched. The shape of the backgrounds are obtained from signal free regions with same sign tau lepton candidates with relaxed isolation criteria.

Results

The mass of the pseudoscalar Higgs boson is reconstructed by combining the Z boson mass and the invariant di-τ mass, which has been reconstructed using the SVFit algorithm (see section 4.1.9). The reconstructed mass is used as the final discriminator between signal and background distributions. No significant deviation between data and the background expectation has been observed and therefore upper limits have been set. In figure 7.5(a) model independent limits on $\sigma(\mathrm{ggA})\cdot\mathcal{B}(\to\mathrm{Zh})\cdot\mathcal{B}(\to ll\tau\tau)$ are presented. Model dependent limits on the MSSM low-$\tan\beta$-high scenario and on the type-2 2HDM are shown in figure 7.5(b) and 7.5(c), respectively. The gg$A$ cross-section is flat in the considered m_A range. It decreases for increasing $\tan\beta$. $\mathcal{B}(A \to Zh)$ is maximal for $m_A = 250\,\mathrm{GeV}$ to $300\,\mathrm{GeV}$ and $\tan\beta = 1.3$. It decreases for increasing $\tan\beta$ and drops for $m_A > 340\,\mathrm{GeV}$. The not excluded region for low m_A and low $\tan\beta$ comes from a reduced $\mathcal{B}(h \to \tau\tau)$ as also seen in the $H \to hh \to b\bar{b}\tau\tau$ results in figure 7.4(b). The exclusion limit in the type-2 2HDM benchmark scenario follow the cross-section and the branching fractions. The sharp edges are due to sudden drops in $\mathcal{B}(A \to Zh)$ or $\mathcal{B}(H \to hh)$.

The analysis includes associated production of the SM Higgs boson to their background estimation. Therefore, this process is part of signal hypothesis and also of the background hypothesis.

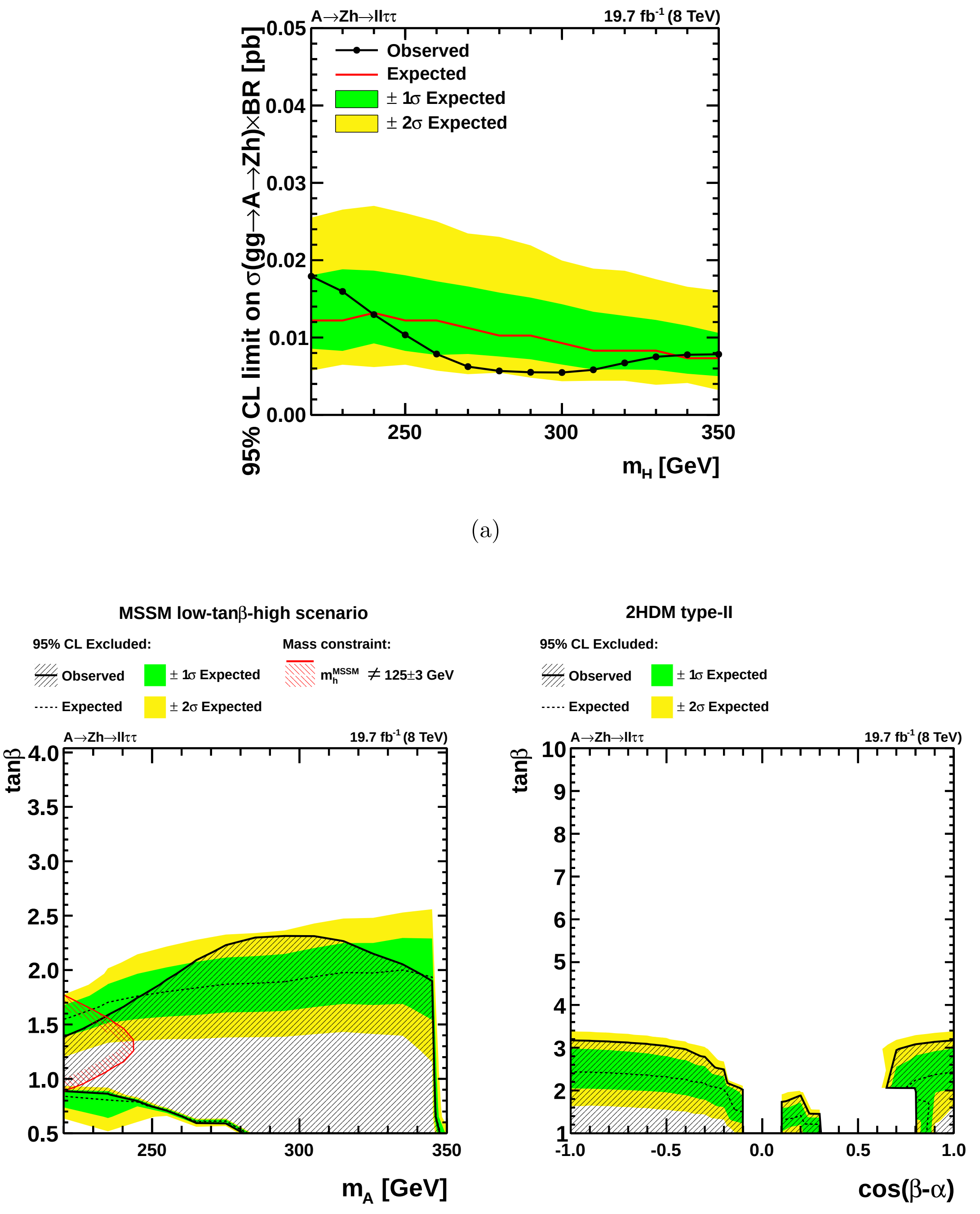

(a)

(b)

(c)

Figure 7.5: Expected and observed 95% confidence level upper limits on $\sigma(\text{ggA})\cdot\mathcal{B}(\to\text{Zh})\cdot\mathcal{B}(\to ll\tau\tau)$ obtained by the $A \to Zh \to ll\tau\tau$ analysis is given in figure 7.5(a). The interpretation in the MSSM low-tan β-high scenario is presented in figure 7.5(b). In figure 7.5(c) the interpretation in the benchmark 2HDM of type-2 is shown.

7.2 Technical Approach of the Combination

Judging only by the excluded parameter space in the considered BSM scenarios the $\phi \to \tau\tau$ analysis yields stronger limits than the above presented analyses. But the different searches are sensitive in different regions of the parameter space and therefore a combination can significantly increase the exclusion contour. Since a combination is computing intensive only those analyses are considered for the combination with the $\phi \to \tau\tau$ analysis which will have an effect on the excluded parameter space in the considered BSM scenario. In table 7.1 the considered analyses for each BSM scenario are listed.

The selection of considered analyses as well as the considered BSM scenarios can be extended in future analyses when these analyses gain sensitivity. The $\phi \to \tau\tau$ analysis is used over the whole parameter space in all models. In the MSSM $m_h^{\text{mod}+}$ scenario the $H^\pm \to \tau\nu$ analysis is considered in the parameter space with $m_A \leq 140\,\text{GeV}$ and $\tan\beta < 10$ to ensure that the charged Higgs boson mass is well below the mass difference between the top and the bottom quark. In the MSSM low-$\tan\beta$-high scenario the $H \to hh \to b\bar{b}\tau\tau$ analysis is considered in the mass region with $260 \leq m_H \leq 350$ and $\tan\beta \leq 4$ where full simulated signal Monte Carlo samples are available. The $A \to Zh \to ll\tau\tau$ is used in the mass range $220 \leq m_A \leq 350\,\text{GeV}$ and $\tan\beta \leq 4$. Both scenarios have no sensitivity for $\tan\beta > 4$. In the benchmark 2HDM of type-2 the full parameter space is covered by all three considered analyses, since in this model the masses of the pseudoscalar and heavy scalar Higgs boson both sit at 300 GeV (the little scalar Higgs boson has $m_h = 125\,\text{GeV}$).

BSM scenario	$\phi \to \tau\tau$	$H^\pm \to \tau\nu$	$H \to hh \to b\bar{b}\tau\tau$	$A \to Zh \to ll\tau\tau$
MSSM $m_h^{\text{mod}+}$	×	×	-	-
MSSM low-$\tan\beta$-high	×	-	×	×
2HDM type-2	×	-	×	×

Table 7.1: Listed are the analyses considered for the combination with the $\phi \to \tau\tau$ analysis depending on the BSM scenario.

7.2.1 Overlap Checks

Next to the selection of the scenarios, the considered analyses have to be checked for possible overlap. Double counted events are problematic to handle in the statistical approach and will lead to results which are hard to interpret. Therefore, it is of importance for a combination that the considered analyses do not select the same events.

- **$H^\pm \to \tau\nu$**:
  There is no overlap with other analyses. Events from the other analyses do not pass the event selection mainly due to the veto in additional leptons apart from the one produced in the searched charged Higgs boson decay.

- $\boldsymbol{H \to hh \to b\bar{b}\tau\tau}$:
  2% of the events in the no-b-tag category have an overlap with the 2jet-0tag event category. Vice versa all events of the 2jet-0tag event category are also part of the no-b-tag category. Thus, the 2jet-0tag category is dropped. The exclusion limit is not effected much, since this category is the least sensitive. Of all events in the 2jet-1tag or 2jet-2tag category 25% (12%) also fall in b-tag category. The overlap is due to the difference in the transverse momentum requirement of the jets: $p_T > 30\,\mathrm{GeV}$ for the $\phi \to \tau\tau$ analysis and $p_T > 20\,\mathrm{GeV}$ for the $H \to hh \to b\bar{b}\tau\tau$ analysis. This overlap is too high to be neglected in the combination with the $\phi \to \tau\tau$ analysis. Therefore, the jet p_T requirement of the $H \to hh \to b\bar{b}\tau\tau$ is raised to $p_T > 30\,\mathrm{GeV}$ for at least two jets while the pseudorapidity cut on the jets is relaxed from $|\eta| < 2.4$ to $|\eta| < 4.7$ as it is used in the $\phi \to \tau\tau$ analysis. There is no overlap with the $H^{\pm} \to \tau\nu$ and the $A \to Zh \to ll\tau\tau$ analysis.

- $\boldsymbol{A \to Zh \to ll\tau\tau}$:
  No overlap with any other analyses is found. The selection of four leptons is rejected by all other analyses due to a veto on additional leptons apart from the ones in the final states. The identification and isolation criteria for the veto cut on additional leptons is less stringent than the cuts on the leptons in the $A \to Zh \to ll\tau\tau$ analysis.

7.2.2 Statistical Approach

Systematic and statistical uncertainties are treated either fully correlated or uncorrelated as explained in chapter 5. Since the $\phi \to \tau\tau$ analysis has the strongest exclusion limits and is part in each combination depending on the BSM scenario it is viewed to be the main analysis and uncertainties of other analyses will be discussed with respect to the $\phi \to \tau\tau$ analysis.

- $\boldsymbol{H^{\pm} \to \tau\nu}$:
  Uncertainties on commonly used objects, like hadronic decaying tau leptons, as well as the uncertainty on the integrated luminosity, are correlated. Uncertainties on the backgrounds are treated uncorrelated due to the different backgrounds and due to different background estimation methods.
  The Barlow-Beeston method, as introduced in section 4.5.2, is used to create a uncertainty for each background in each bin of the final discriminator shape, m_T. The statistical uncertainties are treated uncorrelated.

- $\boldsymbol{H \to hh \to b\bar{b}\tau\tau}$:
  The analysis is very similar to the $\phi \to \tau\tau$ analysis with respect to event selection and background estimation as can be seen in section 7.1.2. As a consequence the event categories in the $H \to hh \to b\bar{b}\tau\tau$ analysis can be viewed as an extension to the categories in the $\phi \to \tau\tau$ analysis. Therefore, all systematic uncertainties are treated in the same way as described in section 4.5.1. In particular uncertainties on the same backgrounds can be correlated among categories, channels or periods. The uncertainty on the integrated luminosity

is fully correlated among channels and categories.
Statistical uncertainties are treated using the Barlow-Beeston method, as described in section 4.5.2, over the whole range with the difference to the $\phi \rightarrow \tau\tau$ analysis that all backgrounds in each bin in a histogram are combined and thus each bin only gets one uncertainty in contrast to the $\phi \rightarrow \tau\tau$ analysis where one uncertainty for each background is added. This has only little effect on the limits but a bigger effect on the computing time of the limit calculation. Statistical uncertainties are treated uncorrelated.

- $\boldsymbol{A \rightarrow Zh \rightarrow ll\tau\tau}$:
  Backgrounds differ from the ones used in the $\phi \rightarrow \tau\tau$ analysis and therefore uncertainties on the backgrounds are not treated correlated in the combination. Differently, the object selection is similar and uncertainties based on the objects, like electron or muon efficiencies, are handled fully correlated. The uncertainty on the integrated luminosity is fully correlated among channels and categories.
  The Barlow-Beeston method, see section 4.5.2, is used to obtain statistical uncertainties on each background in each bin of the final discriminator ($m_{ll\tau\tau}$) distribution in analogy to way it is done in the $\phi \rightarrow \tau\tau$ analysis. All statistical uncertainties are uncorrelated.

More details on the uncertainties used in the different analyses can be found in the respective papers [17; 18].

The combination of different analyses is only possible in well defined models. All parameters in a benchmark scenario, including the two variable parameters of the model (e.g. m_A and $\tan\beta$), have to be fixed since ratios between expectations of different signal processes are defined by the considered point in the parameter space of the model. Letting the signal processes float relative to each other may work technically, but would have non physical meaning in the sense that this does not represent a well defined theory. At each point in the parameter space of a considered model the signal expectation, which can be a combination of multiple Higgs bosons, has to be calculated as explained in section 6.4. This approach is already used for the results of all analyses except the $H^\pm \rightarrow \tau\nu$ analysis. As mentioned in section 7.1.1 it is not possible to use the model dependent limit setting method as used in the $H^\pm \rightarrow \tau\nu$ analysis for a search for multiple Higgs bosons. A model independent limit on a single narrow resonance can not be translated into a model dependent limit on a BSM benchmark scenario which at each point consists of multiple Higgs bosons. The full likelihood model is needed to take all correlation correctly into account. Therefore, the combination is performed on the likelihood model level. In figure 7.2.2 a comparison between the official $H^\pm \rightarrow \tau\nu$ and the reconstructed results, using the approach as in the other analyses, is shown. For the combination only the region $\tan\beta < 10$ and $m_A < 140\,\text{GeV}$ is used to ensure that the charged Higgs boson mass is below 160 GeV and therefore well below $m_t - m_b$. In the method as used in the $\phi \rightarrow \tau\tau$ analysis the two dimensional plane is scanned. That means that at each tested point the signal expectation is fixed to the expected value and the signal strength modifier is set to one. The point is then marked as excluded or not. The exact position of the exclusion limit is obtained by interpolation between nearby excluded and not excluded points. Thus, interpolation errors can shift the exclusion limit, but since the grid in the region where the exclusion limit is expected is finely woven the errors are expected to be small. In contrast, the method used in the $H^{\pm} \to \tau\nu$ analysis performs an extrapolation from the model independent limits to model dependent limits. Here, the signal expectation is fixed to the SM $\mathrm{t\bar{t}}$ production, as described in section 7.1.1. The limit is set on the signal strength modifier which is in units of the branching fraction. Therefore, numerical instabilities for small branching fraction can effect the limit. The differences of the approaches are within the ±1 and $\pm 2\sigma$ error bands. Overall a good agreement is obtained.

The model dependent limits in the $H \to hh \to \bar{b}b\tau\tau$ and the $A \to Zh \to ll\tau\tau$

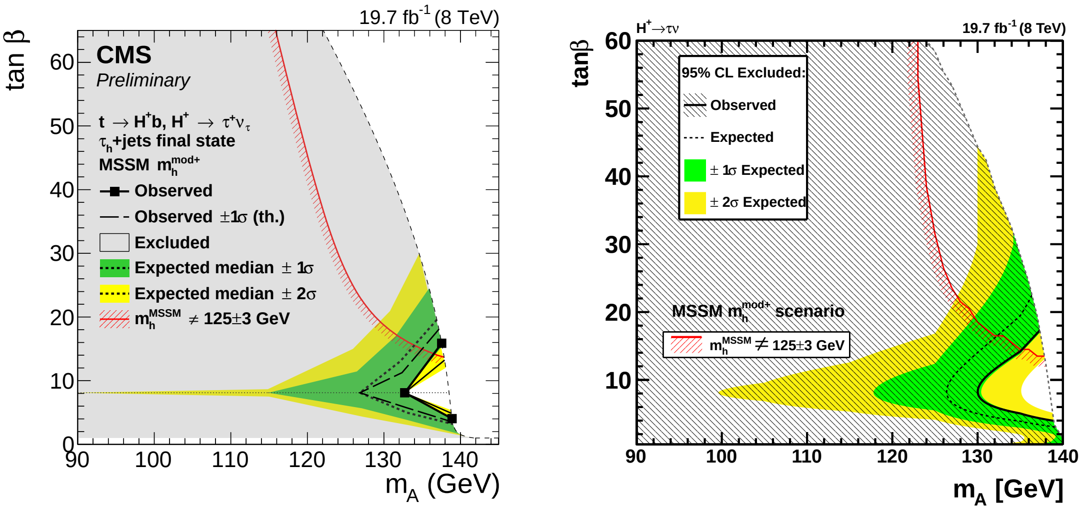

(a) (b)

Figure 7.6: Comparison of the officially published exclusion limit for the $H^{\pm} \to \tau\nu$ analysis and the reconstructed as obtained for the MSSM $m_h^{\mathrm{mod+}}$ scenario. In figure 7.6(a) the result as obtained by translating the model independent branching fraction limits into model dependent limits is shown. In figure 7.6(b) the limit as obtained from a full construction of the likelihood model in the BSM scenario is shown. The white region on the right of the dashed gray line is not plotted since the charged Higgs boson mass is to close to the mass difference of the top and the bottom quark, thus the heavy and light charged Higgs production processes, see figure 7.1.1, interfere and theoretical cross-sections and branching fractions are not reliable. A good agreement between both approaches is obtained. Differences are discussed in the text.

analysis have been obtained using the same method as in the $\phi \to \tau\tau$ analysis.

7.3 Results

The result of the combination of the $\phi \to \tau\tau$ analysis with the $H^{\pm} \to \tau\nu$ analysis in the MSSM $m_h^{\text{mod+}}$ scenario is shown in figure 7.7. The $H_{h_{\text{SM}}+b}$ hypothesis is tested against the MSSM hypothesis including all Higgs bosons, $H_{h+A+H+H^{\pm}+b}$. Therefore, the CL$_\text{s}$ method with the TEV test statistic has been used, as explained in section 6.4.2. The $\phi \to \tau\tau$ analysis is considered in the whole parameter space, whereas the $H^{\pm} \to \tau\nu$ analysis is restricted to $\tan\beta < 10$ and $m_A \leq 140\,\text{GeV}$. For higher $\tan\beta$ no combination is needed because the parameter space is already excluded by the $\phi \to \tau\tau$ analysis. Higher masses are not considered for the $H^{\pm} \to \tau\nu$ analysis either because the mass of the charged Higgs bosons is to close to $m_t - m_b$ or because the exclusion limit of the heavy charged Higgs analysis is dominated by the exclusion of the $\phi \to \tau\tau$ analysis. The effect of the combination is clearly seen. The gap between low and high $\tan\beta$, as shown in the exclusion limit based on the $\phi \to \tau\tau$ analysis only as shown on figure 7.7 (b), is closed for $m_A \leq 140\,\text{GeV}$.

In figure 7.8 the result of the combination in the MSSM low-$\tan\beta$-high scenario of the $\phi \to \tau\tau$ analysis with the $H \to hh \to \bar{b}b\tau\tau$ and the $A \to Zh \to ll\tau\tau$ analyses is shown. The $H_{h_{\text{SM}}+b}$ hypothesis is tested against the $H_{h+A+H+b}$ hypothesis, which includes all neutral Higgs bosons. The $\phi \to \tau\tau$ analysis is considered over the whole mass range. The $H \to hh \to \bar{b}b\tau\tau$ analysis is included for the region $260 \leq m_H \leq 350\,\text{GeV}$ and $\tan\beta \leq 4$. For $\tan\beta > 4$ the $H \to hh \to \bar{b}b\tau\tau$ analysis is insensitive. The $A \to Zh \to ll\tau\tau$ is added to the combination in the region $220 \leq m_A \leq 350\,\text{GeV}$ and $\tan\beta \leq 4$. For higher $\tan\beta$ the analysis becomes insensitive. The high $\tan\beta$ exclusion region is therefore solely a result of the $\phi \to \tau\tau$ analysis. For $\tan\beta \leq 4$ and $m_A > 200\,\text{GeV}$ the contribution of the $H \to hh \to \bar{b}b\tau\tau$ and in particular, the $A \to Zh \to ll\tau\tau$ analysis become visible. The peak in the observed limit at $m_A = 300\,\text{GeV}$ can for example be understood by looking at the individual results of the $A \to Zh \to ll\tau\tau$ analysis (figure 7.8 (b)) and the $\phi \to \tau\tau$ analysis (figure 7.8 (c)).

The result of the combination of the $\phi \to \tau\tau$ analysis with the $H \to hh \to \bar{b}b\tau\tau$ and the $A \to Zh \to ll\tau\tau$ analyses in the benchmark type-2 2HDM is shown in figure 7.9. The $H_{h_{\text{SM}}+b}$ hypothesis is tested against the $H_{h+A+H+b}$ hypothesis. All three analyses are considered over the whole parameter space. The contributions to the combined exclusion limit of each analysis can be seen. Around the alignment limit, $\cos(\beta - \alpha) = 0$, the $\phi \to \tau\tau$ analysis contributes the most, as seen if compared to the standalone result in figure 7.9 (c). Due to statistical fluctuation due to limit number of generated pseudo experiments needed in the creation of the expected limit based on the TEV test statistic, as described in chapter 5, the -2σ exclusion band excludes less than in the $\phi \to \tau\tau$ standalone results around the alignment limit. The excluded region in the bottom left of the parameter space is a result of the combination of the $H \to hh \to \bar{b}b\tau\tau$ and the $A \to Zh \to ll\tau\tau$ results as shown in figure 7.9 (b) and 7.9 (a), respectively. The excluded region in the top left is mainly driven by the $H \to hh \to \bar{b}b\tau\tau$ analysis with a smaller contribution of the $\phi \to \tau\tau$ analysis. In the top right again these both analyses contribute. In the bottom right the $A \to Zh \to ll\tau\tau$ analysis dominates, but the $\phi \to \tau\tau$ and the

$H \rightarrow hh \rightarrow \bar{b}b\tau\tau$ analysis also contribute. At all mentioned regions the combined limit is stronger than a simple addition of the exclusion limits of the three analysis. This is in particular good to see at the bottom right where only the standalone results of the $A \rightarrow Zh \rightarrow ll\tau\tau$ analysis excludes parameter space but the excluded parameter space of the combination is significantly larger.
Numerical results for all three combinations can be found in appendix H.

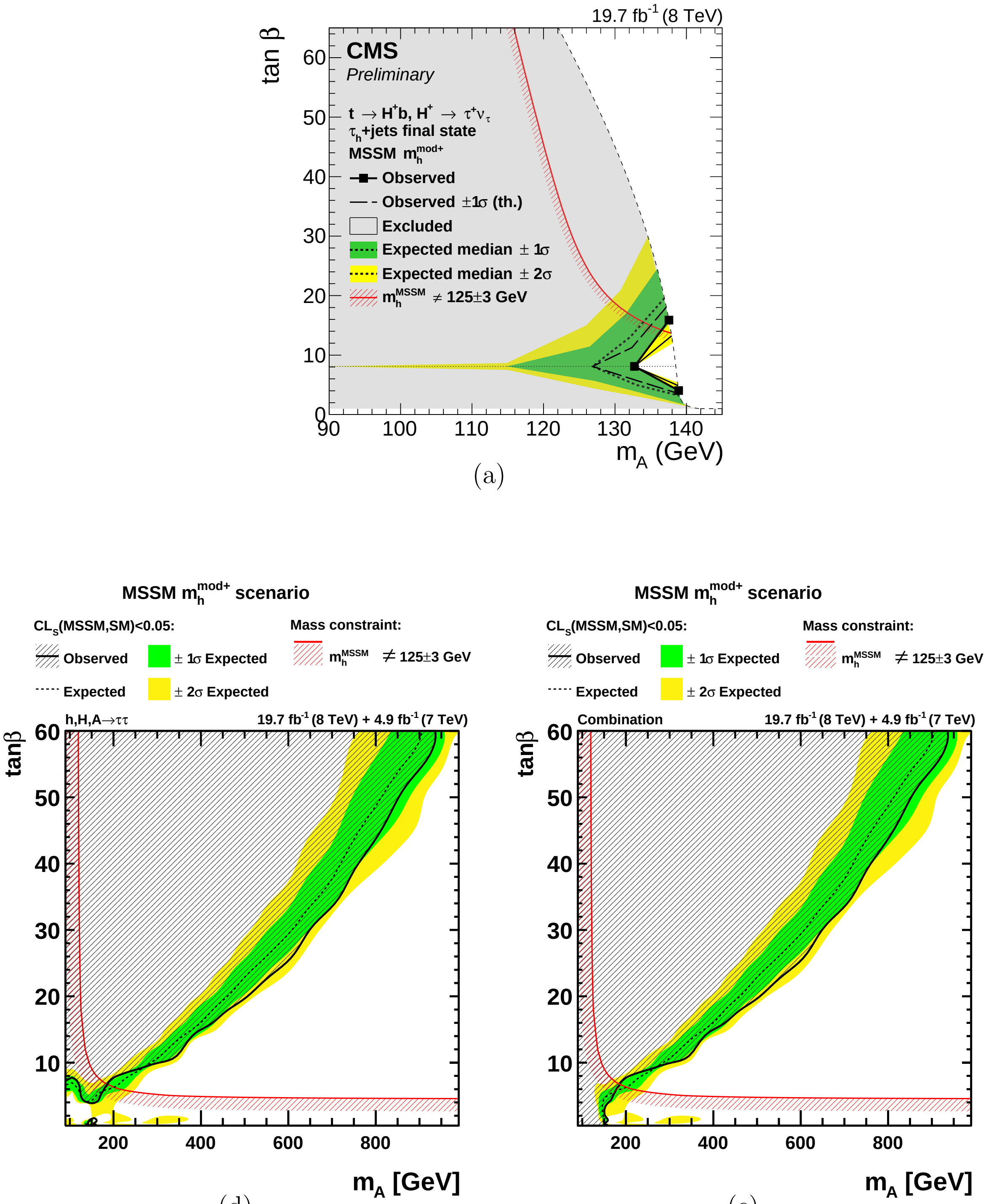

(a)

(d)

(c)

Figure 7.7: The excluded parameter space in the MSSM $m_h^{\text{mod+}}$ scenario for the combination of the $\phi \to \tau\tau$ and the $H^{\pm} \to \tau\nu$ search is shown in figure 7.7 (c) in comparison to the standalone results. The $H_{h_{\text{SM}}+b}$ hypothesis has been tested against the $H_{h+A+H+H^{\pm}+b}$ hypothesis at each point in the parameter space. Over the whole parameter space the $\phi \to \tau\tau$ analysis is used to set limits whereas the $H^{\pm} \to \tau\nu$ search is only added for $\tan\beta < 10$ and $m_A \leq 140\,\text{GeV}$ to the likelihood model. The gap between low and high values of $\tan\beta$ is closed for $m_A \leq 140\,\text{GeV}$ due to the contribution of the charged Higgs boson search. No significant deviation between the expectation and the observation has been found.

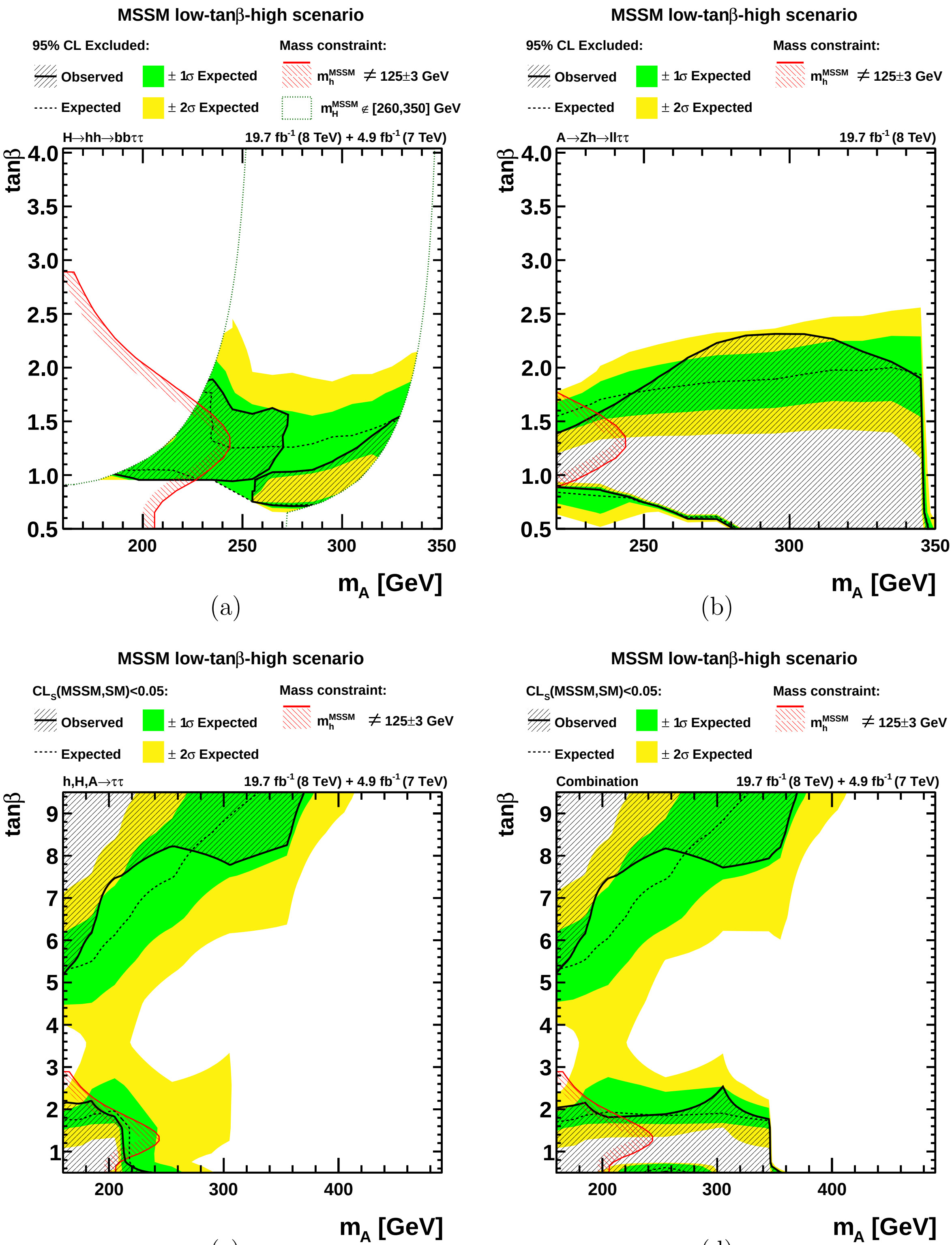

(a) (b) (c) (d)

Figure 7.8: The excluded parameter space in the MSSM low-tan β-high scenario for the combination of the $\phi \to \tau\tau$, the $H \to hh \to \bar{b}b\tau\tau$ and the $A \to Zh \to ll\tau\tau$ search is shown in figure 7.8 (d) in comparison to the standalone results. The $H_{h_{\mathrm{SM}}+b}$ hypothesis has been tested against the $H_{h+A+H+b}$ hypothesis at each point in the parameter space. The $\phi \to \tau\tau$ search is used over the whole parameter space. The $H \to hh \to \bar{b}b\tau\tau$ analysis is used in the parameter space where $260 \leq m_H \leq 350$ GeV. The $A \to Zh \to ll\tau\tau$ search is used in the region with $220 \leq m_A \leq 350$ GeV. No significant deviation between the expectation and the observation has been found.

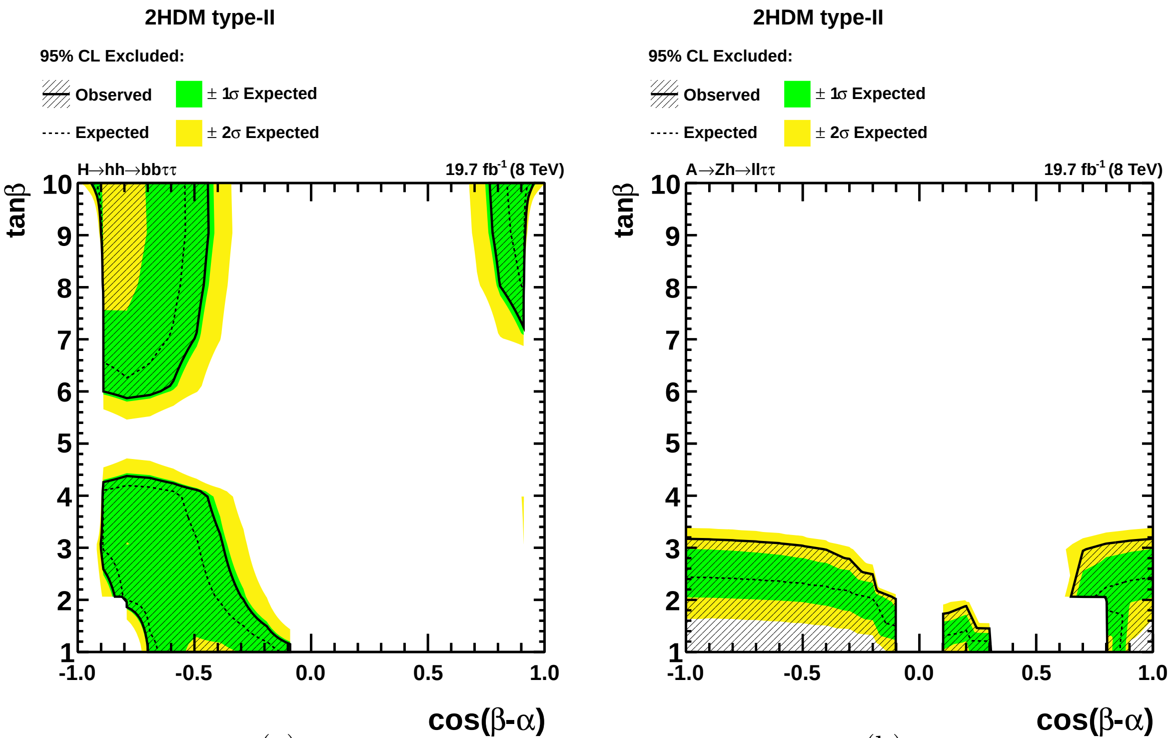

(a) (b)

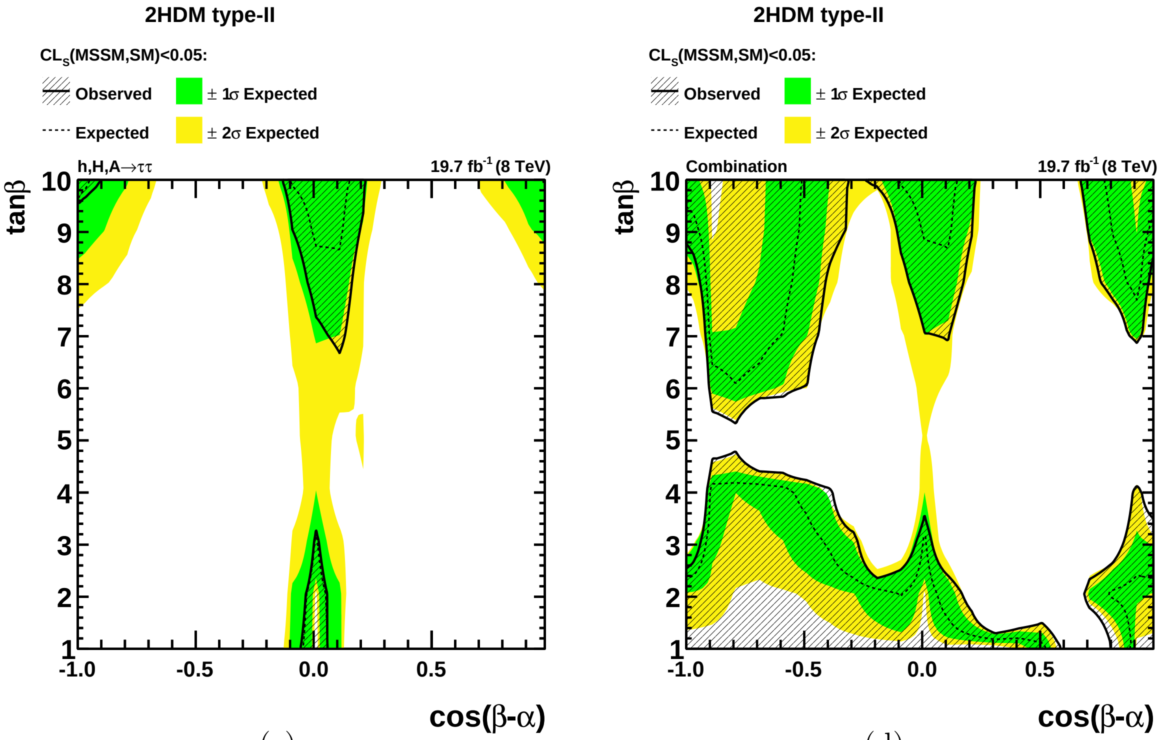

(c) (d)

Figure 7.9: The excluded parameter space in the benchmark type-2 2HDM for the combination of the $\phi \to \tau\tau$, the $H \to hh \to \bar{b}b\tau\tau$ and the $A \to Zh \to ll\tau\tau$ search is shown in figure 7.9 (d) in comparison to the standalone results. The $H_{h_{\mathrm{SM}}+b}$ hypothesis has been tested against the $H_{h+A+H+b}$ hypothesis at each point in the parameter space. All three analyses have been taken into account in the whole parameter space. No significant deviation between the expectation and the observation has been found.

Chapter 8

Summary and Outlook

The discovery of a boson at 125 GeV and the precise measurement of its properties suggests that this boson is the Higgs boson predicted by the Standard Model (SM). In this case the SM is complete. Nevertheless there are open question and phenomena observed in nature which the SM cannot explain. Therefore, the particle hunting continues with the hope to find signs for a theory beyond the Standard Model. Some of these theories predict an extended Higgs sector yielding multiple Higgs bosons. The Minimal Supersymmetric Standard Model, as a type-2 Two-Higgs-Doublet model, predicts five Higgs bosons. The decay channel to tau leptons is a particularly interesting search channel in these kind of models since the coupling to down-type fermions increases with $\tan\beta$, the ratio of the vacuum expectation value of the two Higgs doublets.
The presented search for neutral Higgs bosons decaying to tau leptons has become a flagship analysis in CMS for beyond the Standard Model Higgs bosons searches. Separated by the decay process of the tau lepton, hadronically or leptonically subsequent decays, five different channels have been analysed: the $e\mu$, $e\tau_{\mathrm{had}}$, $\mu\mu$, $\mu\tau_{\mathrm{had}}$ and $\tau_{\mathrm{had}}\tau_{\mathrm{had}}$ channel. Furthermore, the events have been separated into a no-b-tag and a b-tag category, which aim to maximize the sensitivity to the gluon-gluon production process and the Higgs production associated with b-quarks, respectively. No further model assumptions are made. The newest techniques and methods have been used to reconstruct the objects and event properties as accurate as possible. The full dataset from the LHC Run 1, which corresponds to 4.9 fb^{-1} in 2011 and 19.7 fb^{-1} in 2012, has been analysed. The background has been reduced using missing transverse momentum related variables such as the transverse mass. The remaining backgrounds have been estimated using dedicated background methods. The main backgrounds have been predicted with data-driven methods. For example, the so called embedding technique allows a good estimate of the $Z \to \tau\tau$ background while providing a data-driven description of the rest of the event, thus keeping the uncertainties on this background small. The full di-τ mass including the neutrinos has been reconstructed using a maximum likelihood based algorithm. It is used to discriminate between the signal and the background hypothesis. Systematic and statistical uncertainties have been measured and incorporated in the likelihood model to the corresponding processes. The high di-τ mass region is described using an

analytical expression for the main backgrounds to compensate the limited number of events in the Monte Carlo samples for these backgrounds.

Since no excess above the expected background has been found upper limits have been set. A two fold strategy has been pursued. In a first approach model independent limits have been computed to test a broad range of different theories. Therefore, cross-section times branching fraction limits have been computed on the two considered Higgs boson production processes, gluon-gluon fusion and Higgs production in association with b-quarks. A projection of the limits to 13 TeV and 300fb^{-1} has been made to estimate the sensitivity range for the analysis in the upcoming run 2 of the LHC. Furthermore, a two dimensional likelihood spanned by these processes has been scanned for various masses in the range between 90 and 1000 GeV. At each mass point the cross-section times branching fraction for the $\text{gg}\phi \to \tau\tau$ and $\text{bb}\phi \to \tau\tau$ processes have been computed which fit the observation best together with the 65% and 95% confidence level contours. In addition, model dependent limits have been set on eight different MSSM benchmark models and a type-2 Two-Higgs-Doublet model in order to test specific theory features since each benchmark scenario exhibits a specific phenomena. For example, the light scalar Higgs has a enhanced coupling to photons in the MSSM light-stau scenario. For these model dependent limits the statistical approach has been adapted. The BSM signal hypothesis is no longer tested against a background-only hypothesis, but against a hypothesis including the Standard Model Higgs boson in addition to the nominal backgrounds. Thus effectively a single Higgs peak hypothesis is tested against a multiple Higgs peak hypothesis. Therefore, the asymptotic CL_s method could not been used. This part of the thesis has been published as an official CMS paper [14].

In future, the categorization in the $\phi \to \tau\tau$ analysis could be revised. For example, the b-tag and no-b-tag categories could be further divided into leading tau-p_T dependent subcategories. This will boost the sensitivity to new physics, but also increase the model dependencies which has to be validated carefully.

The search for additional Higgs bosons decaying to tau leptons has been combined with other BSM analyses in different benchmark models to give a more complete picture of the status quo, setup the framework and test the difficulties in order to prepare a baseline strategy of a combination for the upcoming data-taking period of the LHC. The combination can be extended to more BSM scenarios and analyses. When adding more analyses the overlap has to be checked carefully. The treatment of the uncertainties has to be discussed. Furthermore, the computation time will increase with the number of combined analyses. Thus an estimate of the expected exclusion range is necessary to check if a combination between different analyses is reasonable. In case of an excess, a combination will, before individual analyses do, reach significances high enough to claim a discovery.

Even thought no significant excess above the SM hypothesis has been observed there is no reason to exclude BSM physics like Supersymmetry. Nature would have been very kind to us if an additional Higgs boson would have been so close to the SM Higgs boson with respect to its mass, cross-sections and branching fractions. With the current data the analyses described in this thesis have helped to constrain the allowed parameter space for BSM physics. In mid-2015 the LHC will start again colliding protons with an increased center-of-mass energy of 13 TeV and later 14 TeV. Till the end of 2022 300 fb^{-1} of proton-proton collision data are expected. Finally, after a longer shutdown starting in 2023 the LHC should finally collect up to 3000 fb^{-1}. With two orders of magnitude increased data sample the parameter space of MSSM will be fully covered at least up to $m_A = 1\,\mathrm{TeV}$.

Bibliography

[1] ATLAS Collaboration, "A particle consistent with the Higgs Boson observed with the ATLAS Detector at the Large Hadron Collider", *Science* **338** (2012) 1576–1582.

[2] CMS Collaboration, "Observation of a new boson at a mass of 125 GeV with the CMS experiment at the LHC", *Phys.Lett.* **B716** (2012) 30–61, `arXiv:1207.7235`.

[3] ATLAS Collaboration, "Measurement of the Higgs boson mass from the $H \to \gamma\gamma$ and $H \to ZZ^* \to 4\ell$ channels with the ATLAS detector using 25 fb^{-1} of pp collision data", *Phys.Rev.* **D90** (2014), no. 5, 052004, `arXiv:1406.3827`.

[4] CMS Collaboration, "Precise determination of the mass of the Higgs boson and tests of compatibility of its couplings with the standard model predictions using proton collisions at 7 and 8 TeV", `arXiv:1412.8662`.

[5] F. Englert and R. Brout, "Broken Symmetriy and the Mass of Gauge Vector Mesons", *Phys.Rev.Lett.* **13** (1964) 321–322.

[6] P. W. Higgs, "Broken symmetries, massless particles and gauge fields", *Phys.Rev.Lett.* **12** (1964) 132–133.

[7] P. W. Higgs, "Broken Symmetries and the Masses of Gauge Bosons", *Phys.Rev.Lett.* **13** (1964) 508–509.

[8] G. S. Guralnik, C. R. Hagen, and T. W. B. Kibble, "Global Conservation Laws and Massless Particles", *Phys. Rev. Lett.* **13** (1964) 585–587.

[9] M. E. Peskin and D. V. Schroeder, "An Introduction To Quantum Field Theory (Frontiers in Physics)". Westview Press, 1995.

[10] V. Trimble, "Existence and nature of dark matter in the universe", *Annual Review of Astronomy and Astrophysics* **25** (1987) 425–472. Provided by the SAO/NASA Astrophysics Data System.

[11] F. Zwicky, "Die Rotverschiebung von extragalaktischen Nebeln", *Helvetica Physica Acta* **6** (1933) 110–127. Provided by the SAO/NASA Astrophysics Data System.

[12] F. Zwicky, “On the Masses of Nebulae and of Clusters of Nebulae”, *Astrophysical Journal* **86** (oct, 1937) 217. Provided by the SAO/NASA Astrophysics Data System.

[13] F. Jegerlehner, “The hierarchy problem of the electroweak Standard Model revisited”, `arXiv:1305.6652`.

[14] CMS Collaboration, “Search for neutral MSSM Higgs bosons decaying to a pair of tau leptons in pp collisions”, *J. High Energy Phys.* **10** (Aug, 2014) 160. 53 p.

[15] CMS Collaboration, “Higgs to tau tau (MSSM)”, Technical Report CMS-PAS-HIG-13-021, CERN, Geneva, 2013.

[16] CMS Collaboration, “Higgs to tau tau (MSSM) (HCP)”, Technical Report CMS-PAS-HIG-12-050, CERN, Geneva, 2012.

[17] CMS Collaboration, “Search for charged Higgs bosons with the H+ to tau nu decay channel in the fully hadronic final state at sqrt s = 8 TeV”, Technical Report CMS-PAS-HIG-14-020, CERN, Geneva, 2014.

[18] CMS Collaboration, “to be published soon”, Technical Report HIG-14-034, CERN, Geneva, 2014.

[19] S. P. Martin, “A Supersymmetry Primer”, *arXiv:hep-ph/9709356v6* **v6** (2011) 498–516.

[20] N. Craig, J. Galloway, and S. Thomas, “Searching for Signs of the Second Higgs Doublet”, `arXiv:1305.2424`.

[21] Wikipedia, “http://en.wikipedia.org/wiki/Standard_Model”.

[22] J. Goldstone, A. Salam, and S. Weinberg, “Broken Symmetries”, *Phys. Rev.* **127** (1962) 965–970.

[23] W. de Boer, “Grand unified theories and supersymmetry in particle physics and cosmology”, *Prog.Part.Nucl.Phys.* **33** (1994) 201–302, `arXiv:hep-ph/9402266`.

[24] J. Goldstone, “Field Theories with Superconductor Solutions”, *Il Nuovo Cimento* **19** (1961) 154–164. 10.1007/BF02812722.

[25] U. Amaldi, W. de Boer, and H. Furstenau, “Comparison of grand unified theories with electroweak and strong coupling constants measured at LEP”, *Phys.Lett.* **B260** (1991) 447–455.

[26] P. J. E. Peebles and B. Ratra, “The cosmological constant and dark energy”, *Rev. Mod. Phys.* **75** (Apr, 2003) 559–606.

[27] Particle Data Group Collaboration, “Review of Particle Physics”, *Chin.Phys.* **C38** (2014) 090001.

[28] M. S. Carena et al., "Suggestions for benchmark scenarios for MSSM Higgs boson searches at hadron colliders", *Eur. Phys. J. C* **26** (2003) 601.

[29] M. Carena, S. Heinemeyer, O. Stål et al., "MSSM Higgs Boson Searches at the LHC: Benchmark Scenarios after the Discovery of a Higgs-like Particle", *Eur. Phys. J.* **C73** (2013) 2552, `arXiv:1302.7033`.

[30] A. Djouadi, L. Maiani, A. Polosa et al., "Fully covering the MSSM Higgs sector at the LHC", `arXiv:1502.05653`.

[31] Heinemeyer, Sven. https://twiki.cern.ch/twiki/pub/LHCPhysics/HXSWG3LowTanB/benchmark5-v0.pdf.

[32] G. Degrassi, S. Heinemeyer, W. Hollik et al., "Towards high precision predictions for the MSSM Higgs sector", *Eur.Phys.J.* **C28** (2003) 133–143, `arXiv:hep-ph/0212020`.

[33] LHC theory group. https://twiki.cern.ch/twiki/bin/view/LHCPhysics/SMInputParameter.

[34] ALEPH Collaboration, DELPHI Collaboration, L3 Collaboration, OPAL Collaboration, LEP Working Group for Higgs Boson Searches Collaboration, "Search for neutral MSSM Higgs bosons at LEP", *Eur.Phys.J.* **C47** (2006) 547–587, `arXiv:hep-ex/0602042`.

[35] J. P. Miller, E. de Rafael, and B. L. Roberts, "Muon (g-2): Experiment and theory", *Rept.Prog.Phys.* **70** (2007) 795, `arXiv:hep-ph/0703049`.

[36] BaBar Collaboration, "Exclusive Measurements of $b \to s\gamma$ Transition Rate and Photon Energy Spectrum", *Phys.Rev.* **D86** (2012) 052012, `arXiv:1207.2520`.

[37] CMS Collaboration, "Search for top squarks decaying to a charm quark and a neutralino in events with a jet and missing transverse momentum", Technical Report CMS-PAS-SUS-13-009, CERN, Geneva, 2014.

[38] CMS Collaboration, "Search for top squarks in multijet events with large missing momentum in proton-proton collisions at 8 TeV", Technical Report CMS-PAS-SUS-13-015, CERN, Geneva, 2013.

[39] CMS Collaboration, "Search for top-squark pair production in the single-lepton final state in pp collisions at $\sqrt{s} = 8$ TeV", *Eur. Phys. J. C* **73** (Aug, 2013) 2677. 61 p.

[40] ATLAS Collaboration, "Measurements of the properties of the Higgs-like boson in the two photon decay channel with the ATLAS detector using 25 fb^{-1} of proton-proton collision data", Technical Report ATLAS-CONF-2013-012, CERN, Geneva, Mar, 2013.

[41] S. L. Glashow and S. Weinberg, "Natural conservation laws for neutral currents", *Phys. Rev. D* **15** (Apr, 1977) 1958–1965.

[42] Lacaprara, Stefano. https://twiki.cern.ch/twiki/bin/view/Main/XsBr2HDM.

[43] J. Gruschke, "Observation of Top Quarks and First Measurement of the $t\bar{t}$ Production Cross Section at a Centre-Of-Mass Energy of 7 TeV with the CMS Experiment at the LHC", *PhD Thesis, Karlsruhe Institute of Technology,* **IEKP-KA/2011-04** (2011).

[44] K. Aamodt et al., "The ALICE Experiment at the LHC", *JINST* **3** (2008) S08002.

[45] A. A. Alves et al., "The LHCb Detector at the LHC", *JINST* **3** (2008) S08005.

[46] CMS Collaboration Collaboration, "The CMS experiment at the CERN LHC", *JINST* **3** (2008) S08004.

[47] G. Aad et al., "The ATLAS Experiment at the LHC", *JINST* **3** (2008) S08003.

[48] CMS collaboration. https://twiki.cern.ch/twiki/bin/view/CMSPublic/LumiPublicResults.

[49] CMS Collaboration, "How was CMS designed?". `http://cms.web.cern.ch/cms/Detector/Designed/index.html` (November 2011).

[50] CMS Collaboration, G. Bayatian et al., "CMS physics: Technical design report". 2006.

[51] CMS Collaboration, G. Bayatian et al., "CMS technical design report, volume II: Physics performance", volume G34. 2007.

[52] D. Kotlinski, "The design of the CMS pixel detector system", *Nucl. Instrum. Methods Phys. Res., A* **477** (2002), no. 1-3, 446–50.

[53] CMS Collaboration, "The Tracker Project Technical Design Report", *CERN/LHCC 98-6, CMS TDR 5* (1998).

[54] CMS Collaboration, "Addendum to the Technical Design Report", *CERN/LHCC 2000-016, CMS TDR 5 Addendum 1* (2000).

[55] CMS Collaboration, "Electromagnetic calorimeter calibration with 7 TeV data",. CMS PAS EGM-10-003.

[56] CMS Collaboration, "The CMS barrel calorimeter response to particle beams from 2-GeV/c to 350-GeV/c", *J.Phys.Conf.Ser.* **160** (2009) 012056.

[57] G. Bayatian, A. Sirunian, I. Emelyanchik et al., “Design, performance and calibration of the CMS forward calorimeter wedges”, *Eur.Phys.J.* **C53** (2008) 139–166.

[58] CMS Collaboration, “CMS Physics Technical Design Report Volume I: Detector Performance and Software”, *Technical Design Report CMS* (2006).

[59] CMS Collaboration, “The TriDAS Project Technical Design Report, Volume 1: The Trigger Systems”, *CERN-LHCC-2000-038* (2000).

[60] CMS Collaboration, “CMS. The TriDAS project. Technical design report, vol. 1: The trigger systems”,.

[61] CMS Collaboration, “The TriDAS Project Technical Design Report, Volume 2: Data Acquisition and High-Level Trigger”, *CERN-LHC-2002-026* (2002).

[62] J. Järvi, M. Marcus, and J. N. Smith, “Programming with C++ concepts”, *Sci. Comput. Program.* **75** (July, 2010) 596–614.

[63] “http://python.org/”.

[64] R. Brun, F. Rademakers, and S. Panacek, “ROOT, an object oriented data analysis framework”, 2000.

[65] W. Verkerke and D. P. Kirby, “The RooFit toolkot for data modeling”, 2003.

[66] L. Moneta, K. Belasco, K. S. Cranmer et al., “The RooStats Project”, *PoS* **ACAT2010** (2010) 057, `arXiv:1009.1003`.

[67] “Procedure for the LHC Higgs boson search combination in summer 2011”, Technical Report ATL-PHYS-PUB-2011-011, CERN, Geneva, Aug, 2011.

[68] Higgs PAG. https://twiki.cern.ch/twiki/bin/viewauth/CMS/SWGuideHiggsAnalysisCombinedLimit.

[69] R. V. Harlander, S. Liebler, and H. Mantler, “SusHi: A program for the calculation of Higgs production in gluon fusion and bottom-quark annihilation in the Standard Model and the MSSM”, *Comput.Phys.Commun.* **184** (2013) 1605–1617, `arXiv:1212.3249`.

[70] R. V. Harlander and W. B. Kilgore, “Next-to-next-to-leading order Higgs production at hadron colliders”, *Phys.Rev.Lett.* **88** (2002) 201801, `arXiv:hep-ph/0201206`.

[71] R. V. Harlander and M. Steinhauser, “Supersymmetric Higgs production in gluon fusion at next-to-leading order”, *JHEP* **0409** (2004) 066, `arXiv:hep-ph/0409010`.

[72] R. V. Harlander and M. Steinhauser, “Hadronic Higgs production and decay in supersymmetry at next-to-leading order”, *Phys.Lett.* **B574** (2003) 258–268, `arXiv:hep-ph/0307346`.

[73] R. Harlander and M. Steinhauser, “Effects of SUSY QCD in hadronic Higgs production at next-to-next-to-leading order”, *Phys.Rev.* **D68** (2003) 111701, `arXiv:hep-ph/0308210`.

[74] R. V. Harlander and W. B. Kilgore, “Higgs boson production in bottom quark fusion at next-to-next-to leading order”, *Phys.Rev.* **D68** (2003) 013001, `arXiv:hep-ph/0304035`.

[75] G. Degrassi and P. Slavich, “NLO QCD bottom corrections to Higgs boson production in the MSSM”, *JHEP* **1011** (2010) 044, `arXiv:1007.3465`.

[76] G. Degrassi, S. Di Vita, and P. Slavich, “NLO QCD corrections to pseudoscalar Higgs production in the MSSM”, *JHEP* **1108** (2011) 128, `arXiv:1107.0914`.

[77] G. Degrassi, S. Di Vita, and P. Slavich, “On the NLO QCD Corrections to the Production of the Heaviest Neutral Higgs Scalar in the MSSM”, *Eur.Phys.J.* **C72** (2012) 2032, `arXiv:1204.1016`.

[78] U. Aglietti, R. Bonciani, G. Degrassi et al., “Two loop light fermion contribution to Higgs production and decays”, *Phys.Lett.* **B595** (2004) 432–441, `arXiv:hep-ph/0404071`.

[79] S. Dittmaier, . Kramer, Michael, and M. Spira, “Higgs radiation off bottom quarks at the Tevatron and the CERN LHC”, *Phys.Rev.* **D70** (2004) 074010, `arXiv:hep-ph/0309204`.

[80] S. Dawson, C. B. Jackson, L. Reina et al., “Exclusive Higgs boson production with bottom quarks at hadron colliders”, *Phys. Rev.* **D69** (2004) 074027, `arXiv:hep-ph/0311067`.

[81] T. Hahn, S. Heinemeyer, W. Hollik et al., “High-Precision Predictions for the Light CP -Even Higgs Boson Mass of the Minimal Supersymmetric Standard Model”, *Phys.Rev.Lett.* **112** (2014), no. 14, 141801, `arXiv:1312.4937`.

[82] M. Frank, T. Hahn, S. Heinemeyer et al., “The Higgs Boson Masses and Mixings of the Complex MSSM in the Feynman-Diagrammatic Approach”, *JHEP* **0702** (2007) 047, `arXiv:hep-ph/0611326`.

[83] S. Heinemeyer, W. Hollik, and G. Weiglein, “The Masses of the neutral CP - even Higgs bosons in the MSSM: Accurate analysis at the two loop level”, *Eur.Phys.J.* **C9** (1999) 343–366, `arXiv:hep-ph/9812472`.

[84] S. Heinemeyer, W. Hollik, and G. Weiglein, “FeynHiggs: A Program for the calculation of the masses of the neutral CP even Higgs bosons in the MSSM”, *Comput.Phys.Commun.* **124** (2000) 76–89, `arXiv:hep-ph/9812320`.

[85] D. Eriksson, J. Rathsman, and O. Stal, “2HDMC: Two-Higgs-Doublet Model Calculator Physics and Manual”, *Comput.Phys.Commun.* **181** (2010) 189–205, `arXiv:0902.0851`.

[86] CMS Collaboration, “Particle-Flow Event Reconstruction in CMS and Performance for Jets, Taus, and MET”,. CMS PAS PFT-09-001.

[87] W. Erdmann, “Offline Primary Vertex Reconstruction with Deterministic Annealing Clustering”, *CMS Note* (2011).

[88] W. Adam, R. Fruhwirth, A. Strandlie et al., “Reconstruction of electrons with the Gaussian sum filter in the CMS tracker at LHC”, *eConf* **C0303241** (2003) TULT009, `arXiv:physics/0306087`.

[89] A. Hoecker, P. Speckmayer, J. Stelzer et al., “TMVA - Toolkit for Multivariate Data Analysis”, *ArXiv Physics e-prints* (March, 2007) `arXiv:physics/0703039`.

[90] CMS Muon POG. https://twiki.cern.ch/twiki/bin/viewauth/CMSPublic/SWGuideMuonId#TightMuon.

[91] CMS Collaboration, “Commissioning of the Particle-Flow reconstruction in Minimum-Bias and Jet Events from pp Collisions at 7 TeV”, technical report, 2010.

[92] M. Cacciari, G. P. Salam, and G. Soyez, “The Anti-k(t) jet clustering algorithm”, *JHEP* **0804** (2008) 063, `arXiv:0802.1189`.

[93] “Calorimeter Jet Quality Criteria for the First CMS Collision Data, and preparations for calibrating their efficiencies”. CMS AN-2009/087.

[94] N. Saoulidou, “Particle Flow Jet Identification Criteria”, *CMS Note* **2010/003** (2010).

[95] M. Cacciari and G. P. Salam, “Pileup subtraction using jet areas”, *Phys. Lett. B* **659** (2008) 119, `arXiv:hep-ph/0707.1378`.

[96] CMS Collaboration, “Determination of Jet Energy Calibration and Transverse Momentum Resolution in CMS”, *JINST* **6** (2011) 11002.

[97] CMS Collaboration Collaboration, “Performance of b tagging at sqrt(s)=8 TeV in multijet, ttbar and boosted topology events”, Technical Report CMS-PAS-BTV-13-001, CERN, Geneva, 2013.

[98] CMS Collaboration, “Identification of b-quark jets with the CMS experiment”, *JINST* **8** (2013) P04013, `arXiv:1211.4462`.

[99] CMS Collaboration, “Tau identification in CMS”, Technical Report CMS-PAS-TAU-11-001, CERN, Geneva, 2011.

[100] M. Bachtis, S. Dasu, and A. Savin, “Prospects for measurement of $\sigma(pp \to Z) \cdot B(Z \to \tau^+\tau^-)$ with CMS in pp Collisions at $\sqrt(s) = 7$ TeV”, *CMS Note* **2010/082** (2010).

[101] C. V. L. Bianchini, I. Naranjo Fong, "The development of a new discriminator to separate electrons from hadronic tau decays is described in this note. We find that the new discriminator significantly reduces the probability for electrons to get misidentified as hadronic tau decays.", *CMS Note* (2012).

[102] M. Bachtis, J. Swanson, A. Savin et al., "Study of the di-tau spectrum using muon-tau and electron-tau final states with CMS detector at $\sqrt{s} = 7$ TeV.", *CMS Note* (2011).

[103] CMS Collaboration, "Performance of Missing Transverse Momentum Reconstruction Algorithms in Proton–Proton Collisions at $\sqrt{s} = 8$ TeV with the CMS Detector", CMS Physics Analysis Summary CMS-PAS-JME-12-002, 2012.

[104] P. Harris et al., "Reducing pile–up depedence of E_T^{miss} with a pile–up jet identifier and a multivariate regression technique", *CMS Note* **2012/226** (2012).

[105] Aachen-Annecy-Birmingham-CERN-Helsinki-London(QMC)-Paris(CdF)-Riverside-Rome-Rutherford-Saclay(CEN)-Vienna Collaboration Collaboration, "Experimental observation of isolated large transverse energy electrons with associated missing energy at $\sqrt{s} = 540 GeV$", *Phys. Lett. B* **122** (Jan, 1983) 103–116. 31 p.

[106] CMS Collaboration Collaboration, "Evidence for the 125 GeV Higgs boson decaying to a pair of τ leptons", *JHEP* **1405** (2014) 104, `arXiv:1401.5041`.

[107] Higgs TauTau group, "Physics Objects in the Higgs to Tau Tau Analysis", *CMS Note* **2013/188** (2013).

[108] EGamma POG. https://twiki.cern.ch/twiki/bin/view/CMS/EgammaCutBasedIdentification.

[109] J. Berger, A. Bethani, A. Burgmeier et al., "Search for Higgs boson decays to tau pairs in the di-muon and di-electron channels", *CMS Note* (2013).

[110] C. Veelken et al., "Search for MSSM Neutral Higgs Bosons Decaying to Tau Pairs in pp Collisions", *CMS Note* (2014).

[111] J. Bendavid et al., "Study of Data–Driven Methods For Estimation of Fake Lepton Backgrounds", *CMS Note* **2009/120** (2009).

[112] CMS Collaboration, "Combination of top pair production cross section measurements", *CMS PAS* **TOP-11-024** (2011).

[113] M. Czakon, P. Fiedler, and A. Mitov, "The total top quark pair production cross-section at hadron colliders through $O(alpha_S^4)$", `arXiv:1303.6254`.

[114] A. Martin, W. Stirling, R. Thorne et al., “Parton distributions for the LHC”, *Eur.Phys.J.* **C63** (2009) 189–285, `arXiv:0901.0002`.

[115] A. Martin, W. Stirling, R. Thorne et al., “Uncertainties on alpha(S) in global PDF analyses and implications for predicted hadronic cross sections”, *Eur.Phys.J.* **C64** (2009) 653–680, `arXiv:0905.3531`.

[116] R. Barlow and C. Beeston, “Fitting using finite Monte Carlo samples”, *Computer Physics Communications* **77** (1993), no. 2, 219 – 228.

[117] J. Conway, “Incorporating Nuisance Parameters in Likelihoods for Multisource Spectra”, `arXiv:1103.0354`.

[118] *CMS Statistic Committee.* https://twiki.cern.ch/twiki/bin/viewauth/CMS/StatisticsCommittee.

[119] R. D. Cousins, “Probability Density Functions for Positive Nuisance Parameters”, *CMS Statistic Committee* (2010).

[120] A. N. Kolmogorov, “Sulla Determinazione Empirica di una Legge di Distribuzione”, *Giornale dell'Istituto Italiano degli Attuari* **4** (1933) 83–91.

[121] N. Smirnov, “Table for Estimating the Goodness of Fit of Empirical Distributions”, *Ann. Math. Statist.* **19** (06, 1948) 279–281.

[122] F. Yates, “Contingency Tables Involving Small Numbers and the chi2 Test”, *Supplement to the Journal of the Royal Statistical Society* **1** (1934), no. 2, pp. 217–235.

[123] B. Effron, “Why Isn't Everyone a Bayesian?”, *The American Statistican* **40** (1986) 11. http://www.jstor.org/pss/2683105.

[124] R. D. Cousins, “Why isn't every physicist a Bayesian?”, *Am. J. Phys.* **63** (1995) 398.

[125] A. Stuart, J. K. Ord, and S. Arnold, “Kendall's advanced theory of statistics. Vol.2A: Classical inference and the linear model”. 1999. Chapter 26 compares different schools of statistical interference.

[126] A. Yuan, “Bayesian frequentist hybrid inference”, *Annals of Statistic* **117** (2009) 2458–2501.

[127] G. Cowan, “Statistical Methods for Discovery and Limits”, *Terascale School on Data Combination and Limit Setting, Oct. 4-6, 2011, DESY Hamburg* (2011). http://www.pp.rhul.ac.uk/ cowan/stat/desy.

[128] G. Cowan, K. Cranmer, E. Gross et al., “Power-Constrained Limits”, *ArXiv e-prints* (May, 2011) `arXiv:1105.3166`.

[129] F. Loparco and M. N. Mazziotta, “A Bayesian approach to evaluate confidence intervals in counting ”, *Nucl.Instrum.Meth.A646* **v1** (2011) 167–173, `arXiv:1105.3041v1`.

[130] A. Read, “Presentation of search results: the CLs technique”, *J.Phys. G: Nucl.Part. Phys.* **28** (2002) 2693–2704.

[131] R. D. Cousins, “Upper Limits: A Personal View of Some History and Foundations”,. Terascale School on Data Combination and Limit Setting, Oct. 4-6, 2011, DESY Hamburg.

[132] S. S. Wilk, “The Large-Sample Distribution of the Likelihood Ratio for Testing Composite Hypotheses”, *Ann. Math. Statist.* **9** (1938) 60–62.

[133] G. Cowan, K. Cranmer, E. Gross et al., “Asymptotic formulae for likelihood-based tests of new physics”, *European Physical Journal C* **71** (February, 2011) 1554, `arXiv:1007.1727`.

[134] G. J. Feldman and R. D. Cousins, “A Unified Approach to the Classical Statistical Analysis of Small Signals”, *PHYS.REV.D* **57** (1998) 3873.

[135] CMS Collaboration, “Search for neutral Higgs bosons decaying to τ pairs in pp collisions at $\sqrt{s} = 7$ TeV”, *Phys.Lett.* **B713** (2012) 68–90, `arXiv:1202.4083`.

[136] Gomez-Ceballos, Guillelmo. http://ceballos.web.cern.ch/ceballos/mcfm/xsec_several_ecm.txt.

[137] The Durham HepData Project. http://hepdata.cedar.ac.uk/pdf/pdf3.html.

[138] LHC Higgs Cross Section Working Group. https://twiki.cern.ch/twiki/bin/view/LHCPhysics/LHCHXSWGMSSMNeutral.

[139] A. L. Read, “Linear interpolation of histograms”, *Nucl.Instrum.Meth.* **A425** (1999) 357–360.

[140] LHC Higgs Cross Section Working Group, “Handbook of LHC Higgs Cross Sections: 1. Inclusive Observables”, CERN Report CERN-2011-002, 2011.

Appendix A

MSSM Benchmark Scenarios

In the the following table, the definition of the MSSM benchmark scenarios [28–31] is given. In most cases, the parameters agree with the scenarios as defined in the cited papers. For some scenarios the parameters have been changed slightly to satisfy newest direct search results.

parameter	m_h^{max}	$m_h^{\text{mod}\pm}$	low-tan β-high	light-stop	light-stau	τ-phobic	low-m_H
m_b [GeV]	4.16	4.16	4.16	4.16	4.16	4.16	4.16
m_t [GeV]	172.5	172.5	172.5	172.5	172.5	172.5	172.5
m_A [GeV]	90–1000	90–1000	150–500	90–600	90–1000	90–1000	110
$\tan\beta$ [ ]	0.5–60	0.5–60	0.5–9.5	0.7–60	0.5–60	1.0–50	1.5–9.5
μ [GeV]	200	200	1500	400	500	2000	300–3100
$M_{\tilde{q}_{1,2}}$ [GeV]	1500	1500	1500	1500	1500	1500	1500
M_{SUSY} [GeV]	1000	1000	see text	500	1000	1500	1500
X_t [GeV]	$2.0 M_{SUSY}$	$1.5/\text{-}1.9 M_{SUSY}$	see text	$2.0 M_{SUSY}$	$1.6 M_{SUSY}$	$2.45 M_{SUSY}$	$1.5 M_{SUSY}$
$M_{\tilde{l}_{1,2}}$ [GeV]	500	500	500	500	500	500	500
$M_{\tilde{l}_3}$ [GeV]	1000	1000	1000	1000	245	500	1000
M_1 [GeV]	fixed by GUT relation to M_2			340	fixed by GUT relation to M_2		
M_2 [GeV]	200	200	2000	400	200	200	200
$m_{\tilde{g}}$ [GeV]	1500	1500	1500	1500	1500	1500	1500
$A_{f_{1,2}}$ [GeV]	0	0	2000	0	0	0	0
A_t [GeV]	fixed by $X_t = A_t - \mu \cot\beta$						
A_b [GeV]	$= A_t$	$= A_t$	2000	$= A_t$	$= A_t$	$= A_t$	$= A_t$
A_τ [GeV]	$= A_t$	$= A_t$	2000	$= A_t$	$= A_t$	0	$= A_t$

Table A.1: List of parameters defining the different MSSM benchmark scenarios. In most cases numbers are taken from [28–31]. Some scenarios were slightly adjusted in order to fulfil the current requirements of experimental results, since the originally proposed scenarios were already excluded.

Appendix B

The $\mathrm{CL_s}$ Method

A technical and detailed description about the limit setting process using the $\mathrm{CL_s}$ approach is given in the following.

Observed Limit Calculation

The calculation of the observed limit using the $\mathrm{CL_s}$ method is step based.

1 First the observed test statistic q_r^{obs} for the signal strength parameter r under test is determined.

2 By maximizing the used likelihood function, equation (5.2) for the LHC test statistic or equation (5.13) for the LEP and TEV case, the nuisance parameters for the background only $\hat{\theta}_0^{\mathrm{obs}}$ and for the signal+background hypothesis $\hat{\theta}_r^{\mathrm{obs}}$ are found. As described above, in the TEV and LHC case these values $\hat{\theta}_0^{\mathrm{obs}}$ ($\hat{\theta}_r^{\mathrm{obs}}$) lead to the best agreement between the background (signal+background) hypothesis and the observation[1].

3 Large number of Monte Carlo measurements n_0^{MC} (n_r^{MC}) are simulated by using the likelihood function (5.2) and fixing the uncertainties to $\hat{\theta}_0^{\mathrm{obs}}$ ($\hat{\theta}_r^{\mathrm{obs}}$)[1].

4 Using a pseudo dataset n_0^{MC} (n_r^{MC}) the test statistic q_0 (q_r) is evaluated. The uncertainties are left floating[1] during the evaluation of the test statistic.

5 By running step **4** for each pseudo dataset n_0^{MC} and n_r^{MC} the probability density functions for the background $f(q_0|r=0)$ and for the signal+background hypothesis $f(q_r|r)$ can be constructed.

6 Two p-values, for the background H_b and the signal+background hypothesis H_s, are calculated:

---

[1] Note that in the LEP likelihood function (5.13) the uncertainties have already been marginalized.

$$\begin{aligned} p_b &= P(q_0 \geq q_r^{\mathrm{obs}}|b) = \int_{q_r^{\mathrm{obs}}}^{\infty} f(q_0|0) \\ p_r &= P(q_r \geq q_r^{\mathrm{obs}}|s+b) = \int_{q_r^{\mathrm{obs}}}^{\infty} f(q_r|r) \ . \end{aligned} \tag{B.1}$$

7 Finally the CL$_\mathrm{s}$ discriminator which depends on the signal strength modifier r is built:

$$\mathrm{CL_s}(r) = \frac{p_r}{p_b} \ . \tag{B.2}$$

In CMS (and ATLAS) analysis exclusion limits are set with 95% confidence level. Therefore, the exclusion limit r_{UL} is defined as the value of the signal strength modifier r for which

$$\mathrm{CL_s}(r_{\mathrm{UL}}) = 0.05 \ . \tag{B.3}$$

In order to find the upper limit r_{UL}, the signal strength modifier r is varied till equation (B.3) is fulfilled. Thus, steps 1-8 are iterated. A tested signal expectation is excluded at 95% confidence level if $\mathrm{CL_s} > 0.05$.

Expected Limit

The calculation of the expected median and the corresponding $\pm 1\sigma$ and $\pm 2\sigma$ bands is done in a similar way as the observed limit. An additional step of generating multiple pseudo datasets for the background hypothesis n_b by using the likelihood function (5.2) with $r = 0$ is needed. These datasets can be obtained either by using the a priori uncertainties or the a posteriori uncertainties $\hat{\theta}_0^{\mathrm{obs}}$. If the analysis is still blind, meaning data is not used, the a priori values are used and the observation is not looked at. The final results will be done with the a posteriori uncertainties. This bias towards the data guarantees a conservative result.

The constructed pseudo datasets are used as if they were observed data. For each of the generated pseudo datasets n_b steps 1-8 are iterated till an upper limit is found with the simplification that the uncertainties $\hat{\theta}_0^{\mathrm{obs}}$ and $\hat{\theta}_r^{\mathrm{obs}}$ in step 2 are either taken from the observed limit calculation or if data should not be used the a priori uncertainties are taken. Therefore, in step 3, the MC measurements n_0^{MC} and n_r^{MC} do not dependent on the value of the pseudo dataset n_b. As a consequence, the test statistic for a fixed r is also independent from the value of the pseudo dataset n_b which reduces the amount of MC generations needed in the expected limit calculations since the probability density functions $f(q_r|r)$ have only to be calculated once for a fixed r. The cumulative probability can than be built using the different outcomes as input. In figure B.1 this is illustrated for an example of a background prediction of 5 events, signal prediction of 1 event and without any uncertainties.

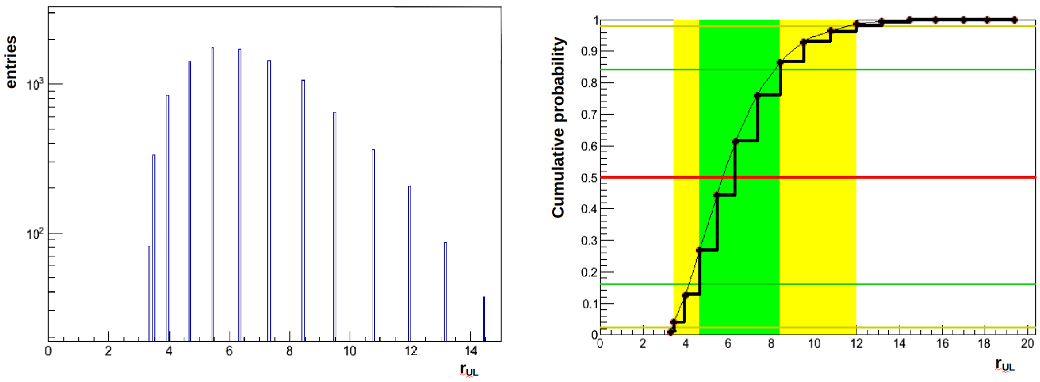

(a) (b)

Figure B.1: On the left B.1(a) the upper limits r_{UL} for 10000 generated Monte Carlo pseudo datasets are shown. The cumulative probability density function of these is shown on the right B.1(b).

Appendix C

Pulls and Constraints

In the following tables the shifts and constraints for the $e\mu$ (figure C.1), $e\tau_{had}$ (figure C.2), $\mu\mu$ (figure C.3) and $\tau_{had}\tau_{had}$ channel (figure C.4) are shown. Barlow-Beeston uncertainties are not shown. Shifts and constraints on the $H_{\phi+b}$ hypothesis assuming a mass of 160 GeV are shown. Overall, the uncertainties behave as expected. Some shifts and constraints are expected due to fluctuations in the observations. The heavy constraints in the $\mu\mu$ channel on the $\not{E}_{\mathrm{T}}$ resolution and on the Z→ $\mu\mu$ number are expected due to the sheer number of events in the Z→ $\mu\mu$ background and due to a conservative choice of the a priori estimates.

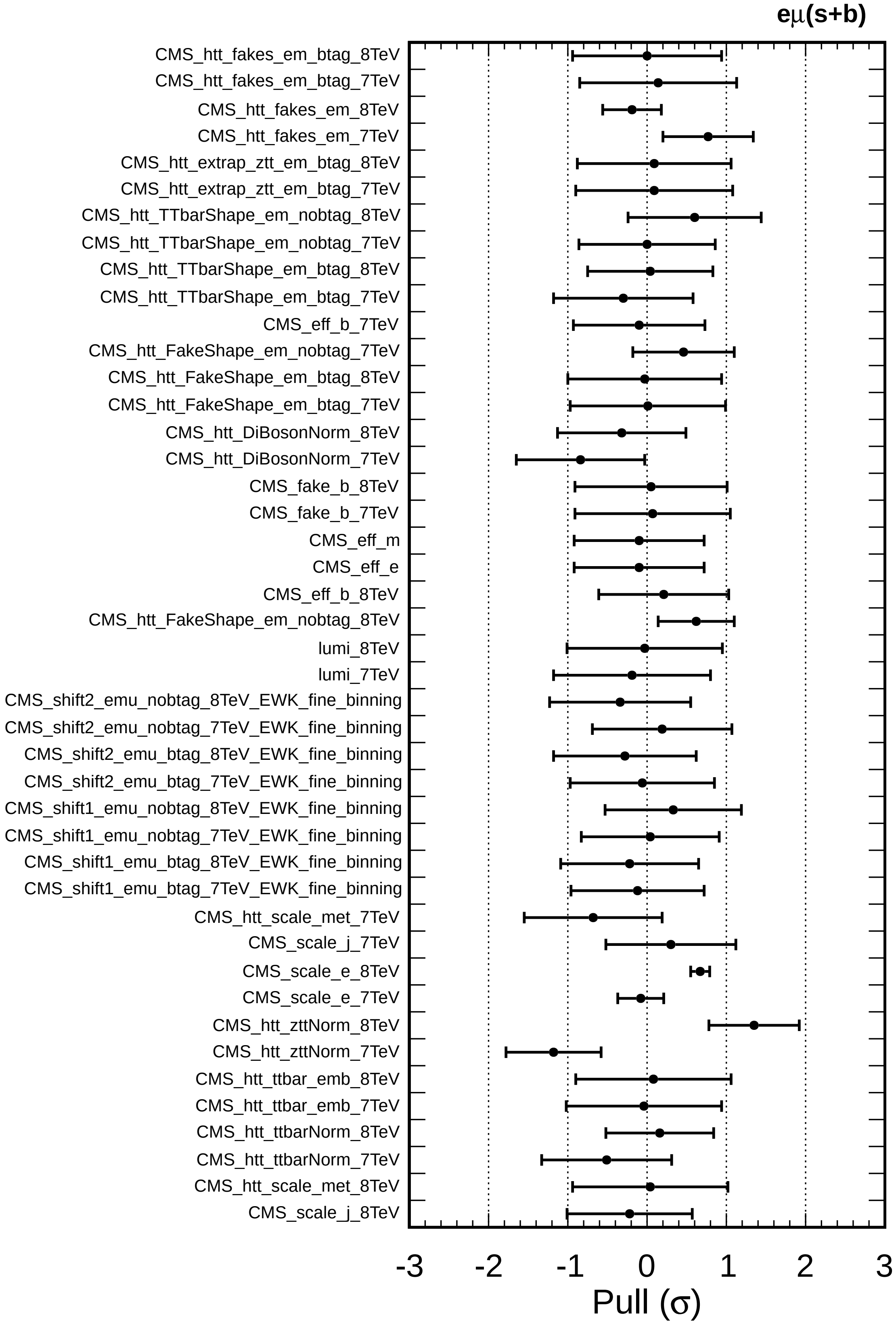

Figure C.1: Constraints and shifts of the uncertainties in the $e\mu$ channel after having performed the maximum likelihood fit for the $H_{\phi+b}$ hypothesis. The signal expectation used here is a single narrow resonance at a mass of 160 GeV. The naming follows official CMS collaboration naming scheme.

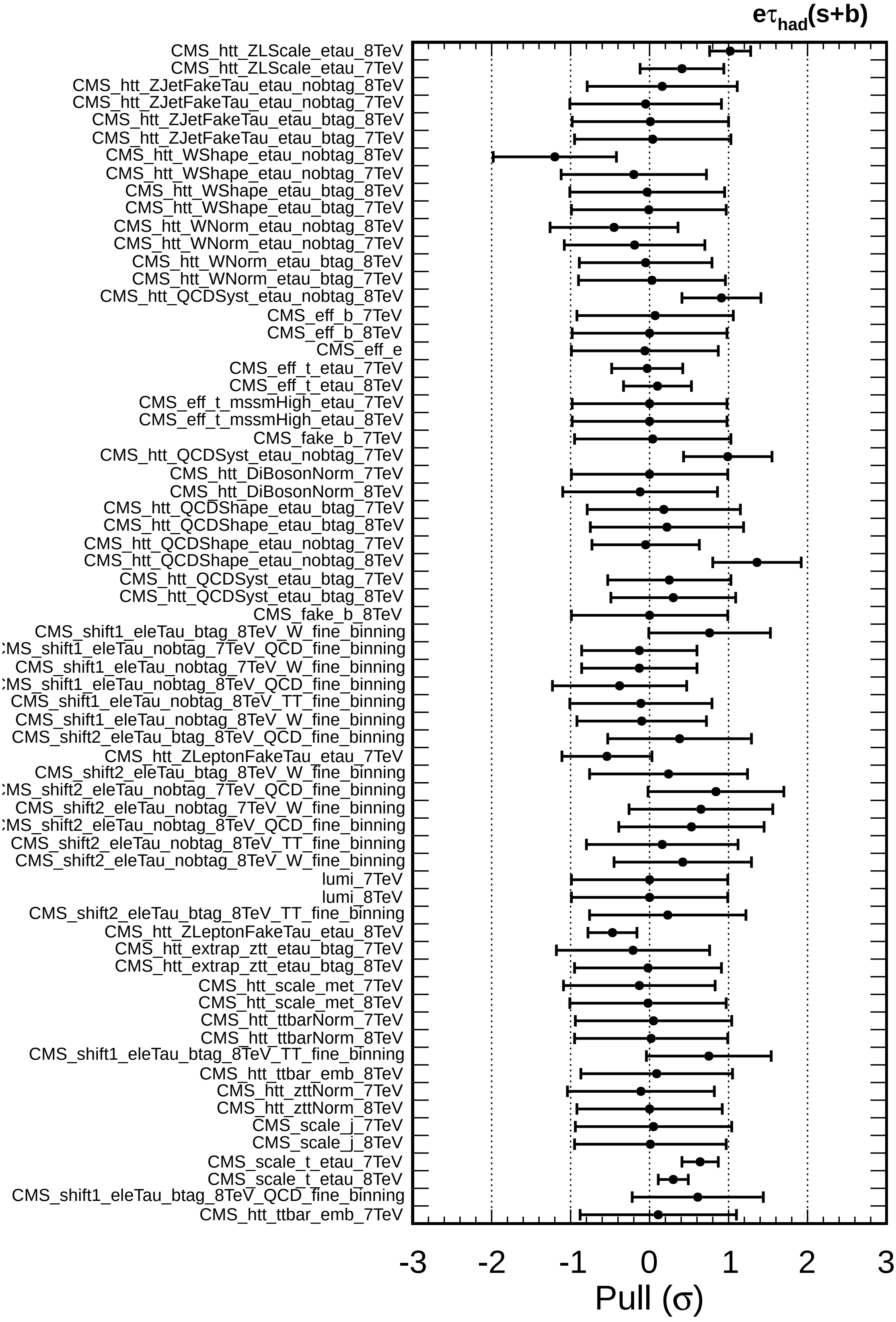

Figure C.2: Constraints and shifts of the uncertainties in the $e\tau_{had}$ channel after having performed the maximum likelihood fit for the $H_{\phi+b}$ hypothesis. The signal expectation used here is a single narrow resonance at a mass of 160 GeV. The naming follows official CMS collaboration naming scheme.

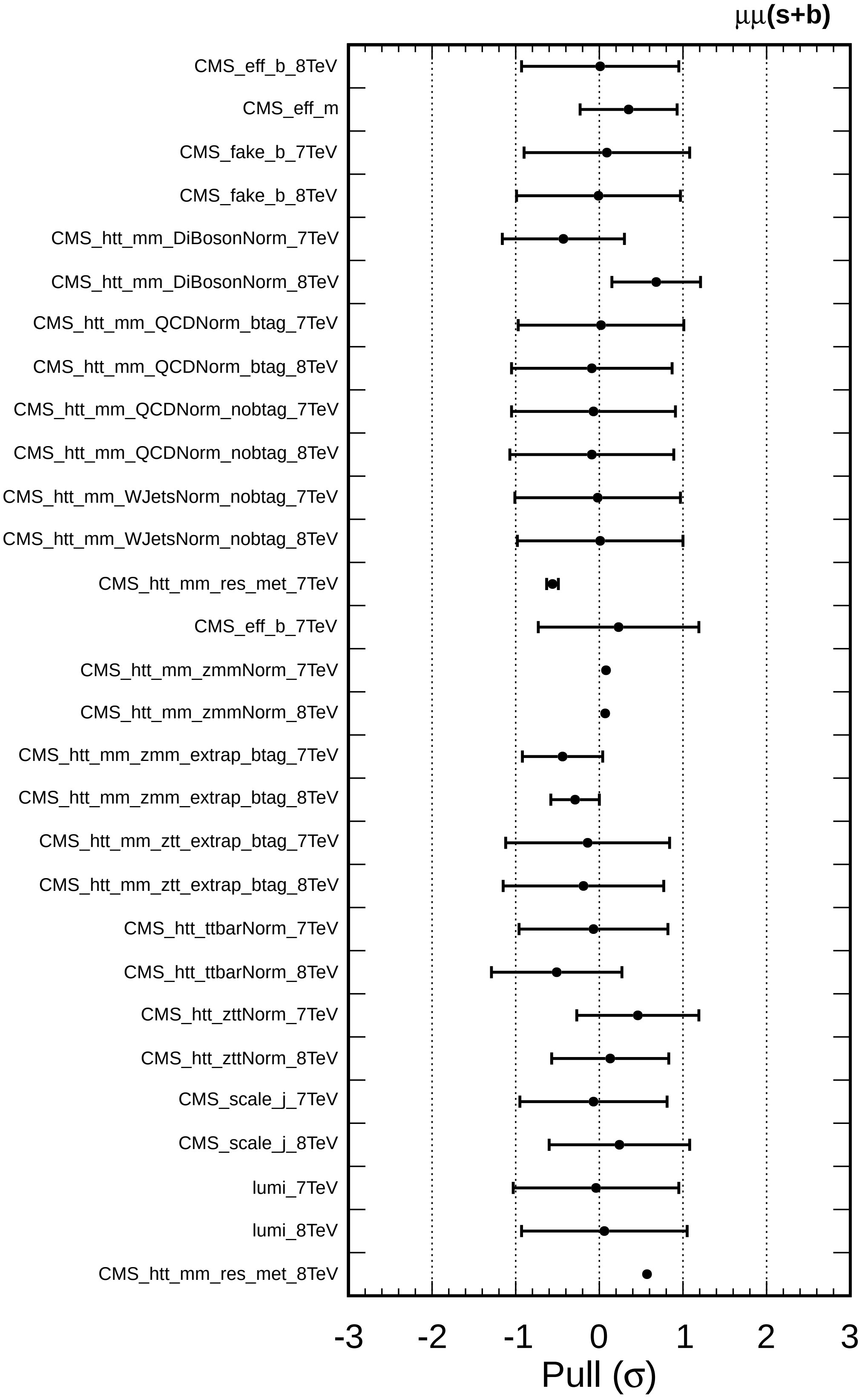

Figure C.3: Constraints and shifts of the uncertainties in the $\mu\mu$ channel after having performed the maximum likelihood fit for the $H_{\phi+b}$ hypothesis. The signal expectation used here is a single narrow resonance at a mass of 160 GeV. The naming follows official CMS collaboration naming scheme.

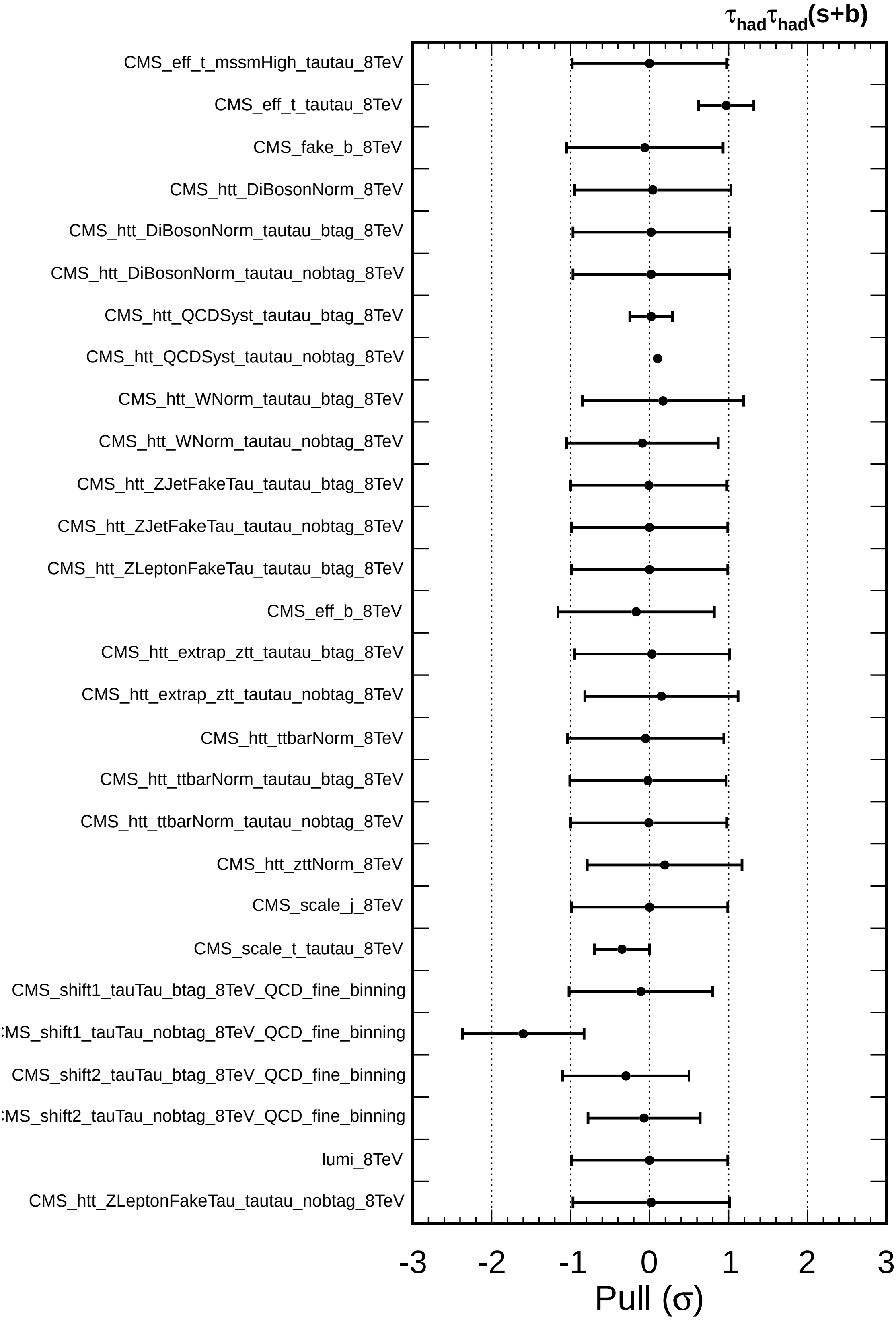

Figure C.4: Constraints and shifts of the uncertainties in the $\tau_{had}\tau_{had}$ channel after having performed the maximum likelihood fit for the $H_{\phi+b}$ hypothesis. The signal expectation used here is a single narrow resonance at a mass of 160 GeV. The naming follows official CMS collaboration naming scheme.

Appendix D

$\sigma \cdot \mathcal{B}$ Limits

Table D.1: Expected and observed 95% confidence level upper limits for $\sigma \cdot \mathcal{B}(\mathrm{gg}\phi)$ (pb) at 8 TeV center-of-mass energy as a function of m_ϕ. The H_b hypothesis is tested against $H_{\phi+b}$ hypothesis assuming a single narrow resonance. In figure 6.11 (a) the corresponding plots are shown.

BSM Higgs	Expected $\sigma \cdot \mathcal{B}$ (ggϕ) limit					Expected
m_ϕ [GeV]	-2σ	-1σ	Median	$+1\sigma$	$+2\sigma$	$\sigma \cdot \mathcal{B}$ (ggϕ) limit
90 GeV	13.81	18.56	26.09	37.21	50.87	50.21
100 GeV	10.50	14.05	19.69	27.93	37.78	31.33
120 GeV	2.29	3.03	4.14	5.71	7.56	7.38
130 GeV	1.33	1.76	2.41	3.26	4.26	4.39
140 GeV	$8.99 \cdot 10^{-1}$	1.20	1.63	2.18	2.82	2.27
160 GeV	$5.44 \cdot 10^{-1}$	$7.02 \cdot 10^{-1}$	$9.26 \cdot 10^{-1}$	1.23	1.58	$8.45 \cdot 10^{-1}$
180 GeV	$3.90 \cdot 10^{-1}$	$5.19 \cdot 10^{-1}$	$6.91 \cdot 10^{-1}$	$9.19 \cdot 10^{-1}$	1.17	$5.49 \cdot 10^{-1}$
200 GeV	$3.14 \cdot 10^{-1}$	$4.17 \cdot 10^{-1}$	$5.72 \cdot 10^{-1}$	$7.62 \cdot 10^{-1}$	$9.72 \cdot 10^{-1}$	$5.17 \cdot 10^{-1}$
250 GeV	$1.47 \cdot 10^{-1}$	$1.91 \cdot 10^{-1}$	$2.59 \cdot 10^{-1}$	$3.54 \cdot 10^{-1}$	$4.67 \cdot 10^{-1}$	$3.15 \cdot 10^{-1}$
300 GeV	$8.16 \cdot 10^{-2}$	$1.09 \cdot 10^{-1}$	$1.52 \cdot 10^{-1}$	$2.12 \cdot 10^{-1}$	$2.83 \cdot 10^{-1}$	$1.50 \cdot 10^{-1}$
350 GeV	$5.74 \cdot 10^{-2}$	$7.65 \cdot 10^{-2}$	$1.07 \cdot 10^{-1}$	$1.50 \cdot 10^{-1}$	$2.00 \cdot 10^{-1}$	$1.12 \cdot 10^{-1}$
400 GeV	$4.39 \cdot 10^{-2}$	$5.91 \cdot 10^{-2}$	$8.20 \cdot 10^{-2}$	$1.15 \cdot 10^{-1}$	$1.54 \cdot 10^{-1}$	$1.03 \cdot 10^{-1}$
450 GeV	$3.43 \cdot 10^{-2}$	$4.59 \cdot 10^{-2}$	$6.41 \cdot 10^{-2}$	$8.99 \cdot 10^{-2}$	$1.21 \cdot 10^{-1}$	$6.07 \cdot 10^{-2}$
500 GeV	$2.88 \cdot 10^{-2}$	$3.84 \cdot 10^{-2}$	$5.34 \cdot 10^{-2}$	$7.52 \cdot 10^{-2}$	$1.01 \cdot 10^{-1}$	$3.83 \cdot 10^{-2}$
600 GeV	$1.80 \cdot 10^{-2}$	$2.42 \cdot 10^{-2}$	$3.34 \cdot 10^{-2}$	$4.75 \cdot 10^{-2}$	$6.48 \cdot 10^{-2}$	$1.93 \cdot 10^{-2}$
700 GeV	$1.35 \cdot 10^{-2}$	$1.86 \cdot 10^{-2}$	$2.61 \cdot 10^{-2}$	$3.65 \cdot 10^{-2}$	$5.03 \cdot 10^{-2}$	$1.44 \cdot 10^{-2}$
800 GeV	$1.06 \cdot 10^{-2}$	$1.47 \cdot 10^{-2}$	$2.06 \cdot 10^{-2}$	$2.95 \cdot 10^{-2}$	$4.01 \cdot 10^{-2}$	$1.12 \cdot 10^{-2}$
900 GeV	$7.82 \cdot 10^{-3}$	$9.98 \cdot 10^{-3}$	$1.47 \cdot 10^{-2}$	$2.08 \cdot 10^{-2}$	$2.94 \cdot 10^{-2}$	$9.39 \cdot 10^{-3}$
1000 GeV	$7.02 \cdot 10^{-3}$	$8.96 \cdot 10^{-3}$	$1.32 \cdot 10^{-2}$	$1.87 \cdot 10^{-2}$	$2.64 \cdot 10^{-2}$	$8.50 \cdot 10^{-3}$

Table D.2: Expected range and observed 95% confidence level upper limits for $\sigma \cdot \mathcal{B}(\mathrm{bb}\phi)$ (pb) at 8 TeV center-of-mass energy as a function of m_ϕ. The H_b hypothesis is tested against $H_{\phi+b}$ hypothesis assuming a single narrow resonance. The corresponding plots are shown in figure 6.11 (b).

BSM Higgs	Expected $\sigma \cdot \mathcal{B}$ (bbϕ) limit					Observed
m_ϕ [GeV]	-2σ	-1σ	Median	$+1\sigma$	$+2\sigma$	$\sigma \cdot \mathcal{B}$ (bbϕ) limit
90 GeV	3.11	4.15	5.79	8.07	10.87	6.04
100 GeV	2.24	2.99	4.16	5.84	7.84	4.13
120 GeV	1.12	1.50	2.09	2.92	3.93	1.76
130 GeV	$8.20 \cdot 10^{-1}$	1.10	1.53	2.13	2.87	1.26
140 GeV	$6.61 \cdot 10^{-1}$	$8.85 \cdot 10^{-1}$	1.22	1.70	2.21	1.25
160 GeV	$3.85 \cdot 10^{-1}$	$4.98 \cdot 10^{-1}$	$6.68 \cdot 10^{-1}$	$9.05 \cdot 10^{-1}$	1.19	$8.14 \cdot 10^{-1}$
180 GeV	$2.68 \cdot 10^{-1}$	$3.47 \cdot 10^{-1}$	$4.73 \cdot 10^{-1}$	$6.49 \cdot 10^{-1}$	$8.56 \cdot 10^{-1}$	$6.59 \cdot 10^{-1}$
200 GeV	$2.44 \cdot 10^{-1}$	$3.12 \cdot 10^{-1}$	$4.15 \cdot 10^{-1}$	$5.55 \cdot 10^{-1}$	$7.18 \cdot 10^{-1}$	$5.53 \cdot 10^{-1}$
250 GeV	$1.39 \cdot 10^{-1}$	$1.79 \cdot 10^{-1}$	$2.39 \cdot 10^{-1}$	$3.20 \cdot 10^{-1}$	$4.18 \cdot 10^{-1}$	$2.16 \cdot 10^{-1}$
300 GeV	$6.88 \cdot 10^{-2}$	$9.15 \cdot 10^{-2}$	$1.28 \cdot 10^{-1}$	$1.80 \cdot 10^{-1}$	$2.43 \cdot 10^{-1}$	$9.75 \cdot 10^{-2}$
350 GeV	$5.26 \cdot 10^{-2}$	$6.90 \cdot 10^{-2}$	$9.54 \cdot 10^{-2}$	$1.32 \cdot 10^{-1}$	$1.77 \cdot 10^{-1}$	$6.38 \cdot 10^{-2}$
400 GeV	$5.11 \cdot 10^{-2}$	$6.53 \cdot 10^{-2}$	$8.66 \cdot 10^{-2}$	$1.17 \cdot 10^{-1}$	$1.54 \cdot 10^{-1}$	$6.13 \cdot 10^{-2}$
450 GeV	$2.98 \cdot 10^{-2}$	$3.97 \cdot 10^{-2}$	$5.53 \cdot 10^{-2}$	$7.86 \cdot 10^{-2}$	$1.06 \cdot 10^{-1}$	$4.31 \cdot 10^{-2}$
500 GeV	$2.45 \cdot 10^{-2}$	$3.33 \cdot 10^{-2}$	$4.69 \cdot 10^{-2}$	$6.59 \cdot 10^{-2}$	$9.02 \cdot 10^{-2}$	$3.20 \cdot 10^{-2}$
600 GeV	$1.64 \cdot 10^{-2}$	$2.27 \cdot 10^{-2}$	$3.19 \cdot 10^{-2}$	$4.53 \cdot 10^{-2}$	$6.19 \cdot 10^{-2}$	$2.03 \cdot 10^{-2}$
700 GeV	$1.31 \cdot 10^{-2}$	$1.80 \cdot 10^{-2}$	$2.53 \cdot 10^{-2}$	$3.62 \cdot 10^{-2}$	$4.93 \cdot 10^{-2}$	$1.73 \cdot 10^{-2}$
800 GeV	$1.11 \cdot 10^{-2}$	$1.54 \cdot 10^{-2}$	$2.16 \cdot 10^{-2}$	$3.08 \cdot 10^{-2}$	$4.20 \cdot 10^{-2}$	$1.65 \cdot 10^{-2}$
900 GeV	$8.54 \cdot 10^{-3}$	$1.18 \cdot 10^{-2}$	$1.66 \cdot 10^{-2}$	$2.42 \cdot 10^{-2}$	$3.36 \cdot 10^{-2}$	$1.48 \cdot 10^{-2}$
1000 GeV	$8.13 \cdot 10^{-3}$	$1.13 \cdot 10^{-2}$	$1.53 \cdot 10^{-2}$	$2.26 \cdot 10^{-2}$	$3.12 \cdot 10^{-2}$	$1.35 \cdot 10^{-2}$

Table D.3: Expected range and observed 95% confidence level upper limits for $\sigma \cdot \mathcal{B}(\mathrm{gg}\phi)$ (pb) at 8 TeV center-of-mass energy as a function of m_ϕ. The $H_{h_{\mathrm{SM}}+b}$ hypothesis is tested against the $H_{\phi+b}$ hypothesis assuming a single narrow resonance. In figure 6.11 (c) the corresponding plots are shown.

BSM Higgs	Expected $\sigma \cdot \mathcal{B}$ (ggϕ) limit					Expected
m_ϕ [GeV]	-2σ	-1σ	Median	$+1\sigma$	$+2\sigma$	$\sigma \cdot \mathcal{B}$ (ggϕ) limit
90 GeV	13.81	18.56	26.09	37.21	50.87	50.21
100 GeV	10.50	14.05	19.69	27.93	37.78	31.33
120 GeV	2.29	3.03	4.14	5.71	7.56	7.38
130 GeV	1.33	1.76	2.41	3.26	4.26	4.39
140 GeV	$8.99 \cdot 10^{-1}$	1.20	1.63	2.18	2.82	2.27
160 GeV	$5.44 \cdot 10^{-1}$	$7.02 \cdot 10^{-1}$	$9.26 \cdot 10^{-1}$	1.23	1.58	$8.45 \cdot 10^{-1}$
180 GeV	$3.90 \cdot 10^{-1}$	$5.19 \cdot 10^{-1}$	$6.91 \cdot 10^{-1}$	$9.19 \cdot 10^{-1}$	1.17	$5.49 \cdot 10^{-1}$
200 GeV	$3.14 \cdot 10^{-1}$	$4.17 \cdot 10^{-1}$	$5.72 \cdot 10^{-1}$	$7.62 \cdot 10^{-1}$	$9.72 \cdot 10^{-1}$	$5.17 \cdot 10^{-1}$
250 GeV	$1.47 \cdot 10^{-1}$	$1.91 \cdot 10^{-1}$	$2.59 \cdot 10^{-1}$	$3.54 \cdot 10^{-1}$	$4.67 \cdot 10^{-1}$	$3.15 \cdot 10^{-1}$
300 GeV	$8.16 \cdot 10^{-2}$	$1.09 \cdot 10^{-1}$	$1.52 \cdot 10^{-1}$	$2.12 \cdot 10^{-1}$	$2.83 \cdot 10^{-1}$	$1.50 \cdot 10^{-1}$
350 GeV	$5.74 \cdot 10^{-2}$	$7.65 \cdot 10^{-2}$	$1.07 \cdot 10^{-1}$	$1.50 \cdot 10^{-1}$	$2.00 \cdot 10^{-1}$	$1.12 \cdot 10^{-1}$
400 GeV	$4.39 \cdot 10^{-2}$	$5.91 \cdot 10^{-2}$	$8.20 \cdot 10^{-2}$	$1.15 \cdot 10^{-1}$	$1.54 \cdot 10^{-1}$	$1.03 \cdot 10^{-1}$
450 GeV	$3.43 \cdot 10^{-2}$	$4.59 \cdot 10^{-2}$	$6.41 \cdot 10^{-2}$	$8.99 \cdot 10^{-2}$	$1.21 \cdot 10^{-1}$	$6.07 \cdot 10^{-2}$
500 GeV	$2.88 \cdot 10^{-2}$	$3.84 \cdot 10^{-2}$	$5.34 \cdot 10^{-2}$	$7.52 \cdot 10^{-2}$	$1.01 \cdot 10^{-1}$	$3.83 \cdot 10^{-2}$
600 GeV	$1.80 \cdot 10^{-2}$	$2.42 \cdot 10^{-2}$	$3.34 \cdot 10^{-2}$	$4.75 \cdot 10^{-2}$	$6.48 \cdot 10^{-2}$	$1.93 \cdot 10^{-2}$
700 GeV	$1.35 \cdot 10^{-2}$	$1.86 \cdot 10^{-2}$	$2.61 \cdot 10^{-2}$	$3.65 \cdot 10^{-2}$	$5.03 \cdot 10^{-2}$	$1.44 \cdot 10^{-2}$
800 GeV	$1.06 \cdot 10^{-2}$	$1.47 \cdot 10^{-2}$	$2.06 \cdot 10^{-2}$	$2.95 \cdot 10^{-2}$	$4.01 \cdot 10^{-2}$	$1.12 \cdot 10^{-2}$
900 GeV	$7.82 \cdot 10^{-3}$	$9.98 \cdot 10^{-3}$	$1.47 \cdot 10^{-2}$	$2.08 \cdot 10^{-2}$	$2.94 \cdot 10^{-2}$	$9.39 \cdot 10^{-3}$
1000 GeV	$7.02 \cdot 10^{-3}$	$8.96 \cdot 10^{-3}$	$1.32 \cdot 10^{-2}$	$1.87 \cdot 10^{-2}$	$2.64 \cdot 10^{-2}$	$8.50 \cdot 10^{-3}$

Table D.4: Expected and observed 95% confidence level upper limits for $\sigma \cdot \mathcal{B}(\mathrm{bb}\phi)$ (pb) at 8 TeV center-of-mass energy as a function of m_ϕ. The $H_{h_{\mathrm{SM}}+b}$ hypothesis is tested against $H_{\phi+b}$ hypothesis assuming a single narrow resonance. The corresponding plots are shown in figure 6.11 (d).

BSM Higgs	Expected $\sigma \cdot \mathcal{B}$ (bbϕ) limit					Observed
m_ϕ [GeV]	-2σ	-1σ	Median	$+1\sigma$	$+2\sigma$	$\sigma \cdot \mathcal{B}$ (bbϕ) limit
90 GeV	3.11	4.15	5.79	8.07	10.87	6.04
100 GeV	2.24	2.99	4.16	5.84	7.84	4.13
120 GeV	1.12	1.50	2.09	2.92	3.93	1.76
130 GeV	$8.20 \cdot 10^{-1}$	1.10	1.53	2.13	2.87	1.26
140 GeV	$6.61 \cdot 10^{-1}$	$8.85 \cdot 10^{-1}$	1.22	1.70	2.21	1.25
160 GeV	$3.85 \cdot 10^{-1}$	$4.98 \cdot 10^{-1}$	$6.68 \cdot 10^{-1}$	$9.05 \cdot 10^{-1}$	1.19	$8.14 \cdot 10^{-1}$
180 GeV	$2.68 \cdot 10^{-1}$	$3.47 \cdot 10^{-1}$	$4.73 \cdot 10^{-1}$	$6.49 \cdot 10^{-1}$	$8.56 \cdot 10^{-1}$	$6.59 \cdot 10^{-1}$
200 GeV	$2.44 \cdot 10^{-1}$	$3.12 \cdot 10^{-1}$	$4.15 \cdot 10^{-1}$	$5.55 \cdot 10^{-1}$	$7.18 \cdot 10^{-1}$	$5.53 \cdot 10^{-1}$
250 GeV	$1.39 \cdot 10^{-1}$	$1.79 \cdot 10^{-1}$	$2.39 \cdot 10^{-1}$	$3.20 \cdot 10^{-1}$	$4.18 \cdot 10^{-1}$	$2.16 \cdot 10^{-1}$
300 GeV	$6.88 \cdot 10^{-2}$	$9.15 \cdot 10^{-2}$	$1.28 \cdot 10^{-1}$	$1.80 \cdot 10^{-1}$	$2.43 \cdot 10^{-1}$	$9.75 \cdot 10^{-2}$
350 GeV	$5.26 \cdot 10^{-2}$	$6.90 \cdot 10^{-2}$	$9.54 \cdot 10^{-2}$	$1.32 \cdot 10^{-1}$	$1.77 \cdot 10^{-1}$	$6.38 \cdot 10^{-2}$
400 GeV	$5.11 \cdot 10^{-2}$	$6.53 \cdot 10^{-2}$	$8.66 \cdot 10^{-2}$	$1.17 \cdot 10^{-1}$	$1.54 \cdot 10^{-1}$	$6.13 \cdot 10^{-2}$
450 GeV	$2.98 \cdot 10^{-2}$	$3.97 \cdot 10^{-2}$	$5.53 \cdot 10^{-2}$	$7.86 \cdot 10^{-2}$	$1.06 \cdot 10^{-1}$	$4.31 \cdot 10^{-2}$
500 GeV	$2.45 \cdot 10^{-2}$	$3.33 \cdot 10^{-2}$	$4.69 \cdot 10^{-2}$	$6.59 \cdot 10^{-2}$	$9.02 \cdot 10^{-2}$	$3.20 \cdot 10^{-2}$
600 GeV	$1.64 \cdot 10^{-2}$	$2.27 \cdot 10^{-2}$	$3.19 \cdot 10^{-2}$	$4.53 \cdot 10^{-2}$	$6.19 \cdot 10^{-2}$	$2.03 \cdot 10^{-2}$
700 GeV	$1.31 \cdot 10^{-2}$	$1.80 \cdot 10^{-2}$	$2.53 \cdot 10^{-2}$	$3.62 \cdot 10^{-2}$	$4.93 \cdot 10^{-2}$	$1.73 \cdot 10^{-2}$
800 GeV	$1.11 \cdot 10^{-2}$	$1.54 \cdot 10^{-2}$	$2.16 \cdot 10^{-2}$	$3.08 \cdot 10^{-2}$	$4.20 \cdot 10^{-2}$	$1.65 \cdot 10^{-2}$
900 GeV	$8.54 \cdot 10^{-3}$	$1.18 \cdot 10^{-2}$	$1.66 \cdot 10^{-2}$	$2.42 \cdot 10^{-2}$	$3.36 \cdot 10^{-2}$	$1.48 \cdot 10^{-2}$
1000 GeV	$8.13 \cdot 10^{-3}$	$1.13 \cdot 10^{-2}$	$1.53 \cdot 10^{-2}$	$2.26 \cdot 10^{-2}$	$3.12 \cdot 10^{-2}$	$1.35 \cdot 10^{-2}$

Table D.5: Expected and observed 95% confidence level upper limits for $\sigma \cdot \mathcal{B}(\mathrm{gg}\phi)$ (pb) at 8 TeV center-of-mass energy as a function of m_ϕ. The expected limit is obtained by replacing the observed by the sum of all backgrounds adding the SM Higgs boson. Then the observed exclusion limit is computed multiple times letting it float within its statistical uncertainties to get 1 and 2σ bands as well as the median expected limit. In figure 6.11 (e) the corresponding plots are shown.

BSM Higgs	Expected $\sigma \cdot \mathcal{B}$ (ggϕ) limit					Expected
m_ϕ [GeV]	-2σ	-1σ	Median	$+1\sigma$	$+2\sigma$	$\sigma \cdot \mathcal{B}$ (ggϕ) limit
90 GeV	16.75	20.36	25.45	31.65	37.34	50.21
100 GeV	13.54	16.66	21.18	27.00	34.57	31.33
120 GeV	2.96	3.88	5.14	6.65	8.09	7.38
130 GeV	1.51	2.05	2.75	3.63	4.55	4.39
140 GeV	$9.42 \cdot 10^{-1}$	1.24	1.68	2.23	2.82	2.27
160 GeV	$4.74 \cdot 10^{-1}$	$6.15 \cdot 10^{-1}$	$8.55 \cdot 10^{-1}$	1.14	1.50	$8.45 \cdot 10^{-1}$
180 GeV	$3.12 \cdot 10^{-1}$	$4.05 \cdot 10^{-1}$	$5.52 \cdot 10^{-1}$	$7.41 \cdot 10^{-1}$	$9.74 \cdot 10^{-1}$	$5.49 \cdot 10^{-1}$
200 GeV	$2.37 \cdot 10^{-1}$	$3.08 \cdot 10^{-1}$	$4.19 \cdot 10^{-1}$	$5.56 \cdot 10^{-1}$	$7.48 \cdot 10^{-1}$	$5.17 \cdot 10^{-1}$
250 GeV	$1.30 \cdot 10^{-1}$	$1.69 \cdot 10^{-1}$	$2.28 \cdot 10^{-1}$	$3.11 \cdot 10^{-1}$	$3.95 \cdot 10^{-1}$	$3.15 \cdot 10^{-1}$
300 GeV	$7.95 \cdot 10^{-2}$	$1.05 \cdot 10^{-1}$	$1.43 \cdot 10^{-1}$	$1.97 \cdot 10^{-1}$	$2.53 \cdot 10^{-1}$	$1.50 \cdot 10^{-1}$
350 GeV	$6.05 \cdot 10^{-2}$	$7.71 \cdot 10^{-2}$	$1.02 \cdot 10^{-1}$	$1.38 \cdot 10^{-1}$	$1.80 \cdot 10^{-1}$	$1.12 \cdot 10^{-1}$
400 GeV	$4.68 \cdot 10^{-2}$	$6.01 \cdot 10^{-2}$	$7.94 \cdot 10^{-2}$	$1.08 \cdot 10^{-1}$	$1.41 \cdot 10^{-1}$	$1.03 \cdot 10^{-1}$
450 GeV	$3.76 \cdot 10^{-2}$	$4.77 \cdot 10^{-2}$	$6.36 \cdot 10^{-2}$	$8.39 \cdot 10^{-2}$	$1.11 \cdot 10^{-1}$	$6.07 \cdot 10^{-2}$
500 GeV	$3.20 \cdot 10^{-2}$	$4.01 \cdot 10^{-2}$	$5.31 \cdot 10^{-2}$	$7.14 \cdot 10^{-2}$	$9.28 \cdot 10^{-2}$	$3.83 \cdot 10^{-2}$
600 GeV	$1.97 \cdot 10^{-2}$	$2.54 \cdot 10^{-2}$	$3.49 \cdot 10^{-2}$	$4.70 \cdot 10^{-2}$	$6.22 \cdot 10^{-2}$	$1.93 \cdot 10^{-2}$
700 GeV	$1.49 \cdot 10^{-2}$	$1.95 \cdot 10^{-2}$	$2.72 \cdot 10^{-2}$	$3.71 \cdot 10^{-2}$	$4.73 \cdot 10^{-2}$	$1.44 \cdot 10^{-2}$
800 GeV	$1.19 \cdot 10^{-2}$	$1.53 \cdot 10^{-2}$	$2.09 \cdot 10^{-2}$	$2.89 \cdot 10^{-2}$	$3.91 \cdot 10^{-2}$	$1.12 \cdot 10^{-2}$
900 GeV	$8.55 \cdot 10^{-3}$	$1.11 \cdot 10^{-2}$	$1.51 \cdot 10^{-2}$	$2.11 \cdot 10^{-2}$	$2.89 \cdot 10^{-2}$	$9.39 \cdot 10^{-3}$
1000 GeV	$7.47 \cdot 10^{-3}$	$9.80 \cdot 10^{-3}$	$1.30 \cdot 10^{-2}$	$1.86 \cdot 10^{-2}$	$2.54 \cdot 10^{-2}$	$8.50 \cdot 10^{-3}$

Table D.6: Expected range and observed 95% confidence level upper limits for $\sigma \cdot \mathcal{B}(\mathrm{bb}\phi)$ (pb) at 8 TeV center-of-mass energy as a function of m_ϕ. The expected limit is obtained by replacing the observed by the sum of all backgrounds adding the SM Higgs boson. Then the observed exclusion limit is computed multiple times letting it float within its statistical uncertainties to get 1 and 2σ bands as well as the median expected limit. The corresponding plots are shown in figure 6.11 (f).

BSM Higgs	Expected $\sigma \cdot \mathcal{B}$ (bbϕ) limit					Observed
m_ϕ [GeV]	-2σ	-1σ	Median	$+1\sigma$	$+2\sigma$	$\sigma \cdot \mathcal{B}$ (bbϕ) limit
90 GeV	3.25	4.19	5.69	7.54	9.74	6.04
100 GeV	2.43	3.07	4.14	5.69	7.19	4.13
120 GeV	1.18	1.53	2.08	2.82	3.72	1.76
130 GeV	$8.31 \cdot 10^{-1}$	1.08	1.47	1.97	2.60	1.26
140 GeV	$6.21 \cdot 10^{-1}$	$8.24 \cdot 10^{-1}$	1.10	1.46	1.91	1.25
160 GeV	$3.80 \cdot 10^{-1}$	$4.99 \cdot 10^{-1}$	$6.68 \cdot 10^{-1}$	$8.94 \cdot 10^{-1}$	1.18	$8.14 \cdot 10^{-1}$
180 GeV	$2.64 \cdot 10^{-1}$	$3.45 \cdot 10^{-1}$	$4.59 \cdot 10^{-1}$	$6.27 \cdot 10^{-1}$	$8.40 \cdot 10^{-1}$	$6.59 \cdot 10^{-1}$
200 GeV	$1.92 \cdot 10^{-1}$	$2.50 \cdot 10^{-1}$	$3.39 \cdot 10^{-1}$	$4.60 \cdot 10^{-1}$	$6.10 \cdot 10^{-1}$	$5.53 \cdot 10^{-1}$
250 GeV	$1.09 \cdot 10^{-1}$	$1.41 \cdot 10^{-1}$	$1.90 \cdot 10^{-1}$	$2.62 \cdot 10^{-1}$	$3.42 \cdot 10^{-1}$	$2.16 \cdot 10^{-1}$
300 GeV	$7.33 \cdot 10^{-2}$	$9.15 \cdot 10^{-2}$	$1.25 \cdot 10^{-1}$	$1.70 \cdot 10^{-1}$	$2.24 \cdot 10^{-1}$	$9.75 \cdot 10^{-2}$
350 GeV	$5.30 \cdot 10^{-2}$	$6.58 \cdot 10^{-2}$	$8.95 \cdot 10^{-2}$	$1.20 \cdot 10^{-1}$	$1.60 \cdot 10^{-1}$	$6.38 \cdot 10^{-2}$
400 GeV	$4.09 \cdot 10^{-2}$	$5.30 \cdot 10^{-2}$	$6.92 \cdot 10^{-2}$	$9.59 \cdot 10^{-2}$	$1.26 \cdot 10^{-1}$	$6.13 \cdot 10^{-2}$
450 GeV	$3.15 \cdot 10^{-2}$	$4.09 \cdot 10^{-2}$	$5.51 \cdot 10^{-2}$	$7.68 \cdot 10^{-2}$	$9.81 \cdot 10^{-2}$	$4.31 \cdot 10^{-2}$
500 GeV	$2.70 \cdot 10^{-2}$	$3.41 \cdot 10^{-2}$	$4.63 \cdot 10^{-2}$	$6.33 \cdot 10^{-2}$	$8.44 \cdot 10^{-2}$	$3.20 \cdot 10^{-2}$
600 GeV	$1.77 \cdot 10^{-2}$	$2.34 \cdot 10^{-2}$	$3.16 \cdot 10^{-2}$	$4.37 \cdot 10^{-2}$	$5.66 \cdot 10^{-2}$	$2.03 \cdot 10^{-2}$
700 GeV	$1.35 \cdot 10^{-2}$	$1.78 \cdot 10^{-2}$	$2.44 \cdot 10^{-2}$	$3.38 \cdot 10^{-2}$	$4.40 \cdot 10^{-2}$	$1.73 \cdot 10^{-2}$
800 GeV	$1.16 \cdot 10^{-2}$	$1.49 \cdot 10^{-2}$	$2.01 \cdot 10^{-2}$	$2.73 \cdot 10^{-2}$	$3.77 \cdot 10^{-2}$	$1.65 \cdot 10^{-2}$
900 GeV	$8.81 \cdot 10^{-3}$	$1.15 \cdot 10^{-2}$	$1.52 \cdot 10^{-2}$	$2.12 \cdot 10^{-2}$	$3.00 \cdot 10^{-2}$	$1.48 \cdot 10^{-2}$
1000 GeV	$8.15 \cdot 10^{-3}$	$1.03 \cdot 10^{-2}$	$1.37 \cdot 10^{-2}$	$1.92 \cdot 10^{-2}$	$2.72 \cdot 10^{-2}$	$1.35 \cdot 10^{-2}$

Table D.7: Expected and observed 95% confidence level upper limits for $\sigma \cdot \mathcal{B}(\mathrm{gg}\phi)$ (pb) at 8 TeV center-of-mass energy as a function of m_ϕ. The H_b hypothesis is tested against the $H_{\phi+b}$ hypothesis. The limits in columns 2-5 are given for the projection to 13 TeV and 300 fb^{-1} while column 6 gives the median expected limit of the $\phi \to \tau\tau$ analysis scaled by the expected parton luminosity to 13 TeV. Both are shown in figure 6.13 (left).

BSM Higgs	Expected limit at 13 TeV and 300 fb^{-1}					Expected (8 → 13 TeV) arXiv:1408.3316
m_ϕ [GeV]	-2σ	-1σ	Median	$+1\sigma$	$+2\sigma$	
90 GeV	8.70	11.6	16.2	22.7	30.5	55.5
100 GeV	7.55	10.0	13.8	18.9	25.0	42.9
120 GeV	1.25	1.68	2.31	3.23	4.31	9.30
130 GeV	$5.77 \cdot 10^{-1}$	$7.66 \cdot 10^{-1}$	1.07	1.48	1.97	5.43
140 GeV	$3.59 \cdot 10^{-1}$	$4.48 \cdot 10^{-1}$	$6.64 \cdot 10^{-1}$	$9.26 \cdot 10^{-1}$	1.23	3.83
160 GeV	$2.11 \cdot 10^{-1}$	$2.83 \cdot 10^{-1}$	$3.91 \cdot 10^{-1}$	$5.45 \cdot 10^{-1}$	$7.23 \cdot 10^{-1}$	2.27
180 GeV	$1.58 \cdot 10^{-1}$	$2.10 \cdot 10^{-1}$	$2.92 \cdot 10^{-1}$	$4.04 \cdot 10^{-1}$	$5.40 \cdot 10^{-1}$	1.84
200 GeV	$1.36 \cdot 10^{-1}$	$1.81 \cdot 10^{-1}$	$2.50 \cdot 10^{-1}$	$3.48 \cdot 10^{-1}$	$4.65 \cdot 10^{-1}$	1.65
250 GeV	$7.79 \cdot 10^{-2}$	$1.04 \cdot 10^{-1}$	$1.44 \cdot 10^{-1}$	$2.01 \cdot 10^{-1}$	$2.68 \cdot 10^{-1}$	$7.77 \cdot 10^{-1}$
300 GeV	$4.85 \cdot 10^{-2}$	$6.44 \cdot 10^{-2}$	$8.97 \cdot 10^{-2}$	$1.25 \cdot 10^{-1}$	$1.67 \cdot 10^{-1}$	$4.68 \cdot 10^{-1}$
350 GeV	$3.87 \cdot 10^{-2}$	$5.18 \cdot 10^{-2}$	$7.16 \cdot 10^{-2}$	$9.99 \cdot 10^{-2}$	$1.33 \cdot 10^{-1}$	$3.42 \cdot 10^{-1}$
400 GeV	$3.16 \cdot 10^{-2}$	$4.22 \cdot 10^{-2}$	$5.89 \cdot 10^{-2}$	$8.26 \cdot 10^{-2}$	$1.11 \cdot 10^{-1}$	$2.68 \cdot 10^{-1}$
450 GeV	$3.20 \cdot 10^{-2}$	$4.26 \cdot 10^{-2}$	$5.95 \cdot 10^{-2}$	$8.30 \cdot 10^{-2}$	$1.12 \cdot 10^{-1}$	$2.22 \cdot 10^{-1}$
500 GeV	$3.35 \cdot 10^{-2}$	$4.46 \cdot 10^{-2}$	$6.22 \cdot 10^{-2}$	$8.68 \cdot 10^{-2}$	$1.12 \cdot 10^{-1}$	$2.03 \cdot 10^{-1}$
600 GeV	$1.89 \cdot 10^{-2}$	$2.53 \cdot 10^{-2}$	$3.50 \cdot 10^{-2}$	$4.91 \cdot 10^{-2}$	$6.59 \cdot 10^{-2}$	$1.42 \cdot 10^{-1}$
700 GeV	$1.38 \cdot 10^{-2}$	$1.83 \cdot 10^{-2}$	$2.54 \cdot 10^{-2}$	$3.70 \cdot 10^{-2}$	$3.54 \cdot 10^{-2}$	$1.12 \cdot 10^{-1}$
800 GeV	$9.07 \cdot 10^{-3}$	$2.37 \cdot 10^{-2}$	$1.21 \cdot 10^{-2}$	$1.69 \cdot 10^{-2}$	$3.18 \cdot 10^{-2}$	$1.00 \cdot 10^{-1}$
900 GeV	$6.55 \cdot 10^{-3}$	$8.69 \cdot 10^{-3}$	$1.21 \cdot 10^{-2}$	$1.69 \cdot 10^{-2}$	$2.26 \cdot 10^{-2}$	$7.35 \cdot 10^{-2}$
1000 GeV	$5.01 \cdot 10^{-3}$	$6.86 \cdot 10^{-3}$	$1.36 \cdot 10^{-2}$	$9.62 \cdot 10^{-3}$	$1.83 \cdot 10^{-2}$	$6.92 \cdot 10^{-2}$

Table D.8: Expected 95% confidence level upper limits for $\sigma \cdot \mathcal{B}(\mathrm{bb}\phi)$ (pb) at 8 TeV center-of-mass energy as a function of m_ϕ. The H_b hypothesis is tested against the $H_{\phi+b}$ hypothesis. The limits in columns 2-5 are given for the projection to 13 TeV and 300 fb^{-1} while column 6 gives the median expected limit of the $\phi \to \tau\tau$ analysis scaled by the expected parton luminosity to 13 TeV. Both are shown in figure 6.13 (right).

BSM Higgs	Expected limit at 13 TeV and 300 fb^{-1}					Expected (8 → 13 TeV)
m_ϕ [GeV]	-2σ	-1σ	Median	$+1\sigma$	$+2\sigma$	arXiv:1408.3316
90 GeV	2.23	2.97	4.09	5.72	7.64	12.3
100 GeV	1.35	1.81	2.50	3.46	4.61	9.06
120 GeV	$5.17 \cdot 10^{-1}$	$6.84 \cdot 10^{-1}$	$9.52 \cdot 10^{-1}$	1.32	1.76	4.70
130 GeV	$3.58 \cdot 10^{-1}$	$4.72 \cdot 10^{-1}$	$6.57 \cdot 10^{-1}$	$9.10 \cdot 10^{-1}$	1.21	3.44
140 GeV	$2.79 \cdot 10^{-1}$	$3.72 \cdot 10^{-1}$	$5.13 \cdot 10^{-1}$	$7.12 \cdot 10^{-1}$	$9.47 \cdot 10^{-1}$	2.88
160 GeV	$1.90 \cdot 10^{-1}$	$2.52 \cdot 10^{-1}$	$3.51 \cdot 10^{-1}$	$4.87 \cdot 10^{-1}$	$6.49 \cdot 10^{-1}$	1.64
180 GeV	$1.48 \cdot 10^{-1}$	$1.97 \cdot 10^{-1}$	$2.73 \cdot 10^{-1}$	$3.79 \cdot 10^{-1}$	$5.08 \cdot 10^{-1}$	1.26
200 GeV	$1.17 \cdot 10^{-1}$	$1.56 \cdot 10^{-1}$	$2.16 \cdot 10^{-1}$	$3.01 \cdot 10^{-1}$	$4.03 \cdot 10^{-1}$	1.19
250 GeV	$7.63 \cdot 10^{-1}$	$1.02 \cdot 10^{-1}$	$1.41 \cdot 10^{-1}$	$1.97 \cdot 10^{-1}$	$2.63 \cdot 10^{-1}$	$7.19 \cdot 10^{-1}$
300 GeV	$5.13 \cdot 10^{-2}$	$6.87 \cdot 10^{-2}$	$9.49 \cdot 10^{-2}$	$1.33 \cdot 10^{-1}$	$1.77 \cdot 10^{-1}$	$3.95 \cdot 10^{-1}$
350 GeV	$3.86 \cdot 10^{-2}$	$5.17 \cdot 10^{-2}$	$7.14 \cdot 10^{-2}$	$1.00 \cdot 10^{-1}$	$1.33 \cdot 10^{-1}$	$3.04 \cdot 10^{-1}$
400 GeV	$3.05 \cdot 10^{-2}$	$4.06 \cdot 10^{-2}$	$5.66 \cdot 10^{-2}$	$7.89 \cdot 10^{-2}$	$1.06 \cdot 10^{-1}$	$2.84 \cdot 10^{-1}$
450 GeV	$2.51 \cdot 10^{-2}$	$3.36 \cdot 10^{-2}$	$4.67 \cdot 10^{-2}$	$6.51 \cdot 10^{-2}$	$8.76 \cdot 10^{-2}$	$1.92 \cdot 10^{-1}$
500 GeV	$2.23 \cdot 10^{-2}$	$2.99 \cdot 10^{-2}$	$4.12 \cdot 10^{-2}$	$5.79 \cdot 10^{-2}$	$7.77 \cdot 10^{-2}$	$1.78 \cdot 10^{-1}$
600 GeV	$1.59 \cdot 10^{-2}$	$2.12 \cdot 10^{-2}$	$2.95 \cdot 10^{-2}$	$4.14 \cdot 10^{-2}$	$5.56 \cdot 10^{-2}$	$1.36 \cdot 10^{-1}$
700 GeV	$1.18 \cdot 10^{-2}$	$1.58 \cdot 10^{-2}$	$2.19 \cdot 10^{-2}$	$3.08 \cdot 10^{-2}$	$4.13 \cdot 10^{-2}$	$1.16 \cdot 10^{-1}$
800 GeV	$8.16 \cdot 10^{-3}$	$1.09 \cdot 10^{-2}$	$1.53 \cdot 10^{-2}$	$2.16 \cdot 10^{-2}$	$2.91 \cdot 10^{-2}$	$1.05 \cdot 10^{-1}$
900 GeV	$5.53 \cdot 10^{-3}$	$7.45 \cdot 10^{-3}$	$1.06 \cdot 10^{-2}$	$1.49 \cdot 10^{-2}$	$2.02 \cdot 10^{-2}$	$8.27 \cdot 10^{-2}$
1000 GeV	$3.66 \cdot 10^{-3}$	$5.27 \cdot 10^{-3}$	$7.89 \cdot 10^{-3}$	$1.15 \cdot 10^{-2}$	$1.60 \cdot 10^{-2}$	$8.01 \cdot 10^{-2}$

Appendix E

Likelihood Scan of the ggϕ-bbϕ Plane

In figure E.1 the masses which have not been shown in the body of this thesis are displayed.

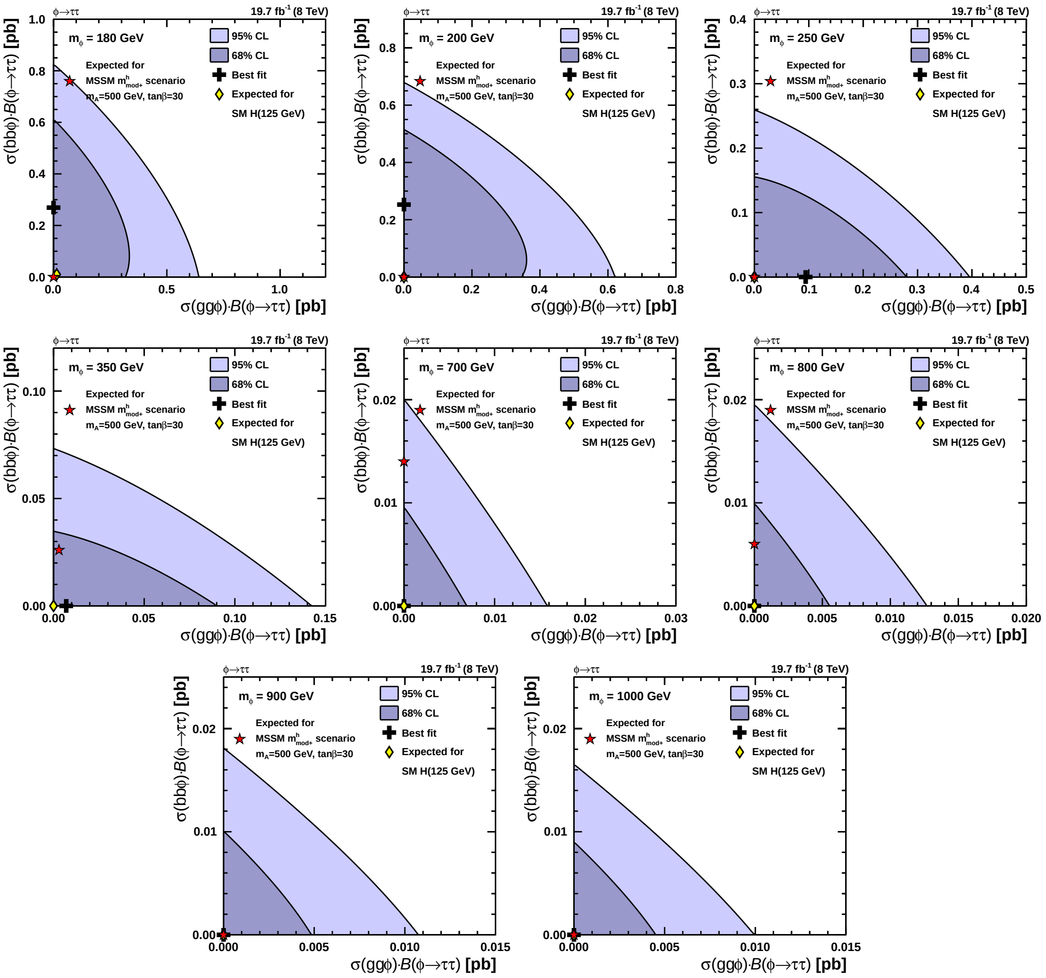

Figure E.1: Likelihood scan of $\sigma{\cdot}\mathrm{BR}(\mathrm{gg}\phi)$ and $\sigma{\cdot}\mathrm{BR}(\mathrm{bb}\phi)$ at 8 TeV center-of-mass energy for different Higgs boson masses. The best fit point of the SM 125 GeV Higgs boson is plotted as a yellow diamond. The red diamond shows the best fit point for a a hypothetical signal in the MSSM $m_h^{\mathrm{mod+}}$ scenario with $m_A = 500\,\mathrm{GeV}$ and $\tan\beta = 30$.

Appendix F

Background against BSM Signal Model

In figure F.1 the results for the MSSM m_h^{max} (a), $m_h^{\text{mod-}}$ (b), τ-phobic (c) and low-m_H (d) scenario are shown. In contrast to all other MSSM scenarios in the low-m_H scenario the heavy scalar Higgs boson H sits at 125 GeV and has the properties of the SM like Higgs boson. No significant deviations from the expectation are observed. The MSSM light-stau (a), light-stop (b), τ-phobic and low$-\tan\beta$-high (c) scenarios are shown in figure F.2 as well as the two Higgs Double Model of type-II (d). The numerical results can be found in tables F.1.

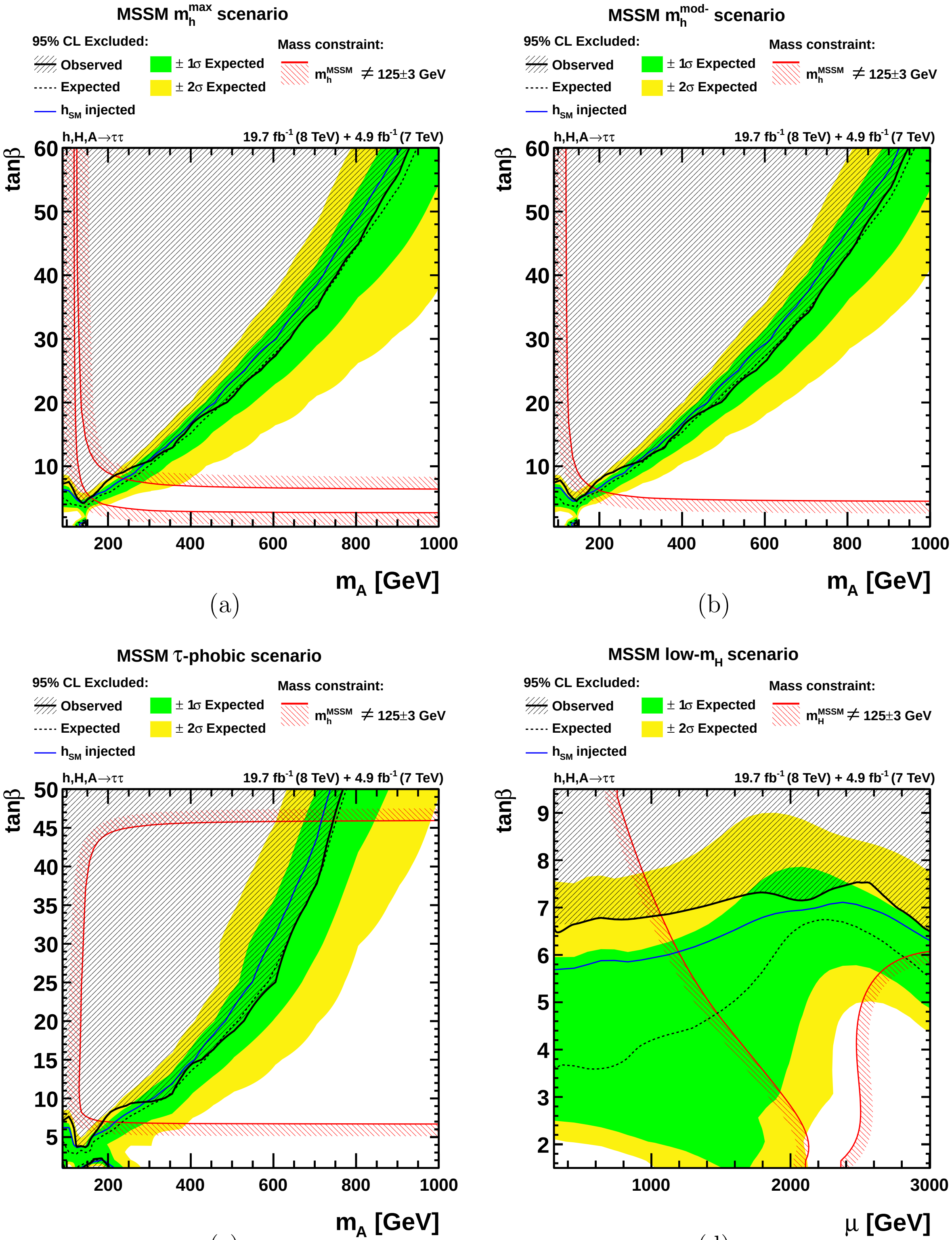

(a) (b)

(c) (d)

Figure F.1: The figures show the 95% confidence level exclusion limit on the MSSM m_h^{max} (a), $m_h^{\text{mod-}}$ (b), τ-phobic (c) and low-m_H (d) scenario. The region where the SM like Higgs boson is not within $125 \pm 3\,\text{GeV}$ is indicated by the red area. The observed excluded area is shaded with black lines. The median expected limit is plotted as a dashed black line. The expected ± 1 and $\pm 2\sigma$ bands are shown as green or yellow bands, respectively. The blue line illustrates the expected exclusion limit if a SM Higgs boson would be present in data additional to the sum of all considered backgrounds.

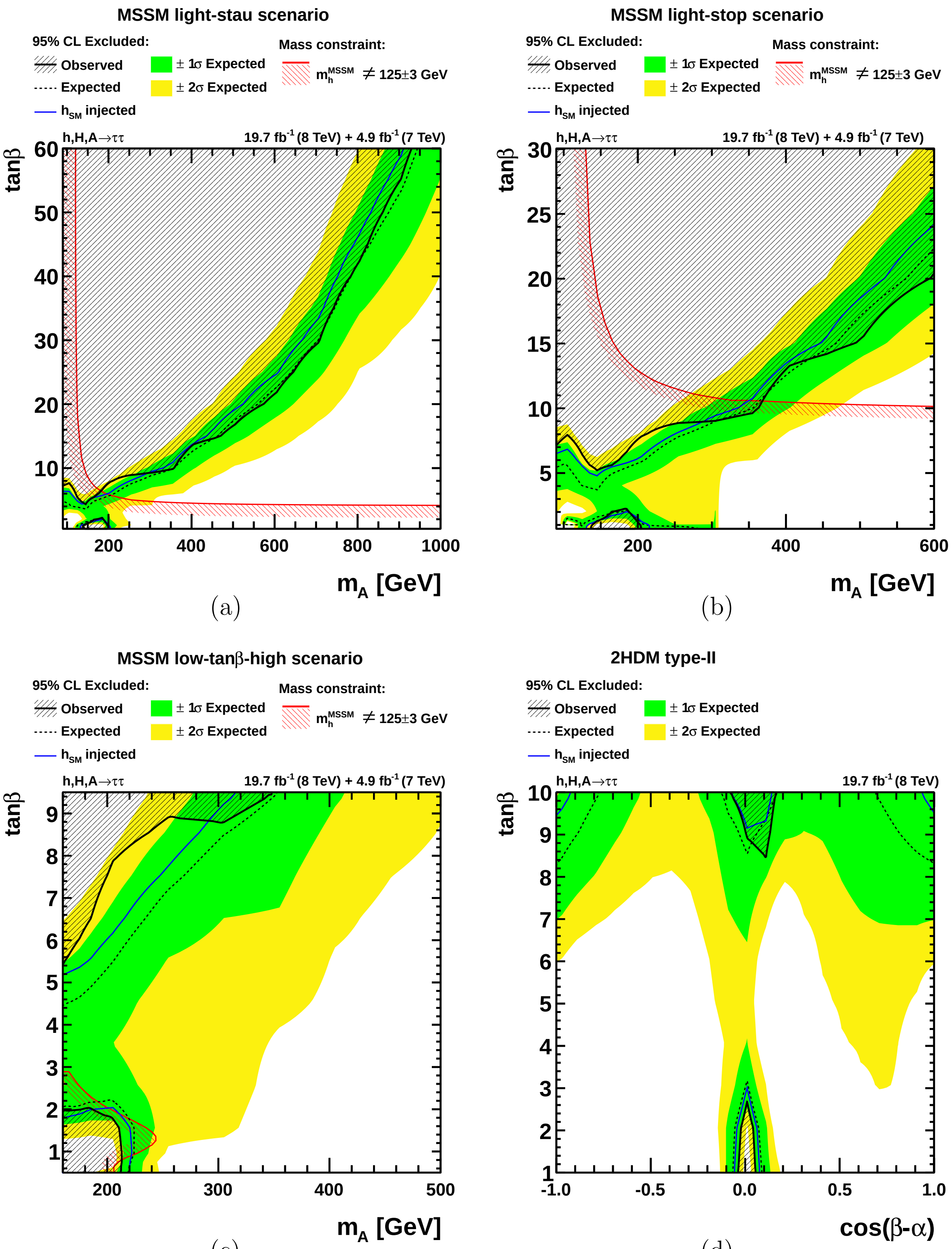

(a) (b)

(c) (d)

Figure F.2: The figures show the 95% confidence level exclusion limit on the MSSM light-stau (a), light-stop (b), low$-\tan\beta$-high (c) scenario are shown. In figure (d) the result for the benchmark type-2 2HDM is shown. The region where the SM like Higgs boson is not within $125 \pm 3\,\text{GeV}$ is indicated by the red area. The observed excluded area is shaded with black lines. The median expected limit is plotted as a dashed black line. The expected ± 1 and $\pm 2\sigma$ bands are shown as green or yellow bands, respectively. The blue line illustrates the expected exclusion limit if a SM Higgs boson would be present in data additional to the sum of all considered backgrounds.

Table F.1: Expected and observed 95% confidence level upper limits in the MSSM $m_h^{\max}$ scenario for $\tan\beta$ as a function of m_A testing H_b versus $H_{h+A+H+b}$.

BSM Higgs	Expected $\tan\beta$ limit					Observed
m_{A} [GeV]	-2σ	-1σ	Median	$+1\sigma$	$+2\sigma$	$\tan\beta$ limit
90 GeV	60.00 – 2.70	60.00 – 3.56	60.00 – 4.98	60.00 – 7.02	60.00 – 8.71	60.00 – 7.19
100 GeV	60.00 – 2.75	60.00 – 3.47	60.00 – 4.38	60.00 – 6.68	60.00 – 8.44	60.00 – 7.47
120 GeV	60.00 – 2.92 1.50 – 0.50	60.00 – 3.42 1.22 – 0.50	60.00 – 3.84 1.00 – 0.57	60.00 – 4.95	60.00 – 6.36	60.00 – 5.02
130 GeV	60.00 – 2.12 1.95 – 0.50	60.00 – 2.95 1.57 – 0.50	60.00 – 3.65 1.26 – 0.50	60.00 – 4.59 1.02 – 0.57	60.00 – 5.79	60.00 – 4.31
140 GeV	60.00 – 0.50	60.00 – 0.50	60.00 – 3.50 1.56 – 0.50	60.00 – 4.80 1.24 – 0.50	60.00 – 5.74 1.03 – 0.59	60.00 – 4.33 1.21 – 0.50
160 GeV	60.00 – 3.45	60.00 – 3.82	60.00 – 4.55	60.00 – 5.55	60.00 – 6.46	60.00 – 5.35
180 GeV	60.00 – 3.86	60.00 – 4.55	60.00 – 5.46	60.00 – 6.33	60.00 – 7.47	60.00 – 6.75
200 GeV	60.00 – 3.99	60.00 – 5.02	60.00 – 5.91	60.00 – 7.23	60.00 – 8.26	60.00 – 7.97
250 GeV	60.00 – 5.29	60.00 – 6.43	60.00 – 7.98	60.00 – 9.27	60.00 – 10.93	60.00 – 9.67
300 GeV	60.00 – 6.09	60.00 – 8.34	60.00 – 10.33	60.00 – 12.17	60.00 – 13.76	60.00 – 10.85
350 GeV	60.00 – 6.77	60.00 – 10.73	60.00 – 12.87	60.00 – 15.14	60.00 – 17.20	60.00 – 12.84
400 GeV	60.00 – 8.33	60.00 – 12.61	60.00 – 15.44	60.00 – 18.32	60.00 – 20.37	60.00 – 16.73
450 GeV	60.00 – 10.48	60.00 – 15.39	60.00 – 18.54	60.00 – 21.60	60.00 – 24.37	60.00 – 18.85
500 GeV	60.00 – 12.04	60.00 – 17.87	60.00 – 21.73	60.00 – 25.01	60.00 – 28.77	60.00 – 21.09
600 GeV	60.00 – 16.40	60.00 – 22.90	60.00 – 27.77	60.00 – 32.56	60.00 – 37.24	60.00 – 27.30
700 GeV	60.00 – 21.02	60.00 – 28.92	60.00 – 35.21	60.00 – 41.77	60.00 – 48.20	60.00 – 34.88
800 GeV	60.00 – 26.17	60.00 – 36.50	60.00 – 44.71	60.00 – 53.55	–	60.00 – 44.81
900 GeV	60.00 – 31.00	60.00 – 43.41	60.00 – 53.89	–	–	60.00 – 56.17
1000 GeV	60.00 – 38.47	60.00 – 54.88	–	–	–	–

Table F.2: Expected and observed 95% confidence level upper limits in the MSSM $m_h^{\text{mod}+}$ scenario on $\tan\beta$ as a function of m_A testing H_b versus $H_{h+A+H+b}$.

BSM Higgs	Expected $\tan\beta$ limit					Observed
m_{A} [GeV]	-2σ	-1σ	Median	$+1\sigma$	$+2\sigma$	$\tan\beta$ limit
90 GeV	60.00 – 2.14	60.00 – 3.36	60.00 – 5.09	60.00 – 7.17	60.00 – 8.65	60.00 – 7.39
100 GeV	60.00 – 2.94	60.00 – 3.57	60.00 – 4.64	60.00 – 7.00	60.00 – 8.53	60.00 – 7.74
120 GeV	60.00 – 2.70 1.60 – 0.50	60.00 – 3.33 1.25 – 0.50	60.00 – 3.85 0.94 – 0.60	60.00 – 5.23	60.00 – 6.71	60.00 – 5.61
130 GeV	60.00 – 2.10 1.96 – 0.50	60.00 – 2.96 1.57 – 0.50	60.00 – 3.70 1.23 – 0.50	60.00 – 4.84 0.98 – 0.62	60.00 – 6.08	60.00 – 4.88
140 GeV	60.00 – 0.50	60.00 – 2.21 1.93 – 0.50	60.00 – 3.58 1.51 – 0.50	60.00 – 4.91 1.20 – 0.50	60.00 – 5.93 0.99 – 0.66	60.00 – 4.46 1.19 – 0.51
160 GeV	60.00 – 3.56	60.00 – 3.90	60.00 – 4.82	60.00 – 5.74	60.00 – 6.78	60.00 – 5.46
180 GeV	60.00 – 3.97	60.00 – 4.86	60.00 – 5.69	60.00 – 6.72	60.00 – 7.69	60.00 – 6.97
200 GeV	60.00 – 4.43	60.00 – 5.35	60.00 – 6.29	60.00 – 7.51	60.00 – 8.50	60.00 – 8.18
250 GeV	60.00 – 5.88	60.00 – 7.16	60.00 – 8.39	60.00 – 9.75	60.00 – 11.17	60.00 – 9.96
300 GeV	60.00 – 7.21	60.00 – 9.01	60.00 – 10.77	60.00 – 12.41	60.00 – 14.01	60.00 – 11.06
350 GeV	60.00 – 8.50	60.00 – 11.18	60.00 – 13.18	60.00 – 15.37	60.00 – 17.39	60.00 – 12.92
400 GeV	60.00 – 10.49	60.00 – 13.29	60.00 – 15.96	60.00 – 18.64	60.00 – 20.74	60.00 – 17.01
450 GeV	60.00 – 12.08	60.00 – 16.03	60.00 – 18.96	60.00 – 22.06	60.00 – 24.59	60.00 – 19.06
500 GeV	60.00 – 14.68	60.00 – 18.57	60.00 – 22.29	60.00 – 25.61	60.00 – 29.07	60.00 – 21.50
600 GeV	60.00 – 18.48	60.00 – 23.78	60.00 – 28.44	60.00 – 33.20	60.00 – 37.77	60.00 – 27.74
700 GeV	60.00 – 23.27	60.00 – 30.06	60.00 – 36.28	60.00 – 42.70	60.00 – 48.97	60.00 – 35.65
800 GeV	60.00 – 29.19	60.00 – 37.97	60.00 – 46.15	60.00 – 54.74	–	60.00 – 45.94
900 GeV	60.00 – 34.29	60.00 – 45.28	60.00 – 55.70	–	–	60.00 – 57.70
1000 GeV	60.00 – 42.88	60.00 – 57.46	–	–	–	–

Table F.3: Expected and observed 95% confidence level upper limits in the MSSM $m_h^{\text{mod-}}$ scenario on $\tan\beta$ as a function of m_A testing H_b versus $H_{h+A+H+b}$.

BSM Higgs	Expected $\tan\beta$ limit					Observed
m_{A} [GeV]	-2σ	-1σ	Median	$+1\sigma$	$+2\sigma$	$\tan\beta$ limit
90 GeV	60.00 – 2.65	60.00 – 3.58	60.00 – 5.20	60.00 – 7.20	60.00 – 8.63	60.00 – 7.37
100 GeV	60.00 – 2.90	60.00 – 3.57	60.00 – 4.79	60.00 – 7.04	60.00 – 8.51	60.00 – 7.72
120 GeV	60.00 – 2.64 1.63 – 0.50	60.00 – 3.30 1.26 – 0.50	60.00 – 3.85 0.92 – 0.62	60.00 – 5.25	60.00 – 6.74	60.00 – 5.66
130 GeV	60.00 – 2.13 1.94 – 0.50	60.00 – 2.99 1.55 – 0.50	60.00 – 3.71 1.22 – 0.50	60.00 – 4.84 0.96 – 0.62	60.00 – 6.08	60.00 – 4.94
140 GeV	60.00 – 0.50	60.00 – 2.16 1.95 – 0.50	60.00 – 3.55 1.51 – 0.50	60.00 – 4.90 1.19 – 0.50	60.00 – 5.93 0.97 – 0.66	60.00 – 4.48 1.19 – 0.51
160 GeV	60.00 – 3.56	60.00 – 3.89	60.00 – 4.79	60.00 – 5.72	60.00 – 6.74	60.00 – 5.44
180 GeV	60.00 – 3.96	60.00 – 4.83	60.00 – 5.66	60.00 – 6.67	60.00 – 7.65	60.00 – 6.92
200 GeV	60.00 – 4.41	60.00 – 5.33	60.00 – 6.25	60.00 – 7.46	60.00 – 8.43	60.00 – 8.09
250 GeV	60.00 – 5.88	60.00 – 7.13	60.00 – 8.36	60.00 – 9.61	60.00 – 11.06	60.00 – 9.78
300 GeV	60.00 – 7.29	60.00 – 8.97	60.00 – 10.63	60.00 – 12.27	60.00 – 13.75	60.00 – 10.83
350 GeV	60.00 – 8.56	60.00 – 11.10	60.00 – 12.93	60.00 – 15.10	60.00 – 16.98	60.00 – 12.75
400 GeV	60.00 – 10.56	60.00 – 13.17	60.00 – 15.58	60.00 – 18.27	60.00 – 20.02	60.00 – 16.51
450 GeV	60.00 – 12.11	60.00 – 15.73	60.00 – 18.60	60.00 – 21.35	60.00 – 24.00	60.00 – 18.68
500 GeV	60.00 – 14.54	60.00 – 18.22	60.00 – 21.65	60.00 – 24.70	60.00 – 28.15	60.00 – 20.64
600 GeV	60.00 – 18.24	60.00 – 23.15	60.00 – 27.49	60.00 – 31.83	60.00 – 35.89	60.00 – 26.63
700 GeV	60.00 – 22.89	60.00 – 29.01	60.00 – 34.55	60.00 – 40.35	60.00 – 46.12	60.00 – 34.08
800 GeV	60.00 – 28.42	60.00 – 36.33	60.00 – 43.65	60.00 – 51.37	60.00 – 58.91	60.00 – 43.40
900 GeV	60.00 – 33.49	60.00 – 43.04	60.00 – 52.22	–	–	60.00 – 53.72
1000 GeV	60.00 – 41.39	60.00 – 53.99	–	–	–	–

Table F.4: Expected and observed 95% confidence level upper limits in the MSSM τ-phobic scenario on $\tan\beta$ as a function of m_A testing H_b versus $H_{h+A+H+b}$.

BSM Higgs	Expected $\tan\beta$ limit					Observed
m_{A} [GeV]	-2σ	-1σ	Median	$+1\sigma$	$+2\sigma$	$\tan\beta$ limit
90 GeV	50.00 – 1.00	50.00 – 1.00	50.00 – 4.46 1.76 – 1.00	50.00 – 6.91 1.38 – 1.00	50.00 – 8.44 1.12 – 1.00	50.00 – 7.06 1.53 – 1.00
100 GeV	50.00 – 1.47	50.00 – 1.80	50.00 – 3.04	50.00 – 6.70	50.00 – 8.45	50.00 – 7.59
120 GeV	50.00 – 1.00	50.00 – 1.00	50.00 – 2.83	50.00 – 3.73	50.00 – 5.50	50.00 – 3.69
130 GeV	50.00 – 1.00	50.00 – 2.48 1.73 – 1.00	50.00 – 3.23 1.32 – 1.00	50.00 – 3.80 1.01 – 1.00	50.00 – 4.84	50.00 – 3.78
140 GeV	50.00 – 1.00	50.00 – 1.00	50.00 – 2.96 1.62 – 1.00	50.00 – 3.88 1.25 – 1.00	50.00 – 5.28 1.02 – 1.00	50.00 – 3.64 1.25 – 1.00
160 GeV	50.00 – 1.00	50.00 – 1.00	50.00 – 4.34 1.97 – 1.00	50.00 – 5.51 1.49 – 1.00	50.00 – 6.57 1.19 – 1.00	50.00 – 5.24 2.09 – 1.00
180 GeV	50.00 – 1.00	50.00 – 1.00	50.00 – 5.06 2.13 – 1.00	50.00 – 6.22 1.53 – 1.00	50.00 – 7.53 1.20 – 1.00	50.00 – 6.71 2.17 – 1.00
200 GeV	50.00 – 1.00	50.00 – 4.25 3.28 – 1.00	50.00 – 5.67 1.23 – 1.00	50.00 – 7.18	50.00 – 8.43	50.00 – 8.15
250 GeV	50.00 – 3.84 2.01 – 1.00	50.00 – 5.84	50.00 – 7.70	50.00 – 9.09	50.00 – 10.92	50.00 – 9.32
300 GeV	50.00 – 3.82	50.00 – 7.19	50.00 – 9.21	50.00 – 11.31	50.00 – 13.13	50.00 – 9.54
350 GeV	50.00 – 5.82	50.00 – 7.98	50.00 – 10.72	50.00 – 13.33	50.00 – 15.83	50.00 – 10.55
400 GeV	50.00 – 7.44	50.00 – 10.65	50.00 – 13.71	50.00 – 16.83	50.00 – 19.68	50.00 – 14.51
450 GeV	50.00 – 9.09	50.00 – 12.85	50.00 – 16.33	50.00 – 19.83	50.00 – 23.86	50.00 – 16.28
500 GeV	50.00 – 10.83	50.00 – 15.29	50.00 – 19.51	50.00 – 24.18	50.00 – 34.19	50.00 – 18.70
600 GeV	50.00 – 14.31	50.00 – 20.42	50.00 – 26.86	50.00 – 36.01	50.00 – 45.63	50.00 – 24.99
700 GeV	50.00 – 19.55	50.00 – 28.49	50.00 – 37.91	50.00 – 49.91	–	50.00 – 37.75
800 GeV	50.00 – 29.68	50.00 – 41.81	–	–	–	–
900 GeV	50.00 – 37.52	–	–	–	–	–
1000 GeV	50.00 – 49.86	–	–	–	–	–

Table F.5: Expected and observed 95% confidence upper limits in the MSSM low-m_H scenario on $\tan\beta$ as a function of μ testing H_b versus $H_{h+A+H+b}$.

BSM Higgs	Expected $\tan\beta$ limit					Observed
μ [GeV]	-2σ	-1σ	Median	$+1\sigma$	$+2\sigma$	$\tan\beta$ limit
300 GeV	9.50 – 2.06	9.50 – 2.45	9.50 – 3.64	9.50 – 5.90	9.50 – 7.50	9.50 – 6.60
400 GeV	9.50 – 1.98	9.50 – 2.41	9.50 – 3.60	9.50 – 5.91	9.50 – 7.46	9.50 – 6.60
500 GeV	9.50 – 1.95	9.50 – 2.36	9.50 – 3.54	9.50 – 6.02	9.50 – 7.61	9.50 – 6.68
600 GeV	9.50 – 1.91	9.50 – 2.30	9.50 – 3.55	9.50 – 6.08	9.50 – 7.63	9.50 – 6.74
700 GeV	9.50 – 1.80	9.50 – 2.22	9.50 – 3.62	9.50 – 6.06	9.50 – 7.55	9.50 – 6.70
800 GeV	9.50 – 1.72	9.50 – 2.12	9.50 – 3.83	9.50 – 5.99	9.50 – 7.63	9.50 – 6.70
1100 GeV	9.50 – 1.50	9.50 – 1.88	9.50 – 4.29	9.50 – 6.24	9.50 – 7.84	9.50 – 6.82
1300 GeV	9.50 – 1.50	9.50 – 1.66	9.50 – 4.47	9.50 – 6.49	9.50 – 8.13	9.50 – 6.95
1400 GeV	9.50 – 1.50	9.50 – 1.55	9.50 – 4.67	9.50 – 6.66	9.50 – 8.34	9.50 – 7.03
1500 GeV	9.50 – 1.50	9.50 – 1.50	9.50 – 4.85	9.50 – 6.89	9.50 – 8.58	9.50 – 7.12
1600 GeV	9.50 – 1.50	9.50 – 1.50	9.50 – 5.10	9.50 – 7.14	9.50 – 8.80	9.50 – 7.20
1700 GeV	9.50 – 1.50	9.50 – 1.59	9.50 – 5.40	9.50 – 7.42	9.50 – 8.93	9.50 – 7.26
1800 GeV	9.50 – 1.50	9.50 – 2.72	9.50 – 5.78	9.50 – 7.65	9.50 – 8.96	9.50 – 7.27
1900 GeV	9.50 – 1.50	9.50 – 3.22	9.50 – 6.22	9.50 – 7.77	9.50 – 8.94	9.50 – 7.16
2000 GeV	9.50 – 1.50	9.50 – 4.23	9.50 – 6.52	9.50 – 7.82	9.50 – 8.86	9.50 – 7.09
2100 GeV	9.50 – 2.32	9.50 – 5.14	9.50 – 6.66	9.50 – 7.79	9.50 – 8.73	9.50 – 7.11
2200 GeV	9.50 – 2.77	9.50 – 5.58	9.50 – 6.70	9.50 – 7.69	9.50 – 8.58	9.50 – 7.29
2300 GeV	9.50 – 4.56	9.50 – 5.71	9.50 – 6.67	9.50 – 7.56	9.50 – 8.48	9.50 – 7.38
2400 GeV	9.50 – 4.91	9.50 – 5.74	9.50 – 6.58	9.50 – 7.42	9.50 – 8.40	9.50 – 7.47
2500 GeV	9.50 – 4.98	9.50 – 5.70	9.50 – 6.43	9.50 – 7.28	9.50 – 8.33	9.50 – 7.52
2600 GeV	9.50 – 4.95	9.50 – 5.57	9.50 – 6.26	9.50 – 7.12	9.50 – 8.24	9.50 – 7.25
2700 GeV	9.50 – 4.84	9.50 – 5.40	9.50 – 6.03	9.50 – 6.94	9.50 – 8.13	9.50 – 6.98
2800 GeV	9.50 – 4.66	9.50 – 5.18	9.50 – 5.84	9.50 – 6.77	9.50 – 7.98	9.50 – 6.79
2900 GeV	9.50 – 4.41	9.50 – 4.92	9.50 – 5.59	9.50 – 6.56	9.50 – 7.80	9.50 – 6.54
3000 GeV	9.50 – 4.16	9.50 – 4.67	9.50 – 5.36	9.50 – 6.37	9.50 – 7.61	9.50 – 6.32
3100 GeV	9.50 – 3.87	9.50 – 4.40	9.50 – 5.13	9.50 – 6.15	9.50 – 7.40	9.50 – 6.06

Table F.6: Expected and observed 95% confidence upper limits in the MSSM light-stau scenario on $\tan\beta$ as a function of m_A testing H_b versus $H_{h+A+H+b}$.

BSM Higgs	Expected $\tan\beta$ limit					Observed
m_A [GeV]	-2σ	-1σ	Median	$+1\sigma$	$+2\sigma$	$\tan\beta$ limit
90 GeV	60.00 – 2.13	60.00 – 3.28	60.00 – 4.77	60.00 – 6.93	60.00 – 8.46	60.00 – 7.19
100 GeV	60.00 – 2.98	60.00 – 3.56	60.00 – 4.33	60.00 – 6.78	60.00 – 8.39	60.00 – 7.59
120 GeV	60.00 – 2.84 1.53 – 0.50	60.00 – 3.38 1.23 – 0.50	60.00 – 3.84 0.96 – 0.58	60.00 – 5.08	60.00 – 6.53	60.00 – 5.36
130 GeV	60.00 – 2.12 1.94 – 0.50	60.00 – 2.97 1.56 – 0.50	60.00 – 3.68 1.24 – 0.50	60.00 – 4.72 1.00 – 0.59	60.00 – 5.95	60.00 – 4.69
140 GeV	60.00 – 0.50	60.00 – 2.18 1.94 – 0.50	60.00 – 3.53 1.52 – 0.50	60.00 – 4.84 1.21 – 0.50	60.00 – 5.85 1.01 – 0.63	60.00 – 4.29 1.20 – 0.50
160 GeV	60.00 – 0.50	60.00 – 0.50	60.00 – 4.78 1.86 – 0.50	60.00 – 5.71 1.43 – 0.50	60.00 – 6.70 1.15 – 0.57	60.00 – 5.42 1.89 – 0.50
180 GeV	60.00 – 0.50	60.00 – 0.50	60.00 – 5.23 1.99 – 0.50	60.00 – 6.29 1.47 – 0.50	60.00 – 7.44 1.14 – 0.63	60.00 – 6.56 2.16 – 0.50
200 GeV	60.00 – 0.50	60.00 – 4.41 1.91 – 0.50	60.00 – 5.70	60.00 – 7.05	60.00 – 8.06	60.00 – 7.82
250 GeV	60.00 – 4.09	60.00 – 5.82	60.00 – 7.52	60.00 – 8.76	60.00 – 10.31	60.00 – 8.87
300 GeV	60.00 – 4.15	60.00 – 6.93	60.00 – 8.84	60.00 – 10.49	60.00 – 12.26	60.00 – 9.23
350 GeV	60.00 – 5.83	60.00 – 7.50	60.00 – 9.83	60.00 – 12.22	60.00 – 14.39	60.00 – 9.81
400 GeV	60.00 – 7.22	60.00 – 9.82	60.00 – 12.71	60.00 – 14.85	60.00 – 17.73	60.00 – 13.66
450 GeV	60.00 – 8.63	60.00 – 11.93	60.00 – 14.63	60.00 – 17.91	60.00 – 20.42	60.00 – 14.62
500 GeV	60.00 – 10.34	60.00 – 13.87	60.00 – 17.54	60.00 – 20.90	60.00 – 24.41	60.00 – 16.77
600 GeV	60.00 – 12.90	60.00 – 17.98	60.00 – 22.60	60.00 – 27.42	60.00 – 32.14	60.00 – 21.80
700 GeV	60.00 – 17.24	60.00 – 23.89	60.00 – 29.98	60.00 – 36.77	60.00 – 43.78	60.00 – 29.53
800 GeV	60.00 – 25.54	60.00 – 34.14	60.00 – 42.50	60.00 – 51.41	–	60.00 – 42.37
900 GeV	60.00 – 31.62	60.00 – 42.66	60.00 – 53.33	–	–	60.00 – 55.24
1000 GeV	60.00 – 40.93	60.00 – 56.11	–	–	–	–

Table F.7: Expected and observed 95% confidence upper limits in the MSSM light-stop scenario on $\tan\beta$ as a function of m_A testing H_b versus $H_{h+A+H+b}$.

BSM Higgs	Expected $\tan\beta$ limit					Observed
m_{A} [GeV]	-2σ	-1σ	Median	$+1\sigma$	$+2\sigma$	$\tan\beta$ limit
90 GeV	60.00 – 1.94	60.00 – 3.55	60.00 – 5.41	60.00 – 7.14	60.00 – 8.50	60.00 – 7.09
100 GeV	60.00 – 2.74 1.84 – 0.94 0.67 – 0.70	60.00 – 3.72 1.63 – 0.95 0.65 – 0.70	60.00 – 5.51 1.45 – 0.97 0.64 – 0.70	60.00 – 7.33 1.32 – 0.98 0.63 – 0.70	60.00 – 8.72 1.23 – 0.98 0.62 – 0.70	60.00 – 7.89
120 GeV	60.00 – 2.27 1.86 – 0.70	60.00 – 3.20 1.39 – 0.70	60.00 – 3.98 1.00 – 0.70	60.00 – 5.65 0.68 – 0.70	60.00 – 7.08 0.66 – 0.70	60.00 – 6.37
130 GeV	60.00 – 0.70	60.00 – 2.88 1.66 – 0.70	60.00 – 3.80 1.30 – 0.70	60.00 – 5.20 1.03 – 0.70	60.00 – 6.41 0.69 – 0.70	60.00 – 5.58
140 GeV	60.00 – 0.70	60.00 – 0.70	60.00 – 3.66 1.56 – 0.70	60.00 – 5.13 1.24 – 0.70	60.00 – 6.19 1.03 – 0.70	60.00 – 5.16 1.24 – 0.69
160 GeV	60.00 – 0.70	60.00 – 0.70	60.00 – 4.90 1.89 – 0.70	60.00 – 5.80 1.45 – 0.70	60.00 – 6.86 1.17 – 0.70	60.00 – 5.56 1.97 – 0.68
180 GeV	60.00 – 0.70	60.00 – 4.17 3.76 – 0.70	60.00 – 5.37 2.08 – 0.70	60.00 – 6.47 1.43 – 0.70	60.00 – 7.56 1.04 – 0.70	60.00 – 6.58 2.18 – 0.68
200 GeV	60.00 – 0.70	60.00 – 4.60 2.71 – 0.70	60.00 – 5.83 1.09 – 0.70	60.00 – 7.19 0.68 – 0.70	60.00 – 8.17 0.66 – 0.70	60.00 – 7.78
250 GeV	60.00 – 4.01 2.34 – 0.70	60.00 – 6.25 0.98 – 0.70	60.00 – 7.76 0.85 – 0.70	60.00 – 8.87 0.74 – 0.70	60.00 – 10.46 0.68 – 0.70	60.00 – 8.82
300 GeV	60.00 – 0.70	60.00 – 7.21 2.09 – 0.70	60.00 – 8.95	60.00 – 10.55	60.00 – 12.29	60.00 – 8.98
350 GeV	60.00 – 5.94	60.00 – 7.95	60.00 – 9.95	60.00 – 12.29	60.00 – 14.45	60.00 – 9.59
400 GeV	60.00 – 8.21	60.00 – 9.98	60.00 – 12.74	60.00 – 14.77	60.00 – 17.61	60.00 – 13.23
450 GeV	60.00 – 9.54	60.00 – 12.14	60.00 – 14.49	60.00 – 17.64	60.00 – 20.11	60.00 – 14.14
500 GeV	60.00 – 11.37	60.00 – 14.02	60.00 – 17.32	60.00 – 20.58	60.00 – 24.24	60.00 – 15.53
600 GeV	60.00 – 14.37	60.00 – 18.22	60.00 – 22.52	60.00 – 27.41	60.00 – 32.46	60.00 – 20.59

Table F.8: Expected and observed 95% confidence upper limits in the MSSM low-$\tan\beta$-high scenario on $\tan\beta$ as a function of m_A testing H_b versus $H_{h+A+H+b}$.

BSM Higgs	Expected $\tan\beta$ limit					Observed
m_{A} [GeV]	-2σ	-1σ	Median	$+1\sigma$	$+2\sigma$	$\tan\beta$ limit
160 GeV	9.50 – 0.50	9.50 – 2.73 2.49 – 0.50	9.50 – 4.42 1.97 – 0.50	9.50 – 5.42 1.59 – 0.50	9.50 – 6.42 1.24 – 0.50	9.50 – 5.41 1.91 – 0.50
200 GeV	9.50 – 0.50	9.50 – 3.51 3.49 – 0.50	9.50 – 5.44 2.15 – 0.50	9.50 – 6.86 1.68 – 0.50	9.50 – 8.10 1.25 – 0.59	9.50 – 7.81 1.73 – 0.50
250 GeV	9.50 – 1.08	9.50 – 5.54	9.50 – 7.15	9.50 – 8.62	–	9.50 – 8.86
300 GeV	9.50 – 1.29	9.50 – 6.48	9.50 – 8.44	–	–	9.50 – 8.74
350 GeV	9.50 – 3.88	9.50 – 6.72	9.50 – 9.47	–	–	–
400 GeV	9.50 – 5.78	9.50 – 9.11	–	–	–	–
450 GeV	9.50 – 7.42	–	–	–	–	–
500 GeV	9.50 – 8.85	–	–	–	–	–

Table F.9: Expected and observed 95% confidence upper limits in the type-2 2HDM on $\tan\beta$ as a function of $\cos(\beta-\alpha)$ testing H_b versus $H_{h+A+H+b}$.

BSM Higgs	Expected $\tan\beta$ limit					Observed
$\cos(\beta-\alpha)$	-2σ	-1σ	Median	$+1\sigma$	$+2\sigma$	$\tan\beta$ limit
-1	10.00 – 5.92 1.04 – 1.00	10.00 – 6.94	10.00 – 8.25	10.00 – 9.81	–	–
-0.9	10.00 – 6.47	10.00 – 7.53	10.00 – 8.96	–	–	–
-0.8	10.00 – 6.81	10.00 – 8.04	10.00 – 9.79	–	–	–
-0.7	10.00 – 7.16	10.00 – 8.77	–	–	–	–
-0.6	10.00 – 7.57	10.00 – 9.60	–	–	–	–
-0.5	10.00 – 7.94	–	–	–	–	–
-0.4	10.00 – 8.10	–	–	–	–	–
-0.3	10.00 – 7.62	–	–	–	–	–
-0.2	10.00 – 6.01	10.00 – 9.33	–	–	–	–
-0.1	10.00 – 1.00	10.00 – 7.17 2.34 – 1.00	10.00 – 9.46	–	–	10.00 – 9.98
0	10.00 – 1.00	10.00 – 6.40 4.13 – 1.00	10.00 – 8.51 3.12 – 1.00	2.47 – 1.00	2.08 – 1.00	10.00 – 8.88 2.63 – 1.00
0.1	10.00 – 6.76 3.04 – 1.00	10.00 – 7.92 2.16 – 1.00	10.00 – 9.30	–	–	10.00 – 8.42
0.2	10.00 – 7.83	10.00 – 8.84	–	–	–	–
0.3	10.00 – 7.06	10.00 – 9.03	–	–	–	–
0.4	10.00 – 5.62	10.00 – 8.79	–	–	–	–
0.5	10.00 – 4.36	10.00 – 7.86	–	–	–	–
0.6	10.00 – 3.56	10.00 – 7.14	–	–	–	–
0.7	10.00 – 2.92	10.00 – 6.85	10.00 – 9.77	–	–	–
0.8	10.00 – 4.01	10.00 – 6.80	10.00 – 9.03	–	–	–
0.9	10.00 – 5.23	10.00 – 6.80	10.00 – 8.53	–	–	–
1	10.00 – 5.92 1.05 – 1.00	10.00 – 6.94	10.00 – 8.25	10.00 – 9.81	–	–

Appendix G

Background including SM Higgs Boson against BSM Signal Model

Numerical results can be found in the following tables.

Table G.1: Expected and observed 95% confidence upper limits in the MSSM $m_h^{\max}$ scenario on $\tan\beta$ as a function of m_A testing $H_{h_{\mathrm{SM}}+b}$ versus $H_{h+A+H+b}$.

BSM Higgs	Expected $\tan\beta$ limit					Observed
m_{A} [GeV]	-2σ	-1σ	Median	$+1\sigma$	$+2\sigma$	$\tan\beta$ limit
90 GeV	60.00 – 4.31 1.29 – 0.50	60.00 – 5.34	60.00 – 6.31	60.00 – 7.59	60.00 – 9.20	60.00 – 6.42
100 GeV	60.00 – 3.59 1.17 – 0.50	60.00 – 5.15	60.00 – 6.28	60.00 – 7.58	60.00 – 9.21	60.00 – 6.83
120 GeV	60.00 – 3.75 0.89 – 0.50	60.00 – 3.91	60.00 – 5.16	60.00 – 6.08	60.00 – 7.26	60.00 – 4.38
130 GeV	60.00 – 3.81 1.10 – 0.50	60.00 – 3.87 1.07 – 0.50	60.00 – 4.66 0.95 – 0.50	60.00 – 5.72	60.00 – 6.64	60.00 – 3.93
140 GeV	60.00 – 3.33 1.38 – 0.50	60.00 – 3.67 1.25 – 0.50	60.00 – 4.77 1.12 – 0.50	60.00 – 5.69 1.05 – 0.50	60.00 – 6.39	60.00 – 3.80 1.22 – 0.50
160 GeV	60.00 – 3.02	60.00 – 4.42	60.00 – 5.46	60.00 – 5.92	60.00 – 6.84	60.00 – 4.80
180 GeV	60.00 – 4.39	60.00 – 5.31	60.00 – 5.82	60.00 – 6.72	60.00 – 7.65	60.00 – 6.20
200 GeV	60.00 – 5.00 2.12 – 0.50	60.00 – 5.55	60.00 – 6.41	60.00 – 7.40	60.00 – 8.87	60.00 – 7.63
250 GeV	60.00 – 6.48 1.23 – 0.96 0.85 – 0.50	60.00 – 7.09	60.00 – 8.25	60.00 – 9.63	60.00 – 11.59	60.00 – 9.16
300 GeV	60.00 – 9.29	60.00 – 9.70	60.00 – 11.38	60.00 – 12.60	60.00 – 13.95	60.00 – 9.77
350 GeV	60.00 – 11.52	60.00 – 12.37	60.00 – 13.65	60.00 – 15.30	60.00 – 16.98	60.00 – 12.21
400 GeV	60.00 – 13.10	60.00 – 14.55	60.00 – 16.35	60.00 – 18.81	60.00 – 20.65	60.00 – 14.85
450 GeV	60.00 – 16.05	60.00 – 17.13	60.00 – 19.51	60.00 – 22.14	60.00 – 24.37	60.00 – 16.83
500 GeV	60.00 – 19.10	60.00 – 20.47	60.00 – 22.74	60.00 – 25.77	60.00 – 29.03	60.00 – 19.48
600 GeV	60.00 – 24.02	60.00 – 26.12	60.00 – 29.35	60.00 – 32.95	60.00 – 37.18	60.00 – 25.02
700 GeV	60.00 – 30.33	60.00 – 33.17	60.00 – 37.66	60.00 – 42.74	60.00 – 48.32	60.00 – 32.52
800 GeV	60.00 – 38.09	60.00 – 42.59	60.00 – 48.06	60.00 – 54.89	–	60.00 – 42.43
900 GeV	60.00 – 46.68	60.00 – 51.17	60.00 – 57.61	–	–	60.00 – 52.66
1000 GeV	60.00 – 58.79	–	–	–	–	–

Table G.2: Expected and observed 95% confidence level upper limits in the MSSM $m_h^{\text{mod}+}$ scenario on $\tan\beta$ as a function of m_A testing $H_{h_{\text{SM}}+b}$ versus $H_{h+A+H+b}$.

BSM Higgs	Expected $\tan\beta$ limit					Observed
m_{A} [GeV]	-2σ	-1σ	Median	$+1\sigma$	$+2\sigma$	$\tan\beta$ limit
90 GeV	60.00 – 4.85 1.22 – 0.50	60.00 – 5.77	60.00 – 6.93	60.00 – 7.90	60.00 – 8.96	60.00 – 7.40
100 GeV	60.00 – 5.71 0.88 – 0.50	60.00 – 5.77	60.00 – 7.13	60.00 – 7.98	60.00 – 9.06	60.00 – 7.77
120 GeV	60.00 – 3.74 0.91 – 0.89	60.00 – 4.19	60.00 – 5.49	60.00 – 7.07	60.00 – 7.91	60.00 – 5.49
130 GeV	60.00 – 3.75 1.12 – 0.50	60.00 – 3.86 1.07 – 0.57	60.00 – 4.98 0.83 – 0.77	60.00 – 5.94	60.00 – 7.55	60.00 – 4.50
140 GeV	60.00 – 3.07 1.51 – 0.50	60.00 – 3.73 1.22 – 0.50	60.00 – 4.76 1.11 – 0.50	60.00 – 5.76 1.02 – 0.60	60.00 – 7.30	60.00 – 3.81 1.22 – 0.50
160 GeV	60.00 – 1.94 0.70 – 0.68	60.00 – 3.85	60.00 – 5.47	60.00 – 6.36	60.00 – 7.62	60.00 – 4.56
180 GeV	60.00 – 2.83 1.58 – 0.81 0.54 – 0.50	60.00 – 5.07	60.00 – 5.91	60.00 – 7.44	60.00 – 7.92	60.00 – 6.82
200 GeV	60.00 – 0.85 0.78 – 0.51	60.00 – 5.53	60.00 – 6.80	60.00 – 7.78	60.00 – 8.71	60.00 – 7.90
250 GeV	60.00 – 6.59	60.00 – 8.18	60.00 – 8.73	60.00 – 10.56	60.00 – 11.63	60.00 – 8.97
300 GeV	60.00 – 9.26 1.72 – 0.79	60.00 – 9.91	60.00 – 11.75	60.00 – 12.75	60.00 – 14.64	60.00 – 9.97
350 GeV	60.00 – 11.52	60.00 – 12.44	60.00 – 14.33	60.00 – 15.73	60.00 – 18.11	60.00 – 12.22
400 GeV	60.00 – 14.33	60.00 – 14.74	60.00 – 17.87	60.00 – 19.41	60.00 – 22.24	60.00 – 15.44
450 GeV	60.00 – 17.28	60.00 – 18.71	60.00 – 19.77	60.00 – 23.49	60.00 – 24.84	60.00 – 18.48
500 GeV	60.00 – 19.51	60.00 – 21.42	60.00 – 23.98	60.00 – 27.18	60.00 – 29.62	60.00 – 19.93
600 GeV	60.00 – 24.45	60.00 – 27.77	60.00 – 29.83	60.00 – 34.22	60.00 – 38.68	60.00 – 26.34
700 GeV	60.00 – 33.20	60.00 – 34.30	60.00 – 38.76	60.00 – 44.13	60.00 – 49.79	60.00 – 34.19
800 GeV	60.00 – 39.49	60.00 – 43.62	60.00 – 49.38	60.00 – 56.99	–	60.00 – 44.44
900 GeV	60.00 – 48.91	60.00 – 52.72	–	–	–	60.00 – 54.64
1000 GeV	–	–	–	–	–	–

Table G.3: Expected and observed 95% confidence level upper limits in the MSSM $m_h^{\text{mod-}}$ scenario on $\tan\beta$ as a function of m_A testing $H_{h_{\text{SM}}+b}$ versus $H_{h+A+H+b}$.

BSM Higgs	Expected $\tan\beta$ limit					Observed
m_{A} [GeV]	-2σ	-1σ	Median	$+1\sigma$	$+2\sigma$	$\tan\beta$ limit
90 GeV	60.00 – 4.99 1.10 – 0.50	60.00 – 5.64	60.00 – 6.94	60.00 – 7.85	60.00 – 8.95	60.00 – 7.38
100 GeV	60.00 – 4.65 0.98 – 0.50	60.00 – 5.61	60.00 – 7.03	60.00 – 7.90	60.00 – 8.99	60.00 – 7.72
120 GeV	60.00 – 3.75	60.00 – 4.17	60.00 – 5.51	60.00 – 7.03	60.00 – 7.84	60.00 – 5.50
130 GeV	60.00 – 3.80 1.09 – 0.50	60.00 – 3.89 1.04 – 0.57	60.00 – 5.00 0.82 – 0.73	60.00 – 5.93	60.00 – 7.52	60.00 – 4.50
140 GeV	60.00 – 3.24 1.41 – 0.50	60.00 – 3.69 1.23 – 0.50	60.00 – 4.81 1.11 – 0.50	60.00 – 5.79 1.02 – 0.62	60.00 – 7.31	60.00 – 3.83 1.22 – 0.50
160 GeV	60.00 – 2.68	60.00 – 4.24	60.00 – 5.48	60.00 – 6.34	60.00 – 7.63	60.00 – 4.73
180 GeV	60.00 – 3.12 0.98 – 0.85	60.00 – 5.16	60.00 – 5.88	60.00 – 7.41	60.00 – 7.90	60.00 – 6.66
200 GeV	60.00 – 4.27 3.15 – 0.82 0.76 – 0.53	60.00 – 5.42	60.00 – 6.71	60.00 – 7.74	60.00 – 8.67	60.00 – 7.83
250 GeV	60.00 – 7.34	60.00 – 8.10	60.00 – 8.70	60.00 – 10.43	60.00 – 11.59	60.00 – 8.92
300 GeV	60.00 – 9.32	60.00 – 9.69	60.00 – 11.45	60.00 – 12.63	60.00 – 14.55	60.00 – 9.81
350 GeV	60.00 – 11.30	60.00 – 12.25	60.00 – 13.63	60.00 – 15.55	60.00 – 17.72	60.00 – 12.09
400 GeV	60.00 – 14.09	60.00 – 14.67	60.00 – 17.52	60.00 – 19.28	60.00 – 20.51	60.00 – 14.93
450 GeV	60.00 – 16.73	60.00 – 18.35	60.00 – 19.58	60.00 – 22.96	60.00 – 24.57	60.00 – 18.06
500 GeV	60.00 – 19.26	60.00 – 20.39	60.00 – 23.56	60.00 – 25.31	60.00 – 29.16	60.00 – 19.52
600 GeV	60.00 – 23.89	60.00 – 26.13	60.00 – 29.17	60.00 – 33.28	60.00 – 37.16	60.00 – 24.83
700 GeV	60.00 – 29.56	60.00 – 33.09	60.00 – 37.13	60.00 – 42.02	60.00 – 47.13	60.00 – 32.88
800 GeV	60.00 – 38.41	60.00 – 41.41	60.00 – 46.76	60.00 – 53.45	60.00 – 59.73	60.00 – 42.23
900 GeV	60.00 – 45.36	60.00 – 49.65	60.00 – 55.90	–	–	60.00 – 51.93
1000 GeV	60.00 – 57.85	–	–	–	–	–

Table G.4: Expected and observed 95% confidence level upper limits in the MSSM τ-phobic scenario on $\tan\beta$ as a function of m_A testing $H_{h_{\mathrm{SM}}+b}$ versus $H_{h+A+H+b}$.

BSM Higgs	Expected $\tan\beta$ limit					Observed
m_{A} [GeV]	-2σ	-1σ	Median	$+1\sigma$	$+2\sigma$	$\tan\beta$ limit
90 GeV	50.00 – 1.00	50.00 – 4.25 3.77 – 1.00	50.00 – 5.54 2.62 – 1.00	50.00 – 6.88 2.24 – 1.00	50.00 – 7.89 2.08 – 1.00	50.00 – 4.80 3.27 – 1.00
100 GeV	50.00 – 5.24	50.00 – 5.64	50.00 – 6.26	50.00 – 7.89	50.00 – 9.78	50.00 – 5.85
120 GeV	50.00 – 3.95	50.00 – 5.18	50.00 – 6.55	50.00 – 7.78	50.00 – 8.82	50.00 – 6.96
130 GeV	50.00 – 3.54 1.23 – 1.00	50.00 – 3.78 1.12 – 1.00	50.00 – 4.79	50.00 – 6.21	50.00 – 7.69	50.00 – 5.53
140 GeV	50.00 – 1.00	50.00 – 2.81 1.64 – 1.00	50.00 – 3.90 1.25 – 1.00	50.00 – 5.66 1.08 – 1.00	50.00 – 7.32	50.00 – 3.89 1.26 – 1.00
160 GeV	50.00 – 1.00	50.00 – 1.00	50.00 – 1.00	50.00 – 5.69 1.25 – 1.00	50.00 – 7.41 1.09 – 1.00	50.00 – 1.00
180 GeV	50.00 – 1.00	50.00 – 1.00	50.00 – 4.56 3.43 – 1.00	50.00 – 6.44 1.71 – 1.00	50.00 – 7.72 1.17 – 1.00	50.00 – 1.00
200 GeV	50.00 – 1.00	50.00 – 1.00	50.00 – 4.91 3.30 – 1.00	50.00 – 7.22 2.02 – 1.00	50.00 – 8.09 1.20 – 1.00	50.00 – 7.12 2.90 – 1.00
250 GeV	50.00 – 1.00	50.00 – 1.00	50.00 – 7.39 2.16 – 1.00	50.00 – 8.72 1.11 – 1.00	50.00 – 10.98	50.00 – 8.13 1.52 – 1.00
300 GeV	50.00 – 1.00	50.00 – 7.04 4.94 – 1.00	50.00 – 9.07 2.88 – 1.00	50.00 – 10.72	50.00 – 12.59	50.00 – 7.75 3.99 – 1.00
350 GeV	50.00 – 3.33	50.00 – 8.03	50.00 – 9.90	50.00 – 12.56	50.00 – 15.12	50.00 – 8.45
400 GeV	50.00 – 9.15	50.00 – 10.96	50.00 – 13.79	50.00 – 15.27	50.00 – 19.01	50.00 – 12.07
450 GeV	50.00 – 12.16	50.00 – 13.71	50.00 – 15.08	50.00 – 18.99	50.00 – 22.46	50.00 – 13.18
500 GeV	50.00 – 13.95	50.00 – 15.31	50.00 – 18.94	50.00 – 22.79	50.00 – 25.94	50.00 – 14.33
600 GeV	50.00 – 18.59	50.00 – 20.64	50.00 – 24.63	50.00 – 29.71	50.00 – 35.39	50.00 – 19.05
700 GeV	50.00 – 24.93	50.00 – 29.08	50.00 – 34.60	50.00 – 42.68	–	50.00 – 28.05
800 GeV	50.00 – 34.10	50.00 – 40.11	50.00 – 49.17	–	–	50.00 – 39.46
900 GeV	50.00 – 45.10	–	–	–	–	–
1000 GeV	–	–	–	–	–	–

Table G.5: Expected and observed 95% confidence level upper limits in the MSSM low-m_H scenario on $\tan\beta$ as a function of μ testing $H_{h_{\mathrm{SM}}+b}$ versus $H_{h+A+H+b}$.

BSM Higgs	Expected $\tan\beta$ limit					Observed
μ [GeV]	-2σ	-1σ	Median	$+1\sigma$	$+2\sigma$	$\tan\beta$ limit
300 GeV	9.50 – 3.37	9.50 – 4.73	9.50 – 6.00	9.50 – 7.25	9.50 – 8.42	9.50 – 6.58
400 GeV	9.50 – 3.24	9.50 – 4.74	9.50 – 6.01	9.50 – 7.23	9.50 – 8.42	9.50 – 6.65
500 GeV	9.50 – 3.26	9.50 – 4.87	9.50 – 6.15	9.50 – 7.34	9.50 – 8.49	9.50 – 6.69
600 GeV	9.50 – 3.40	9.50 – 5.03	9.50 – 6.19	9.50 – 7.40	9.50 – 8.45	9.50 – 6.75
700 GeV	9.50 – 3.44	9.50 – 5.02	9.50 – 6.12	9.50 – 7.30	9.50 – 8.45	9.50 – 6.72
800 GeV	9.50 – 4.04	9.50 – 5.19	9.50 – 6.14	9.50 – 7.34	9.50 – 8.48	9.50 – 6.72
1100 GeV	9.50 – 4.53	9.50 – 5.27	9.50 – 6.30	9.50 – 7.45	9.50 – 8.71	9.50 – 6.81
1300 GeV	9.50 – 4.69	9.50 – 5.41	9.50 – 6.44	9.50 – 7.64	9.50 – 8.87	9.50 – 6.93
1400 GeV	9.50 – 4.86	9.50 – 5.51	9.50 – 6.49	9.50 – 7.74	9.50 – 8.96	9.50 – 6.94
1500 GeV	9.50 – 5.03	9.50 – 5.60	9.50 – 6.62	9.50 – 7.82	9.50 – 9.05	9.50 – 6.98
1600 GeV	9.50 – 5.08	9.50 – 5.71	9.50 – 6.68	9.50 – 7.88	9.50 – 9.08	9.50 – 6.99
1700 GeV	9.50 – 5.18	9.50 – 5.77	9.50 – 6.75	9.50 – 7.90	9.50 – 9.09	9.50 – 7.01
1800 GeV	9.50 – 5.26	9.50 – 5.86	9.50 – 6.77	9.50 – 7.89	9.50 – 9.12	9.50 – 6.96
1900 GeV	9.50 – 5.25	9.50 – 5.90	9.50 – 6.76	9.50 – 7.88	9.50 – 9.19	9.50 – 6.79
2000 GeV	9.50 – 5.31	9.50 – 5.89	9.50 – 6.72	9.50 – 7.94	9.50 – 9.22	9.50 – 6.63
2100 GeV	9.50 – 5.25	9.50 – 5.78	9.50 – 6.63	9.50 – 8.08	9.50 – 9.17	9.50 – 6.41
2200 GeV	9.50 – 5.10	9.50 – 5.64	9.50 – 6.68	9.50 – 8.13	9.50 – 9.15	9.50 – 6.27
2300 GeV	9.50 – 4.96	9.50 – 5.53	9.50 – 6.95	9.50 – 8.12	9.50 – 9.14	9.50 – 6.66
2400 GeV	9.50 – 4.66	9.50 – 5.39	9.50 – 7.03	9.50 – 8.03	9.50 – 9.11	9.50 – 7.27
2500 GeV	9.50 – 4.40	9.50 – 5.72	9.50 – 6.99	9.50 – 7.98	9.50 – 9.11	9.50 – 7.44
2600 GeV	9.50 – 3.96	9.50 – 6.07	9.50 – 6.94	9.50 – 7.94	9.50 – 9.10	9.50 – 7.17
2700 GeV	9.50 – 3.84	9.50 – 6.06	9.50 – 6.84	9.50 – 7.85	9.50 – 9.00	9.50 – 6.90
2800 GeV	9.50 – 5.11 4.82 – 3.49	9.50 – 5.92	9.50 – 6.71	9.50 – 7.73	9.50 – 8.90	9.50 – 6.75
2900 GeV	9.50 – 5.21	9.50 – 5.76	9.50 – 6.49	9.50 – 7.53	9.50 – 8.74	9.50 – 6.49
3000 GeV	9.50 – 5.08	9.50 – 5.56	9.50 – 6.34	9.50 – 7.35	9.50 – 8.49	9.50 – 6.30
3100 GeV	9.50 – 4.64	9.50 – 5.27	9.50 – 6.07	9.50 – 7.13	9.50 – 8.27	9.50 – 5.98

Table G.6: Expected and observed 95% confidence level upper limits in the MSSM light-stau scenario on $\tan\beta$ as a function of m_A testing $H_{h_{\mathrm{SM}}+b}$ versus $H_{h+A+H+b}$.

BSM Higgs	Expected $\tan\beta$ limit					Observed
m_{A} [GeV]	-2σ	-1σ	Median	$+1\sigma$	$+2\sigma$	$\tan\beta$ limit
90 GeV	60.00 – 4.54 1.23 – 0.50	60.00 – 5.48	60.00 – 6.77	60.00 – 7.82	60.00 – 8.91	60.00 – 7.29
100 GeV	60.00 – 3.82 1.03 – 0.50	60.00 – 5.38	60.00 – 6.87	60.00 – 7.90	60.00 – 8.99	60.00 – 7.66
120 GeV	60.00 – 3.78 0.87 – 0.67	60.00 – 3.95	60.00 – 5.34	60.00 – 6.73	60.00 – 7.76	60.00 – 5.05
130 GeV	60.00 – 3.76 1.11 – 0.50	60.00 – 3.88 1.05 – 0.56	60.00 – 4.68 0.91 – 0.68	60.00 – 5.85	60.00 – 7.40	60.00 – 3.98
140 GeV	60.00 – 3.28 1.40 – 0.50	60.00 – 3.70 1.22 – 0.50	60.00 – 4.67 1.11 – 0.50	60.00 – 5.73 1.03 – 0.59	60.00 – 7.13	60.00 – 3.81 1.21 – 0.50
160 GeV	60.00 – 0.50	60.00 – 4.11 3.81 – 0.50	60.00 – 5.48 1.53 – 0.50	60.00 – 6.24 1.17 – 0.50	60.00 – 7.61 1.06 – 0.60	60.00 – 4.66 3.19 – 0.50
180 GeV	60.00 – 0.50	60.00 – 4.08 3.92 – 0.50	60.00 – 5.58 2.27 – 0.50	60.00 – 7.10 1.34 – 0.50	60.00 – 7.81 1.10 – 0.61	60.00 – 5.93 2.70 – 0.50
200 GeV	60.00 – 0.50	60.00 – 4.30 3.66 – 0.50	60.00 – 5.88 1.45 – 0.50	60.00 – 7.52	60.00 – 8.27	60.00 – 7.63 1.65 – 0.50
250 GeV	60.00 – 0.50	60.00 – 6.44 2.36 – 0.66	60.00 – 8.21	60.00 – 8.89	60.00 – 11.17	60.00 – 8.59
300 GeV	60.00 – 6.40 5.50 – 0.50	60.00 – 8.37 2.58 – 0.50	60.00 – 9.46	60.00 – 11.26	60.00 – 12.63	60.00 – 8.86
350 GeV	60.00 – 6.86	60.00 – 8.96	60.00 – 10.55	60.00 – 12.63	60.00 – 15.06	60.00 – 9.20
400 GeV	60.00 – 9.74	60.00 – 12.41	60.00 – 14.09	60.00 – 15.46	60.00 – 18.99	60.00 – 13.33
450 GeV	60.00 – 13.28	60.00 – 14.27	60.00 – 16.06	60.00 – 19.08	60.00 – 21.75	60.00 – 14.10
500 GeV	60.00 – 14.56	60.00 – 16.69	60.00 – 19.16	60.00 – 22.56	60.00 – 24.76	60.00 – 14.89
600 GeV	60.00 – 19.00	60.00 – 20.75	60.00 – 24.34	60.00 – 28.80	60.00 – 33.25	60.00 – 19.70
700 GeV	60.00 – 24.62	60.00 – 28.50	60.00 – 32.75	60.00 – 38.42	60.00 – 44.53	60.00 – 28.33
800 GeV	60.00 – 35.93	60.00 – 40.16	60.00 – 45.90	60.00 – 53.66	–	60.00 – 41.08
900 GeV	60.00 – 45.42	60.00 – 50.56	60.00 – 58.40	–	–	60.00 – 53.62
1000 GeV	60.00 – 59.52	–	–	–	–	–

Table G.7: Expected and observed 95% confidence level upper limits in the MSSM light-stop scenario on $\tan\beta$ as a function of m_A testing $H_{h_{\mathrm{SM}}+b}$ versus $H_{h+A+H+b}$.

BSM Higgs	Expected $\tan\beta$ limit					Observed
m_{A} [GeV]	-2σ	-1σ	Median	$+1\sigma$	$+2\sigma$	$\tan\beta$ limit
90 GeV	60.00 – 5.29 1.15 – 0.70	60.00 – 5.71	60.00 – 6.78	60.00 – 7.79	60.00 – 8.86	60.00 – 7.06
100 GeV	60.00 – 5.20	60.00 – 5.92	60.00 – 7.23	60.00 – 8.01	60.00 – 9.57	60.00 – 7.80
120 GeV	60.00 – 3.98	60.00 – 5.02	60.00 – 5.83	60.00 – 7.37	60.00 – 7.94	60.00 – 6.64
130 GeV	60.00 – 3.79 1.12 – 0.70	60.00 – 4.00 1.07 – 0.70	60.00 – 5.43	60.00 – 6.55	60.00 – 7.67	60.00 – 5.46
140 GeV	60.00 – 3.20 1.43 – 0.70	60.00 – 3.76 1.23 – 0.70	60.00 – 5.14 1.12 – 0.70	60.00 – 5.97 1.04 – 0.70	60.00 – 7.54	60.00 – 4.56 1.26 – 0.70
160 GeV	60.00 – 0.70	60.00 – 4.23 3.55 – 0.70	60.00 – 5.51 1.52 – 0.70	60.00 – 6.51 1.17 – 0.70	60.00 – 7.66 1.07 – 0.70	60.00 – 4.88 2.99 – 0.70
180 GeV	60.00 – 0.70	60.00 – 0.70	60.00 – 5.56 2.36 – 0.70	60.00 – 7.16 1.36 – 0.70	60.00 – 7.85 1.06 – 0.70	60.00 – 5.88 2.94 – 0.70
200 GeV	60.00 – 0.70	60.00 – 0.70	60.00 – 5.81 2.01 – 0.70	60.00 – 7.50	60.00 – 8.36	60.00 – 7.48 2.10 – 0.70
250 GeV	60.00 – 0.70	60.00 – 6.12 5.41 – 0.70	60.00 – 8.10 1.03 – 0.70	60.00 – 8.88	60.00 – 11.19	60.00 – 8.35
300 GeV	60.00 – 0.70	60.00 – 7.46 4.40 – 0.70	60.00 – 9.21 2.09 – 0.70	60.00 – 10.90	60.00 – 12.58	60.00 – 7.93 2.89 – 0.70
350 GeV	60.00 – 0.70	60.00 – 8.38	60.00 – 10.04	60.00 – 12.52	60.00 – 14.97	60.00 – 8.55
400 GeV	60.00 – 9.19	60.00 – 11.10	60.00 – 13.72	60.00 – 14.90	60.00 – 18.81	60.00 – 12.16
450 GeV	60.00 – 11.73	60.00 – 13.55	60.00 – 14.84	60.00 – 18.65	60.00 – 20.87	60.00 – 13.09
500 GeV	60.00 – 13.69	60.00 – 14.85	60.00 – 18.49	60.00 – 21.53	60.00 – 24.58	60.00 – 14.12
600 GeV	60.00 – 18.55	60.00 – 19.67	60.00 – 23.85	60.00 – 28.48	60.00 – 33.26	60.00 – 19.21

Table G.8: Expected and observed 95% confidence level upper limits in the MSSM low-tan β-high scenario on tan β as a function of m_A testing $H_{h_{\mathrm{SM}}+b}$ versus $H_{h+A+H+b}$.

BSM Higgs	Expected tan β limit					Observed
m_{A} [GeV]	-2σ	-1σ	Median	$+1\sigma$	$+2\sigma$	tan β limit
160 GeV	9.50 − 3.96 2.38 − 0.50	9.50 − 4.42 1.90 − 0.50	9.50 − 5.24 1.65 − 0.50	9.50 − 6.12 1.48 − 0.50	9.50 − 7.06 1.03 − 0.50	9.50 − 5.13 2.04 − 0.50
180 GeV	9.50 − 0.50	9.50 − 4.47 2.43 − 0.50	9.50 − 5.46 1.82 − 0.50	9.50 − 6.50 1.59 − 0.50	9.50 − 7.52 1.23 − 0.50	9.50 − 6.13 2.14 − 0.50
200 GeV	9.50 − 0.50	9.50 − 4.89 2.68 − 0.50	9.50 − 6.07 1.90 − 0.50	9.50 − 7.24 1.62 − 0.50	9.50 − 8.34 1.28 − 0.55	9.50 − 7.42 1.77 − 0.50
250 GeV	9.50 − 5.15 2.60 − 0.50	9.50 − 6.25 0.59 − 0.50	9.50 − 7.42	9.50 − 8.83	−	9.50 − 8.17
300 GeV	9.50 − 6.11 3.29 − 1.21	9.50 − 7.44	9.50 − 8.88	−	−	9.50 − 7.74
350 GeV	9.50 − 6.32	9.50 − 7.95	−	−	−	9.50 − 8.20
400 GeV	9.50 − 8.97	−	−	−	−	−
450 GeV	−	−	−	−	−	−
500 GeV	−	−	−	−	−	−

Table G.9: Expected and observed 95% confidence level upper limits in the type-2 2HDM on $\tan\beta$ as a function of $\cos(\beta-\alpha)$ testing $H_{h_{\mathrm{SM}}+b}$ versus $H_{h+A+H+b}$.

BSM Higgs	Expected $\tan\beta$ limit					Observed
$\cos(\beta-\alpha)$	-2σ	-1σ	Median	$+1\sigma$	$+2\sigma$	$\tan\beta$ limit
-1	10.00 – 7.47	10.00 – 8.43	10.00 – 9.62	–	–	10.00 – 9.52
-0.9	10.00 – 7.91	10.00 – 8.96	–	–	–	10.00 – 9.95
-0.8	10.00 – 8.52	10.00 – 9.84	–	–	–	–
-0.7	10.00 – 9.60	–	–	–	–	–
-0.6	–	–	–	–	–	–
-0.5	–	–	–	–	–	–
-0.4	–	–	–	–	–	–
-0.3	–	–	–	–	–	–
-0.2	10.00 – 9.47	–	–	–	–	–
-0.1	10.00 – 6.38 3.22 – 1.00	10.00 – 8.44 2.21 – 1.00	10.00 – 9.83	–	–	10.00 – 8.99
0	10.00 – 1.00	10.00 – 6.81 3.99 – 1.00	10.00 – 8.68 3.11 – 1.00	2.31 – 1.00	2.06 – 1.00	10.00 – 7.32 3.22 – 1.00
0.1	10.00 – 5.48 3.28 – 1.00	10.00 – 6.97 2.22 – 1.00	10.00 – 8.62	–	–	10.00 – 6.63
0.2	10.00 – 6.76 5.46 – 4.40	10.00 – 9.16	–	–	–	10.00 – 9.31
0.3	–	–	–	–	–	–
0.4	–	–	–	–	–	–
0.5	–	–	–	–	–	–
0.6	–	–	–	–	–	–
0.7	10.00 – 9.71	–	–	–	–	–
0.8	10.00 – 9.15	10.00 – 9.88	–	–	–	–
0.9	10.00 – 8.28	10.00 – 9.10	–	–	–	–
1	10.00 – 7.57	10.00 – 8.41	10.00 – 9.61	–	–	10.00 – 9.51

Appendix H

Combination

Numerical results of the combination can be found in the following tables.

Table H.1: Combined expected and observed 95% confidence level upper limits in the MSSM $m_h^{\mathrm{mod}+}$ scenario on $\tan\beta$ as a function of m_A testing $H_{h_{\mathrm{SM}}+b}$ versus $H_{h+A+H+H^{\pm}+b}$.

BSM Higgs	Expected $\tan\beta$ limit					Observed
m_{A} [GeV]	-2σ	-1σ	Median	$+1\sigma$	$+2\sigma$	$\tan\beta$ limit
90 GeV	60.00 – 0.50	60.00 – 0.50	60.00 – 0.50	60.00 – 0.50	60.00 – 0.50	60.00 – 0.50
100 GeV	60.00 – 0.50	60.00 – 0.50	60.00 – 0.50	60.00 – 0.50	60.00 – 0.50	60.00 – 0.50
120 GeV	60.00 – 0.50	60.00 – 0.50	60.00 – 0.50	60.00 – 0.50	60.00 – 0.50	60.00 – 0.50
130 GeV	60.00 – 0.50	60.00 – 0.50	60.00 – 0.50	60.00 – 0.50	60.00 – 6.93 3.18 – 0.50	60.00 – 0.50
140 GeV	60.00 – 0.50	60.00 – 0.50	60.00 – 0.50	60.00 – 5.60 1.50 – 0.50	60.00 – 7.220.98 – 0.67	60.00 – 0.50
160 GeV	60.00 – 1.94 0.70 – 0.68	60.00 – 3.85	60.00 – 5.47	60.00 – 6.36	60.00 – 7.62	60.00 – 4.56
180 GeV	60.00 – 2.83 1.58 – 0.81 0.54 – 0.50	60.00 – 5.07	60.00 – 5.91	60.00 – 7.44	60.00 – 7.92	60.00 – 6.82
200 GeV	60.00 – 0.85 0.78 – 0.51	60.00 – 5.53	60.00 – 6.80	60.00 – 7.78	60.00 – 8.71	60.00 – 7.90
250 GeV	60.00 – 6.59	60.00 – 8.18	60.00 – 8.73	60.00 – 10.56	60.00 – 11.63	60.00 – 8.97
300 GeV	60.00 – 9.26 1.72 – 0.79	60.00 – 9.91	60.00 – 11.75	60.00 – 12.75	60.00 – 14.64	60.00 – 9.97
350 GeV	60.00 – 11.52	60.00 – 12.44	60.00 – 14.33	60.00 – 15.73	60.00 – 18.11	60.00 – 12.22
400 GeV	60.00 – 14.33	60.00 – 14.74	60.00 – 17.87	60.00 – 19.41	60.00 – 22.24	60.00 – 15.44
450 GeV	60.00 – 17.28	60.00 – 18.71	60.00 – 19.77	60.00 – 23.49	60.00 – 24.84	60.00 – 18.48
500 GeV	60.00 – 19.51	60.00 – 21.42	60.00 – 23.98	60.00 – 27.18	60.00 – 29.62	60.00 – 19.93
600 GeV	60.00 – 24.45	60.00 – 27.77	60.00 – 29.83	60.00 – 34.22	60.00 – 38.68	60.00 – 26.34
700 GeV	60.00 – 33.20	60.00 – 34.30	60.00 – 38.76	60.00 – 44.13	60.00 – 49.79	60.00 – 34.19
800 GeV	60.00 – 39.49	60.00 – 43.62	60.00 – 49.38	60.00 – 56.99	–	60.00 – 44.44
900 GeV	60.00 – 48.91	60.00 – 52.72	–	–	–	60.00 – 54.64
1000 GeV	–	–	–	–	–	–

Table H.2: Combined expected and observed 95% confidence level upper limits in the MSSM low-tan β-high scenario on tan β as a function of m_A testing $H_{h_{\mathrm{SM}}+b}$ versus $H_{h+A+H+b}$.

BSM Higgs	Expected tan β limit					Observed
m_{A} [GeV]	-2σ	-1σ	Median	$+1\sigma$	$+2\sigma$	tan β limit
160 GeV	9.50 − 4.00 2.30 − 0.50	9.50 − 4.47 1.89 − 0.50	9.50 − 5.25 1.65 − 0.50	9.50 − 6.15 1.44 − 0.50	9.50 − 7.07 1.03 − 0.50	9.50 − 5.17 1.99 − 0.50
180 GeV	9.50 − 0.50	9.50 − 4.66 2.42 − 0.50	9.50 − 5.48 1.81 − 0.50	9.50 − 6.50 1.60 − 0.50	9.50 − 7.50 1.23 − 0.50	9.50 − 6.11 2.11 − 0.50
200 GeV	9.50 − 0.50	9.50 − 4.89 2.71 − 0.50	9.50 − 5.99 1.89 − 0.50	9.50 − 7.21 1.62 − 0.50	9.50 − 8.35 1.28 − 0.57	9.50 − 7.41 1.76 − 0.50
250 GeV	9.50 − 5.51 2.71 − 0.50	9.50 − 6.23 2.36 − 0.50	9.50 − 7.39 1.80 − 0.58	9.50 − 8.83 1.60 − 0.66	1.30 − 0.68	9.50 − 8.12 1.83 − 0.52
300 GeV	9.50 − 6.17 3.27 − 0.50	9.50 − 7.39 2.50 − 0.50	9.50 − 8.77 1.86 − 0.50	1.63 − 0.50	1.52 − 0.50	9.50 − 7.67 2.50 − 0.50
340 GeV	9.50 − 6.16 2.18 − 0.50;	9.50 − 7.7 1.98 − 0.50;	1.68 − 0.50;	1.50 − 0.50;	1.04 − 0.50;	9.50 − 7.89 1.72 − 0.50;
350 GeV	9.50 − 5.97 0.55 − 0.50	9.50 − 7.90 0.53 − 0.50	0.51 − 0.50	–	–	9.50 − 8.15 0.51 − 0.50
400 GeV	9.50 − 9.03	–	–	–	–	–
450 GeV	–	–	–	–	–	–
500 GeV	–	–	–	–	–	–

Table H.3: Part one of the combined expected and observed 95% confidence level upper limits in the type-2 2HDM on $\tan\beta$ as a function of $\cos(\beta-\alpha)$ testing $H_{h_{\mathrm{SM}}+b}$ versus $H_{h+A+H+b}$.

BSM Higgs	Expected $\tan\beta$ limit					Observed
$\cos(\beta-\alpha)$	-2σ	-1σ	Median	$+1\sigma$	$+2\sigma$	$\tan\beta$ limit
-1	10.00 – 7.88 2.76 – 1.00	10.00 – 8.52 2.72 – 1.00	10.00 – 9.46 2.29 – 1.00	2.03 – 1.00	1.31 – 1.00	10.00 – 8.72 2.49 – 1.00
-0.9	10.00 – 5.57 4.53 – 1.00	10.00 – 5.85 4.28 – 1.00	10.00 – 6.41 4.11 – 1.00	10.00 – 6.99 2.59 – 1.00	10.00 – 8.80 1.42 – 1.00	10.00 – 5.51 4.58 – 1.00
-0.8	10.00 – 5.34 4.68 – 1.00	10.00 – 5.69 4.35 – 1.00	10.00 – 6.04 4.14 – 1.00	10.00 – 7.11 3.94 – 1.00	2.12 – 1.00	10.00 – 5.28 4.73 – 1.00
-0.7	10.00 – 5.76 4.34 – 1.00	10.00 – 5.86 4.26 – 1.00	10.00 – 6.44 4.11 – 1.00	10.00 – 8.28 3.60 – 1.00	2.28 – 1.00	10.00 – 5.75 4.36 – 1.00
-0.6	10.00 – 5.88 4.31 – 1.00	10.00 – 5.99 4.18 – 1.00	10.00 – 7.01 4.06 – 1.00	3.03 – 1.00	2.09 – 1.00	10.00 – 5.79 4.33 – 1.00
-0.5	10.00 – 5.95 4.18 – 1.00	10.00 – 6.94 4.12 – 1.00	3.53 – 1.00	2.41 – 1.00	1.85 – 1.00	10.00 – 5.99 4.19 – 1.00
-0.4	10.00 – 7.60 3.74 – 1.00	10.00 – 9.97 3.79 – 1.00	2.81 – 1.00	2.15 – 1.00	1.45 – 1.00	10.00 – 8.36 4.03 – 1.00
-0.3	10.00 – 9.33 3.30 – 1.00	3.00 – 1.00	2.31 – 1.00	2.02 – 1.00	1.23 – 1.00	3.18 – 1.00
-0.2	10.00 – 9.76 2.48 – 1.00	2.33 – 1.00	2.10 – 1.00	1.45 – 1.00	1.14 – 1.00	10.00 – 9.81 2.31 – 1.00
-0.1	10.00 – 7.09 2.66 – 1.00	10.00 – 8.48 2.46 – 1.00	10.00 – 9.84 1.98 – 1.00	1.27 – 1.00	1.09 – 1.00	10.00 – 8.54 2.47 – 1.00

Table H.4: Part two of the the combined expected and observed 95% confidence level upper limits in the type-2 2HDM on $\tan\beta$ as a function of $\cos(\beta-\alpha)$ testing $H_{h_{\mathrm{SM}}+b}$ versus $H_{h+A+H+b}$.

BSM Higgs	Expected $\tan\beta$ limit					Observed
$\cos(\beta-\alpha)$	-2σ	-1σ	Median	$+1\sigma$	$+2\sigma$	$\tan\beta$ limit
0	10.00 – 1.00	10.00 – 6.97 3.95 – 1.00	10.00 – 8.80 3.12 – 1.00	2.30 – 1.00	2.05 – 1.00	10.00 – 7.02 3.50 – 1.00
0.1	10.00 – 6.20 2.61 – 1.00	10.00 – 7.25 2.28 – 1.00	10.00 – 8.66 1.54 – 1.00	1.17 – 1.00	1.05 – 1.00	10.00 – 6.88 2.35 – 1.00
0.2	10.00 – 8.19 1.68 – 1.00	10.00 – 9.26 1.44 – 1.00	1.21 – 1.00	1.10 – 1.00	1.06 – 1.00	10.00 – 8.87 1.67 – 1.00
0.3	1.27 – 1.00	1.23 – 1.00	1.13 – 1.00	1.08 – 1.00	1.04 – 1.00	1.25 – 1.00
0.4	1.31 – 1.00	1.29 – 1.00	1.16 – 1.00	1.07 – 1.00	1.00 – 1.00	1.34 – 1.00
0.5	1.45 – 1.00	1.25 – 1.00	1.07 – 1.00	–	–	1.44 – 1.00
0.6	–	–	–	–	–	–
0.7	10.00 – 8.39 2.35 – 1.81	10.00 – 8.85 2.10 – 1.90	–	–	–	10.00 – 8.78 2.29 – 1.73
0.8	10.00 – 7.56 2.57 – 1.31	10.00 – 7.73 2.48 – 1.53	10.00 – 8.87 2.08 – 1.91	–	–	10.00 – 7.64 2.62 – 1.00
0.9	10.00 – 6.84 4.10 – 1.00	10.00 – 6.89 3.22 – 1.00	10.00 – 7.65 2.36 – 1.00	10.00 – 8.93 1.81 – 1.00	1.15 – 1.00	10.00 – 6.82 4.07 – 1.00
1	10.00 – 8.24 3.01 – 1.00	10.00 – 8.63 2.84 – 1.00	10.00 – 9.51 2.29 – 1.00	2.04 – 1.00	1.32 – 1.00	10.00 – 8.84 3.36 – 1.00